



HAL
open science

Development of a portable gamma camera for accurate 3-D localization of radioactive hotspots

Vincenzo Paradiso

► **To cite this version:**

Vincenzo Paradiso. Development of a portable gamma camera for accurate 3-D localization of radioactive hotspots. Other [cond-mat.other]. Normandie Université, 2017. English. NNT : 2017NORMC209 . tel-03669788

HAL Id: tel-03669788

<https://theses.hal.science/tel-03669788>

Submitted on 17 May 2022

HAL is a multi-disciplinary open access archive for the deposit and dissemination of scientific research documents, whether they are published or not. The documents may come from teaching and research institutions in France or abroad, or from public or private research centers.

L'archive ouverte pluridisciplinaire **HAL**, est destinée au dépôt et à la diffusion de documents scientifiques de niveau recherche, publiés ou non, émanant des établissements d'enseignement et de recherche français ou étrangers, des laboratoires publics ou privés.



Normandie Université

THÈSE

Pour obtenir le diplôme de doctorat

Spécialité : Physique

Préparée au sein de l'Université de Caen Normandie

**Development of a portable gamma camera for accurate
3-D localization of radioactive hotspots**

Présentée et soutenue par
Vincenzo Paradiso

**Thèse soutenue publiquement le 31 Mars 2017
devant le jury composé de**

M. Jean-Claude Angélique	Professeur des universités, ENSICAEN	Examineur
Mme Irène Buvat	Directeur de Recherche, CNRS, Université Paris-Sud	Rapporteur
M. Olivier Limousin	Ingénieur chercheur HDR, CEA, Saclay	Rapporteur
M. Etienne Liénard	Professeur des universités, UNICAEN	Directeur de thèse
M. Khalil Amgarou	Docteur en Physique, CEA, Marcoule	Examineur
M. Nicolas Blanc de Lanaute	Docteur Ingénieur, Mirion Technologies Canberra	Examineur

Thèse dirigée par Etienne Liénard, Laboratoire de Physique Corpusculaire de Caen



Acknowledgements

I would like to express my sincere gratitude to my advisor, Etienne Liénard. His guidance and support have been a constant reference for me. Thank you for being always there, for our numerous and lengthy conversations, and for your precious suggestions during this long journey.

I am deeply grateful to Khalil Amgarou, for supervising and encouraging my research from the very beginning, during his stay at CANBERRA as well as when he joined CEA. Thank you for your dedication and for teaching me the principles of proper and unbiased experimental physics.

A special thanks goes to my manager, Nicolas Blanc de Lanaute. I greatly appreciate the freedom he has given me, both as an engineer and as a doctoral researcher. During our collaboration, we have been able to reach all our objectives in a constructive and trustworthy environment.

I wish to thank also the rest of the committee members, Jean-Claude Angélique, Irène buvat, and Olivier Limousin, for their insightful and valuable feedback. I am proud and honoured that you have accepted to be on my thesis committee.

I gratefully acknowledge the funding received towards my PhD by the Marie Skłodowska-Curie Actions, via the EDUSAFE research program. I am especially grateful to Olga Beltramello, EDUSAFE network coordinator, and I would like to acknowledge all of the research fellows with whom I collaborated in the lively and stimulating CERN environment.

Almost every experiment described in this thesis would not have been possible without the support I received from the CANBERRA team. Many thanks go especially to Florent Bonnet, Audrey Patoz, Pierre Couturier, Adrien Gallozzi, Xavier Ducoux, and Thierry Guillaume.

My appreciation goes also to the support received through the collaborative work with CEA. I would especially like to thank Vincent Schoepff, Guillaume Amoyal, and Frédéric Carrel, for our helpful discussions and for the experiments performed together.

I wish to express my deep gratitude to my teachers at the department of Computer Science of the University of Turin, for their invaluable contribution to my formation. In particular, I would like to thank Sandro Coriasco, Piergiorgio Odifreddi, Elio Giovannetti, Susanna Donatelli, Simona Ronchi Della Rocca, Maria Luisa Sapino, Marco Maggiora, Maurizio Lucenteforte, and Marco Grangetto.

Finally, I thank my life partner, Sabah, to whom this dissertation is dedicated.

Abstract

A coded aperture gamma camera for retrieving the three-dimensional (3-D) position of radioactive sources is presented. This is of considerable interest for a wide number of applications, ranging from the retrieval of the 3-D shape of radioactive objects to augmented reality systems.

Current portable γ -cameras only provide the relative directional position of the hotspots within their field of view. That is, they do not provide any metric information concerning the located sources.

In this study, we propose two approaches to estimate the distance of the surrounding hotspots, and to autonomously determine if they are occluded by an object. The first consists in combining and accurately calibrating the gamma camera with a structured-light depth sensor. The second approach allows the estimation of the source-to-detector distance by means of stereo gamma imaging.

To geometrically align the images obtained by the gamma, depth, and optical cameras used, a versatile calibration procedure has been designed and carried out. Such procedure is flexible, since it employs as a calibration target a phantom intentionally easy to build and inexpensive, allowing the calibration of the γ -camera with the other sensors using only one radioactive point source.

Experimental results showed that such calibration procedure yields to sub-pixel accuracy both in the re-projection error and the overlay of radiation and optical images. A quantitative analysis concerning the accuracy and resolution of the retrieved source-to-detector distance is also provided, along with an insight into the respective most influential factors.

Moreover, the results obtained validated the choice of the geometry of the pinhole model for a coded aperture gamma camera.

Table of contents

1	Introduction	1
1.1	Motivation of the work	1
1.2	Pinhole and coded aperture gamma imaging	2
1.2.1	Pinhole gamma cameras	3
1.2.2	Coded aperture gamma cameras	6
1.3	Manuscript overview	11
2	Experimental characterization of the iPIX gamma camera	13
2.1	Overview of the iPIX gamma camera	13
2.2	Timepix chip with CdTe semiconductor	14
2.2.1	Counting modes	15
2.2.2	Pixel output signal	16
2.2.3	Charge sharing between adjacent pixels	16
2.2.4	Pulse summation and pile-up effects	17
2.2.5	Threshold equalization	18
2.3	Coded aperture masks	19
2.4	Experimental characterization	20
2.4.1	ToT data quality	22
2.4.2	ToT-energy calibration	24
2.4.3	Dose rate linearity	25
2.4.4	Dose calibration factor vs. incident photon energy	26
2.4.5	Cluster sizes vs. incident photon energy	26
2.4.6	Sensitivity and influence of background radiation	28
2.4.7	Off-axis response	33
2.4.8	Angular resolution	37
2.5	Conclusions	38
3	Development of a panoramic gamma camera for the ATLAS detector	41
3.1	Introduction to the Large Hadron Collider	42
3.1.1	The ATLAS experiment	44
3.1.2	Radiation background at ATLAS	45

3.1.3	Safety and radiation protection at ATLAS	47
3.2	The EduPIX gamma camera	52
3.2.1	Data acquisition	53
3.2.2	Preliminary tests with extended sources	57
3.2.3	EduPIX software and interfacing	63
3.3	Panoramic Gamma Imaging	66
3.3.1	Basic concepts	68
3.3.2	Features search and matching	71
3.3.3	Homography estimation between adjacent images	72
3.3.4	Multi-band blending	74
3.3.5	Radiation image stitching	75
3.3.6	Outline of the procedure for generating panoramic images	76
3.4	Results and discussion	76
3.4.1	Radiation image stitching with planar sources	77
3.4.2	Panoramic images with planar and point sources	82
3.4.3	Testing at the ATLAS detector	84
3.5	Conclusions	87
4	3-D localization of radioactive hotspots via portable gamma cameras	89
4.1	General context	89
4.2	A portable proof of concept for 3-D gamma imaging	92
4.2.1	Combining a coded aperture gamma camera with a structured-light sensor	92
4.2.2	A portable stereo gamma imager	94
4.3	A versatile multi-modal camera calibration	95
4.3.1	Basic concepts	96
4.3.2	Design of an experimental calibration phantom	102
4.3.3	Multi-modal camera calibration	102
4.3.4	Summary of the experimental setup	106
4.4	Calibration results and multimodal image registration	107
4.4.1	Evaluation of the reprojection error	107
4.4.2	Registration of optical and radiation images	109
4.5	Automatic retrieval of the distance of surrounding radioactive sources	110
4.5.1	Depth maps and radiation images mapping	110
4.5.2	Stereo gamma imaging	112
4.5.3	Integration of structured-light techniques and stereo gamma imaging for portable gamma cameras	118
4.5.4	Accuracy evaluation of the stereo gamma camera	122
4.6	Volumetric representation of radioactive hotspots	124
4.6.1	Data acquisition for 3-D gamma point clouds	126
4.6.2	Multimodal fusion with the 3-D position of radiation sources	127

4.7	Conclusions	130
5	General conclusions and perspectives	133
	References	137
	Appendix A Radiation protection basics	151
	Appendix B KIT measurement results	161
	Appendix C Summary of the laboratory radioactive sources used	169
	List of tables	173
	List of figures	175

Chapter 1

Introduction

*“With this apparatus, powerful in its way,
very fair shadow pictures were obtained.”*

— T. Glover Lyon, in *Roentgen’s rays as a cure of disease*.
The Lancet, 1896.

1.1 Motivation of the work

In-situ localization of radiation emitting objects or hotspots is of prime concern regarding maintenance, decommissioning, and clean-up activities of nuclear facilities [1, 2]. It is also of considerable importance for delimiting contaminated areas in radiological emergency situations [3] as well as in homeland security for detecting illicit traffic of nuclear materials [4, 5].

Dose and survey meters are currently among the most common portable radiation detection instruments used. However, they do not provide directional information regarding the location in space of the radiation sources. On the other hand, portable gamma cameras allow the operators to remotely localize the position of the surrounding radioactive sources by superimposing a radiation map onto the respective optical images.

An earlier attempt to develop a portable gamma imaging system was carried out in the 1990s by CEA¹. The outcome of this effort was the ALADIN² prototype [6], which in turn led to the development of the CARTOGAM gamma camera [7], widely commercialized by CANBERRA³ during the last decade.

CARTOGAM is a mature technology combining an inverted double-cone collimator⁴ to be used as a single pinhole aperture, a CsI(Tl)⁵ scintillation crystal, a micro-channel plate, and a CCD camera. With the exception of the pinhole aperture, the whole instrument is fully shielded against

¹The French Alternative Energies and Atomic Energy Commission.

²ALADIN is a French acronym for *Appareil de Localisation de l’Activité γ Dans les Installations Nucléaires*.

³Now Mirion Technologies Canberra.

⁴Two right circular cones placed apex-to-apex.

⁵Thallium activated Cesium Iodide.

background radiation. Although such instrument is still demonstrating satisfactory performances, namely at severe irradiation conditions, its heavy weight (15 kg for the detection head, including the shield) poses several constraints from a practical point of view.

Nowadays, more compact γ -cameras for industrial applications [8–16] are undergoing impressive developments and improvements in terms of lightness, usability, response sensitivity, angular resolution, and spectrometric capabilities. Nevertheless, such instruments only provide the two-dimensional (2-D) position concerning the radioactive emitting objects in the surrounding environment. That is, they do not provide any information concerning the distance between the located sources and the instrument used. This is of significant importance also for those scenarios that require the possibility of localizing and identifying radioactive sources when an occluding object is present between the hotspot and the gamma camera.

Besides, the adoption of different types of sensors, such as gamma and optical cameras, leads to significant parallax errors between the respective acquired images, which are currently corrected only by manually inferring the average source-to-detector distance.

The geometric alignment (i.e. registration) of multimodal⁶ images allows the assessment of the relationship between the coordinate systems of different types of cameras [17]. In the medical imaging field, extensive study has been conducted concerning multimodal image registration [18–21]. Fusion of different imaging methodologies such as X-ray computed tomography (CT), single-photon emission computed tomography (SPECT), positron emission tomography (PET), and magnetic resonance imaging (MRI) yields the accurate registration and overlay of the respective reconstructed images, and therefore the combination of their clinical advantages as well as the development of image-guided neurosurgery techniques [22–25].

Nonetheless, little work has been done in the past concerning image registration in the context of *portable* gamma cameras for nuclear facilities, and thus also regarding the accurate fusion of multimodal images generated by such instruments, including the autonomous estimation of the distance of the surrounding radioactive sources respect to the camera.

The design and development of a portable gamma camera capable of accurately registering multimodal images and automatically retrieving the 3-D location of any detected radioactive object are the main focus of the present study. A special emphasis is dedicated to the distance measurements estimated between the γ -camera and the sought radioactive hotspots, discussing also the capability of the prototype to autonomously determine if an object is occluding the located radioactive sources.

1.2 Pinhole and coded aperture gamma imaging

The development of imaging instruments capable of retrieving the location of radiation sources have found applications in a number of disciplines and domains, such as medical imaging, astronomy, and the nuclear power industry.

⁶Multimodality refers to images acquired by means of different types of cameras.

In what follows of the present section, we introduce the history and the main concepts regarding pinhole and coded aperture gamma cameras, on which all methods discussed and proposed in the present dissertation are based. Cameras based on Compton scattering imaging [26, 15, 16, 27], on the other hand, go beyond the scope of this study, and are thus not addressed here.

1.2.1 Pinhole gamma cameras

The concept of pinhole camera was applied to penetrating radiations as early as 1896 [28]. By using a sheet of metal with a small circular hole and a photographic plate, Wilhelm Röntgen obtained a projected image of the anode of one of his first X-ray tubes.

Only after more than 50 years, in 1949, Copeland and Benjamin [29] demonstrated the effectiveness of a pinhole camera also with gamma-ray sources. In their experiment, they first made a hole with a diameter of 0.1 mm in a lead shield. Then, they placed such shield between an X-ray film and a radium needle with 222 MBq activity, obtaining a projected and inverted image of the source with a total exposure time of 24 hours.

The scintillation gamma camera

In 1952, Hal Anger designed and built a gamma camera [30] based on the same principle of that of Copeland and Benjamin, but employing a NaI(Tl)⁷ crystal as an intensifying screen, in order to improve the sensitivity of the camera, and thus decrease the exposure time needed to obtain a radiation image.

In 1958, Anger himself proposed an improved version of his gamma camera [31]. In addition to the lead shield with a pinhole aperture, the employed scintillating crystal within the shield was viewed by *multiple* (seven) photomultiplier tubes (see Figure 1.1).

As explained in more detail in his paper [31], the light produced by any scintillation resulting from the interaction of the gamma-rays with the NaI(Tl) crystal was emitted isotropically and received by all phototubes. The pulses so obtained from the latter were given as input to a signal matrix circuit, which in turn returned three output signals (X , Y , and Z). Two of them (X and Y) were *positioning* signals, whereas the third one, Z , was the sum of all pulses from all seven phototubes used.

The adoption of multiple phototubes was possible because regardless of where the scintillation originated in the crystal, the produced Z signal had the same magnitude. The first two signals so obtained were applied to the X and Y input terminals of an oscilloscope, whereas the Z signal was first processed (filtered) by a pulse-height selector⁸. When the Z signal was not filtered by the pulse-height selector, the oscilloscope beam was deflected according to the positioning X and Y signals to the point corresponding to the location of the original scintillations in the crystal. The

⁷Thallium-activated sodium iodide.

⁸A pulse-height selector is a circuit that accepts pulses with amplitudes between two adjacent levels (thresholds) and rejects all others. When a pulse is within the thresholds, an output pulse of constant amplitude and profile is produced.

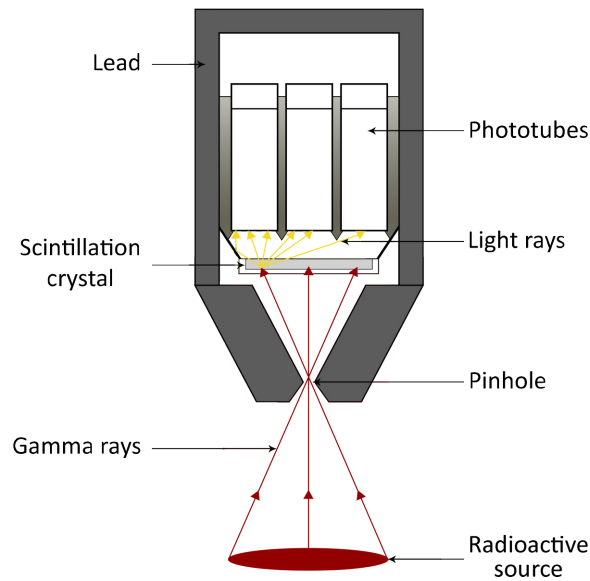


Fig. 1.1: Illustration of the scintillation camera proposed by Anger in [31].

latter were therefore reproduced as flashes on the oscilloscope screen at increased brightness, and then photographed by a Polaroid-Land camera⁹.

Compared to the originally proposed gamma camera, the advantages of this new version proposed by Anger were multiple. For example, the response within the camera field of view (FOV) was more uniform, and the area to be imaged could be changed by simply moving the camera closer or further away from the radiation emitting source.

The scintillation camera has been subject ever since of many improvements, such as the use of multichannel collimators [32] or the adoption of arrays of parallel holes [33], to constrain the angles of incidence by which the decay photons could enter the detector material. With applications ranging from astronomy and medical imaging [34–36] to the nuclear industry [6], gamma cameras based on the pinhole configuration have been proposed in a number of alternative configurations.

In the last decades, moreover, the photographic films typically employed in scintillator-based imaging detectors have been gradually replaced by CCD¹⁰ [39] and CMOS¹¹ image sensors, mainly due to their high quantum efficiency and the possibility of storing the obtained radiation images in digital formats, leading, therefore, to the proposal and adoption of new associated digital image processing techniques.

Since the active areas of CCD and CMOS sensors are usually smaller in comparison to the films previously used in scintillator detectors, a de-magnification process was typically employed in the coupling of the scintillator to these sensor. This allowed the extension of the detection area while retaining an acceptable spatial resolution, and was achieved by using for example

⁹Land cameras are instant cameras with self-developing film named after their inventor, Edwin Land.

¹⁰The Charge-Coupled Device or CCD was invented in 1969 at AT&T Bell Labs by Willard Boyle and George E. Smith [37], for which they were awarded in 2009 the Nobel Prize for Physics [38].

¹¹Complementary Metal Oxide Semiconductor.

(a) *The ALADIN prototype [41].*(b) *The CARTOGAM gamma camera [7].*

Fig. 1.2: Main pinhole gamma cameras developed by CEA and CANBERRA.

fibre-optic tapers¹² [40]. In the context of gamma imaging for nuclear facilities, an example of such type of instruments is the CARTOGAM [7] (Fig. 1.2b), which was the industrialized version developed by CANBERRA of the ALADIN gamma camera [6] (Fig. 1.2a), a prototype designed and developed from the CEA Reactor Design Department at Saclay in collaboration with the CEA Nuclear Facilities Decommissioning Unit (UDIN).

The CARTOGAM gamma camera

As explained in [7], the CARTOGAM consists mainly of a CsI(Tl) scintillator with a thickness between 2 and 4 mm, a CCD camera, and an image intensifier. The main components of the latter were in turn a photocathode, a micro-channel plate where the signal was amplified, and a phosphor screen. The optical couplings were performed by fibre-optic tapers (see Fig. 1.3).

The CARTOGAM system had a diameter of 8 cm and a mass of 15 kg. The detection efficiency of the 4 mm thick scintillator used was 12.5% for ^{137}Cs and 8.5% for ^{60}Co . Similarly to the ALADIN, the collimator had a double-cone aperture with a FOV of 30° or 50°, respectively. The optical images are captured by the same detector used for acquiring gamma images, due to the scintillator transparency also to photons with energy in the visible spectrum.

At the collimator centre of the detector, there was a small removable lens. After capturing the optical image, such lens was remotely removed, the detector was plunged into darkness, the intensifier gain increased, and the images were acquired by the CCD camera at a frequency of ~ 1 Hz.

The spatial resolution and signal-to-noise ratio (SNR) of the images obtained by the instrument were considered satisfactory [7, 42]. For this reason, the CARTOGAM gamma camera has been employed since its release in many nuclear facilities to help locating radioactive sources in contaminated cells.

As suggested in [43], although considerable progress was made concerning pinhole gamma cameras, with these instruments only a very small fraction (0.1 - 0.01%) of the gamma ray photons

¹²Fibre-optic tapers use a coherent fibre-optic plate for transmitting an image from its input surface to its output surface.

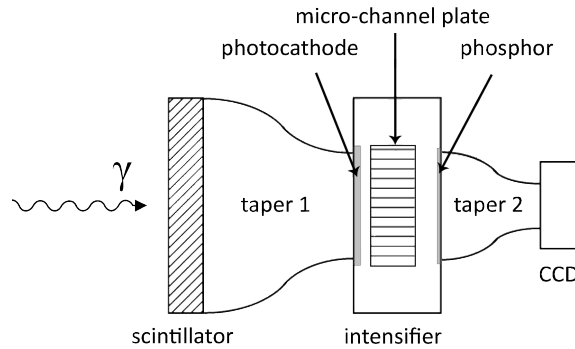


Fig. 1.3: Diagram of the detector of the CARTOGAM gamma imaging system [7].

emitted by the source is transmitted to the detector plane (i.e. the scintillator crystal in the case of the ALADIN and the CARTOGAM). This fraction can be incremented only by increasing the diameter of the pinhole, thus significantly degrading the spatial resolution of the gamma images obtained. In order to improve the sensitivity and meanwhile the overall signal-to-noise ratio of the radiation images obtained, CEA developed in collaboration with the Kurchatov Institute [44] a gamma camera based on the coded aperture technique [8].

The main concepts of the coded aperture imaging approach are provided in the section below, with a focus on the Modified Uniformly Redundant Arrays (MURA) [45], which is the family of patterns of the masks used by all the gamma cameras discussed and developed in the following chapters of the present dissertation.

1.2.2 Coded aperture gamma cameras

Imaging systems based on the coded aperture technique typically employ a mask, consisting of an array of opaque and transparent elements to the source fluxes, together with a position sensitive detection plane [46]. Every source element within the field of view of the system projects a shadow of the aperture onto the detector (see illustration of Fig. 1.4). Therefore, if the source is a single point source, the detected two-dimensional distribution of events reproduces a mask pattern (or part of it), whereas in case of a more complex source or arrangement of point sources the recorded shadowgram is the *sum* of such distributions.

The first coded aperture imaging technique known in the literature is the Fresnel Zone Plate (FZP) [47], proposed by Mertz and Young in 1961. This technique was successfully demonstrated, for example, in X- and γ -ray tomographic imaging [48]. Referred to in the early days as *Zone-plate coded imaging*, the mask used consisted of a circularly-symmetric aperture, where a series of concentric annuli were alternately opaque and transparent, with the n^{th} annulus being given by:

$$r_n = r_0\sqrt{n}, \quad (1.1)$$

where r_0 is the radius of the central disk, which may be either opaque or transparent.

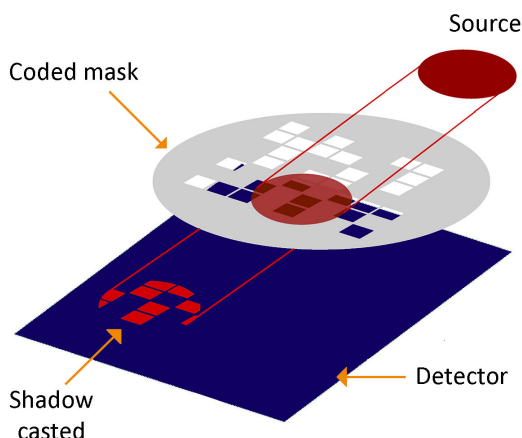


Fig. 1.4: Illustration of the principle of the coded aperture technique. In this example, incoming photons emitted from a radioactive source hit a coded mask, casting a shadow of part of its pattern onto a position-sensitive detector.

Such pattern is illustrated in Fig. 1.5a, whose one of the main properties is that each annulus has the same area, thus resulting into an overall transmission of the source fluxes of $\sim 50\%$. As noted in [46], the FZP has in the ideal case an autocorrelation function consisting of a single peak surrounded by a perfectly flat background. However, in practice, the resulting point spread function (PSF) is surrounded by a series of concentric lobes (sidelobes), as shown in Fig. 1.5b.



Fig. 1.5: (a) A Fresnel Zone Plate (FZP) pattern with three opaque rings and (b) its autocorrelation function [46].

Multiplexing imaging has received though greater attention and use with aperture arrays based on multiple pinholes, originally proposed in 1968 by Dicke [49] and Ables [50], independently. Their approach has played a crucial role in astronomy (and still does) to help resolving, for example, the origin of X-ray bursts from distant galaxies [51].

As suggested in [52], while improving the signal-to-noise ratio of the acquired images, a second important motivation of the coded aperture approach was to perform tomography, as shown by Barret [43]. In fact, depending on the distance from the aperture, radiation sources cast shadows of the aperture onto the detector with different sizes, allowing the reconstruction of an

object in a specific depth (distance). More specifically, this is achieved by treating the resulting radiation image as it is was formed by an aperture scaled to the size of the shadow produced by the object at the depth under consideration. This property results particularly beneficial in medical imaging.

Various algorithms have been proposed in the literature for reconstructing the original source distribution [53, 54]. Two categories of such algorithms have received though greater consideration, respectively called *matched filtering* and *mismatched filtering* techniques [53]. Matched filtering refers to coded aperture algorithms where the reconstructed point spread function is the periodic autocorrelation function of the aperture pattern. On the other hand, mismatched filtering refers to those methods where the detector image is cross-correlated with the periodic inverse filter of the aperture array [54].

As explained in [53], if the periodic autocorrelation function of the aperture array has *constant* sidelobes (i.e. lobes surrounding the main peak of the PSF), matched and mismatched filtering become identical, except for a constant scaling and offset. Arrays with this specific property are commonly referred to as *Uniformly Redundant Arrays* (URA), term introduced the first time by Fenimore and Cannon in 1978 [52]. They are widely considered as being the optimum aperture arrays [55, 56, 52], since they combine the advantages of matched filtering methods, which are optimal with respect to the contribution of quantum noise in the detector measurements to the reconstruction, and mismatched filtering reconstruction that allows the avoidance of systematic noise.

Consequently, in the context of portable gamma cameras for industrial applications, the Kurchatov Institute and CEA initiated a collaboration aiming at developing and testing coded masks belonging to the URA family, by fabricating masks with patterns of type *HURA* (*Hexagonal Uniformly Redundant Arrays*) [57], and integrating them with the ALADIN and CARTOGAM systems. Each mask was classified by its rank¹³ and its thickness in mm (see Fig. 1.6).



(a) Mask rank 6 (127 transparent elements), 12 mm-thick.

(b) Mask rank 9 (271 transparent elements), 6 mm-thick.

Fig. 1.6: HURA masks designed and built (in tungsten) for the ALADIN and CARTOGAM gamma cameras [8].

¹³The rank of a mask indicates the number of transparent elements (holes). A detailed table with the main information of each rank can be found in [45].

Furthermore, the CsI(Tl) scintillator used in the ALADIN and CARTOGAM systems was replaced by a pixellated semiconductor detector, allowing therefore a *direct* conversion of the incident gamma photons into electrical signal. The semiconductor material used was a 1 mm thick CdTe¹⁴ detector directly bump-bonded to the Medipix2 chip [58], manufactured in a six-metal 0.25 μm CMOS and consisting of an active area of 256×256 square pixels with 55 μm side. The resulting sensitive detection area was thus 1.98 cm², representing 87% of the entire chip area. The adoption of the CdTe crystal allowed the Medipix2 chip to be used for a wide photon energy range [59].

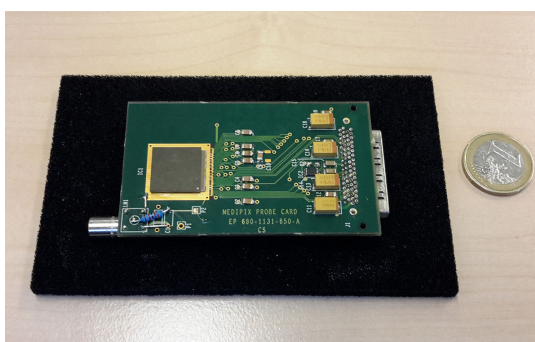


Fig. 1.7: The Medipix2 chip.

Compared to the original pinhole configuration, by integrating such masks and detector with the ALADIN and CARTOGAM systems, preliminary results obtained in laboratory showed a gain of a factor between 5 and 20 in terms of needed exposure time for localizing a source (depending on the energy of the incident photons), and a factor between 2 and 2.5 concerning the achieved angular resolution (depending on the mask used and its distance from the detector) [60]. Due to such satisfactory results, CEA LIST (*Laboratoire d'Intégration de Systèmes et des Technologies.*) presented in 2010 a new compact gamma camera, called GAMPIX [9] (Fig. 1.8), using coded masks based on the MURA family [45], which were employed according to the energy of the incoming photons on the detector. An evaluation of its performances can be found in [9].

The GAMPIX prototype led to the development of the iPIX gamma camera [10], the industrialized gamma imaging system proposed by CANBERRA and based on the coded aperture technique. The iPIX is extensively discussed in Chapter 2.

As mentioned above, as the MURA masks are also used by all gamma cameras discussed hereinafter for the present study, we provide below an overview of the corresponding encoding and decoding processes applied for retrieving the position of radioactive sources with respect to the FOV of a given γ -camera.

Encoding and Decoding process of Modified Uniformly Redundant Arrays (MURA)

As thoroughly explained in [45], the data modulated by a MURA coded mask is represented as a 2-D matrix, D , with each component D_{ij} representing the number of photon interactions registered

¹⁴Cadmium telluride.



Fig. 1.8: The GAMPIX gamma camera developed by CEA LIST [9].

in the $(i, j)^{\text{th}}$ detector element. The coded aperture itself is also represented as a matrix, where each component (cell) A_{ij} is assigned $A_{ij} = 1$ if the $(i, j)^{\text{th}}$ mask element is transparent to the incident radiation (a hole), and $A_{ij} = 0$ otherwise (opaque). The sought source spatial distribution within the γ -camera FOV is represented as a matrix S with each component S_{ij} containing the number of emitted photons that have been registered by the pixelated detector.

With these definitions, the recorded data (matrix) D is given by the following equation:

$$D = S \otimes A + B, \quad (1.2)$$

being the symbol \otimes the correlation operator and the last term B a matrix representing the background contribution not modulated by the coded aperture mask. This term thus includes, for example, electronic noise as well as photons that pass through opaque regions of the aperture, high energy cosmic ray particles, etc.

In order to reconstruct the recorded data (i.e. decode it), the matrix D is then correlated with a decoding matrix G representing the coded aperture pattern, multiplied by a scaling factor. G must be the correlational inverse of A and unimodular¹⁵. Then, the computed source distribution is denoted as \hat{S} (the caret ^ indicates that the quantity is an estimate) and is given by:

$$\hat{S} = D \otimes G. \quad (1.3)$$

Substitution of Eq. (1.2) into Eq. (1.3) yields:

$$\hat{S} = (S \otimes A) \otimes G + B \otimes G. \quad (1.4)$$

By construction, G is the correlational inverse of A , and, therefore:

$$A \otimes G \equiv \delta, \quad (1.5)$$

where δ is the Kronecker delta function [45]. Consequently, Eq. (1.4) reduces to:

¹⁵As a reminder, a matrix unimodular is a matrix with all components equal in magnitude.

$$\hat{S} = S + B \otimes G, \quad (1.6)$$

which means that the source location can be easily reconstructed, as the background term, in our specific context, is usually neglected.

The source location \hat{S} reconstructed with such method and rendered on the gamma camera FOV is hereinafter also referred to as *radiation image*, *decoded γ -image*, or simply *γ -image*, the terms are all synonymous.

As explained in [61], an important limitation of such reconstruction technique is due to the systematic variations of the background level measured by different segments of the detector plane. A solution to this problem is to observe the source field in alternate measurements, by *inverting* the mask pattern by a 90° rotation. Such rotation creates an *antimask* of the original mask, except for the central element, without additional weight and complex mechanical manipulations. By performing alternate measurements with a mask and with an antimask for equal time durations, the systematic effects are significantly decreased. This technique was widely used with the GAMPIX, above introduced, as well as with the iPIX and all the gamma cameras discussed hereinafter. The interested reader is referred to [61] for more details concerning the antimask method.

1.3 Manuscript overview

The remainder of the present manuscript is organized as follows.

Chapter 2 analyses and discusses the results of a comprehensive experimental characterization of the iPIX gamma camera, in which I actively collaborated, conducted by means of the wide-range irradiation equipment located at one of the CANBERRA sites, and also by means of the ISO narrow X-ray beams at the KIT (Karlsruhe Institute of Technology) irradiation facility, where I performed the measurements in collaboration with the CANBERRA team. We published the main results of this study in the Journal of Instrumentation [10], in an article whose I am the corresponding author.

Chapter 2 aims thus mainly at exploring the localization capabilities of the iPIX, since they represent the *starting point* of all methods and prototypes proposed and discussed in the following chapters of the manuscript. On the other hand, the algorithms proposed in Chapter 3 and Chapter 4 address and represent my personal contribution with this thesis.

Chapter 3 reports on the development, under the EU-funded EDUSAFE project, of a *panoramic γ -camera* prototype, called EduPIX, for the ATLAS experiment [62] at CERN¹⁶. In this chapter, the algorithms designed for automatically acquiring and combining both optical and radiation images into a final coherent panorama image with a 360° FOV are described¹⁷. The associated

¹⁶Conseil Européen pour la Recherche Nucléaire.

¹⁷Part of the work related to Chapter 3 has been accepted for poster presentation at the conference ANIMMA 2017, and it is subject of an article whose I am the first author, which is at the time of writing under preparation and it is entitled "*A panoramic coded-aperture gamma camera for radioactive hotspot localization*".

methods are discussed in detail along with their validation, namely with both point and planar radioactive sources, and at the ATLAS facility, in the proximity to the ATLAS beam pipes.

Chapter 4 provides a comprehensive description of the proof-of-concept and methods developed for reliably estimating the 3-D position of radioactive hotspots. An experimental multimodal calibration procedure is proposed for registering all images obtained with the different types of sensors integrated within the prototype. The results of the measurements performed and processed with the proposed methods are discussed in detail, highlighting the main advantages and disadvantages of each technique as well as comparing them in terms of feasibility and accuracy¹⁸.

Finally, Chapter 5 concludes the whole work and provides its main future perspectives.

¹⁸Part of the work related to Chapter 4 has been accepted for poster presentation at the conference ANIMMA 2017, and it is subject of an article whose I am the first author, which is at the time of writing under preparation and it is entitled "*Towards the development of a portable 3-D gamma imager*". Another article whose I am the first author and related to Chapter 4, with title "*A Versatile Calibration Procedure for Portable Coded Aperture Gamma Cameras*", has been submitted to the Journal "IEEE Transactions on Nuclear Science".

Chapter 2

Experimental characterization of the iPIX gamma camera

CANBERRA has recently developed a second-generation gamma camera, called iPIX, in the framework of a partnership agreement with CEA [8–10].

Aiming at exploring its main features and performances, we have carried out a comprehensive experimental characterization of the iPIX gamma camera [10], resulting from more than 280 different experiments.

The corresponding results are analysed and discussed in the present chapter.

2.1 Overview of the iPIX gamma camera

The iPIX system (Fig. 2.1) is a portable γ -camera integrating a 1 mm-thick CdTe detector directly bump-bonded to a Timepix chip [63], a tungsten coded mask (see Section 1.2.2), and an optical USB color board camera.

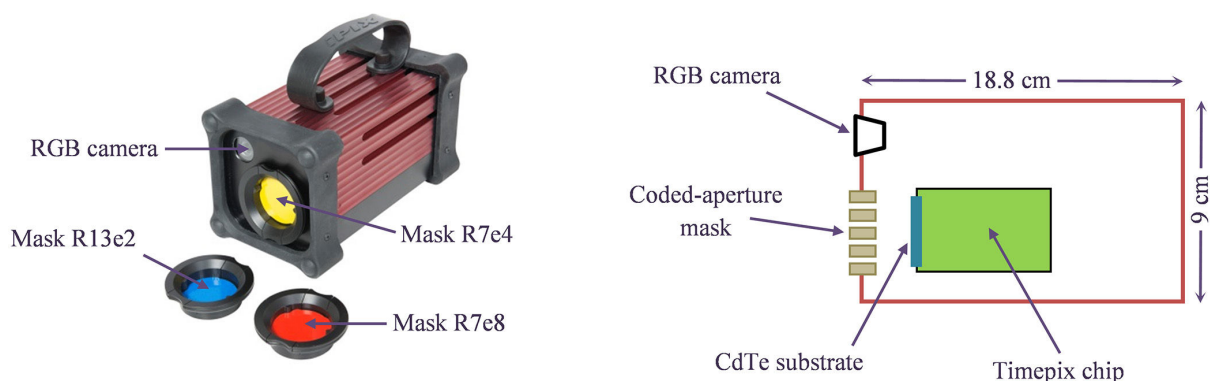


Fig. 2.1: The iPIX gamma camera (left) and a cross-sectional view (right), not to scale, showing its main components and relevant dimensions. The camera has three coded masks (see Section 2.3), which are labelled by different colours to facilitate their identification during measurements.

As explained in Section 1.2.2, a mask/antimask rotation technique is employed for minimizing the interference of the background noise. This allows for a portable (2.35 kg) and compact ($9 \times 9 \times 18.8 \text{ cm}^3$) instrument, as radiation shielding is less needed.

The iPIX is remotely controlled via an Ethernet cable (up to 80 meters long) by means of a graphical user interface (GUI). As explained in more detail in the remainder of this chapter, the system systematically configures the main parameters of the acquisition to be launched. For this reason, the instrument provides an interface called *automatic mode*, so that each measurement can be easily started and performed.

The main components of the iPIX γ -camera are below described.

2.2 Timepix chip with CdTe semiconductor

The Timepix chip from the Medipix2 collaboration [63] used with the iPIX is a pixelated CMOS ASIC consisting of 256×256 square pixels with $55 \mu\text{m}$ side, providing a global detection area of $\sim 14 \times 14 \text{ mm}^2$. Each pixel contains ~ 550 transistors with $\sim 13.5 \mu\text{W}$ static power consumption and it has its own electronic circuitry: charge-sensitive amplifier, discriminator with polarity control pin, 4-bit DAC offset for threshold adjustment, synchronization logic, 8-bit configuration register, and 14-bit counter.

The Timepix chip used with the iPIX is directly bump-bounded to a 1 mm-thick cadmium telluride (CdTe) semiconductor substrate. CdTe is a II-VI compound semiconductor material with atomic numbers of 48 (Cd) and 52 (Te), a wide band gap of 1.44 eV, a high density ($\rho = 5.85 \text{ g/cm}^3$), and a high resistivity ($\geq 10^9 \Omega \text{ cm}$) [64, 65]. Such properties allow the capability of operation of the detector at room temperature, and thus of the iPIX γ -camera as well.

When compared to silicon (Si), which is another alternative semiconductor that could have been used with the Timepix chip, CdTe offers a considerably higher photon interaction probability for energies between 20 keV and 200 keV [66, 67] (up to a factor 20 in the case of the 59 keV γ -rays of ^{241}Am), significantly improving therefore the signal-to-background ratio within this energy range.

The number of collected charge carriers (electrons and holes) is expected to be proportional to the amount of the energy deposited in the CdTe substrate by the passage of ionizing radiation. The Timepix chip allows the comparison of the resulting signal with a pre-set threshold value (THL), and signals lower than such value are disregarded. In other terms, pixels are set to measure only photons whose transmitted energy exceeds the energy determined by THL. The 14-bit counter of each pixel operates only when the Timepix shutter is open (see Section 2.2.1), and has an overflow control that stops at 11810 counts [63].

All the Timepix parameters are configured via Pixelman, a cross-platform and modular software tool developed by the Czech Technical University, in Prague [68].

2.2.1 Counting modes

Every pixel of the Timepix sensor can be independently configured to run in one of the following four different operating modes:

- Masked mode: individual pixels can be filtered.
- Medipix (MPX) mode: the pixel counter is incremented by one each time its output signal exceeds the pre-set threshold level.
- Time-over-Threshold (ToT) or energy mode: the counter is incremented continuously as long as the pixel output signal is above the pre-set threshold level. The number of clock cycles is counted until the pixel output signal crosses back below this threshold. As stated in Section 2.2.2, the number of clock cycles can be directly related to the voltage amplitude of the pixel output signal.
- Time-of-Arrival (ToA) or time mode: the counter is incremented continuously from the time the pixel output signal crosses the pre-set threshold level until the closure of the shutter. This mode is used at the Large Hadron Collider (LHC) at CERN for accurate tracking of fundamental particles [69].

A reference clock with up to 100 MHz frequency is used for the last two counting modes. However, as the iPIX default clock frequency is fixed to 9.6 MHz, each ToT unit corresponds to a time period of 1.042×10^{-7} sec.

All the above counting modes rely on the configured shutter time, which is the active time during which the Timepix sensor is kept switched on. When this shutter time ends, pixel values are retrieved from the buffer and cleared. The process is repeated for the duration of the measurement (i.e. until the chosen number of frames is reached). A comparison between MPX and ToT modes is illustrated in Fig. 2.2.

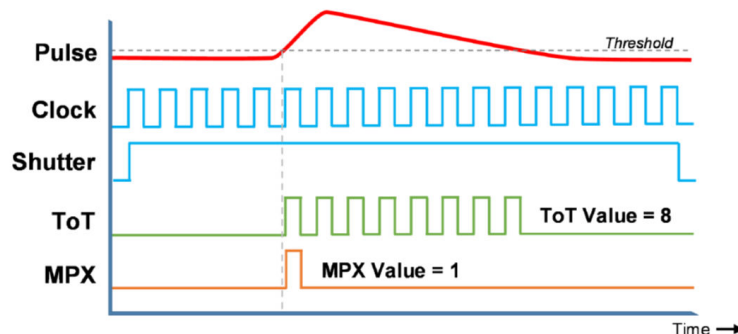


Fig. 2.2: Comparison between MPX and ToT modes of the Timepix chip.

2.2.2 Pixel output signal

The pixel output signal is approximated to a triangular pulse, with 100 ns rise time and a fall time that can reach several tens of microseconds for the photon energy of interest, ranging between 10 keV and 1.5 MeV. Due to this triangular shape, the time duration¹ of any pixel output signal above the pre-set threshold level remains proportional to its voltage amplitude, which in turn is directly related to the portion of the total energy deposited by the incident photon that has been transferred to the considered pixel.

Fig. 2.3 shows how the ToT values vary as a function of the associated energy deposited by the incident photon. The green curve in this figure is to emphasise that the resulting ToT-energy calibration curve can be generally described by the following non-linear function, depending on four parameters (a, b, c , and d):

$$E_\gamma = f(\text{ToT}) = a * \text{ToT} + b - \frac{c}{\text{ToT} - d} \quad (2.1)$$

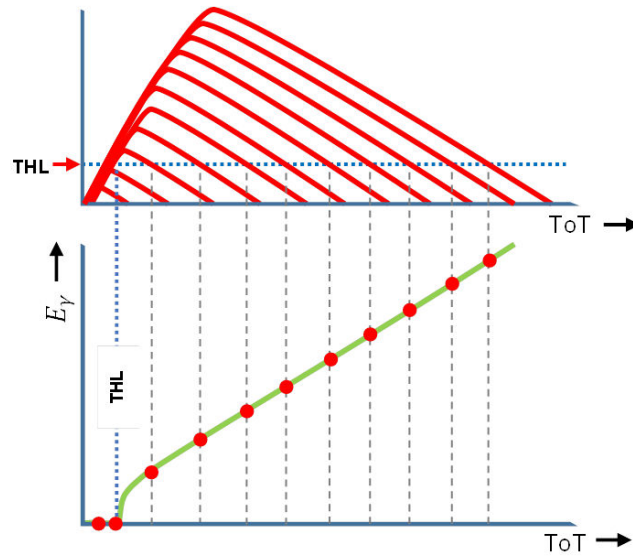


Fig. 2.3: ToT value vs. full deposited gamma energy for single-pixel clusters.

Such function has been experimentally confirmed by Jakubek et al. [70], showing a linear behaviour down to a given critical energy (usually near 10 keV), due to the threshold level that must be applied to avoid unwanted leakage current contribution (see Section 2.2.5). Below such critical energy, the calibration curve deviates from linearity.

2.2.3 Charge sharing between adjacent pixels

When an incident photon interacts with an electron within the CdTe substrate, mainly via photoelectric effect or Compton scattering, such primary electron then ionizes nearby atoms releasing

¹In ToT mode, the time duration is simply the number of clock cycles divided by the clock frequency.

electron hole pairs. Consequently, these charge carriers drift in opposite directions towards the corresponding electrodes because of the electric field, and may be collected at the same time by several adjacent pixels, resulting in a "cluster".

Therefore, each registered cluster can be directly associated to the original photon interaction. In other terms, each cluster can be interpreted as a "count" for conventional radiation detectors. The whole charge created by any incident photon can be revealed by summation of the fractional charges collected by all the pixels forming its associated cluster. The extent of charge sharing effect generally depends on the incident photon energy, pixel size, substrate layer, bias voltage applied, and the interaction depth within the sensitive volume [71].

A *cluster reconstruction* method has been applied to correct for the above charge sharing effect. As illustrated in Fig. 2.4, it consists in determining the span of each registered cluster, and defining the associated pixel with the highest ToT value as the possible location on the sensor surface of the original photon interaction. All the registered clusters can thus be reduced to just the origin interaction pixels, improving the accuracy of the measurement. Moreover, when using the ToT mode, the reading value of all nearby pixels forming a given cluster can be summed to return the total energy deposited by the primary incident photon.

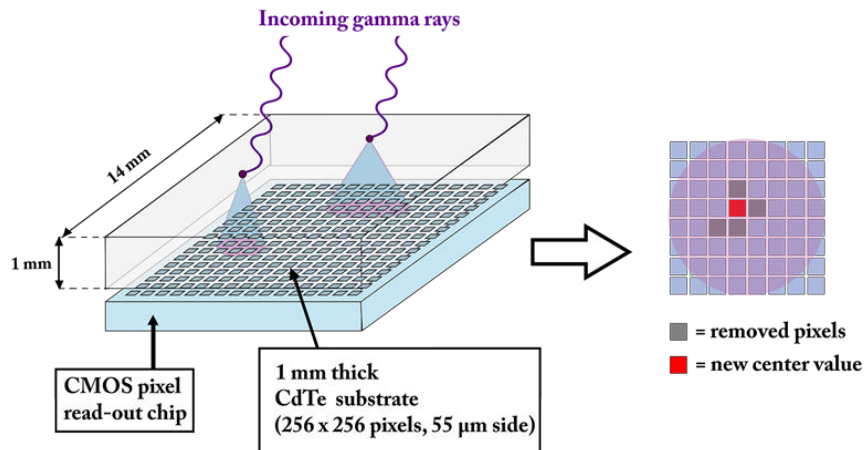


Fig. 2.4: Illustration of the charge sharing effect (left) and the application of the cluster reconstruction method (right).

The cluster reconstruction method also allows for a direct integration of the whole clusters registered along successive frames acquired during the same measurement. Therefore, the amount of registered clusters divided by the detection "live-time" (i.e. the preset shutter time multiplied by the number of recorded frames) directly provides the conventional "count rate" or "cps".

2.2.4 Pulse summation and pile-up effects

When selecting an excessive shutter time (details are provided in Section 2.4.1), even in the case of low incident photon fluxes, successive signals can be collected and accumulated before it expires (see Fig. 2.5). The resulting reading value under ToT mode is hence the sum of all of the individual signals that are detected on the specific pixel within this excessive shutter time.

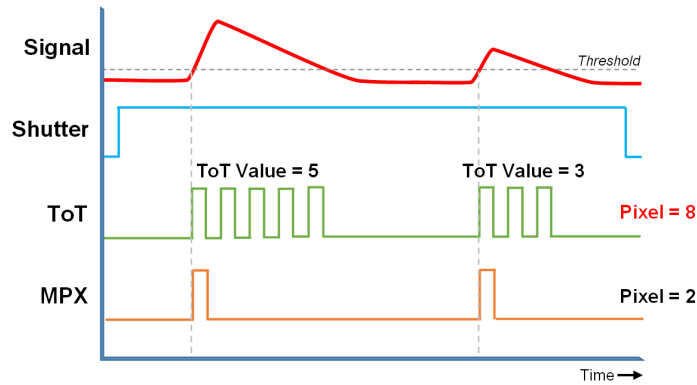


Fig. 2.5: Summation of succeeding pulses due to excessive shutter time.

For this purpose, the shutter time must be conveniently chosen to avoid the pulse summation effect. If successive signals are recorded on the same pixel under ToT mode, the corresponding reading would lead to a misleading numerical value. This effect can be minimized by decreasing the shutter time, as long as the latter is not shorter than the time needed by the pulse to be fully collected by the pixel.

Moreover, as illustrated in Fig. 2.6, when successive pulses are very close in time, the system wrongly records them as a single count with combined amplitudes, resulting in pulse pile-up.

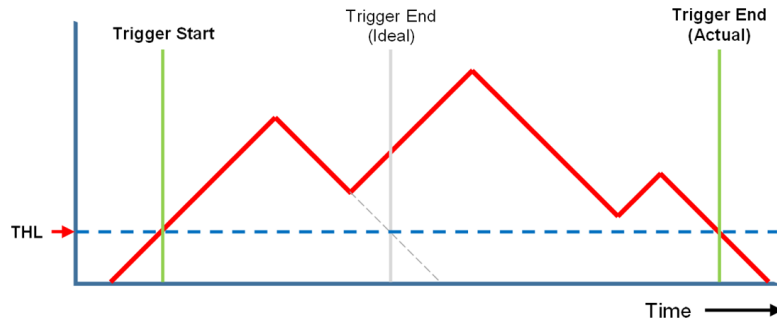


Fig. 2.6: Illustration of the pulse pile-up effect.

Due to these effects, the iPIX response dependence with regards to the pre-set shutter time has been further explored, resulting into a qualitative study documented in Section 2.4.1.

2.2.5 Threshold equalization

Threshold equalization is used to compensate the pixel-to-pixel threshold variations of the Timepix readout chip due to local transistor mismatches. This procedure is normally applied using the inherent electronic noise as a trigger². In such case, the system tries to automatically fine-tune the 4-bit DAC offset for each pixel, aiming at remaining as close as possible to an optimum

²That is, the measurement is carried out in a radiation-free environment.

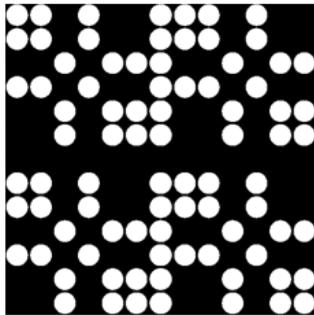
threshold level common to all Timepix pixels. In this way, unwanted leakage current contribution is conveniently discarded and only the input pulses of interest are considered.

A new equalization method was specifically developed for iPIX to deal with the leakage current problem. This method considers the real sensor response, instead of the inherent electronic noise, under a homogeneous photon flux in the energy range of 50 – 100 keV.

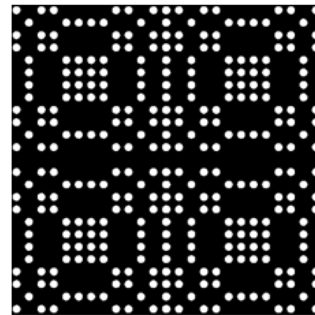
2.3 Coded aperture masks

Three coded masks are currently available for the iPIX platform, providing two mask ranks (Fig. 2.7) and three different thicknesses. They are thus classified according to their rank and thickness: R7e4, R7e8, and R13e2. The label e is an abbreviation of the word "épaisseur" (a French translation of "thickness"), expressed in mm. The planar area of such masks is four times that of the CdTe detector used, and their patterns were designed according to the MURA arrays (see Section 1.2.2).

Moreover, the iPIX gamma camera allows the automatic rotation of the two masks of rank 7 by an angle of 90° , allowing for antimask measurements.



(a) Rank 7.



(b) Rank 13.

Fig. 2.7: Pattern designs for the iPIX coded aperture masks.

In general, a higher mask rank leads to a higher angular resolution. Its drawback, however, is the decrease of the detection efficiency due to the smaller total area of its holes. Furthermore, whereas increasing the mask thickness provides more photon filtering, enhancing thus the overall signal-to-noise ratio, it reduces in turn the instrument off-axis response (in Section 2.4.7 more details are provided concerning such aspect). The application of the mask R13e2 is therefore only limited for low photon energies. More specifically, such mask is used to detect the presence of plutonium in nuclear wastes via the 59 keV γ -ray of ^{241}Am .

2.4 Experimental characterization

A comprehensive experimental characterization study of the iPIX gamma camera has been carried out [10], in order to explore its main features and performances, by means of ISO narrow X-ray beams or N-Series [72] at the KIT (Karlsruhe Institute of Technology) irradiation facility (Fig. 2.8), equipped with secondary standards, and also by means of the wide-range irradiation equipment located at CANBERRA's Loches site.

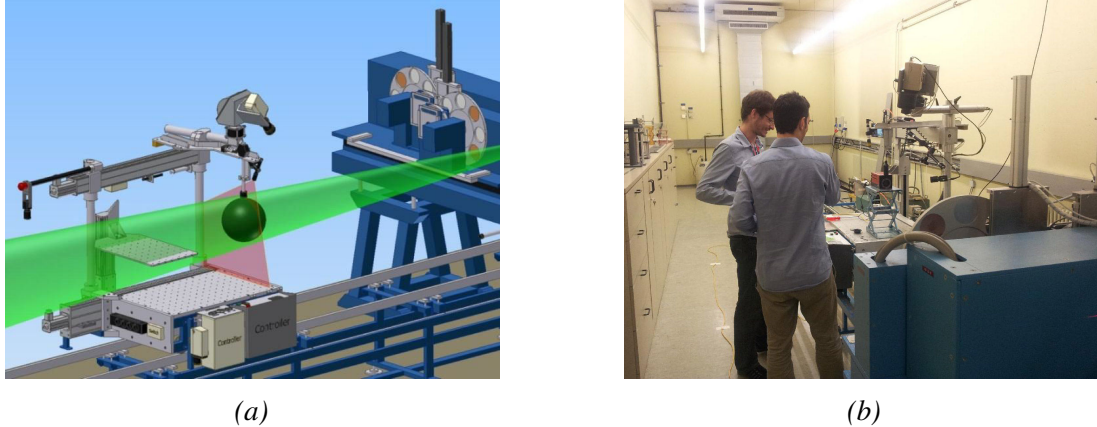


Fig. 2.8: (a) Drawing of the KIT X-ray irradiation facility with a reference ionization chamber located at the measurement point, and (b) preparing the respective measurements with the iPIX γ -camera.

The CANBERRA irradiation equipment consists of:

1. A "big" irradiator (Fig. 2.9) with six interchangeable standard ^{137}Cs sources of nominal activities between 3 GBq and 30 TBq, to provide an ambient dose equivalent rate ranging from 20 $\mu\text{Sv/h}$ to 20 Sv/h at several source-to-detector distances.
2. A "small" irradiator (Fig. 2.10a) with two interchangeable standard ^{137}Cs (300 MBq) and ^{60}Co (70 MBq) sources, to provide an ambient dose equivalent rate at the chosen measurement point ranging from 2 $\mu\text{Sv/h}$ to 100 $\mu\text{Sv/h}$.
3. A "portable" irradiator (Fig. 2.10b) based on a standard ^{241}Am source with 1.85 GBq nominal activity, to provide an ambient dose equivalent rate ranging from 1 to 50 $\mu\text{Sv/h}$.

A summary concerning the decay scheme of each mentioned radionuclide is provided in Appendix C, along with a list of the radioactive sources used hereinafter and the respective main information available. On the other hand, all KIT X-ray beams used in this study, along with their theoretical energy distributions, are listed in Appendix B, in Tables B.1 and B.2.

Increasing input electron currents were applied for each X-ray energy in order to increase the associated flux at the considered measurement point. For each irradiation run, the following steps were carried out:



Fig. 2.9: CANBERRA "big" ^{137}Cs irradiator.



(a) "small" ^{137}Cs / ^{60}Co irradiator.



(b) "portable" ^{241}Am irradiator.

Fig. 2.10: Other CANBERRA irradiation equipment.

- Firstly, a basic quantity such as air kerma rate, or $\dot{\mathbf{K}}_{air}$ (see Appendix A), expressed in mGy/h units, was directly measured with a calibrated ionization chamber at the considered distance (~ 2 meters).
- Then, the ambient dose equivalent rate, or $\dot{H}^*(10)$ (see Appendix A), expressed in mSv/h units, was derived by the application of the associated conversion coefficient derived from [73]. The corresponding values for each X-ray beam at varied input currents are also summarized in Tables B.1 and B.2.
- Lastly, the iPIX device under test was placed at the same measurement distance to evaluate its response.

Similar steps were followed also at the CANBERRA irradiation facilities. The only difference consisted in previously using the calibrated ionization chamber at five reference distances for the considered standard source, in order to derive the associated fitting parameters (a and b) of the following empirical relationship:

$$\dot{\mathbf{K}}_{air} = a x^{-b}, \quad (2.2)$$

where x is the source-to-detector distance in cm.

2.4.1 ToT data quality

In this section, a qualitative study of the measurement data collected at the KIT X-ray facility is provided. In this case, the iPIX count rates measured at each X-ray beam have been normalized to the corresponding dose rate (see Tables B.1 and B.2) in order to facilitate a comparison between the different shutter times used. Indeed, when increasing the X-ray beam currents, the whole area of the measured spectra must be linearly proportional to the associated dose rates. Regarding such specific aspect, measurements performed with masks R7e8 and R7e4 provided adequate and quite similar results. However, the results obtained with the R13e2 mask, due to its small thickness, were quite unsatisfactory when the incident photon energy was above 200 keV (i.e. the radioactive hotspot was not anymore localized).

Moreover, the evolution of the cluster ToT distributions with respect to the incident X-ray beam energy and current as well as to the Timepix shutter time has been analysed. In Fig 2.11, the cluster ToT distributions are shown for the KIT N-100 X-ray narrow beams ($E_{mean} = 83.8$ keV) with varied currents, measured with the mask R7e8 and with different shutter times. To ease the reading of the present section, all other plots concerning the other beam energies (still using mask R7e8) are also shown in Appendix B, in Figures B.1 - B.10.

According to all these figures, when the shutter time is correctly chosen (i.e. avoiding signal distortions eventually due to pulse pile-up and/or summation effects, as explained in Section 2.2.4), the associated count rates per unit of mSv/h do not change when only the X-ray beam

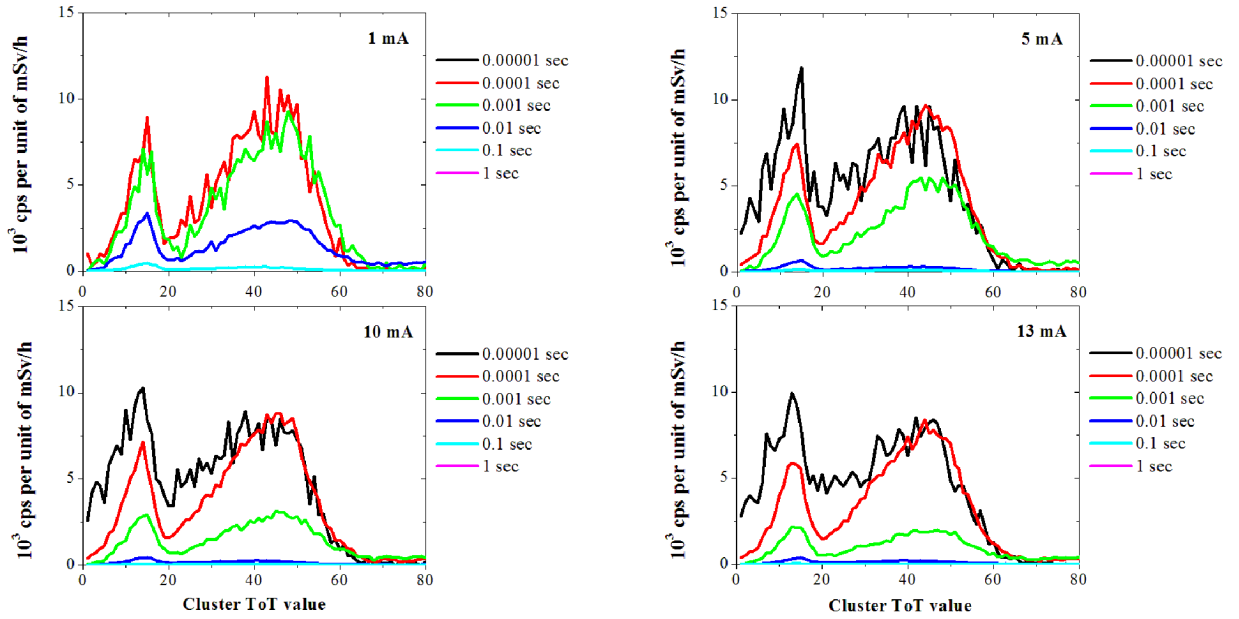


Fig. 2.11: Cluster ToT distributions measured with the mask R7e8 under different shutter times for the N-100 ($E_{mean} = 83.8$ keV) X-ray narrow beams of varied currents. When the shutter time is correctly chosen (i.e. 10^{-4} sec), the associated count rates per unit of mSv/h do not change when only the X-ray beam current is varied. Data obtained with a 10^{-5} sec shutter time and at low (1 mA) beam input current were statistically insignificant, and are not reproduced here. Unlike the full-energy peak, the additional one does not move to the right with increasing the incident photon energy.

current is varied. This is the case when 10^{-4} sec shutter time is chosen for all the considered ISO X-ray narrow beams and at practically the whole range of applied currents.

Conversely, caution should be taken when choosing a shutter time of 10^{-5} sec, since it cannot be applied for photon energies above 150 keV. In fact, above this energy, the effect of incomplete charge collection of the pixel output signals becomes quite apparent. Shutter times between 10^{-3} sec and 0.1 sec can only be applied for a limited range of X-ray beams and at very low currents, whereas that of 1 sec has simply failed in providing physically meaningful results for all experiments. Furthermore, a clear distinction needs to be made between radioactive hotspot localization (possible even under pulse pile-up and/or summation effects) and dose rate evaluation, which in fact can be carried out only when the dose rate linearity is fully guaranteed.

Interactions of low energy photons with the CdTe substrate occur primarily via the photoelectric process giving rise to a single full-energy peak, which expectedly shifts to the highest ToT values when increasing the beam acceleration voltage. When the incident photon energy is above 40 keV, an additional peak appears on the left at around 13 ToT (i.e. $1.4 \mu\text{s}$), as shown in Fig. 2.11. Contrary to the full-energy peak, such peak does not shift to the right when increasing the incident photon energy. This might be due to a direct detection of extra characteristic fluorescence X-rays emitted by other elements outside the CdTe substrate. The lack of knowledge about the actual composition of all surrounding materials did not allow us to make any kind of prediction regarding such additional peak.

2.4.2 ToT-energy calibration

Only clearly differentiated and sharp full-energy peaks were considered for the ToT-energy calibration. This was the case in most of the cluster ToT distributions measured with 10^{-4} sec shutter time (Appendix B, Figures B.1 - 2.11). Each one of these peaks was fitted with a Gaussian function to derive the associated ToT value of its geometric centre. ToT values were divided by the default clock frequency, to express them in time units. The results obtained are plotted in Fig. 2.12. A satisfying linearity is observed between incident photon energies and their respective ToT values.

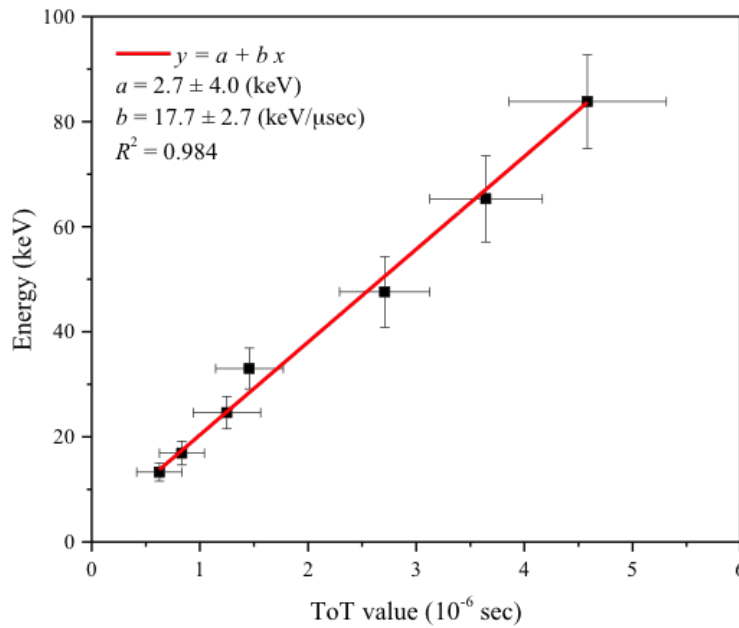


Fig. 2.12: ToT-photon energy calibration curve for the iPIX gamma camera.

The ToT-energy calibration relationship has been derived for low-energy photons only (see Fig. 2.12). However, it was tested and applied also to measure the ^{137}Cs spectrum at the CANBERRA's big irradiator, as shown in Fig. 2.13. The chosen experimental conditions were a dose rate of 1 Sv/h at the measurement point, acquiring a total of 2000 frames with a shutter time of 10^{-4} sec (i.e. 1000 frames using the mask position and 1000 frames using the antimask position). According to this figure, two full-energy peaks can be easily distinguished, associated to 32 keV X-ray of ^{137}Cs and to the characteristic fluorescence photons (58 – 85 keV), emitted from the tungsten (W) atoms in the coded mask and/or from the irradiator Pb-based collimator. The current energy resolution of the detector of the iPIX does not allow resolving W and Pb characteristic lines. Despite the small thickness of the CdTe substrate, the corresponding 662 keV peak of ^{137}Cs as well as its Compton edge (478 keV) are also visible on logarithmic scale (Fig. 2.13). This ultimately ratifies the validity of the ToT-energy linearity also at high energies. The energy resolution for the 662 keV peak was estimated to be approximately 9%.

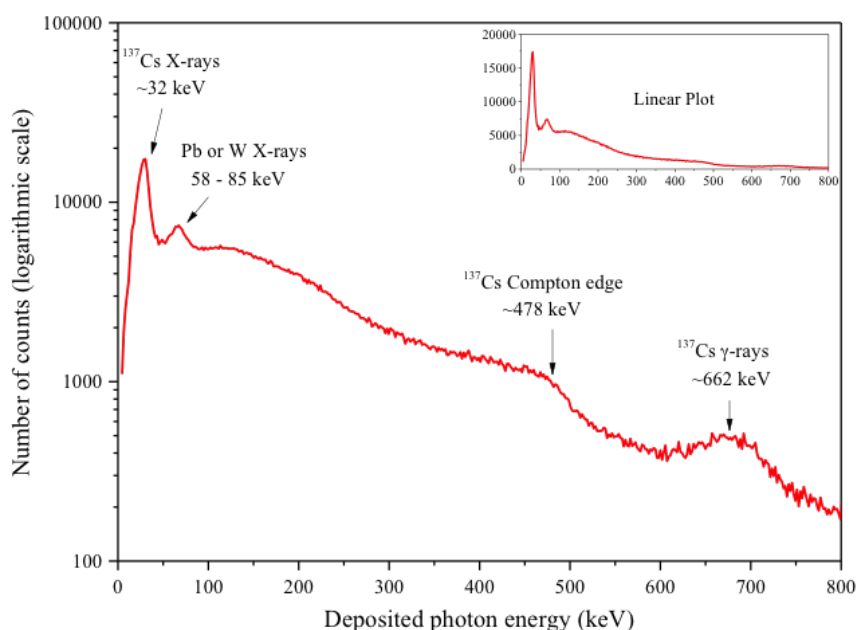


Fig. 2.13: Measured ^{137}Cs spectrum with iPIX.

Similar ^{137}Cs spectra were obtained for other dose rates, but considering only highly significant statistics as well as appropriate shutter times, avoiding thus signal distortions due to pulse pile-up and/or summation effects, as explained in Section 2.2.4.

Taking into account the above ToT-energy calibration relationship, the expected ToT for the 1500 keV energy is $\sim 85 \mu\text{s}$ so that, as a general rule, the iPIX shutter time should never decrease below 10^{-4} sec to assure that all pixel output signals generated in the photon energy range of interest (10 keV – 1.5 MeV) are fully recorded.

2.4.3 Dose rate linearity

The variation of the iPIX count rates with respect to the reference dose rates was studied at the CANBERRA big irradiator considering the two masks R7e4 (see Fig. 2.14) and R7e8. Again, these masks provided quite similar results. In fact, depending on the chosen shutter time, almost all the dose rate response curves are linear along a given range, until reaching a maximum, after which the radioactive hotspot is no longer localized. These curves finally drop off towards a full saturation of the Timepix detector when a single cluster containing all of its pixels is registered. It can be also seen in Fig. 2.14 that, from a qualitative point of view, the iPIX dose rate response may be considered as linear over a wide range, reaching nearly 8 decades ($10^{-6} - 10^1$ Sv/h) if the Timepix shutter time is correctly chosen to avoid signal distortions due to pulse pile-up and/or summation effects.

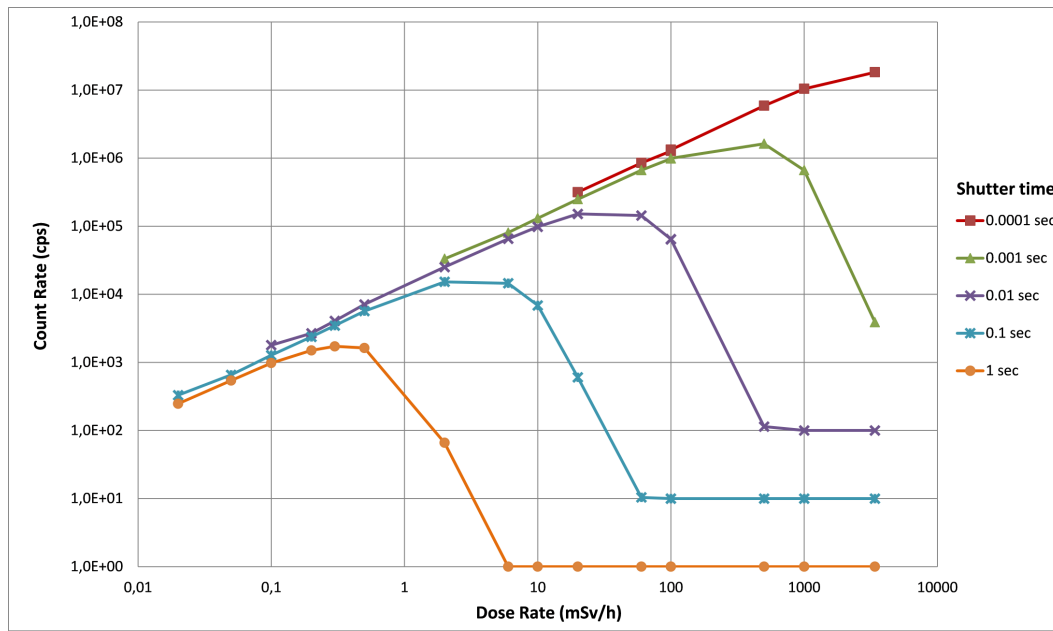


Fig. 2.14: Dose response curves for the ^{137}Cs radioactive source measured directly with iPIX using the mask R7e4. A similar behavior was also observed with the mask R7e8.

2.4.4 Dose calibration factor vs. incident photon energy

The iPIX dose calibration factor is energy dependent and is defined as the number of the registered net counts per second (cps) divided by the photon ambient dose equivalent rate (in mSv/h units) at the measurement point. The corresponding values obtained for all the CANBERRA radioactive sources as well as for the KIT X-ray narrow beams are displayed on Fig. 2.15. This figure shows the similar response provided by the masks R7e4 and R7e8, whereas that of R13e2 is almost two times lower, as a result of its high rank. As expected, the dose calibration factor for an ^{241}Am radioactive source is ~ 30 and ~ 50 times higher than that for ^{137}Cs and ^{60}Co , respectively, due to the lower efficiency of the 1-mm CdTe substrate at higher energy.

2.4.5 Cluster sizes vs. incident photon energy

In this section, we examine the dependence of the cluster size with respect to incident photon energy. In each case, the shutter time was accordingly chosen by a dedicate procedure implemented for the iPIX to avoid signal distortions on the Timepix detector due to pulse pile-up and/or summation effects. Once again, as all coded aperture masks provide quite similar results, only those obtained with the mask R7e8 are shown in Figures 2.16 and 2.17.

According to these figures, a discrimination criterion can be applied, especially between low (e.g. ^{241}Am) and high photon energies (e.g. ^{137}Cs and ^{60}Co), but only if concerning a qualitative analysis to estimate an energy range of the observed hotspot(s).

Conversely, the same criterion is not practical to quantify the individual contribution of a given radionuclide to the overall dose rate, as the cluster size distributions generated by different

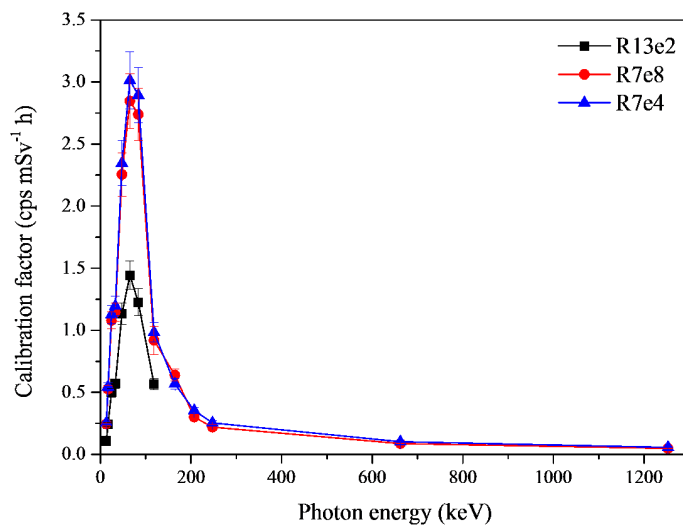


Fig. 2.15: Dose calibration factor of the iPIX as a function of the incident photon energy.

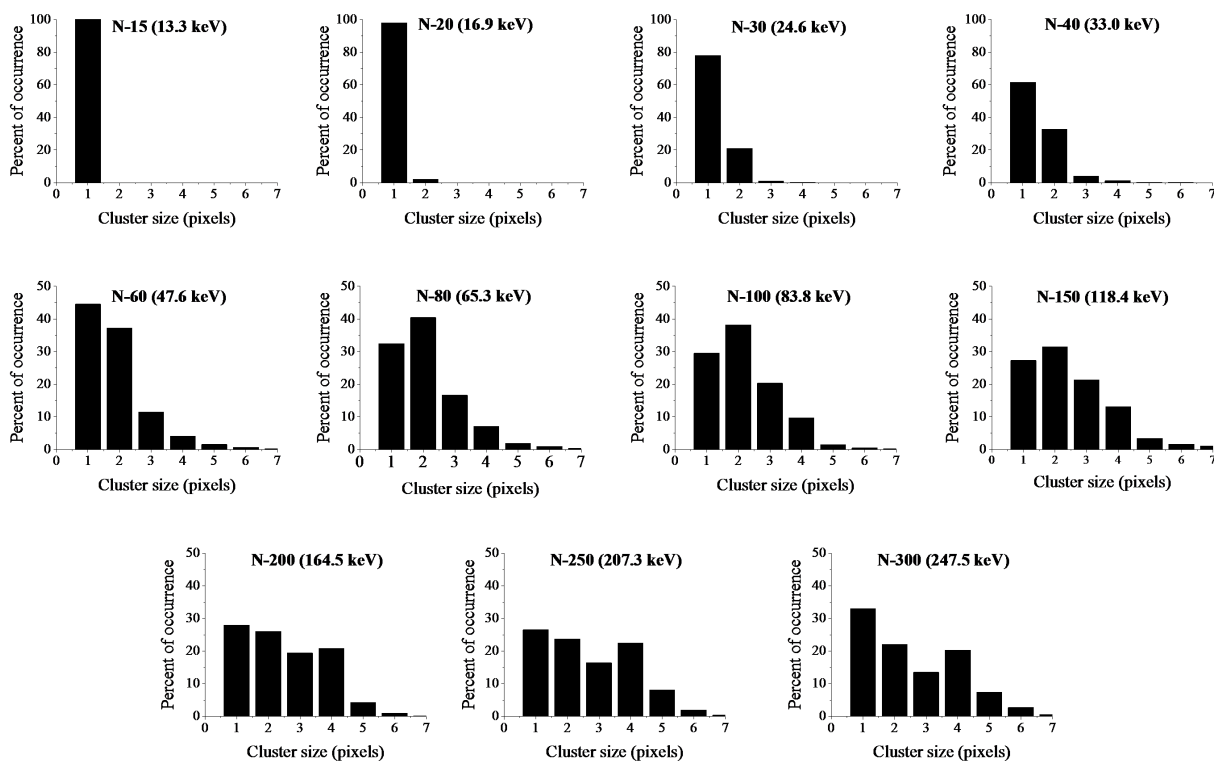


Fig. 2.16: Cluster size distributions measured with the mask R7e8 for X-ray narrow beams.

photon energies are significantly overlapping. In other words, there is not a clearly distinguishable signature in terms of cluster size distribution allowing both identification and quantification of radionuclides.

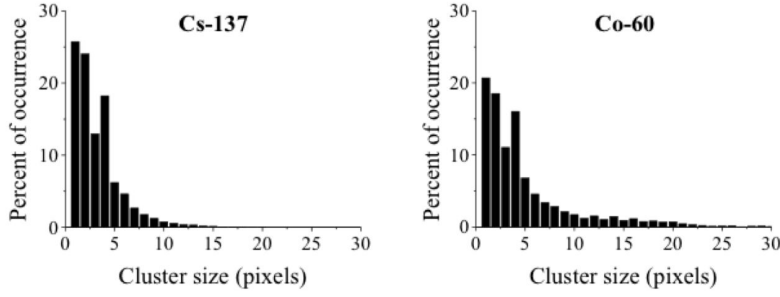


Fig. 2.17: Cluster size distributions measured with the mask R7e8 for ^{137}Cs and ^{60}Co .

Another aspect to remark is that an upper size threshold of 20 pixels can be applied to discard undesired cluster events, such as the ones that may be generated by cosmic rays.

2.4.6 Sensitivity and influence of background radiation

The iPIX sensitivity regarding its localization performance has been evaluated with the low-activity point sources listed on Table 2.1. The experiments involved several levels of energy and different distances between the γ -camera and the sources, also depending on the coded mask used.

The first experiments were performed using the iPIX in *automatic mode*. In this case, therefore, the needed total number of frames for each measurement and the associated shutter time were estimated automatically by the iPIX system. The first set of measurements was conducted with the natural background radiation dose rate at the iPIX location, previously estimated within 0.1 – 0.2 $\mu\text{Sv/h}$. Subsequently, the same tests were perturbed with a *simulated* background dose rate of 2 $\mu\text{Sv/h}$ at the measurement point (measured with the Canberra instrument Colibri), generated by placing the ^{137}Cs of the CANBERRA small irradiator (Fig. 2.10a) behind the iPIX.

The results of such evaluation, summarized in Figures 2.18 - 2.20, show that in the case of natural background radiation dose rate at the camera location, the iPIX was able to localize all the low-activity sources listed in Table 2.1. However, by observing the associated results, a significant parallax error occurred during the superimposition phase in some cases, due to the low distance between the located sources and the γ -camera (i.e. < 1 m). The quantification of such error was behind the scope of this specific set of measurements. Nonetheless, this aspect is addressed in more detail in Chapter 4, where a comprehensive solution regarding this limitation is also proposed.

Table 2.1: Low-activity point sources used for sensitivity measurements.

Radionuclide	Current activity	Distance	$\dot{H}^*(10)$
^{60}Co	226 kBq	22.3 cm	2 $\mu\text{Sv/h}$
^{241}Am	412 kBq	48.0 cm	10 nSv/h
^{137}Cs	368 kBq	61.5 cm	100 nSv/h

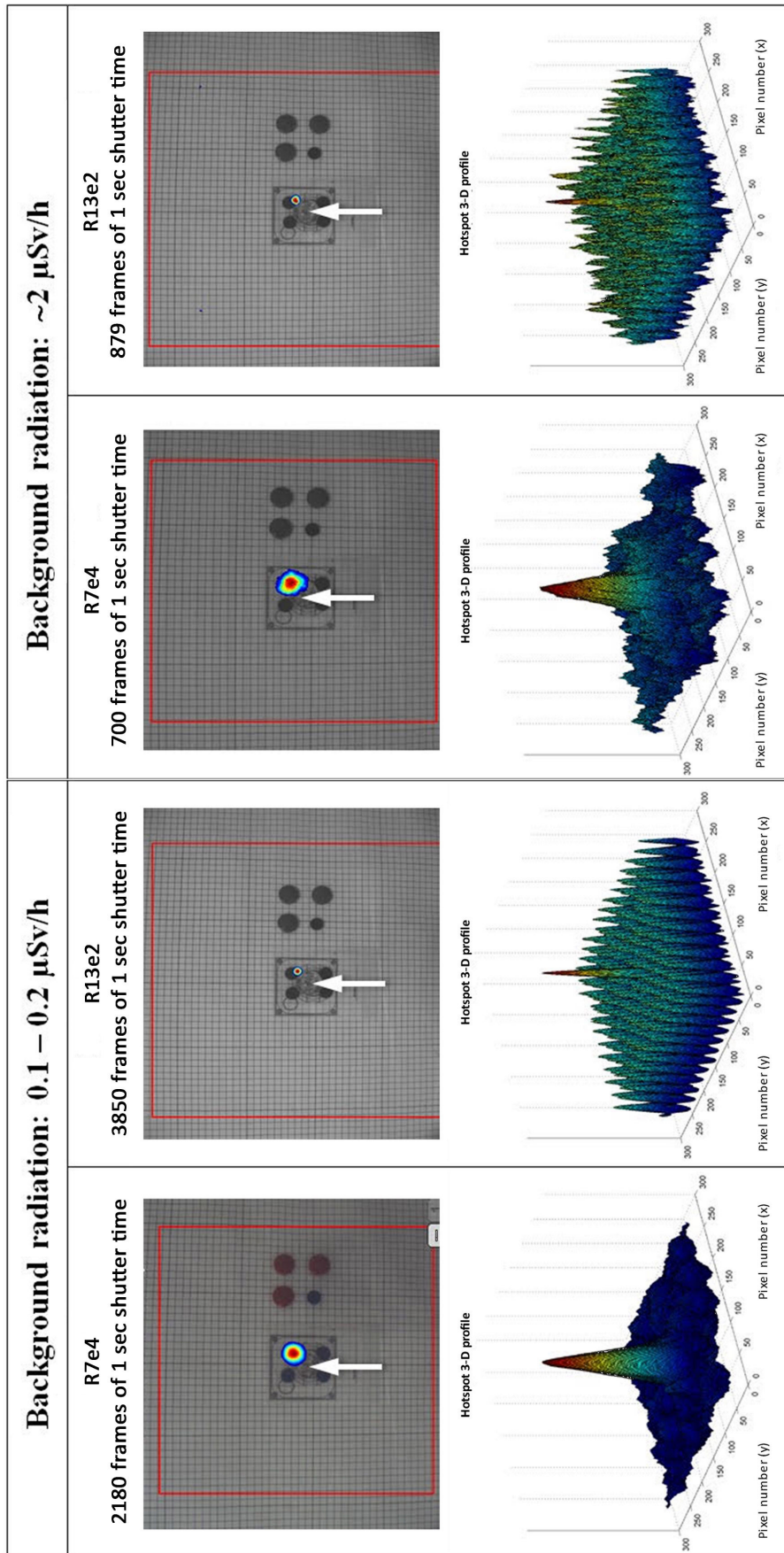


Fig. 2.18: Measurement results of the iPIX obtained in automatic mode with a 412 kBq ^{241}Am point source located at a distance of 48 cm with varied background radiation. With the exception of the mask R13e2, all measurements were performed both in mask and animask positions. The location of the considered radioactive sources are indicated by white arrows. At very close source-to-detector distances (i.e. less than 50 cm), slight mismatches occurred when superimposing the radiation image onto the respective optical image.

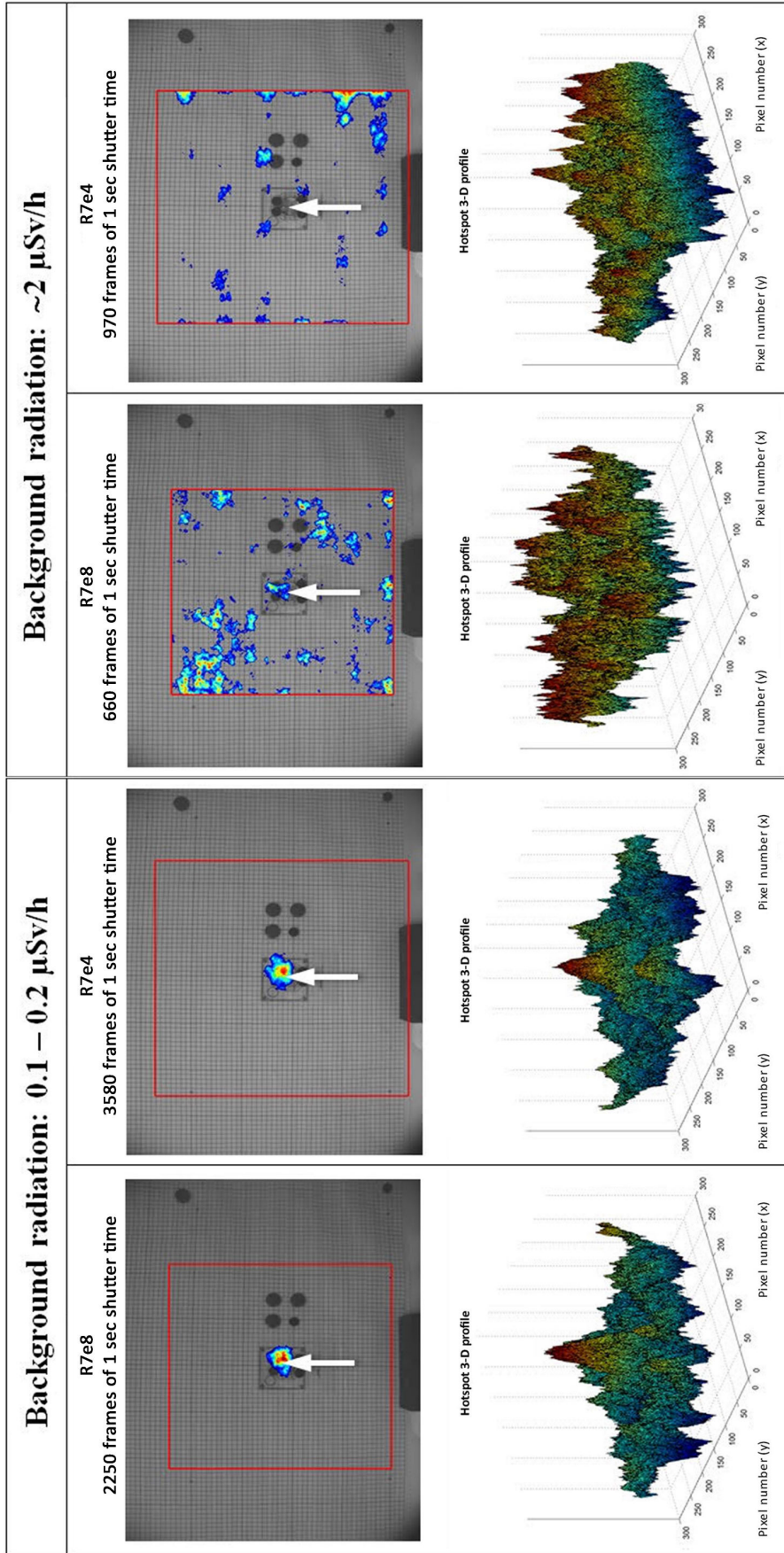


Fig. 2.19: Measurement results of iPIX obtained in automatic mode with a 368 kBq ^{137}Cs point source located at a distance of 64.5 cm with varied background radiation. All measurements were performed both in mask and antimask positions. The location of the considered radioactive sources are indicated by white arrows.

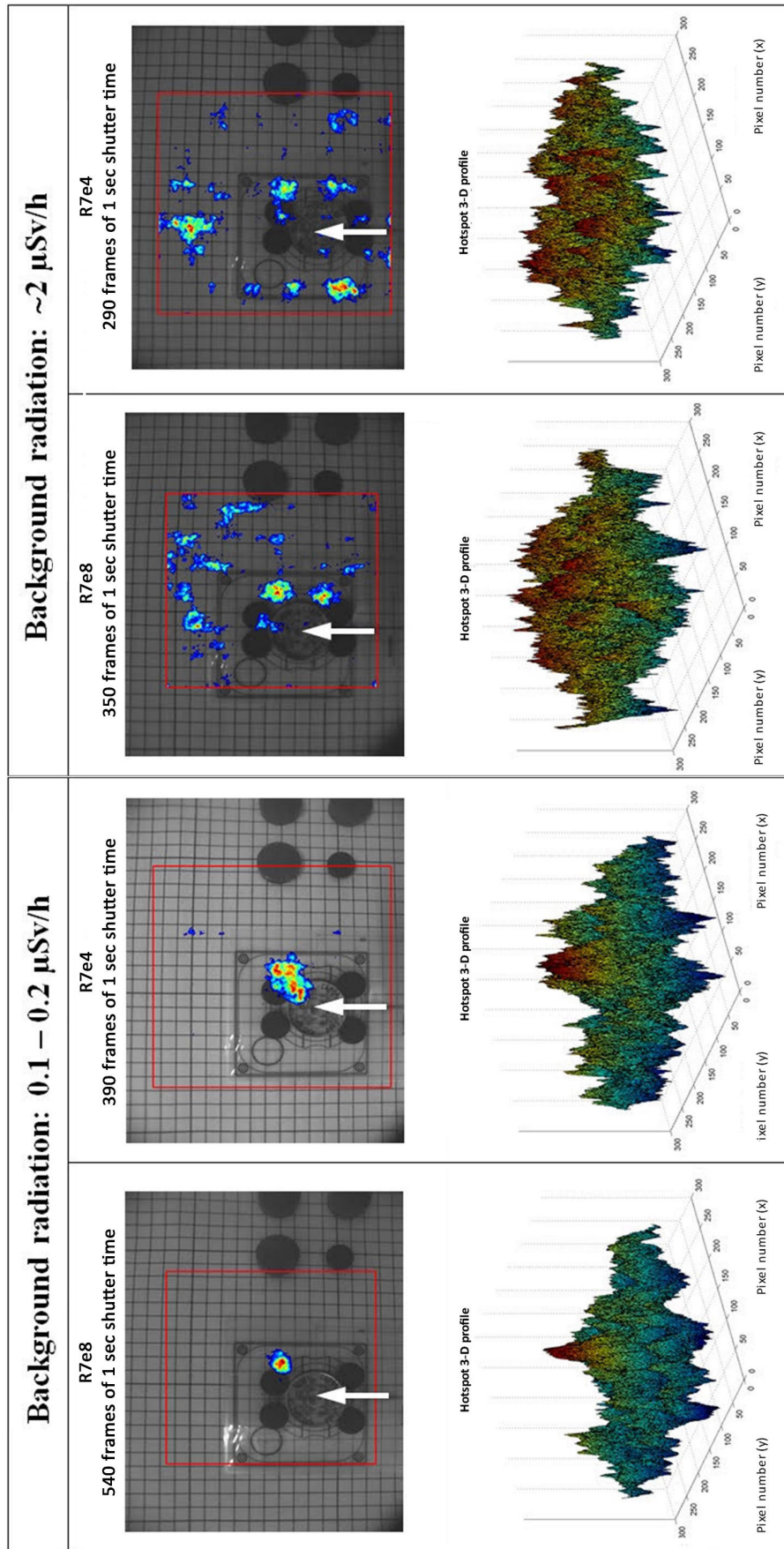


Fig. 2.20: Measurement results of iPIX obtained in automatic mode with a 226 kBq ^{60}Co point source located at a distance of 22.3 cm with varied background radiation. All measurements were performed both in mask and antimask positions. The location of the considered radioactive sources are indicated by white arrows.

Table 2.2: Minimum localization time (considering data collection only).

	^{241}Am (10 nSv/h)	^{137}Cs (100 nSv/h)	^{60}Co (2.0 $\mu\text{Sv/h}$)
R13e2	50 s	---	---
R7e4	4 s	190 s	70 s
R7e8	---	120 s	60 s

Table 2.3: Comparison between CARTOGAM and iPIX in terms of minimum localization time (considering data collection only).

	^{137}Cs (100 nSv/h)	^{60}Co (1.0 $\mu\text{Sv/h}$)
CARTOGAM	240 s	480 s
iPIX	120 s	140 s

When simulating a background dose rate of 2 $\mu\text{Sv/h}$ at the measurement point, the iPIX was still able to localize the 412 kBq ^{241}Am point source, independently of the coded mask used. In addition, the quality of the superimposed pictures is quite comparable to the ones obtained under natural background radiation (0.1 – 0.2 $\mu\text{Sv/h}$). Nevertheless, the γ -camera failed in localizing the 226 kBq ^{60}Co and 368 kBq ^{137}Cs point sources when the background dose rate at the measurement was increased to 2 $\mu\text{Sv/h}$. Moreover, as already mentioned above, at source-to-detector distances less than 1 m, during the superimposition phase slight mismatches occurred between the actual location of the localized radioactive sources and that of the associated colored hotspots.

Considering instead the *minimum localization time* and data collection only, the minimum number of frames needed to localize the above low-activity point sources are summarized in Table 2.2. When using the mask R7e4, the iPIX localised each of the sources tested. Furthermore, despite an estimated dose rate at the measurement point of only 10 nSv/h, the iPIX was able to localize the 412 kBq ^{241}Am point source with 4 frames of 1 sec shutter time when using the mask R7e4. On the other hand, when using the mask R7e8, the low-activity ^{241}Am point source was not localised, although with such mask a faster localization time was achieved with the other sources. Finally, the results obtained and summarized in Table 2.2 showed that the mask R13e2 was suitable only for localising the 412 kBq ^{241}Am point source.

Additional measurements were also carried out to compare the iPIX and the CARTOGAM system, as shown in Table 2.3, proving that the iPIX γ -camera has better performances in terms of minimum localization time.

Further measurements with a similar configuration were performed, but by using this time the portable ^{241}Am source shown in Section 2.4 in Figure 2.10b. The source-to-detector distance was 330 cm, providing an ambient dose equivalent rate of ~ 1 $\mu\text{Sv/h}$ at the measurement point.

To simulate different levels of radiation background dose rate for this test, the following three configurations were used for such experiments:

- CANBERRA small irradiator entirely shielded.
- The ^{60}Co source of the CANBERRA small irradiator behind the iPIX, providing a background dose rate of $215 \mu\text{Sv/h}$ at the measurement point.
- The ^{137}Cs source of the CANBERRA small irradiator to provide a background dose rate of $310 \mu\text{Sv/h}$ at the measurement point.

The shutter time was automatically set by the iPIX to 1 sec, and 200 frames were collected for each measurement. The results obtained are presented in Figures 2.21 - 2.23.

With the exception of the mask R13e2, the two enhanced background radiation levels have caused a minimal impact to localize the portable ^{241}Am radioactive source.

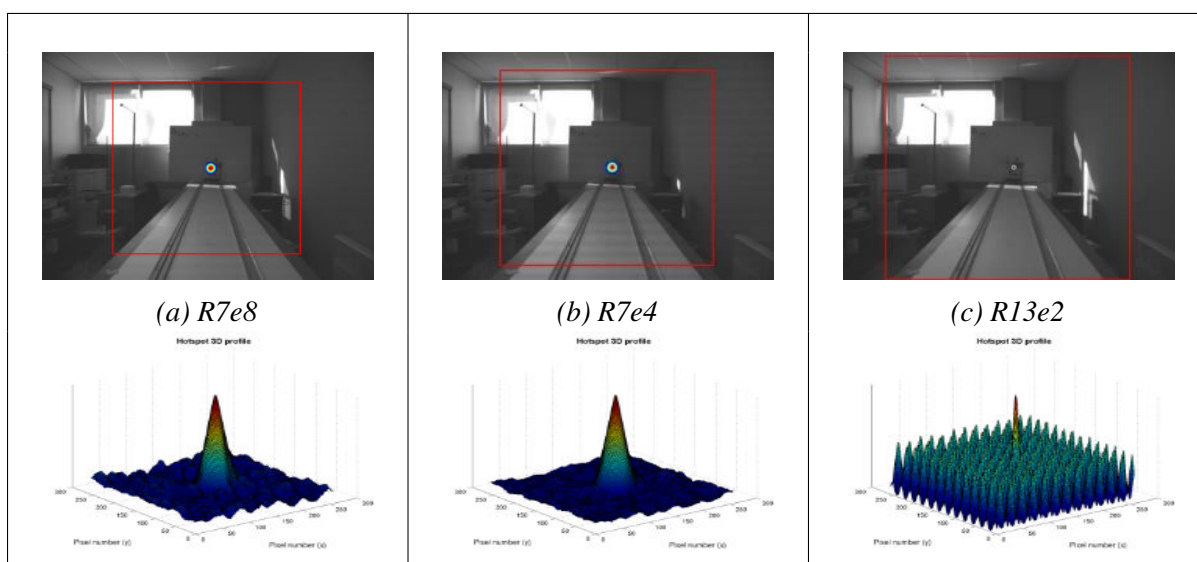


Fig. 2.21: Results obtained with the $1.85 \text{ GBq } ^{241}\text{Am}$ source located at a distance of 330 cm from the iPIX with natural background radiation condition ($0.1 - 0.2 \mu\text{Sv/h}$). The shutter time was set by the iPIX to 1 sec, and 200 frames were collected in mask and antimask positions ($100 + 100$) for the measurements performed with masks R7e8 and R7e4, whereas 200 frames only in mask position were collected with the R13e2 mask. The cut-off threshold applied for the superimposition of the radiation image onto the optical image is 70% for all measurements.

2.4.7 Off-axis response

The evaluation of the iPIX off-axis response was carried out by means of the CANBERRA big irradiator. The iPIX gamma camera was firstly oriented so that the corresponding hotspot was visualized exactly at the center of its field of view. Thereafter, only its pan (horizontal) angle was varied sequentially between -25° to $+25^\circ$ in steps of 5° , while keeping its tilt (vertical) position

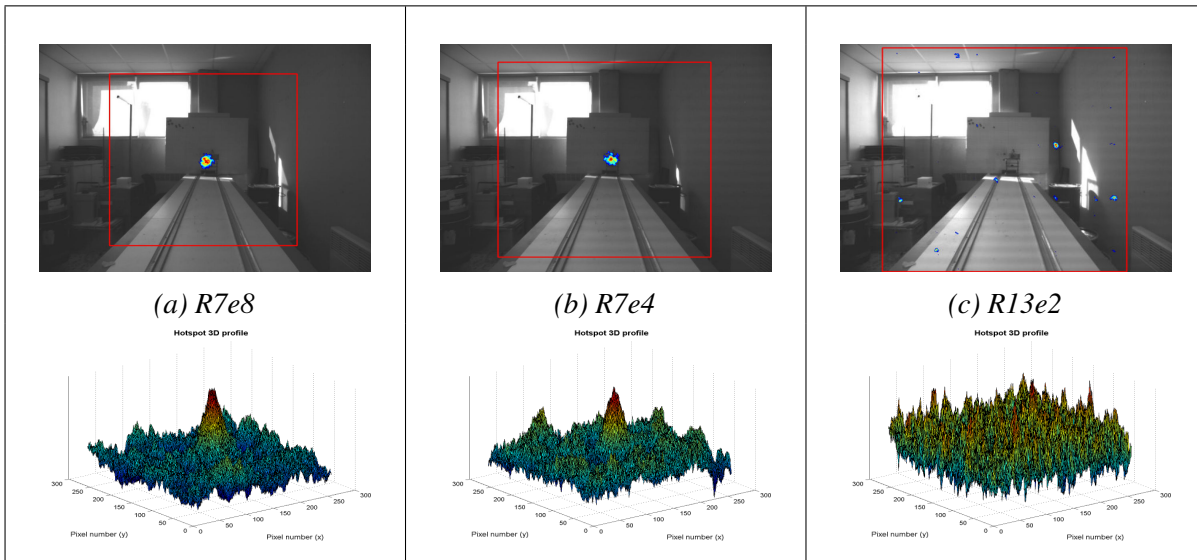


Fig. 2.22: Results obtained with the $1.85 \text{ GBq } ^{241}\text{Am}$ source located at a distance of 330 cm from the iPIX with an enhanced background dose rate of $310 \mu\text{Sv/h}$ generated by the ^{137}Cs source of the CANBERRA small irradiator. The shutter time was set by the iPIX to 1 sec , and 200 frames were collected in mask and antimask positions ($100 + 100$) for the measurements performed with masks R7e8 and R7e4, whereas 200 frames only in mask position were collected with the R13e2 mask. The cut-off threshold applied for the superimposition of the radiation image onto the optical image is 70% for all measurements.

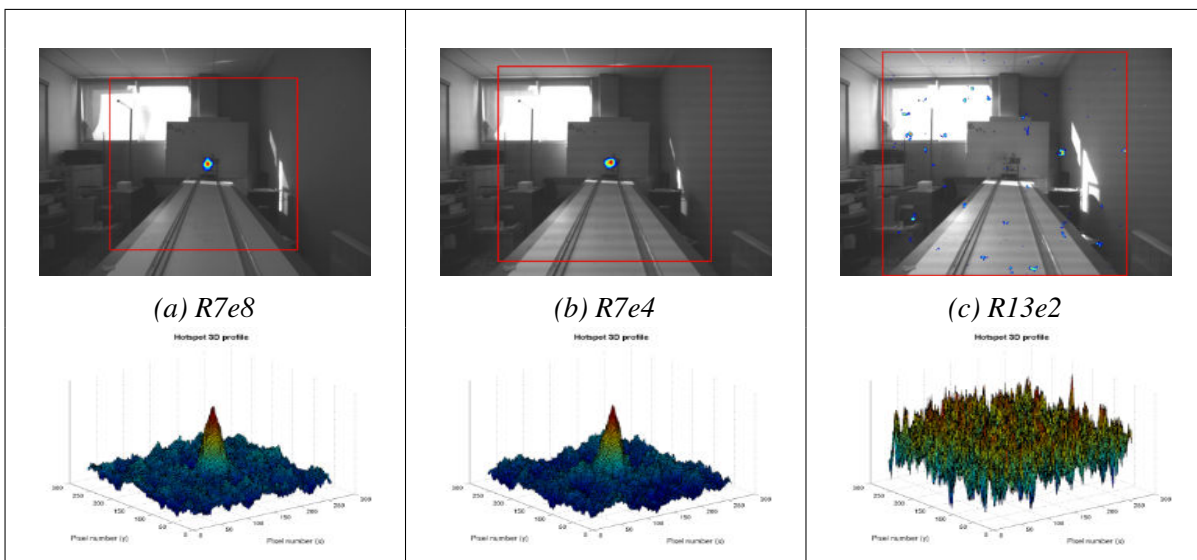


Fig. 2.23: Results obtained with the $1.85 \text{ GBq } ^{241}\text{Am}$ source located at a distance of 330 cm from the iPIX with an enhanced background dose rate of $215 \mu\text{Sv/h}$ generated by the ^{60}Co source of the CANBERRA small irradiator. The shutter time was set by the iPIX to 1 sec , and 200 frames were collected in mask and antimask positions ($100 + 100$) for the measurements performed with masks R7e8 and R7e4, whereas 200 frames only in mask position were collected with the R13e2 mask. The cut-off threshold applied for the superimposition of the radiation image onto the optical image is 70% for all measurements.

fixed to 0° , and vice versa. The measurements were performed using masks R7e4 and R7e8. The $\pm 25^\circ$ variation was considered in order to include the whole iPIX field of view.

The observed loss in counts for each mask was very similar with respect to both pan and tilt rotation angles. Figure 2.24 shows the average count rates, normalized to normal incidence (pan = tilt = 0°), measured with these two masks at varied pan or tilt rotation angles.

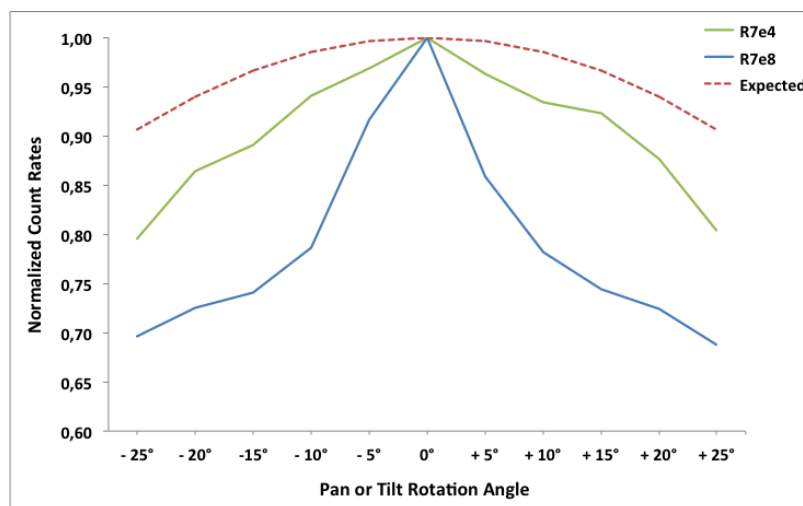


Fig. 2.24: Normalized count rates observed for the masks R7e4 and R7e8 at varied pan or tilt rotation angles obtained with the ^{137}Cs source.

The response deviation from an ideal behaviour (i.e. following the cosine function represented by a red dashed curve in Fig. 2.24) is within 3% - 12% for the mask R7e4, and never exceeds the limit of 25% for the mask R7e8. These deviations are mainly due to the collimation effect of incident photons at the same coded aperture mask.

Admittedly, as illustrated in Fig. 2.25, the number of transmitted photons is decreased under non-normal incidences and thicker masks, and it affects, moreover, the shape of the projected open holes (they become oval instead of round) at the detector surface.

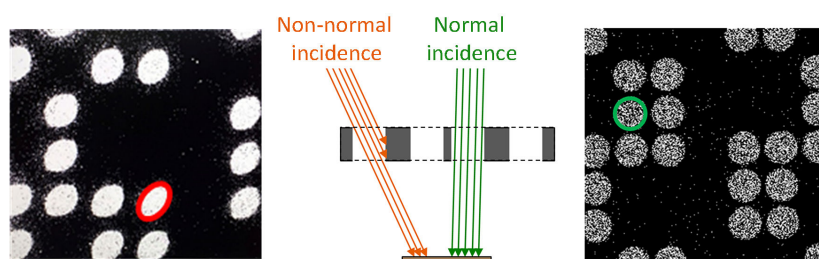


Fig. 2.25: Mask self-collimation effect.

Nevertheless, as proved with a preliminary proof-of-concept prototype of the iPIX [74], the self-attenuation effect is even more accentuated at low-energy photons (^{241}Am -like sources). In that case, the corresponding decrease in the iPIX response may surpass 50% for both the mask R13e2 and R7e4, or even 80% for the mask R7e8, when the non-normal incidence is above 10° .

Concerning hotspot visualization, Fig. 2.26 displays an example of the superimposed pictures obtained at varied pan angles. According to this figure, a mirroring effect (i.e. false hotspot localization on the opposite side) may occur at the limit of the iPIX field of view ($\pm 25^\circ$). As illustrated in Fig. 2.27, this misleading artifact is caused by the projection of *identical portions* of the mask pattern onto the detector surface. Therefore, measurements resulting in a peripheral radioactive hotspot should be repeated until the source is being targeted further from the extreme limits of the FOV of the γ -camera. This has also the benefit of increasing the measurement statistics by mitigating the mask self-collimation effect.

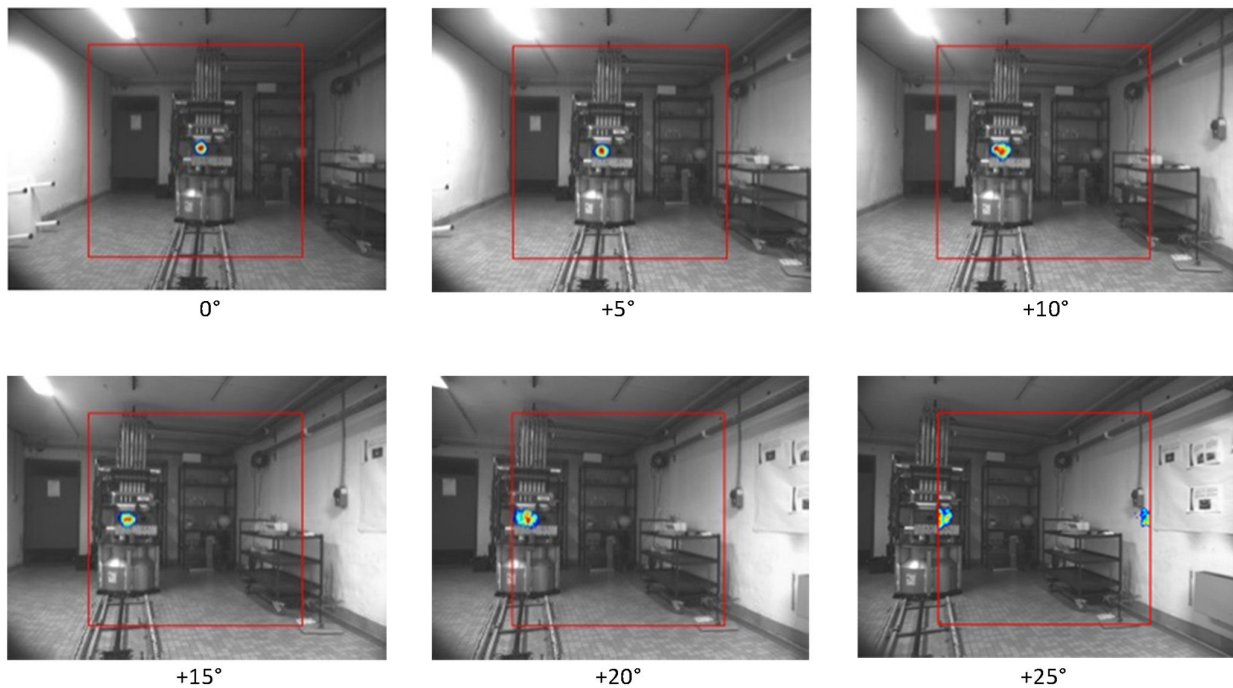


Fig. 2.26: *iPIX* results at varied pan angles.

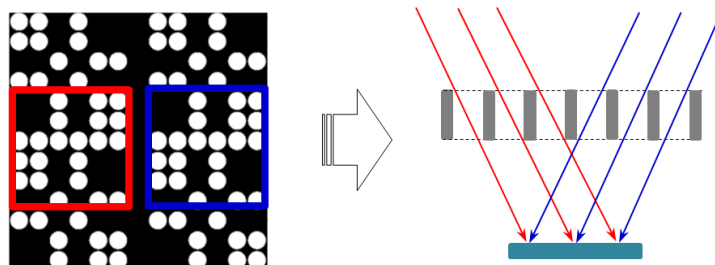


Fig. 2.27: Illustration of the mirroring effect at the limit of the *iPIX* field of view. Radiation of the two peripheral sources (radiation direction indicated with red and blue arrows) project identical portions of the mask pattern onto the detector surface.

2.4.8 Angular resolution

An important requirement in gamma imaging is the ability to track several radioactive sources at the same time. The angular resolution, θ , is a convenient parameter to define the distinction limit between two small and adjacent radioactive sources. Generally speaking, such parameter depends on the diameter of the open holes on the coded aperture mask used, d , and the length between the outer surface of this mask and the Timepix detector, l , as follows:

$$\theta_{\text{calculated}} = \arctan \frac{d}{l}. \quad (2.3)$$

As illustrated in Fig. 2.28, the angular resolution can also be experimentally estimated from the vertical or horizontal axial profile of the hotspot peak, taking into account the associated FWHM (*Full Width at Half Maximum*). Since the iPIX field of view (FOV) has a square shape, its side corresponds to the maximum number of available pixels (i.e. 256) on the considered axis, and therefore:

$$\theta_{\text{measured}} = \frac{FOV \times FWHM}{256} \quad (2.4)$$

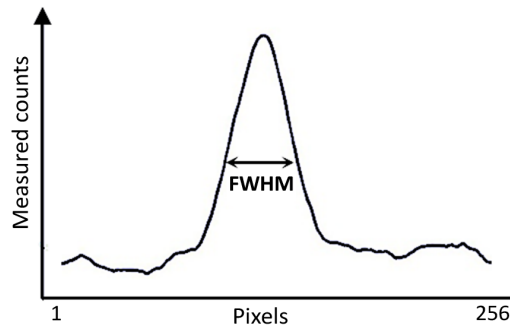


Fig. 2.28: Vertical and horizontal axial profile of the hotspot peak.

The theoretical and experimental angular resolutions for the three iPIX masks are summarized in Table 2.4. According to this table, the experimental values obtained with the three masks agree to within 68% ($\pm 1 \sigma$) confidence level of their associated uncertainties with the theoretical ones. They also confirm that the angular resolution does not depend on the incident photon energy.

To illustrate the optimal angular resolution of iPIX when compared to the existing gamma cameras [16, 7], additional measurements were also carried out using three identical low-activity ^{241}Am point sources (340 kBq). These sources were placed on a horizontal line at 40 cm distance (i.e. providing 3×12 nSv/h dose rates at the measurement point). As summarized in Fig. 2.29, the following experimental configurations were considered:

- All sources were close to each other, but the outside sources remained separated from the central one by ~ 4 cm, which is the diameter of their circular support. This represents around $\pm 6^\circ$ separation angle.

Table 2.4: Determination of the iPIX angular resolution.

	$\theta_{calculated}$	$\theta_{measured}$		
		^{241}Am	^{137}Cs	^{60}Co
R13e2	2.5°	$2.8^\circ \pm 0.6^\circ$	---	---
R7e4	6.0°	$6.2^\circ \pm 0.6^\circ$	$6.0^\circ \pm 0.6^\circ$	$5.9^\circ \pm 0.6^\circ$
R7e8	5.0°	---	$5.6^\circ \pm 0.7^\circ$	$5.4^\circ \pm 0.7^\circ$

- The outside sources were separated by ± 5 cm (i.e. $\pm 7^\circ$) from the central source.
- The outside sources were separated by ± 10 cm (i.e. $\pm 14^\circ$) from the central source.

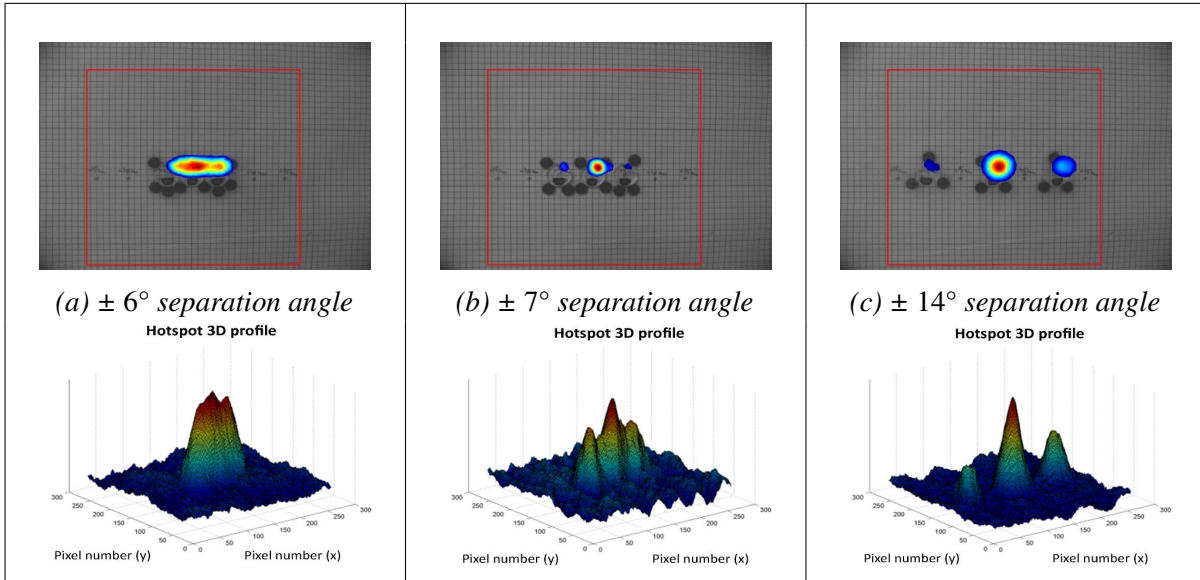


Fig. 2.29: Measurement results of three identical ^{241}Am sources with mask R7e4 at different separation angles.

Satisfying results were obtained with masks R7e4 and R7e8 (see Fig. 2.29 and Fig. 2.30, respectively). However, in the case where the sources have a separation angle of $\pm 6^\circ$, it was needed to manually retrieve the exact location of the three sources from the respective hotspot profiles. In addition, the strong decrease of count rates at non-normal incidences corroborated the mask self-collimation effect, discussed in the previous section. Due to such effect, the outside sources were less visible at a separation angle of $\pm 14^\circ$.

2.5 Conclusions

In view of the results obtained with ISO narrow X-ray beams at varied acceleration voltages and currents, we have observed that the Timepix shutter time is the most critical parameter for an

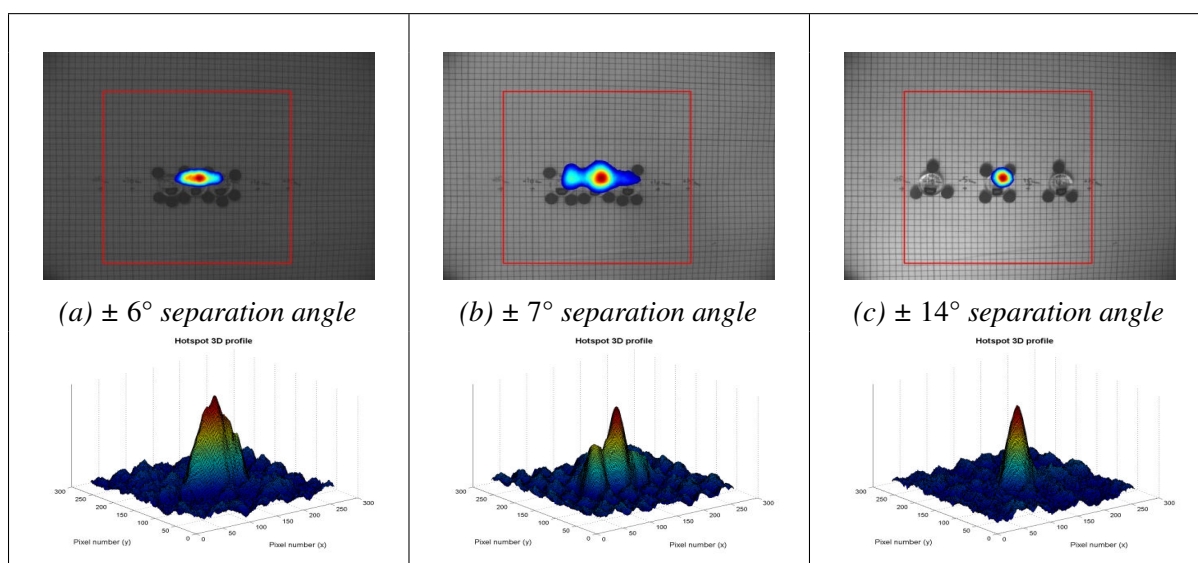


Fig. 2.30: Measurement results of three identical ^{241}Am sources with mask R7e8 at different separation angles.

effective localization of radioactive hotspots, as it has to be conveniently chosen to avoid signal distortions on the Timepix detector due to pulse pile-up and/or summation effects.

Compared to existing gamma cameras, iPIX has an enhanced angular resolution (between 2.5° and 6.0° , depending on the coded mask used), and a high response sensitivity at low energies, tolerating at the same time high levels of simulated background radiation (around 200 – 310 $\mu\text{Sv/h}$).

Regarding its localization capability, an ^{241}Am source providing only 10 nSv/h dose rate at the measurement point was distinctly spotted within 4 sec of data collection time. Similarly, the iPIX γ -camera was able to localize low-activity ^{137}Cs and ^{60}Co sources (providing 100 nSv/h and 1 $\mu\text{Sv/h}$ dose rates at the measurement point, respectively) with less than 150 sec of data collection time.

The iPIX experimental characterization has demonstrated that the mask R7e8 can be applied at almost the whole energy range of interest (10 keV - 1.5 MeV), whereas mask R13e2 is limited to low photon energies only (e.g. 59 keV γ -rays of ^{241}Am , whose detection usually indicates the presence of plutonium in nuclear wastes). As an intermediate application, mask R7e4 is able to localize radioactive sources in the medium photon energy range of ^{137}Cs .

Finally, the iPIX dose rate response curve was analysed with several standard ^{137}Cs sources of different activities, showing a linear behaviour over a wide range, covering nearly 8 decades (10^{-6} – 10^1 Sv/h).

Chapter 3

Development of a panoramic gamma camera for the ATLAS detector

High levels of radiation background are inevitably present at the Large Hadron Collider (LHC), posing significant challenges with respect to radiation protection for several types of activities, such as detector maintenance, upgrade, or repair operations.

As an integral part of the personnel safety system used at the LHC, and more specifically at ATLAS, a panoramic gamma imaging prototype — the EduPIX — has been developed, allowing the localisation of the main surrounding radiation-emitting objects with a field of view of 360 degrees, so that operators can perform their work accordingly. The associated algorithms, proposed and described in the present chapter, may be integrated in the future also into the next version of the iPIX system, whose localization capabilities represent the starting point of the EduPIX prototype and have been documented in Chapter 2.

Chapter 3 is organized as follows. Section 3.1 provides an introduction to the LHC, to the ATLAS environment, and to its main radiological aspects, since the last motivated the development of the gamma camera prototype described in the present chapter. Section 3.2 reports the main specifications of such prototype, with a focus on the preliminary experiments performed for evaluating its response in proximity to *planar sources*, as the main benefits from panoramic radiation images come from measurements involving extended sources with sizes potentially exceeding the FOV of the detector while being localized. Sections 3.3 and 3.4 describe the methods and algorithms developed for combining both optical and radiation images into a final coherent panorama image. A validation of the associated results is also provided, namely with point and planar radioactive sources made available by two CEA laboratories¹, and at the ATLAS detector, in proximity to the ATLAS beam pipes.

¹The "*Laboratoire simulation et techniques de démantèlement nucléaire*", at Marcoule, and the "*Laboratoire d'Intégration de Systèmes et des Technologies*", at Saclay.

3.1 Introduction to the Large Hadron Collider

Based at the European particle physics laboratory CERN, near Geneva, the Large Hadron Collider (LHC) is a superconducting-hadron accelerator and collider consisting of a 27-kilometres ring below the surface, with a depth ranging between 45 m and 170 m, on a plane inclined at 1.4% sloping towards the Geneva lake (*Léman lake*).

The LHC was installed in the pre-existing 26.7 km tunnel that was constructed between 1984 and 1989 for the CERN LEP machine [75]. There are two transfer tunnels, each approximately 2.5 km in length, linking the LHC to the CERN accelerator complex, which acts as injector [76].

The Standard Model (SM) of particle physics [77–80] has been subject of convincing experimental verifications over the last four decades, and has been shown to successfully describe high energy particle interactions [81–87]. Similarly, the search for the Higgs boson and other particles (e.g. supersymmetric) were among the most compelling motivations behind the design of the LHC [88], with centre of mass collision energies of up to 14 TeV.

The LHC has two high luminosity² experiments, ATLAS [62] and CMS [89], both aiming at a peak luminosity of $L = 10^{34} \text{ cm}^{-2}\text{s}^{-1}$ for proton operation. There are also two low luminosity experiments: LHCb [90] for B-physics, aiming at a peak luminosity of $L = 10^{32} \text{ cm}^{-2}\text{s}^{-1}$, and TOTEM [91], for the detection of protons from elastic scattering at small angles, aiming at a peak luminosity of $L = 2 \times 10^{29} \text{ cm}^{-2}\text{s}^{-1}$ with 156 bunches. In addition to the proton beams, the LHC will also be operated with ion beams. The Large Hadron Collider has one dedicated ion experiment, ALICE [92], aiming at a peak luminosity of $L = 10^{27} \text{ cm}^{-2}\text{s}^{-1}$ for nominal lead-lead ion operation.

Colliding two counter-rotating proton beams requires *opposite* magnetic dipole fields in both rings. The LHC is therefore designed as a proton-proton collider with separate magnet fields and vacuum chambers in the main arcs, and with common sections only at the insertion regions where the experimental detectors are located (see Fig. 3.1).

The electromagnets used for the LHC are built from coils of special electric cables that operate in a superconducting state, efficiently conducting electricity without resistance or loss of energy. This requires chilling the magnets to -271.3° C , a temperature colder than outer space. For this reason, a significant part of the accelerator is connected to a distribution system of liquid helium, which cools the magnets.

All the controls for the accelerator, its services, and technical infrastructure are housed under one roof, the CERN Control Centre (Fig. 3.2).

For more information about the main experiments at the LHC, the interested reader can start with [93] and [94].

As the main testing campaigns of the EDUSAFE project (introduced in Section 3.1.3) and the respective gamma camera prototype have been held in the ATLAS environment, a general

²In scattering theory, luminosity (L) is a quantity that measures the ability of a particle accelerator to produce the required number of interactions, and it is defined as the ratio of the number of the generated events (dN) in a certain time (dt) to the interaction cross-section (σ): $L = \frac{1}{\sigma} \frac{dN}{dt}$.

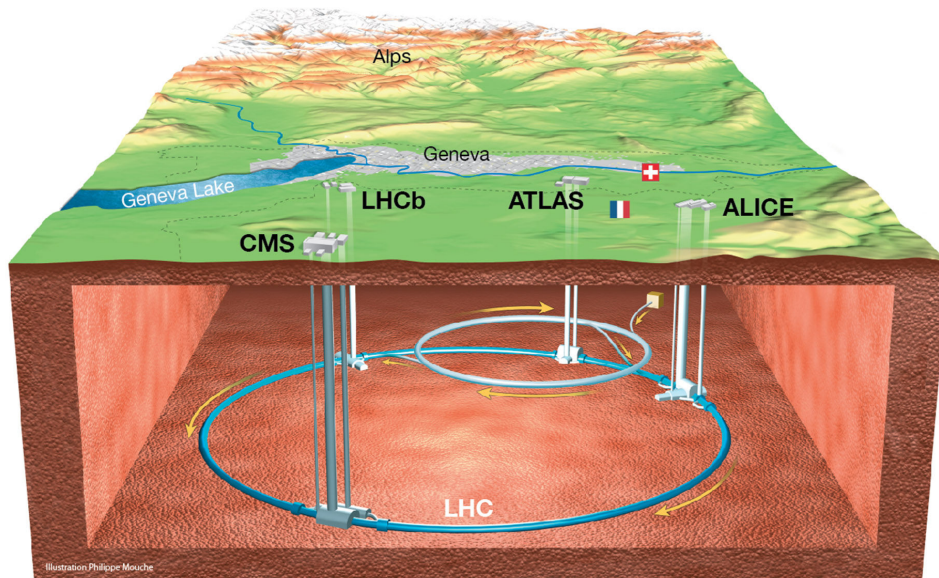


Fig. 3.1: Diagram of the CERN accelerator complex. Protons are initially accelerated through a series of particle accelerators to increasingly higher energies (at time of writing, up to 13 TeV). Afterwards, such accelerated particles enter in two separate beam pipes and travel in opposite directions through the main LHC ring with circumference of 27 km, colliding in four particle detectors: ATLAS, CMS, ALICE, and LHCb. Image: CERN.



Fig. 3.2: CERN Control Centre during the first high-energy collisions in the LHC on 30 March 2010. Image: CERN.

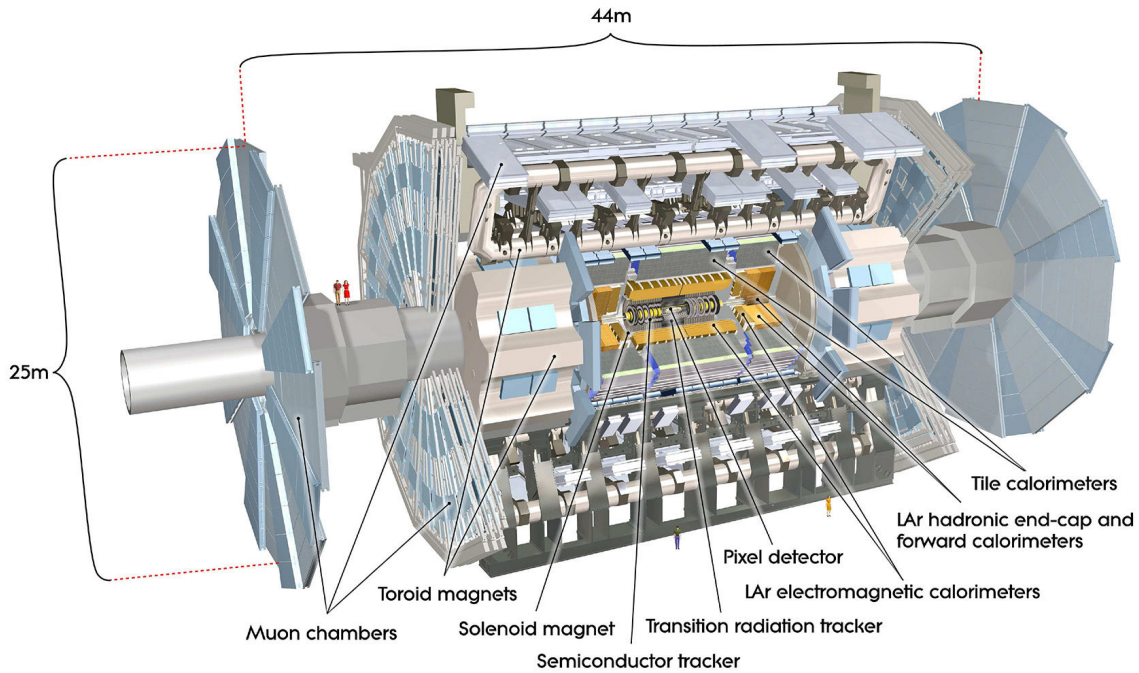


Fig. 3.3: Cut-away view of the ATLAS detector. The dimensions of the detector are 25 m in height and 44 m in length. The overall weight of the detector is approximately 7000 tonnes [62]. Image: CERN.

overview to the ATLAS experiment is also below provided, along with the main aspects concerning its safety and maintenance procedures.

3.1.1 The ATLAS experiment

The ATLAS detector is a multipurpose particle physics apparatus with forward-backward symmetric cylindrical geometry [62, 95]. The inner tracking detector (ID) consists of a silicon pixel detector, a silicon microstrip detector, and a straw-tube transition radiation tracker. The ID is surrounded by a thin superconducting solenoid which provides a 2 T magnetic field, and by high-granularity liquid-argon sampling electromagnetic calorimetry. The muon spectrometer surrounds the calorimeters and consists of three large air-core superconducting magnets, providing a toroidal field (each with eight coils), a system of precision tracking chambers, and fast detectors for triggering.

The combination of all these systems provides charged particle measurements along with efficient and precise lepton and photon measurements. The overall ATLAS detector layout is shown in Fig. 3.3.

The Large Hadron Collider provides a rich physics potential, ranging from more precise measurements of Standard Model parameters to the search for new physics phenomena. Furthermore, as observed in [62], nucleus-nucleus collisions at the LHC provide an unprecedented opportunity to study the properties of strongly interacting matter at extreme energy density, including the possible phase transition to a colour-deconfined state: the quark-gluon plasma. Requirements for

the ATLAS detector system [96] have been defined using a set of processes covering much of the new phenomena potentially observable at the TeV scale.

To analyse and interpret the collision events recorded, complex data-acquisition and computing systems are used. Six different detecting subsystems arranged in layers around the collision point record the paths, momentum, and energy of the particles, allowing them to be individually identified. A large magnet system bends the path of charged particles so that their momenta can be measured. Such interactions create a massive flow of data to be analysed, which is filtered by using an advanced *trigger system* that, loosely speaking, sends to the detector the information needed for selecting which event to record and which to ignore.

Among the most significant results worth of mention obtained with the LHC complex, the ATLAS and CMS experiments announced on 4 July 2012 that they had each observed, independently, a new particle in the mass region around 126 GeV, compatible with the production and decay of the Standard Model Higgs boson [97].

While for a detailed description of the ATLAS experiment the interested reader is referred to [62] and [95], Section 3.1.2 provides an introduction concerning the main radiation protection and safety aspects in the ATLAS environment.

3.1.2 Radiation background at ATLAS

The high collision rates at the TeV scale and at such significant luminosity regime of the LHC give rise to extreme radiation environments, especially in the inner regions of the experiments [98]. The deleterious effects of background radiation fall into a number of general categories: increased background and occupancies, radiation damage and ageing of detector components and electronics, and creation of radionuclides which impact access and maintenance scenarios [62].

Radiation environments at the LHC and its upgrades are complex, comprising a full spectrum of particles (pion, proton, neutron, photon, electron, muon, etc.), with energies ranging from TeV down to thermal in the case of neutrons. A radiological analysis of such environments goes beyond the scope of the present study. However, a brief introduction is below provided as the radiological aspects of the ATLAS environments motivated the development of the gamma camera prototype described in the present chapter in the following sections.

The dominant primary source of background radiation at LHC is collisions at the interaction point [99].

A large effort has been made to calculate the fluence of particles in different parts of the ATLAS experiment, widely documented in [100], resulting also in the categorization and description of three different access scenarios during ATLAS shutdowns. They are summarized below, and two of the scenarios are depicted in Figures 3.4 and 3.5.

- a) In the very short access scenario, all detector components remain in place as well as the magnetic fields. These accesses are typically on the order of a few hours long.

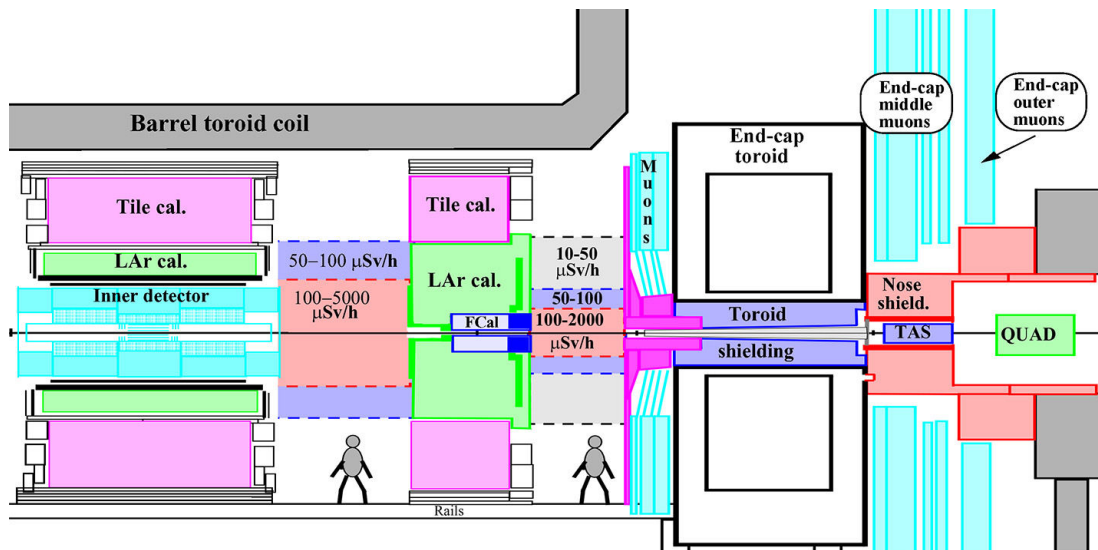


Fig. 3.4: Short access scenario. One half of the inner region of the ATLAS experiment during standard access. The dose rates in the two access areas are also shown. The calculation was performed for one year of running at $10^{34} \text{ cm}^{-2} \text{ s}^{-1}$ luminosity and five days of cooling off [100].

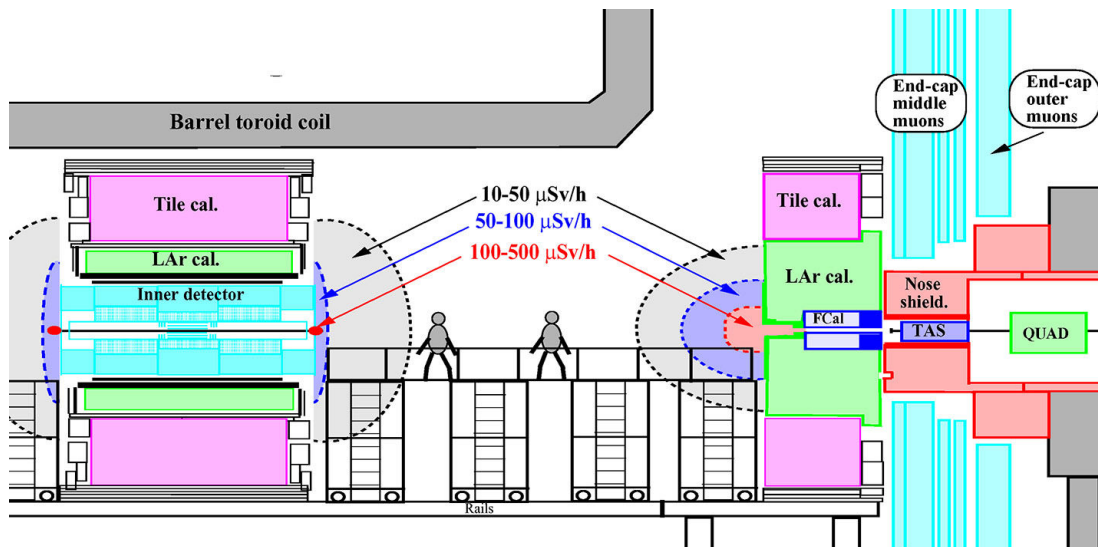


Fig. 3.5: Long access scenario. The central part of the ATLAS experiment during Inner Detector access. The dose rates in the two access areas are also shown. The calculation was performed for one year of running at $10^{34} \text{ cm}^{-2} \text{ s}^{-1}$ luminosity and five days of cooling off [100].

- b) In the short access scenario, the beam-pipe remains in place, acting as a linear source of photon radiation, as can be seen in Fig. 3.4. Because of the high level of radiation, the area around the beam-pipe is fenced off to a radius of about 1 m. This ensures operators working in ATLAS during short access not to be exposed to dose rates higher than 0.1 mSv/h. The only detector which remains inside the barrier is the inner detector. During short access, maintenance of the inner detector is therefore significantly limited.
- c) In the long access scenario, all beam-pipe sections except the one inside the inner detector volume are removed as well as the small muon wheel (or inner end-cap muon stations) and

the end-cap toroids. Two main hotspots can clearly be seen in the final configuration, as shown in Fig. 3.5. One is the end-piece of the inner detector beam-pipe, made of aluminum at time of measurements, whereas the rest of the inner detector beam-pipe is made of beryllium. The other main hotspot is in front of the forward calorimeters, where the dose rate reaches values of up to 0.5 mSv/h. These relatively small-size regions are therefore temporarily shielded with lead blocks during maintenance of the inner detector.

The beam-pipe can be therefore highly radioactive with a contact dose rate of 3–5 mSv/h, and has to be removed in the case of long access scenario. Such interventions could in certain cases inflict several mSv of integrated dose to personnel performing the intervention.

It is worth mentioning that, at the beginning of 2013, the ATLAS detector underwent the first of three planned long shutdown phases, aimed to extend the LHC physics programme into the years 2020 through dedicated upgrades. During such period, a fourth layer instrumented with pixel sensors, the Insertable B-Layer (IBL), was added to the Pixel Detector [62], between a new narrower Beryllium beam-pipe and the innermost Pixel Detector layer (B-Layer) [101, 102].

As extensively explained in [62], in order to limit the effects of radiation on the detector, ATLAS relies on the use of almost 3000 tonnes of shielding. The shielding procedure is based on a three-layer concept. The inner layer is designed to stop high energy hadrons and secondaries. It is built from materials such as iron or copper, which pack a large number of interaction lengths into a limited volume. A second layer, consisting of doped polyethylene rich in hydrogen, is used to moderate the neutron radiation escaping from the first layer; the low energy neutrons are then captured by a boron dopant. Photon radiation is created in the neutron capture process and these photons are stopped in the third shielding layer, which consists of steel or lead.

For a detailed review of the radiation background at ATLAS and its main impact on the detector, the interested reader is referred to [100].

3.1.3 Safety and radiation protection at ATLAS

CERN's standards for the protection of the environment and the workers are based on the European Council Directive 96/29/EURATOM [103]³, together with the French and the Swiss National Legislations on Radiation Protection [105–109]. CERN's Radiation Protection Manual [110] meets the legal radiation protection requirements of the two host states by following the most advanced regulations of the two. As all member states of the European Union (EU) committed themselves to include the EURATOM recommendations into their national legislations, France acted accordingly by releasing the "*Décret No 2002-460 relatif à la Protection générale des personnes contre les dangers des rayonnement ionisants*" on 4 April 2002 [107] and the "*Décret No. 2003-296 relatif à la protection des travailleurs contre les dangers des rayonnement ionisants*" on 31 March 2003 [108]. Although Switzerland does not belong to the EU, the Swiss radiation

³The European Directive 96/29/Euratom takes into account the recommendations of international bodies like the International Commission on Radiological Protection ICRP [104].

protection legislation [109] is compatible with the European Directive. Furthermore, with the latest developments in France and Switzerland, CERN decided to revise its Radiation Protection Manual [110].

Within the EU, radiation workers are classified according to the professional risk involved in their job and are sub-divided into Category B workers (< 6 mSv/year) and Category A workers (< 20 mSv/year)⁴. CERN's RP Safety Manual [110] has been adapted to the classification of workers, which is already common practice in France and within the EU. Table 3.1 gives an overview of these limits.

Table 3.1: Annual limits for personal effective doses as laid down in European legislations.

	Public	Radiation Workers	
		B	A
EU-Directive	< 1 mSv	< 6 mSv	< 20 mSv
France	< 1 mSv	< 6 mSv	< 20 mSv
Switzerland	< 1 mSv	< 20 mSv	
CERN	< 0.3 mSv	< 6 mSv	< 20 mSv

As explained in [111], CERN is following the Suisse Directive HSK-R-11 of the "*Hauptabteilung für die Sicherheit in Kernanlagen*" (HSK). Such directive is based on the recommendation of the "International Commission on Radiological Protection" (ICRP) [104]. Respecting a limit of $300 \mu\text{Sv}/\text{year}$ permits the coexistence of several installations that might potentially contribute to the effective dose of the same critical group of members of the public.

The dose rate limits to be respected in the ATLAS environment are the same applied to all LHC premises, which are below summarized.

Design Limits for occupied areas at the LHC

The specifications of LHC shielding parameters are either derived from analysis based on the consequences of a full beam loss or on continuous loss processes during normal operation. In the case of a full beam loss, the following limits for effective doses are set [111]:

- 20 mSv maximum for persons working in the LHC underground areas,
- 1 mSv for persons working within CERN's premises, and
- $300 \mu\text{Sv}$ for the persons living outside CERN's fences.

⁴In Switzerland only one category of radiation workers exists (< 20 mSv/year).

The limits for ambient dose equivalent rates are based on continuous losses and should not exceed 10 $\mu\text{Sv/h}$ for a controlled area, 1 $\mu\text{Sv/h}$ for a public area within CERN, and 0.1 $\mu\text{Sv/h}$ for a public area outside CERN. The choice of these limits is justified by:

1. The legal limits for effective doses will be not exceeded, even in the case of a full beam loss,
2. the dose rate of 10 $\mu\text{Sv/h}$ is the upper limit for a simple controlled area according to the Swiss legislation [109]. Taking into account that the results of Monte Carlo calculations include considerable safety margins and that the decision making is always based on the results for the worst case (loss close to the shielding wall), a reasonably low ambient dose equivalent rate can be expected for the fixed working places in these types of area.

Dose limits and protection of persons at CERN

As stated in the CERN Radioprotection manual [110], CERN has to designate all workers who are occupationally exposed to radiation⁵, inform them on their classification, and provide them the necessary information concerning the potential radiation exposure in the course of their work and of the dose limits applicable to them.

Practices involving ionizing radiation leading to an effective dose less than 100 μSv per year for individuals working on the CERN site and less than 10 μSv per year for members of the general public do not need to be justified.

The dose limits at CERN are also defined in the CERN Radioprotection manual [110]. Such limits can be exceeded only to remedy significant failures, provided that they are necessary for protecting the population and especially in order to save human lives. Such limits are summarised in Table 3.2.

Table 3.2: Dose limits in any consecutive 12-month period at CERN during maintenance and emergency activities.

	Effective dose limit	Equivalent dose limit
Maintenance activities	20 mSv	150 mSv
Exceptional activities	Up to 50 mSv (or 250 mSv for tasks involving the saving of human lives)	Not specified

Moreover, all occupationally exposed persons are classified in one of two categories:

- (a) Category A: persons who may be exposed in the exercise of their profession to *more than* 3/10 of the limit in terms of effective dose in 12 consecutive months.

⁵An occupationally exposed person is a person subject to a potential exposure incurred at work from practices liable to result in doses exceeding the dose limits for members of the public.

- (b) Category B: persons who may be exposed in the exercise of their profession to *less than* 3/10 of the limit in terms of effective dose in 12 consecutive months.

In case an item under repair has to be taken out of the LHC, it must be first transferred into a properly equipped and radiologically classified workshop. Transport as well as the workshop activities have to be clearly also optimized. The legal requirements for a radioactive workshop depend on the type of job and on the radionuclide inventory of the accelerator component [109].

For a more detailed description of the radiation protection aspects on all main premises of the LHC Project, including the pre-injectors for protons (LINAC II [112], PS-Booster [113]), and ions (LINAC III, LEIR [114]), the two injectors PS and SPS [115], the LHC main ring and the LHC experimental areas, the interested reader is referred to the CERN Radioprotection manual [110] and [111].

Safety and operation management system at ATLAS

The ATLAS detector is not accessible during operation. Due to such inaccessibility, its size, and complexity, advanced control and safety systems are needed.

As explained in [116], the normal operation of the experiment is supervised by the Detector Control System (DCS) [117], responsible for continuous control and monitoring of the detector equipment. The DCS is supervised by a human operator in the control room shown in Fig. 3.2.

In case of anomalies, the CERN Safety Alarm Monitoring system (CSAM) [118] provides CERN with an integrated safety alarm system covering detection, transmission, logging, and display for the LHC machine, LHC experiments, Meyrin, and Preveessin sites. The CSAM system gathers information generated by equipment such as fire and gas leak detectors, emergency stops and other safety related systems, which are located in both surface and underground areas. In case of anomaly, such information is transmitted as a high priority and in a diversely redundant way to the Safety Control Room (SCR) for immediate intervention of the CERN Fire Brigade.

The protection of equipment in abnormal and potentially dangerous operating conditions is covered by the Detector Safety System (DSS). The definition of the DSS was established together by the four LHC experiments in the frame of the Joint Controls Project (JCOP), and the implementation was carried out by the CERN controls group "IT/CO" [119].

The DSS is in operation since 2006, when the installation of the ATLAS detector has started. As detector elements at ATLAS were added, the DSS has been continuously growing, and consists by now of 615 sensor inputs, 570 alarms, with 343 actions defined [116].

At time of writing, not a single unexpected behaviour of the DSS has been observed, after several years of operation. To further improve safety during regular maintenance or upgrade activities in radioactive areas at ATLAS, the EDUSAFE project has been initiated [120–122], below introduced.

EDUSAFE project overview

EDUSAFE was a 4-years (2013–2016) research project, funded by the Innovative Training Networks (ITN) Marie Skłodowska-Curie Actions, under the European Union Seventh Framework Programme (FP7). It meant to provide training for 10 "Early Stage Researchers" (ESR) and 2 "Experienced Researchers" (ER) from different countries, in the framework of a consortium consisting of different host organisations from both academic and non-academic sectors:

- CERN, which acted also as the project coordinator
- University of Caen Normandy ("*Université de Caen Normandie*")
- CANBERRA
- EPFL ("*Ecole Polytechnique Fédérale de Lausanne*")
- National Technical University of Athens
- TUM (Technical University of Munich)
- Athens University of Economics and Business
- Aristotle University of Thessaloniki
- Democritus University of Thrace
- INFN ("*Istituto Nazionale di Fisica Nucleare*")
- Institute of Accelerating Systems and Applications (IASA)
- Novocaptis Cognitive Systems And Robotics
- Prisma Electronics SA
- The National and Kapodistrian University of Athens

The original idea behind the EDUSAFE project was to develop and combine new techniques and technologies into a prototype to integrate with the personnel safety system used at the LHC, in order to assist large-scale operators and to further improve their safety during regular maintenance or upgrade activities. The technical outcome of the project has been an integrated wearable augmented reality (AR) prototype [120, 121], tested and demonstrated as a whole for the first time in June 2016.

As part of the new version of the personnel safety system of the Large Hadron Collider, one of the main technologies to be integrated into the prototype was the capability to localise the main surrounding radioactive hotspots. The main hotspots can be therefore visualized directly on the display interfaced with the other subsystems of the EDUSAFE prototype, so that operators can perform their work accordingly. For this purpose, a new gamma imaging system—called EduPIX⁶— has been developed. In what follows, we describe in detail such development, during

⁶The prefix "Edu" stands for "EDUSAFE" while the suffix "PIX" comes from the name of the Timepix chip.

which multiple technologies and requirements have been explored with the aim of meeting the EDUSAFE project goals.

3.2 The EduPIX gamma camera

Similarly to the iPIX γ -camera, documented in Chapter 2, the EduPIX (Fig. 3.6) is an embedded gamma camera integrating a 1 mm thick CdTe (cadmium telluride) substrate directly bump-bonded to a Timepix chip [63], and a tungsten coded aperture mask [49].



Fig. 3.6: The battery-powered EduPIX γ -camera prototype developed for EDUSAFE.

One of the key differences of the EduPIX respect to iPIX consists in the capability to perform *panoramic measurements*. That is, the ability to locate sources of gamma radiation within a 360° FOV, and to render the resulting image via spherical projection. The description of the reconstruction techniques applied and the validation of the results are reported in Sections 3.3 and 3.4.

Another distinctive feature of the EduPIX prototype is that all acquisition and processing algorithms fully run on its embedded computing board, the ODROID-XU3 [123], a Single Board Computer (SBC) which runs on operating systems based on the Linux kernel, such as Ubuntu or Android. Among its main characteristics, the ODROID-XU3 provides several USB interfaces, allowing a data transfer speed sufficiently rapid to support the "FITPix" USB interface [124], an

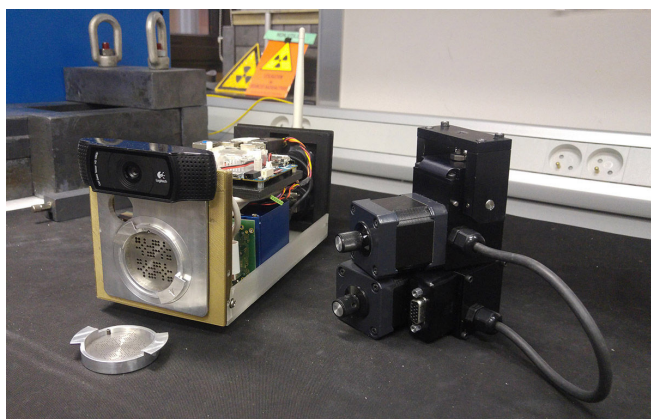


Fig. 3.7: The EduPIX prototype (left) and the motorized pan-tilt unit adopted for remotely changing its position and orientation (right).

alternative interface to the USB 1.22 Interface for Medipix2/Timepix data readout and acquisition control, which allows achieving up to 90 frames per second with a single Timepix detector.

Moreover, one of the goals behind the design of the EduPIX prototype was the capability to perform measurements without requiring any physical interaction between operators and the camera, once installed on the site. For this reason, the system allows full remote control over data networks (including Wi-Fi) using a motorised pan-tilt device, the FLIR PTU-D46-17 pan-tilt unit. Both γ -camera and the pan-tilt system are completely battery-powered, and no cables are thus required for operating the prototype (see Figures 3.6 and 3.7).

In Section 3.2.1 the main aspects concerning data acquisition with the prototype are reported.

3.2.1 Data acquisition

As mentioned in Section 3.2, one important requirement for the EduPIX prototype users and operators was to eliminate the need to be in proximity to the γ -camera while collecting data, as its use is foreseen in environments that can be potentially highly radioactive during both planned and emergency interventions (see Section 3.1.2). Due to such requirement, EduPIX allows full remote control via network (either via Ethernet or Wi-Fi), and the procedure for obtaining panoramic images has been also entirely automated, including its acquisition phase.

Acquisition of optical images

The automation of the whole panoramic image creation procedure requires the acquisition of homogeneous and high-quality optical frames in terms of exposure, sharpness, noise, and distortion. For this reason, a special effort has been made for choosing an adequate optical camera and optimizing the acquisition process of visible images, in order to provide to the stitching algorithm suitable frames to be stitched together (an overview of image stitching is provided in Section 3.3). Such effort turned out to be strictly necessary for obtaining an acceptable probability of automatically generating full 360° images without significant artifacts.

Several aspects had to be taken in account, such as lens distortion, the presence of different exposures in two images with overlapping regions, the sensor sensitivity in low-light conditions, etc. For this purpose, the following sensors have been tested:

- Point Grey "BlackFly"
- E-con System "See3CAM 11CUG CH"
- iDS "UI-1250ML"
- Imaging Source "DFM 72BUC02-ML"
- Logitech "C920 HD Pro"

Surprisingly, despite most of the sensors above were coupled with professional wide-angle lens, the most versatile optical camera for our context turned out to be the Logitech "C920 HD Pro", which can be counter-intuitive since it is the only camera of the list that is not intended for industrial applications. Consequently, it has been chosen as the optical camera to be integrated in the EduPIX prototype. It is worth mentioning that such optical camera would plausibly not have been the optimal solution for a gamma camera intended to be an industrial final product, in which case the reliability of electronics, overall lifespan, and other aspects would have been otherwise additionally considered.

The interface between the EduPIX and the motorized pan-tilt unit has been implemented in Python, proving to be considerably flexible to create and adapt, as the pan-tilt device is completely controllable by simply sending ASCII strings to it.

For each perspective of the camera, the approach for choosing autonomously the most suitable optical frames consists in selecting the frame based on their *brightness* and *sharpness*.

More specifically, during the acquisition phase, for every position/orientation of the camera, several optical images are captured. For each optical image captured from the same exact perspective, the brightness is estimated, by first calculating its brightness *Luma*, L , using the formula provided by the ITU-R Recommendation BT.601 [125]:

$$L = \frac{(299 \times R) + (587 \times G) + (114 \times B)}{1000}, \quad (3.1)$$

where R , G and B denote respectively the Red, Green and Blue channels of the color image. Once the Luma is computed, the corresponding Root Mean Square (RMS) is also computed, as follows:

$$RMS_L = \sqrt{\frac{\sum_{M,N} L(m,n)^2}{M \times N}}, \quad (3.2)$$

where M and N are the number of rows and columns in the input image L , respectively.

RMS_L can be interpreted as a measure of the magnitude of all values occurring on the Luma channel. For this reason, it is a convenient measure of the brightness of a given image.

Once all images from the same perspective have been captured and associated with their RMS_L , the median of all RMS_L values regarding that perspective is calculated. The images are so ordered based on the minimum of the difference between their RMS_L and the median value from that perspective. Such comparison is intended to decrease the brightness differences between source images that are used for the stitching algorithm. Such approach helps not only to get a uniform result for the final panorama image, but also to optimize the calculations performed during several phases of the stitching algorithm implemented for the EduPIX, described in Section 3.3.

After the brightness of all frames from a given perspective has been considered, a similar process is carried out concerning their sharpness. Roughly speaking, we can define the sharpness of an image as the amount of boundaries between zones of different tones or colors in the image itself. A number of methods has been proposed to estimate the sharpness of an image with no a priori knowledge of it [126, 127]. However, compared to such methods, an easier approach to estimate how sharp an image is consists in computing its gradient. This is also intuitive, as a sharp image is expected to have sharp edges, which in turn can be interpreted as directional sudden changes in the intensity within the image. For this reason, the Sobel operator⁷ [128] is applied on each frame, which locates the edges of an image and finds the approximate absolute gradient magnitude at each point of a greyscale image. More specifically, the Sobel operator is based on the convolution of the image with a pair of integer-valued 3×3 convolution kernels in the horizontal and vertical directions, allowing thus the computation of the approximations of the gradient component in both directions.

After the edges of the image are computed, the following step is completely analogous to what above described for estimating the brightness. The RMS on the images containing the edges returned by the Sobel Operator is computed, as follows:

$$RMS_S = \sqrt{\frac{\sum_{M,N} S(m,n)^2}{M \times N}}, \quad (3.3)$$

where M and N are the number of rows and columns in the input image S , respectively.

RMS_S is thus a measure of how sharp a given image is. In this case, the image with the *maximum* sharpness value is assigned the highest score.

By simply summing the position obtained by all images from a given perspective concerning both their sharpness and brightness, respectively, the visible image is selected and stored (if two images have equal score, one of the two will be randomly chosen). The camera won't capture other optical frames until the motorized pan-tilt system performs a further step to the following position/orientation.

For each perspective of the gamma camera during the acquisition phase, ten images candidates are sequentially captured by the optical camera, in automatic mode (i.e. the firmware of the camera manages the main settings such as exposure, focus, saturation, etc.), and then processed by the selection procedure above described, so that only one picture is finally chosen and stored.

⁷The Sobel operator is sometimes referred to as Sobel–Feldman operator or simply Sobel filter.

Such procedure has been implemented in Python, and when the corresponding thread⁸ is running on the computing board of the EduPIX, takes averagely 0.84 seconds per perspective.

Undoubtedly, I could have adopted alternative methods for this task. For example, the edges of each image could have been retrieved by means of other operators, such as the Prewitt operator [129] or the more effective but also computationally intensive Canny algorithm [130] (the interested reader is referred to [131] for a comprehensive comparison of the main operators in image processing for edge detection). Or, moreover, the scoring mechanism for determining the most suitable images could also have considered the image noise level [132] of each candidate optical frame and the respective estimation.

However, the implemented approach was finally adopted due to its low computational cost and as it led to fully satisfactory results, reported in Section 3.4.3.

Acquisition of radiation images

The EduPIX prototype has been developed as a device meant to be handled in highly radioactive environments. Consequently, operators need to perform their activities rapidly and efficiently. Due to this important requirement, the EduPIX needed to be as easy to use as possible, which usually is not necessarily a priority for research prototypes. To conform to such requirement, the gamma camera is quite straightforward to operate, and its graphical user interface (GUI), described in Section 3.2.3, have been designed so that the prototype is *completely* independent from its client devices used by operators⁹. For this reason, also the acquisition of radiation information is embedded in the EduPIX computing board, using the D2XX library for Linux [133], developed by FTDI¹⁰ primarily to support direct access in Linux to USB devices, such as the FITPix USB interface.

Once the acquisition is complete and the corresponding frames returned by the Timepix chip are collected and stored, they are provided as input to the processing algorithm also used by the iPIX gamma camera when performing a single measurement (i.e. not panoramic). Consequently, in such case, radiation information is superimposed on the respective optical images similarly to how done for the iPIX, documented in Chapter 2. Nevertheless, when performing panoramic measurements, the algorithm implemented for the EduPIX prototype performs a further step when processing radiological information, which is documented in Section 3.3.5.

In fact, the main benefits from panoramic images come from measurements involving extended sources that have sizes potentially exceeding the FOV of the gamma camera while being localized. For this reason, a series of experiments with planar sources has been carried out in the context of Panoramic Gamma Imaging. More specifically, several measurements have been performed by placing and combining several planar sources in proximity to the gamma camera prototype.

⁸A thread can be defined as an independent sequence of execution running in a shared memory space of a computer system.

⁹Generally speaking, a client device is a component of a larger system from which it typically retrieves information or uses resources both provided by another component of the same system, usually called server.

¹⁰Future Technology Devices International.

The main aspects and results concerning such experiments are reported in detail in Sections 3.2.2 and 3.3.5.

3.2.2 Preliminary tests with extended sources

All measurements involved in the iPIX characterization study (see Chapter 2) were performed while placing the gamma camera in proximity to a point source. That is, a source of radiations which can be approximated and represented by a point in space.

However, in the case of the panoramic EduPIX prototype, we have instead considered sources that may potentially exceed the FOV of the gamma camera. For this reason, we conducted preliminary tests with the gamma camera placed in proximity to *planar sources*.

To provide a more specific idea, Figure 3.8 illustrates an ideal representation of the instrument placed in front of a planar source. The flow of radiation through each element dS of the source S is independent from its position on the surface, and no scattering of radiation occurs after its emission from surface S . The flux is the radiation intensity per solid angle traveling in the direction θ with respect to the z -axis.

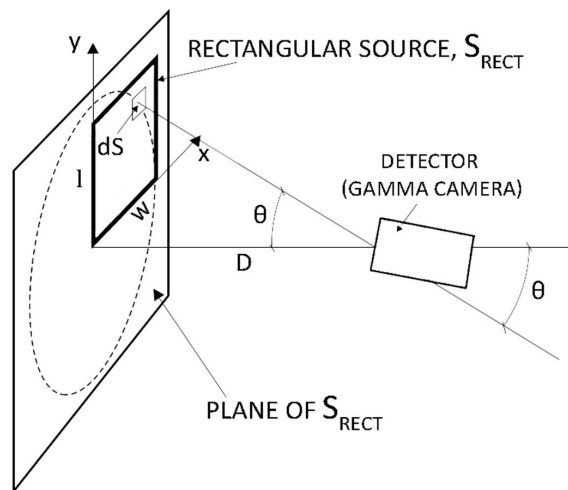


Fig. 3.8: Representation of a rectangular (planar) source S of width w and length l . The detector is at distance D from the center of plane S .

Such configuration has been therefore simulated, in order to study the behaviour of the prototype and the performances of the algorithm described in Section 1.2.2 when performing measurements in proximity to a planar source.

The response of the gamma camera has been studied with the low-activity planar sources listed in Table 3.3, whose homogeneity has been assessed by means of an auto-radiographer (10 min exposure time). The standard deviation obtained was 13% for 10 mm^2 and 9% for 40 mm^2 , respectively (see in Appendix C for complementary information regarding such sources). Several configurations and combinations have been experimented, placing the gamma camera at several

Table 3.3: Low-activity planar sources used at CEA-LIST Saclay.

Number of units	Radionuclide	Current activity	Size
3	^{57}Co	429 kBq	7 cm \times 5.5 cm
3	^{57}Co	143 kBq	7 cm \times 5.5 cm
3	^{241}Am	144 kBq	7 cm \times 5.5 cm

distances and angles. For all the experiments with planar sources below described, the mask R7e4 has been employed.

The first test that was carried out involved only with one ^{57}Co planar source with 429 kBq activity (see Table 3.3). The gamma camera prototype was oriented so that the center of the source was placed at exactly 50 cm from the center of the coded aperture of the camera, providing a dose rate at the measurement point of ~ 340 nSv/h (measured by means of the CANBERRA instrument Colibri VLD). Fig. 3.9 shows the source and the experimental setup chosen for this first measurement.



Fig. 3.9: Planar ^{57}Co source of size 7 cm \times 5.5 cm with activity of 429 kBq at 50 cm from the gamma camera, providing an ambient dose equivalent rate of ~ 340 nSv/h at the measurement point.

with activity of 143 kBq were thus stitched to the pipe so that they would be visualized in the center area of the FOV of the gamma camera prototype, while the sources with stronger activity (429 kBq) were placed in the left or bottom-left areas of the resulting image.

The resulting 3-D profile plot is shown in Fig. 3.10. As already mentioned above, the profile of the decoded matrix shows the registered counts associated to each Timepix pixel after the de-convolution process (see Section 1.2.2 for more details). With this specific configuration, the gamma camera was able to localize the above source with 40 frames of 1 sec shutter time (that is, considering data collection only). See Fig. 3.11.

The γ -camera was thus clearly able to localize the planar source in a setup that was an approximation of the (ideal) representation shown in Fig. 3.8.

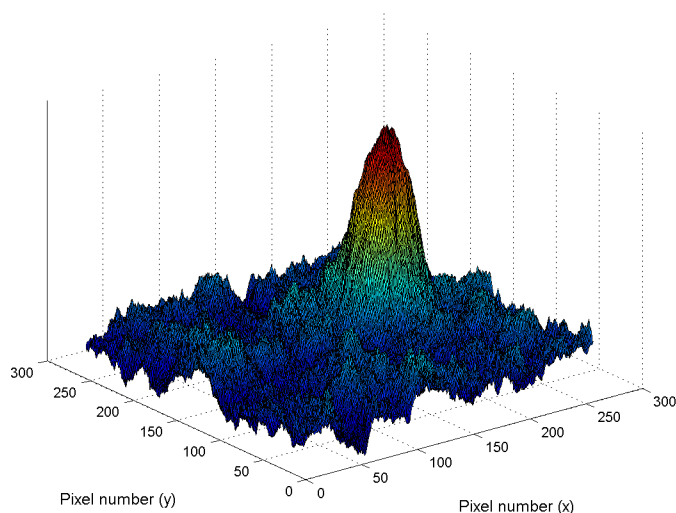


Fig. 3.10: 3-D hotspot profile resulting from a measurement of a planar ^{57}Co source with activity of 429 kBq at 50 cm from the gamma camera, providing an ambient dose equivalent rate of ~ 340 nSv/h at the measurement point.

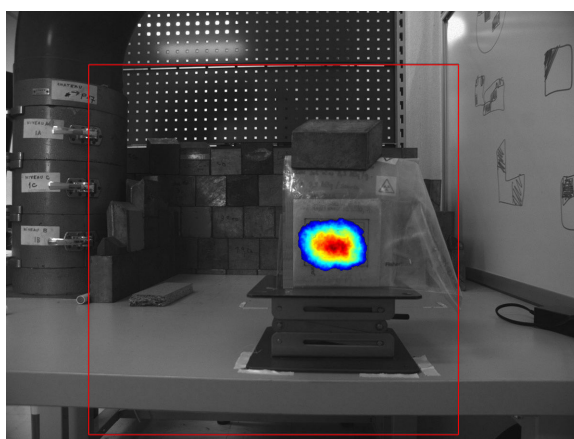


Fig. 3.11: Measurement results obtained with a 429 kBq planar source located at a distance of 50 cm.

Combining multiple planar sources

In order to simulate situations closer to real-life scenarios, additional different combinations and configurations have also been experimented. This was possible also due to the availability of several sources of this type (i.e. planar), which are more adequate for such simulations compared to point sources.

For this reason, we placed a tube with angular shape in front of the camera, and we covered it with the six low-activity planar ^{57}Co sources listed in Table 3.3. A part of the setup of such experiment is shown in Fig. 3.12.

This type of tube, called *elbow*, is typically installed between two lengths of pipe (or tubing) to allow a change of direction, usually of 90° or 45° angle. This specific set-up was chosen since, typically, measurements conducted in nuclear power plants reveal radioactive contamination due

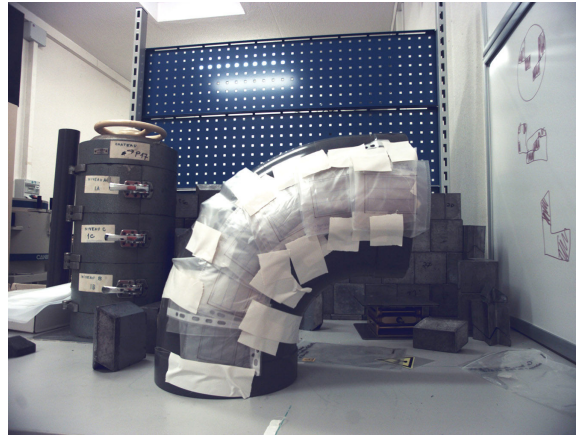


Fig. 3.12: Combination of planar ^{57}Co sources by placing them all adjacently respect to each other in order to simulate a pipeline elbow with 1716 kBq of total activity, at an average distance of 64 cm from the gamma camera. The three ^{57}Co sources with stronger activity (429 kBq) were placed on the left respect to the FOV of the γ -camera, whereas the ^{57}Co sources with activity of 143 kBq were stitched to the pipe so that they would be visualized in the center area of the FOV of the gamma camera prototype. The associated ambient dose equivalent rate at the measurement point was ~ 280 nSv/h.

to radioisotope accumulation near the region where the elbows and adjacent wedges are welded into a piping loop.

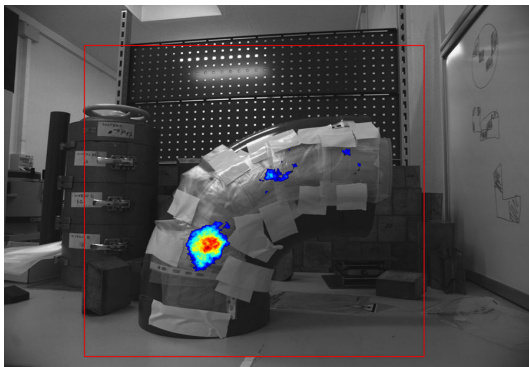
While planning the measurements, several aspects had to be inevitably taken in consideration when placing the sources and interpreting the results.

In the first place, not all planar sources had the same activity, so it was not possible to emulate a source with the shape of the tube with an activity uniformly distributed along its *complete* surface. Nevertheless, that was not necessarily a problem for this specific experiment, as one of its main purposes was to simulate a situation closer to real life scenarios, where large surfaces rarely present a uniformly radioactive surface anyway. In addition to the difference of activity of some sources, a loss in counts occurs in the Timepix detector when increasing the horizontal or vertical angle respect to the center of its FOV. This was observed in Chapter 2 in Section 2.4.7, and it is mainly due to the collimation effect of incident photons at the same coded aperture mask. Such effect is even more emphasized at low-energy photons, where the gamma camera can have a decrease of its response to more than 50% when using the R7e4 mask.

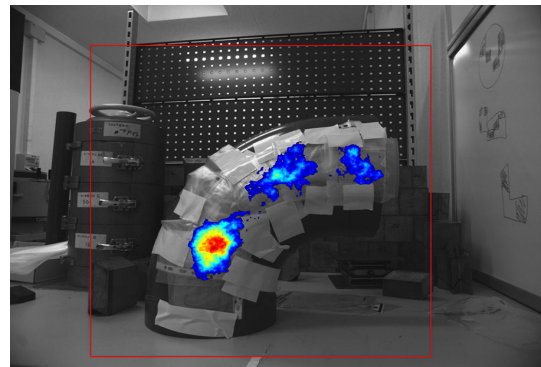
Due to the considerations above, the ^{57}Co sources with activity of 143 kBq were thus stitched to the pipe so that they would be visualized in the center area of the FOV of the gamma camera prototype, while the sources with stronger activity (429 kBq) were placed in the left or bottom-left areas of the resulting image.

Once the 3-D hotspot profile of a given measurement was generated, only pixels with a cut-off threshold of 70% above background level were considered, in order to superimpose the most meaningful information concerning radiations of a given scene on the optical image. Such threshold was empirically found and it was ideal for measurements concerning point-sources.

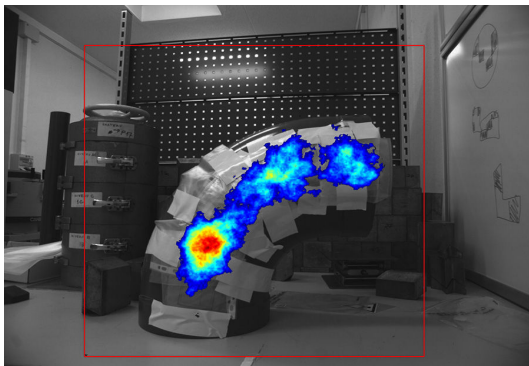
Nevertheless, in this case, it was clear that a lower threshold could also have taken in consideration. As Fig. 3.13a shows, while applying a 70% cut-off threshold, the sources with the highest activity were correctly considered as the most intense sources of radiation in the scene, whereas the sources with the lowest activity were not displayed and indicated as radioactive during the superimposition phase. For this reason, other thresholds were also tested. Fig. 3.13 shows the corresponding results obtained with four different cut-off thresholds, namely 70%, 60%, 50%, and 40%.



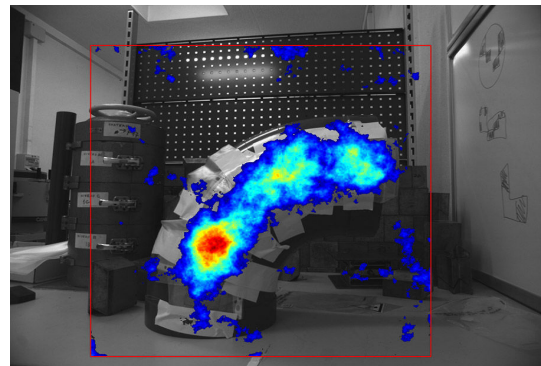
(a) Decoded gamma information superimposed with a cut-off threshold of 70%.



(b) Decoded gamma information superimposed with a cut-off threshold of 60%.



(c) Decoded gamma information superimposed with a cut-off threshold of 50%.



(d) Decoded gamma information superimposed with a cut-off threshold of 40%.

Fig. 3.13: Results obtained with mask R7e4 and by placing several ^{57}Co sources adjacently to simulate a pipeline elbow with 1716 kBq of total activity, at an average distance of 64 cm from the gamma camera. Several cut-off thresholds were applied during the superimposition phase for comparison purposes.

As Fig. 3.13 shows, by adopting a cut-off threshold of 60% or 50%, also sources with the lowest activity were detected and superimposed onto the respective optical image. If the chosen threshold is too low, nonetheless, the background noise becomes visible. It is worth noticing that the noise surrounding the peak in the radiation image and the associated 3-D hotspot profile (Fig. 3.14b) significantly depends also on the amount of data (i.e. number of acquisition frames) collected during the acquisition.

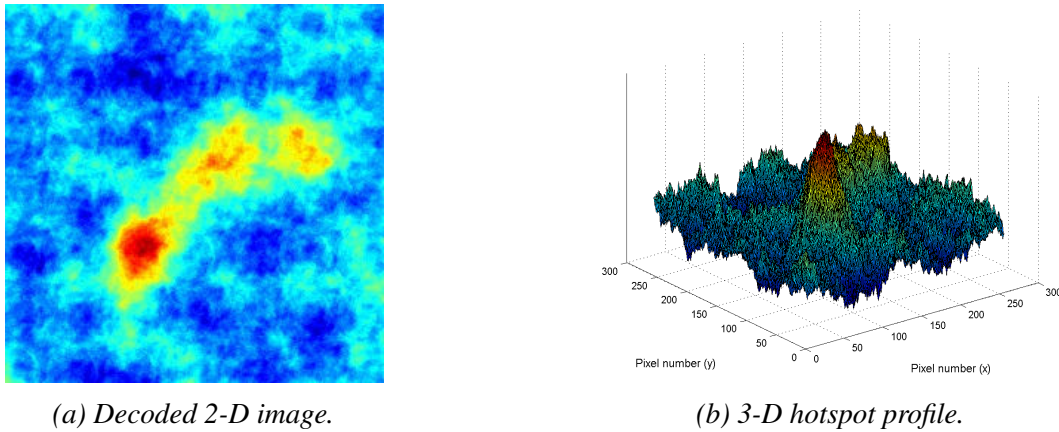


Fig. 3.14: Results obtained with mask R7e4 and by placing several ^{57}Co sources adjacently in order to simulate a pipeline elbow.

A future perspective that can be envisaged regarding this aspect is the collection of a sufficient number of measurements with extended sources, in order to evaluate, from a quantitative standpoint, which measures could be considered in order to establish and propose a solution for a more systematic computation of a suitable cut-off threshold.

Response to different incident photon energies within the same measurement

As shown Chapter 2 in Fig. 2.15, the Timepix detector is highly sensitive in the energy range between 50 and 70 keV, but its sensitivity is significantly less important for energies higher than 120 keV, which is the case for the ^{57}Co source. As a consequence of such aspect and as planar ^{241}Am sources were also available, few experiments concerning extended sources involved the presence of both radionuclides within the same measurement.

Taking in consideration the off-axis response of the gamma camera, the high energy dependency of the Timepix detection sensitivity, and the activity of the available sources, two ^{57}Co sources with activity of 143 kBq were overlapped and placed on the right respect to the FOV of the gamma camera prototype, while two ^{241}Am sources with activity of 144 kBq were placed in the same manner, but on its left.

For this measurement, 180 frames of 1 sec shutter time were collected, both in mask and antimask position. The resulting profile plot and superimposed γ -image are shown in Fig. 3.15.

The radiation image concerning the ^{241}Am deceptively indicates that the source on the left contributes to the ambient dose equivalent rate at the measurement point more than the source on the right. This is a misleading result because of several reasons:

- the ^{241}Am and ^{57}Co sources were both placed on purpose at the same distance from the centre of the detector of the gamma camera (50 cm),
- they had comparable activities (288 kBq and 286 kBq, respectively),

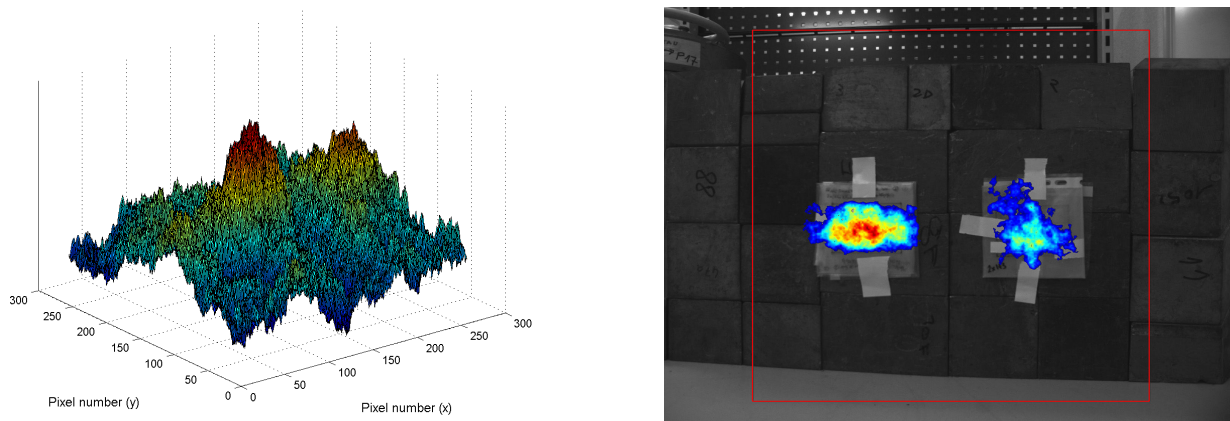


Fig. 3.15: Hotspot profile and superimposition results of a measurement performed involving two different radionuclides. Two ^{57}Co sources with activity of 143 kBq (total 286 kBq) were overlapped and placed on the right respect to the image plane of the gamma camera prototype, while two ^{241}Am sources with activity of 144 kBq (total 288 kBq) were overlapped and placed on its left.

- and ^{57}Co emits γ -rays with an energy which is more than double than that of the γ -rays emitted by the ^{241}Am .

Nonetheless, the current version of the γ -camera aims at the spatial localization of the surrounding hotspots rather than their activity quantification, both absolute and relative, for which the energy of the source under study, the source-to-detector distance, specific energy response of the detector, auto-collimation effect of the coded aperture (see Section 2.4.7), and several other aspects would need to be considered, and which are not in the scope of the capabilities of the current version of the γ -camera under study.

All above experiments were useful to test the response of the coded aperture gamma camera when in proximity to sources that are not punctual. Moreover, all sources were visible within the FOV of the gamma camera prototype. Nevertheless, as already mentioned above, a drawback of the coded aperture imaging approach is its limited FOV. For this reason, a Panoramic Gamma Imaging method for *portable* coded aperture gamma cameras has been designed, implemented, and tested.

Before describing the main aspects concerning the reconstruction techniques of such method, a brief overview of the software, the connectivity, and the graphical user interface of the EduPIX prototype is provided, in order to introduce the main functionalities of the system that have been implemented and described in more detail in Section 3.3.

3.2.3 EduPIX software and interfacing

The EduPIX gamma camera has been developed as a device meant to be used rapidly and efficiently. Consequently, a software architecture able to satisfy such requirement and at the same time allowing fast prototyping was required. This is one of the reasons for which the design of the EduPIX follows a modular approach.

Software design

In order to obtain a *modular system*, several technologies have been chosen and combined. A main aspect was the handling of the communication between the server and client sides implemented for the embedded EduPIX. For this task, the JSON¹¹ format [134] is mainly used, an efficient data interchange language inspired by the JavaScript object literal syntax. JSON is a human readable text format which is completely language independent, helping thus in obtaining a *loosely coupled* system¹².

On the server side, a number of libraries are employed, namely the Numpy and Scipy packages [135], supported in Python, and the OpenCV libraries [136], supported by both Python and C++, which are the main languages adopted for the server side.

The client side of the prototype is an HTML5 application [137]. Consequently, any device with a web browser supporting HTML5, such as a portable computer, a tablet, or a smartphone, can be connected to the EduPIX prototype and benefit of all its functionalities. For rendering the panoramic images and the graphical user interface, the system uses the WebGL¹³ and Javascript technologies, without the need for any additional browser extensions¹⁴.

The EduPIX gamma camera communicates with other devices via network (both via Ethernet or WiFi). In the configuration implemented at the time of writing, it acts also as a DHCP server (Dynamic Host Configuration Protocol), thus dynamically distributing network configuration parameters, such as IP addresses, to its client(s).

Any possible latency or packet loss do not influence the accuracy of the measurements performed, as both acquisition and processing algorithms are computed completely on the computing board of the EduPIX. Latency and packet loss might influence only the reactivity and reliability of the interaction between the operator and the GUI of the system.

A brief description of the user interface designed and implemented for the EduPIX is below reported.

Graphical user interface

The graphical user interface of the EduPIX supports three types of client devices: desktop computers, tablets, and smartphones. Depending on the device, the dedicated GUI is automatically loaded in the browser. The interface designed and implemented for tablets is illustrated in Fig. 3.16 (only the main functionalities are highlighted).

The main functionalities provided by the GUI of the EduPIX prototype can be summarized as follows:

- Scene selector: it provides the operator the possibility to easily navigate through the scenes (single and panorama measurements) previously performed.

¹¹JSON stands for *JavaScript Object Notation*.

¹²That is, a system whose components have almost no knowledge of the definitions of other separate components.

¹³WebGL stands for *Web Graphics Library*.

¹⁴Browser extensions are sometimes referred to also as *plugins*.

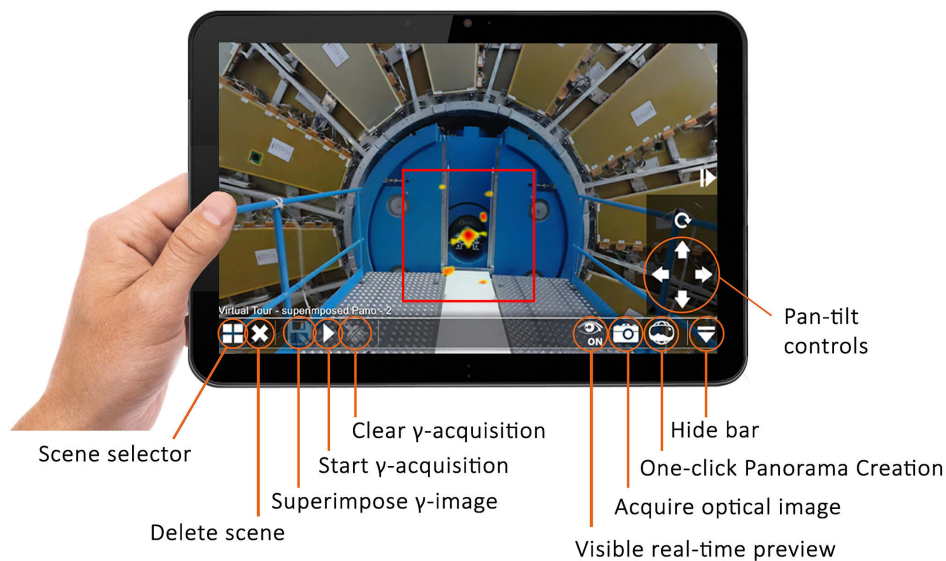


Fig. 3.16: Main functionalities of the EduPIX system provided by its graphical user interface. In this example, the buttons "clear γ -acquisition" and "superimpose γ -image" are greyed out as they are available only when an acquisition is in progress.

- Delete scene: it deletes a scene from both the GUI and from the embedded memory (eMMC) of the ODROID-XU3 of the EduPIX.
- Superimpose γ -image: it overlays the gamma image (treated as a layer containing an image RGB with an additional alpha channel¹⁵) onto the optical image, and stores the respective result.
- Start " γ -acquisition": it launches both gamma acquisition and processing, whose results are displayed and updated each second as a layer, directly on the visible image within the red square representing the field of view of the gamma sensor.
- Clear " γ -acquisition": it clears all radiation information not previously stored, and deletes the corresponding superimposed layer, if present.
- Visible real-time preview: it displays on the GUI the visible stream with a frame rate of 24 frames per second.
- Single shot: it acquires an optical image of the respective scene, stores it, and loads it on the browser. Before starting a " γ -acquisition", it is necessary to acquire such optical image.
- Panorama creation: it launches with one tap the panorama image creation procedure. At the end of the process, such scene is automatically loaded and rendered on the GUI. Once loaded, by tapping and holding on the touchscreen, the user can rotate the panorama image around its centre towards all directions.

¹⁵The alpha channel is a color component of an image that represents the degree of transparency (or opacity) of a color (i.e. the red, green and blue channels). It is used to determine how a pixel is rendered when blended with another, first proposed in [138].

- Pan-tilt arrows: they change the orientation of the EduPIX camera via the motorized pan-tilt unit.

3.3 Panoramic Gamma Imaging

The need to combine two or more images into a single larger image has arisen in a number of contexts not that recently. Back in 1979, for example, mosaics of Jupiter and Saturn have been generated by using multiple frames captured from the cameras aboard the Voyager 1 and Voyager 2 spacecrafts [139, 140].

Nowadays, such process is usually referred to as *image stitching*, which can be thought of as a method consisting of three main phases: *image registration*, *image reprojection*, and *image compositing*. During the image registration phase, portions of adjacent images are compared to find the transformations so that, roughly speaking, the points in one image can be related to their corresponding points in the other. Once the images have been registered, they are reprojected according to the transformations found in the previous step. Finally, the image compositing phase consists in merging the registered images in order to mitigate the transition colour discontinuities between adjacent stitched images, typically referred to as *seams*¹⁶. An overview of the image stitching process is illustrated schematically in Fig. 3.17.

The stitching algorithm of the EduPIX gamma camera is implemented in C++ using the Open Source Computer Vision Library (OpenCV) [136], made available under a BSD license (Berkeley Software Distribution). Its pipeline is described below in the present section and it is inspired by the one proposed in [141]. Nevertheless, while Brown and Lowe [141] use the SIFT algorithm [142] to extract and match features between all images, the procedure designed for the gamma camera relies on the computationally more efficient ORB algorithm (Oriented FAST and Rotated BRIEF) [143], which in turn relies on the well-known BRIEF descriptor [144] and FAST keypoint detector [145].

Moreover, in the context of the EduPIX prototype, also the acquisition phase is automated, by sequentially capturing all images using the motorized pan-tilt unit. For this reason, it has been possible to adapt and optimize the feature matching and projective transformation estimation steps according to the time of acquisition of each optical image: All images are labelled depending on their order while being captured by the camera. This significantly eases the process, as each image is thus matched only to the one that is adjacent and whose is already known having an overlapping area. Such region is proportional to the angle of rotation of the pan-tilt device (angle per step), pre-set as parameter in the implementation code of the prototype.

More specifically, depending on the *vertical* FOV of the final panorama image, a number of frames are vertically acquired and then stitched together using the algorithm below described (Fig.

¹⁶A seam is the artificial edge generated by the intensity differences of pixels immediately next to where the images are merged.

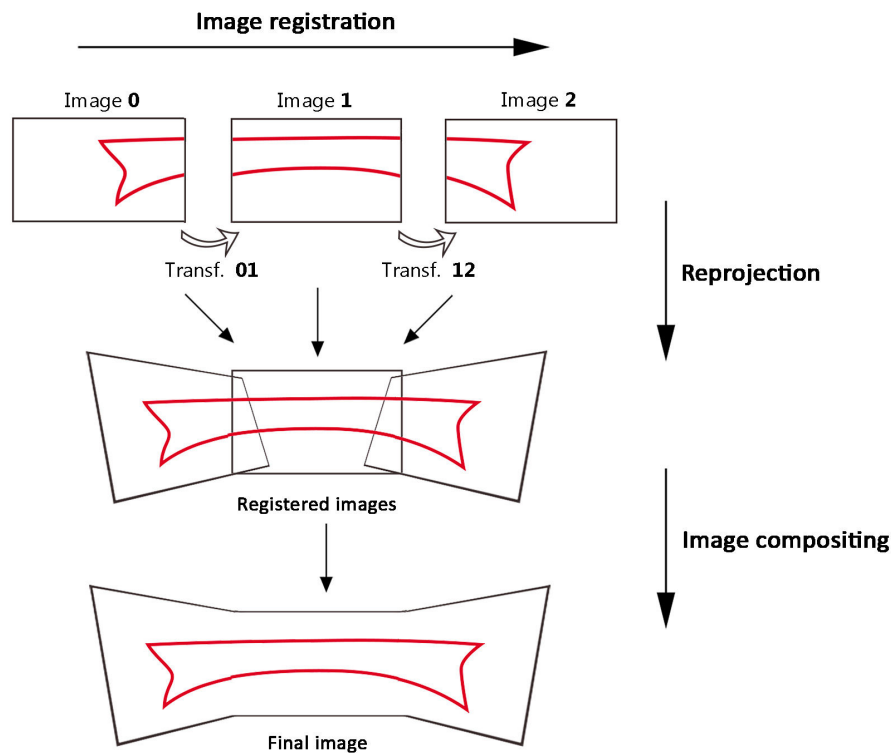


Fig. 3.17: A general outline of the main steps of image stitching. Given a sequence of images, the geometric transformations between consecutive pairs of images are computed during the image registration phase. Once the images have been registered, they are reprojected according to the transformations found in the previous step, resulting in one single, wider image. Finally, the image compositing phase consists in compensating and mitigating the remaining colour discontinuities occurring in the overlapping regions, in order to create an image without any evident artifacts detectable by a human being.

3.18a). Once the 360° horizontal FOV has been covered, each vertical result obtained in the first phase is an input for the final horizontal stitching phase (Fig. 3.18b).

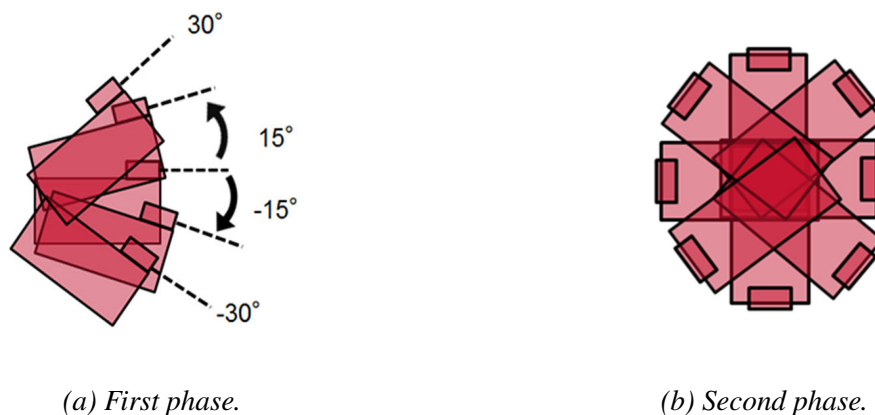


Fig. 3.18: Illustration of the two automated main acquisition phases with the EduPIX prototype of the optical images to be stitched. During the first phase of the acquisition, the images are acquired vertically (a). Once the horizontal 360° FOV has been entirely covered, each image previously vertically stitched is then horizontally stitched with the remaining ones.

Another distinctive aspect concerning the acquisition phase derives from the automatic selection of the most suitable optical frames (described in Section 3.2.1), which significantly contributes to further optimize the stitching pipeline designed and implemented.

Before describing in more detail the stitching algorithm for optical and radiation images implemented for the EduPIX, in order to establish a common vocabulary, Section 3.3.1 begins with a general description of the homogeneous notation for points and an introduction of the basics behind image stitching.

3.3.1 Basic concepts

As explained in [146], the ideas and notation of projective geometry are central to an analysis of multiple view geometry. For example, the use of homogeneous coordinates allows us to represent *non-linear* mappings (such as perspective projection) by *linear* matrix equations. For this reason, we briefly provide below the concept of homogeneous coordinates and projective transformation (or homography, the terms are synonymous), widely used hereinafter.

Homogeneous representation of points

Considering \mathbb{R}^2 as a vector space, a point with coordinates (x, y) in the 2-D plane can be interpreted as a vector. A line in the plane is represented by an equation such as $ax + by + c = 0$, where different choices of a , b , and c give of course rise to different lines. A line may be thus represented by the vector $(a, b, c)^\top$. We can in this way introduce the *homogeneous representation of points*.

A point $\mathbf{x} = (x, y)^\top$ lies on the line $\mathbf{l} = (a, b, c)^\top$ if and only if $ax + by + c = 0$. This may be written in terms of an inner product of vectors representing the point as $(x, y, 1)(a, b, c)^\top = (x, y, 1)\mathbf{l} = 0$. Therefore, the point $(x, y)^\top$ in \mathbb{R}^2 is represented as a 3-vector by adding a final coordinate of 1.

For any non-zero constant k and line \mathbf{l} , we have $(kx, ky, k)\mathbf{l} = 0$ if and only if $(x, y, 1)\mathbf{l} = 0$. It is thus possible to consider the set of vectors $(kx, ky, k)^\top$ for varying values of k to be a representation of the point $(x, y)^\top$ in \mathbb{R}^2 . Consequently, an arbitrary homogeneous vector representative of a point is of the form $\mathbf{x} = (x_1, x_2, x_3)^\top$, representing the point $(x_1/x_3, x_2/x_3)^\top$ in \mathbb{R}^2 .

Planar projective transformation

A planar projective transformation is a linear transformation on homogeneous 3-vectors represented by a non-singular 3×3 matrix [146], which can be described as follows:

$$\begin{pmatrix} x'_1 \\ x'_2 \\ x'_3 \end{pmatrix} = \begin{bmatrix} h_{11} & h_{12} & h_{13} \\ h_{21} & h_{22} & h_{23} \\ h_{31} & h_{32} & h_{33} \end{bmatrix} \begin{pmatrix} x_1 \\ x_2 \\ x_3 \end{pmatrix}, \quad (3.4)$$

or, more briefly, $\mathbf{x}' = \mathbf{H}\mathbf{x}$.

The matrix \mathbf{H} occurring in this equation may be changed by multiplication by an arbitrary non-zero scale factor without altering the projective transformation. As a reminder, a projective transformation projects every image into another *projectively equivalent* image¹⁷. For this reason, we say that \mathbf{H} is a homogeneous matrix, since as in the homogeneous representation of a point, only the ratio of the matrix elements is significant.

The interested reader regarding projective geometry and the specializations of projective transformations, such as affine and similarity transformations, is referred to [146] and [147].

Image registration

Algorithms for registering optical images (i.e. the first main phase of image stitching in our context) are among the oldest and most widely known algorithms in Computer Vision. Back in 1981, Lucas and Kanade proposed one of the most currently known registration techniques [148]. Still up to this day, several methods and video compression schemes as important as the ones used by MPEG and H.264 [149], for example, are deeply inspired by such technique.

Given two images acquired by a camera rotated about its centre, the basic geometry of the image registration problem consists of estimating the 3×3 homography matrix \mathbf{H} of Eq. 3.4, for each image.

Several issues need to be dealt with when stitching images captured from different perspectives and/or at different times, such as blurring or ghosting caused by parallax as well as varying image exposures or other distortions, some of which mentioned in Section 3.2.1. In our case, we consider the image registration methods typically referred to as *feature-based*, which often consist at least of the following four main steps [150]:

- Feature detection: For each image, distinctive objects such as edges, corners, closed-boundary regions are detected.
- Feature matching: Using the features found during the previous step, the correspondence between the images is established (see Fig. 3.19). For that purpose, various feature descriptors and similarity measures along with spatial relationships among the features can be used [146]. In other terms, the main objective of this step is to determine which features come from corresponding locations in different images.
- Transform model estimation: The type and parameters of the functions for aligning the sensed images are estimated. The parameters of such functions (called mapping functions) are computed by means of the established feature correspondence in the previous step.
- Image resampling and transformation: The images are transformed by means of the mapping functions. Image values in non-integer coordinates are computed by the appropriate interpolation technique.

¹⁷That is, leaving all its projective properties invariant.

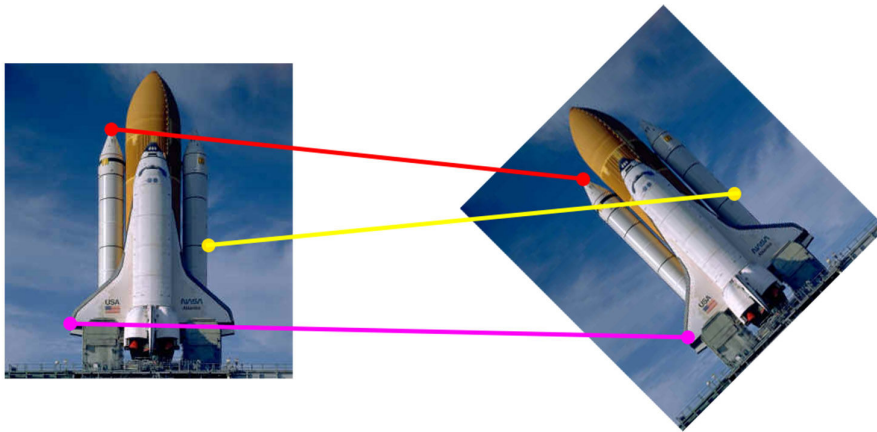


Fig. 3.19: After a set of distinctive keypoints are found, they are matched and interpreted as local descriptors, in order to establish the correspondence between the features detected in the first image and those detected in the reference image.

During the feature detection and matching phases, since the features can appear at different orientations or scales, a view invariant representation¹⁸ must be used [151].

For an exhaustive review of general-purpose image registration methods, the interested reader can refer to [152].

Image Compositing

Once all input images are registered with respect to each other, the next step is Image Compositing. Such step mainly consists in choosing which pixels contribute to the final stitched image and *blending* those that have been selected in order to minimize the visible blur, seams, and ghosting effects.

In an ideal case, the overlapping region of adjacent images is identical. That is, the intensity values of each pixel within the overlapping region in the first image equal the intensity values of the corresponding point in the second image. In practice, however, geometric discontinuities as well as radiometric discrepancies¹⁹ are present, caused by approximations of the registration method used.

One of the first algorithms for digital image compositing is credited to Milgram [154], published back in 1975, for seamlessly combining two satellite images. The approach considered only two images though, horizontally registered. For this reason, two years later, the same author proposed an improved version of his first method [155], which found the smoothest transition among several adjacent images for each row, and allowed to smooth the transition using a weighted average of the luminance values.

¹⁸That is, the descriptors should be distinctive and at the same time robust to changes in viewing conditions as well as to errors of the point detector.

¹⁹Radiometric discrepancies are due to uneven responses of the sensor used, which in turn are caused by variations of one or more parameters during the image conversion process of the sensor itself, such as intensity values, spectral character of incident photons and, in some cases, phase and polarization [153].

Given a set of grayscale images, the weighted average of luminance values became the first approach to the transition smoothing problem and a basic principle used by several methods that arose in the following decades.

Obtaining output seamless composed images has been subject of considerable research efforts since the very beginning of digital image processing. A survey concerning such methods goes beyond the scope of the present study. A starting point for the interested reader can be found in [156].

In what follows, an overview is provided concerning the main steps of the algorithms implemented for the the EduPIX for stitching both optical and radiation images.

3.3.2 Features search and matching

As mentioned at the beginning of Section 3.3, the features within all images are extracted using the ORB algorithm [143]. The authors of ORB showed that by steering BRIEF according to the orientation of keypoints (*steered BRIEF*), the resulting descriptor tends to be *invariant to in-plane rotation*. However, such modification also led to a loss of the associated variance²⁰ and to higher correlation²¹ among the binary tests of the BRIEF descriptor [143]. To recover from this loss of variance and to reduce correlation among the tests, ORB uses a learning method for choosing a convenient subset of binary tests. The method consists in searching among all possible binary tests to find *uncorrelated points* in a training set of 300k keypoints drawn from images in the PASCAL 2006 set [157]. Subsequently, it performs a greedy search using such set until it finds 256 tests that have both larger variance as well as being uncorrelated. The result was called by the authors *rBRIEF*, representing thus an improvement in the variance and correlation over steered BRIEF. For a more detailed description concerning ORB and BRIEF, the interested reader is referred to [143] and [144], respectively.

As a consequence, since ORB is invariant under both scale and rotation changes, the EduPIX can handle images from different perspectives with varying orientations.

When stitching images obtained while the camera rotates about its optical centre, the group of transformations the captured images may undergo is a specific group of homographies. As explained in [141], each camera can be parameterised by a rotation vector $\boldsymbol{\theta} = [\theta_1, \theta_2, \theta_3]$ and focal length f . This gives *pairwise* homographies $\tilde{\mathbf{x}}_i = \mathbf{H}_{ij}\tilde{\mathbf{x}}_j$, where

$$\mathbf{H}_{ij} = \mathbf{K}_i \mathbf{R}_i \mathbf{R}_j^T \mathbf{K}_j^{-1}, \quad (3.5)$$

and $\tilde{\mathbf{x}}_i, \tilde{\mathbf{x}}_j$ are the homogeneous image positions.

The 4-parameter camera model is defined by

²⁰High variance makes a feature more discriminative, since it responds differentially to inputs.

²¹Uncorrelated tests yield to better performance in nearest-neighbor applications, since then each test contributes to the result.

$$\mathbf{K} = \begin{bmatrix} f_i & 0 & 0 \\ 0 & f_i & 0 \\ 0 & 0 & 1 \end{bmatrix}, \quad (3.6)$$

and, using the exponential representation for rotations,

$$\mathbf{R}_i = e^{[\boldsymbol{\theta}_i]^\times}, [\boldsymbol{\theta}_i]^\times = \begin{bmatrix} 0 & -\theta_{i3} & \theta_{i2} \\ \theta_{i3} & 0 & -\theta_{i1} \\ -\theta_{i2} & \theta_{i1} & 0 \end{bmatrix}. \quad (3.7)$$

Once features have been extracted from all n images (linear time), they must be matched. Since multiple images may overlap a single ray, each feature is matched to its k nearest neighbours in feature space (we use $k = 4$). This can be done in $O(n \log n)$ time and by using a k -d²² tree to find the approximate nearest neighbours [160].

3.3.3 Homography estimation between adjacent images

At this stage of the algorithm, for each image, a set of features has been computed and matched between each pair of (optical) images.

Generally speaking, given two images I_1 and I_2 , homography \mathbf{H} is such that the descriptors in the first image I_1 best match the descriptors in the second image I_2 .

As already mentioned, in our context it is not needed to perform a comparison involving all images captured by the EduPIX. Features found in a given image captured by its optical camera are compared only with the features found in one and only one other image, known to be sharing an overlapping region. However, a subset of the features found during the previous step has typically false matches, which thus should not be used to compute the homography, as it would clearly lead to a wrong result.

As we want to recover a projective transformation \mathbf{H} , which is a 3×3 matrix (see Eq. 3.4), we need to solve a system of equations with 8 unknowns. For this reason, we actually need only 4 matching points in the two images of interest. This is carried out using the RANdom SAMple Consensus (RANSAC) algorithm, a general parameter estimation approach proposed by Fischler and Bolles [161] in 1981. For each pair of images with an overlapping region, there is a set of feature matches that are geometrically consistent (RANSAC inliers) and a set of features that are inside the area of overlap although they are not consistent (RANSAC outliers). The idea of the verification model is to compare iteratively the probabilities that this set of inliers/outliers was generated by a correct image match or by a false image match. Such approach is able to cope with a large proportion of outliers in the input data.

²²A k -d tree (short for k -dimensional tree) is a specific data structure where points are described in a k -dimensional space [158]. If a certain point represents an object of interest, k -d trees are typically used for finding the point in a given set that is most similar to it (Nearest Neighbor Search [159]).

Algorithm RANSAC overview, implemented for the EduPIX γ -camera

- 1: Select randomly 4 matching points in the two images I_1 and I_2 .
 - 2: Compute the projective transformation \mathbf{H} for images I_1 and I_2 using the 4 matching points selected in step 1.
 - 3: Determine how many points from the set of all features matches fit with a predefined tolerance ε .
 - 4: If the fraction of the number of inliers over the total number points in the set exceeds a predefined threshold τ , re-estimate the model parameters using all the identified inliers and terminate.
 - 5: Otherwise, repeat steps 1 through 4 (maximum of N times).
-

Unlike many of the common robust estimation techniques that have been adopted from the statistics literature, such as *M-estimators* [162] and *least median of squares* [163], RANSAC was developed within the Computer Vision community, which is probably one of the reasons of its popularity in the field of digital image processing.

RANSAC is a resampling technique that generates candidate solutions by using the smallest set possible of observations (in our case, features pairs in the two images of interest) required to estimate the underlying model parameters, and proceeds to enlarge this set with consistent data points.

Given a pair of images I_1 and I_2 and a set of corresponding features matches, the basic algorithm is summarized in Algorithm RANSAC overview.

The number of iterations, N , is chosen high enough to ensure that with probability p (set to 0.99) at least one of the sets of random samples does not include an outlier. Let u represent the probability that any selected data point is an inlier and $v = 1 - u$ the probability of observing an outlier. N iterations of the minimum number of points denoted m are required, where

$$1 - p = (1 - u^m)^N, \quad (3.8)$$

and thus

$$N = \frac{\log(1 - p)}{\log(1 - (1 - v)^m)}. \quad (3.9)$$

Once the homography has been estimated and the correspondences which are consistent are found, the images can be registered and reprojected (see Fig. 3.17).

For more details on the basic RANSAC formulation, see [146, 161]. Extensions of RANSAC include a Maximum Likelihood framework [164] and importance sampling [165].

3.3.4 Multi-band blending

The acquisition procedure implemented for the EduPIX tries to automatically select only frames with uniform exposure (see Section 3.2.1 for details). However, a further effort in some cases is needed to further compensate the remaining colour discontinuities within the images. The intensities discontinuities are further mitigated by using the multi-band blending approach suggested in [166].

In order to combine information from multiple images, a weight function is assigned to each image $w(x,y) = w(x)w(y)$, where $w(x)$ varies linearly from 1 at the centre of the image to 0 at the edge. The idea behind multi-band blending is to blend low frequencies over a large spatial range, and high frequencies over a short range. This can be performed over multiple frequency bands using a Laplacian Pyramid [167].

More specifically, two band schemes are used. A low pass image is formed with spatial frequencies of wavelength greater than 2 pixels relative to the rendered image, and a high pass image with spatial frequencies less than 2 pixels. The low frequency information is the blended using a linear weighted sum, and the high frequency information is selected from the image with the maximum weight. Such approach has proved to alleviate the remaining intensity discontinuities, yielding to visually convincing results. Note that no radiation information has been taken in consideration, yet.

Figure 3.20 shows a result obtained using the algorithm above summarized. This image was acquired and generated using the EduPIX prototype and its pan-tilt unit. The features were robustly matched and the overall approach yielded a seamless panorama. In this case, the prototype autonomously captured 80 images, and a $4 \times 80 = 320$ parameter optimization problem was solved for the final registration. Using the ODROID-XU3 of the EduPIX and its optical camera, the 80 input images were automatically captured in 67 seconds, and they were matched, registered, and composed in 40 seconds, resulting into a final 7234×1681 pixels output panorama, and requiring thus a total time of 107 seconds.



Fig. 3.20: A panorama image with size 7234×1681 pixels captured and generated by the EduPIX prototype, using one single optical camera and a motorized pan-tilt unit, and resulting from the stitching of 80 optical images. The implemented algorithm allows the prototype to autonomously capture high-quality pictures, find and match consistent sets of invariant features, correctly register the images, and compose them together. Clearly, no radiation sources were present in this example. The images that have been stitched together were thus not superimposed by any radiation map in this example.

3.3.5 Radiation image stitching

The basics regarding algorithms for registering and stitching optical images have been summarized in Section 3.3.1, which are among the most widely studied techniques in Computer Vision. Similarly, an impressive amount of investigation has been conducted also in the medical imaging field concerning image registration, as a component of a wide number of applications, ranging from diagnostic to areas such as surgical and radiotherapeutic procedures. For a general introduction and review of medical image registration, the interested reader is referred to [19, 18, 20].

However, compared to such efforts, little work has been done in the past concerning registration and stitching of radiation images generated by *portable* γ -cameras for nuclear power plants and radiation facilities. Such type of cameras, contrarily to the instruments used in the medical imaging fields (e.g. positron emission tomography and magnetic resonance imaging), does not yet necessarily provide a sufficient spacial resolution and amount of visual details required for performing image registration using *only* radiation images. This is mainly due to the impossibility of retrieving distinctive features for using robust local descriptors concerning the radiation emitting sources found, such as precise intensity variations in different radiation images regarding the same point on a given surface, the accurate shape of the edges and corners of the radioactive object, boundary regions, and so on.

During the previous steps of the stitching algorithm designed for the EduPIX prototype, including the multi-band blending phase, only optical images (i.e. not superimposed by any γ -image) were considered. Conversely, the presence of radiation information (if any) overlaid on each respective optical image would have led to inconsistencies during all the phases above described.

In case radioactive hotspots are present in the scene under study, the corresponding γ -images can be superimposed only at this stage of the algorithm, since the correct homographies among all pairs of optical images have been already estimated and stored.

For this reason, we apply the homographies retrieved for each pair of adjacent optical images *to their corresponding superimposed radiation images*. More specifically, for each couple of adjacent optical images, I_1 and I_2 , the 3×3 homography matrix $\tilde{\mathbf{H}}_{12}$ for registering I_1 with I_2 is applied to their respective superimposed decoded gamma images, \hat{S}_1 and \hat{S}_2 (see Eq. 1.6). Therefore, if R_v is the overlapping region of I_1 and I_2 (v stands for *visible*), and R_δ is the overlapping region of \hat{S}_1 and \hat{S}_2 such that:

- $R_\delta \neq 0$,
- A radioactive source S is partially or entirely observed in a subset of R_δ , and
- such source S refers to the objects visible in the optical images,

we apply $\tilde{\mathbf{H}}_{12}$ also for registering \hat{S}_1 with \hat{S}_2 . This is possible as both gamma images were previously already consistently superimposed onto I_1 and I_2 , respectively, and all images involved are two-dimensional.

Once the radiation images have been registered (i.e. aligned), if pixels from both \hat{S}_1 and \hat{S}_2 occur at the same location in the united coordinate system, they need to be *blended* before being overlaid on the correct location of the final stitched panorama, as their intensity may not be exactly the same (similarly to what happens when registering and stitching optical images).

In the context of radiation images, this can be solved by simply computing an *average* value at each pixel:

$$B(\mathbf{x}) = \frac{\sum_k w_k(\mathbf{x}) \tilde{S}(\mathbf{x})}{\sum_k w_k(\mathbf{x})}, \quad (3.10)$$

where $\tilde{S}(\mathbf{x})$ are the reprojected γ -images and $w_k(\mathbf{x})$ is 1 at valid pixels and 0 elsewhere, creating in such way a final coherent composite gamma image.

We refer to the process of combining multiple γ -ray images as *radiation image stitching*.

The resulting radiation image can be finally superimposed on the optical stitched image, and the respective result can be rendered. Typically, composed panoramas use a cylindrical [168, 169] or spherical projection [170]. However, any surface adopted for environment mapping in Computer Graphics can be used, including a cube map that represents the full viewing sphere with the six square faces of a box [170, 171].

In our context, the final image is rendered in spherical coordinates (θ, ϕ) , which for this reason is the format accepted by the EduPIX GUI for rendering and displaying all stored panorama images.

A summary of the overall image stitching procedure here proposed is provided in Section 3.3.6.

3.3.6 Outline of the procedure for generating panoramic images

A description of all steps performed by the EduPIX prototype for creating a panorama with both optical and gamma images has been provided.

The overall procedure consists of two main phases: the acquisition phase, where the optical images are autonomously acquired along with their superimposed γ -images, and the processing phase, where the images acquired are provided as input and stitched together by the processing algorithm. We refer to the latter as *Multimodal image stitching* algorithm. Its outline is provided in Algorithm 1, whereas the overall procedure designed and implemented for the EduPIX (Automatic Multimodal Panorama Creation) is summarized in Algorithm 2.

3.4 Results and discussion

In this section, the main results obtained with panoramic EduPIX gamma camera are shown. Section 3.4.1 deals with a simulated scenario where a portion of the surface of a radioactive source is localized and superimposed also in proximity to the borders of an image. This might happen in

Algorithm 1: Multimodal image stitching

Input: 2 overlapping optical images, I_1 and I_2 , and the respective gamma images, γ_1 and γ_2

/ Optical image stitching */*

Extract features using *ORB* from I_1 and I_2 and match them (Section 3.3.2)

Estimate homography \mathbf{H}_{12} for registering I_1 with I_2 , using *RANSAC* (Section 3.3.3)

Apply homography \mathbf{H}_{12} , obtaining a *new* wider image I_{12}

Remove last colour discontinuities from I_{12} using the Multi-band Blending technique (Section 3.3.4)

/ Radiation image stitching */*

Apply homography \mathbf{H}_{12} also on γ_1 with γ_2 , obtaining a *new* wider γ_{12}

Blend and stitch pixels from γ_1 and γ_2 in γ_{12} (Section 3.3.5)

Output: Stitched images I_{12} and γ_{12}

real-context scenarios either due to the position of the source respect to the camera or because of its size, which, once localized, might exceed the FOV of both optical and gamma camera of the EduPIX.

Sections 3.4.2 and 3.4.3 provide instead results concerning panoramic images with a complete 360° horizontal FOV, at the CEA laboratory in Marcoule and at ATLAS, respectively.

3.4.1 Radiation image stitching with planar sources

Using the ^{57}Co planar sources of Table 3.3, a radioactive surface of rectangular shape has been simulated so that its size would exceed the FOV of the gamma camera prototype. In order to achieve this, the sources have been installed at an average distance from the gamma camera of only 16 cm, as follows (see Fig. 3.21): starting from the left respect to the FOV of the prototype, the three ^{57}Co planar sources with activity of 429 kBq were placed adjacently, with almost no overlapping region between them. In fact, between the second and the third source, a horizontal space of approximately 3 cm has been left, in order to see if the angular response of the gamma camera was sufficiently high to characterize the surface of a source with an activity not perfectly uniform. On the right, instead, the three ^{57}Co sources with 143 kBq activity (total activity 429 kBq) were overlapped, so that their activity equaled that of the other three sources on the left.

The width of all sources placed next to each others was 32 cm. At 16 cm of distance, neither the FOV optical camera nor the one of the gamma sensor are sufficiently wide to contain all sources shown in 3.21. The distance of 16 cm was decided so that the angular size of the source respect to the prototype was 90°. In this case, at least two measurements were needed, changing the angle of the camera respect to the sources at each time.

Algorithm 2: Automatic Multimodal Panorama Creation

Define main parameters of the pan-tilt of the EduPIX:

Pan range $[p_1 : p_2]$ // *Horizontal FOV of the final panorama image*

Tilt range $[t_1 : t_2]$ // *Vertical FOV of the final panorama image*

Angle per step i in horizontal range $[p_1 : p_2]$ // *Horizontal overlapping*

Angle per step j in vertical range $[t_1 : t_2]$ // *Vertical overlapping*

for each pan step i in range $[p_1 : p_2]$ **do**

for each tilt step j in range $[t_1 : t_2]$ **do**

/ Automatic selection of the most suitable optical frame */*

 Acquire N optical images

 Initialize the candidates sets $\mathcal{C}_1 \leftarrow \emptyset$ and $\mathcal{C}_2 \leftarrow \emptyset$

while $c < N$ **do**

 Compute luminance RMS_L (Eq. 3.2) of image I_c , and add it to set \mathcal{C}_1

 Compute sharpness RMS_S (Eq. 3.3) of image I_c , and add it to set \mathcal{C}_2

end while

 Select from $(\mathcal{C}_1 \cup \mathcal{C}_2)$ the most suitable optical image, and label it (Section 3.2.1)

/ Radiation information acquisition and reconstruction */*

 Acquire and decode γ -image \hat{S} (Eq. 1.6), and label it

 Stitch I_{j-1} with I_j and \hat{S}_{j-1} with \hat{S}_j using Algorithm 1

end for // *Vertical acquisition for pan position i is terminated*

if $i > 1$ **then**

 Stitch I_{i-1} with I_i and \hat{S}_{i-1} with \hat{S}_i using Algorithm 1

end if

end for // *Panorama acquisition terminated*

Superimpose the stitched radiation image \hat{S}_{final} on the stitched optical image I_{final}

Render the resulting panorama in spherical coordinates (θ, ϕ)



Fig. 3.21: Combination of six planar ^{57}Co sources with 1716 kBq of total activity.

Before starting such experiment, we performed an initial measurement at an average distance between the prototype and the sources of 52 cm. This allowed the comparison between the results of the two experiments, and also to observe the response of the camera with such set-up.

The results of this first test confirmed the satisfactory performance of the camera in proximity to extended sources, as the line was correctly overlaid using a cut-off threshold of 50% and, moreover, the little space of ~ 3 cm left out between the second and third source from the left has been correctly pointed it out in the reconstructed γ -image. See Fig. 3.22 and Fig. 3.23.

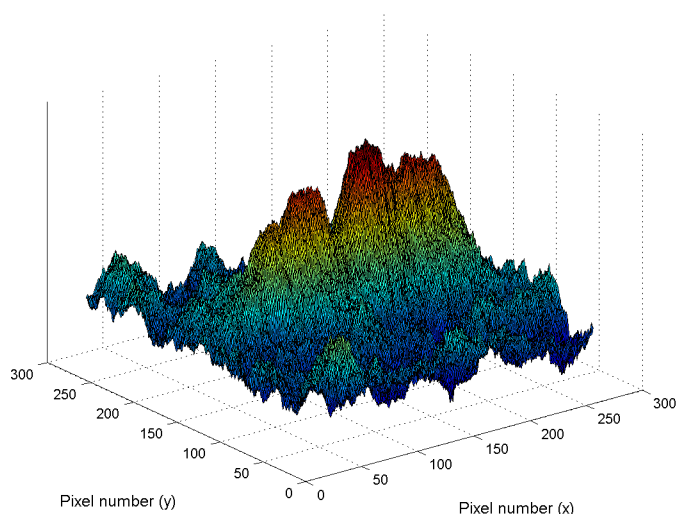


Fig. 3.22: Hotspot profile resulting from the combination of six planar ^{57}Co sources with 1716 kBq of total activity, at an average distance of 52 cm from the gamma camera, providing an ambient dose equivalent rate of ~ 330 nSv/h at the measurement point. As the sources had equal activity, it is possible to notice a loss in counts while approaching the limits of the FOV (see Section 2.4.7 for more details concerning the off-axis response of the gamma camera).

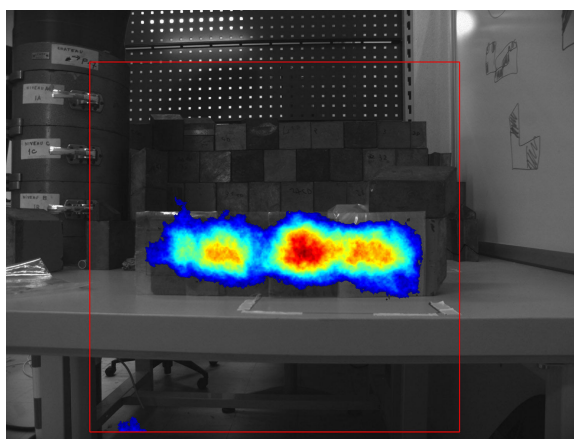


Fig. 3.23: Radiation image superimposed on the respective optical image resulting from the combination of six planar ^{57}Co sources with 1716 kBq of total activity, at an average distance of 52 cm from the gamma camera, providing an ambient dose equivalent rate of ~ 330 nSv/h at the measurement point.

Consequently, we performed the originally intended experiment and placed the prototype at 16 cm from the sources, with the same set-up, in order to compare the results of the two experiments.

At an average distance of 16 cm, the data was collected at three different pan angles: -30° , 0° , and 30° , acquiring 180 frames of 1 sec shutter time for each of the three measurement, both in mask and antimask modes. The results of such measurements are three gamma images with partially overlapping regions, shown in Fig. 3.24.

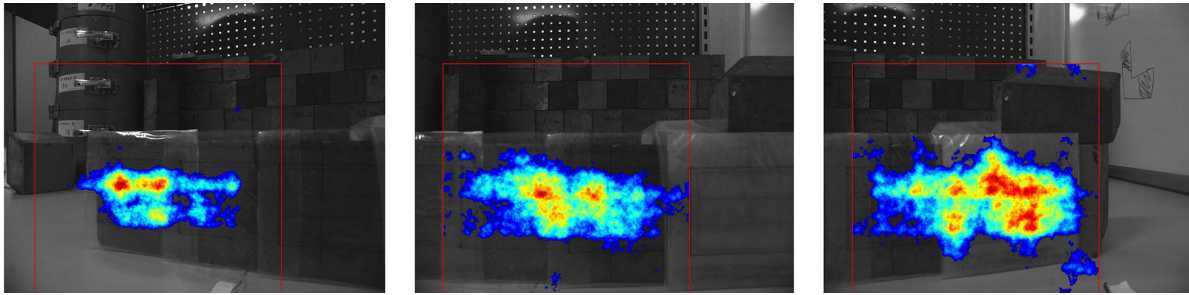


Fig. 3.24: The results of the superimposition of three different measurements performed with the gamma camera prototype, placed at three different pan angles (-30° , 0° , and 30°) from a combination of six planar ^{57}Co sources with 1716 kBq of total activity. The average distance between the sources and the gamma camera was 16 cm, providing an ambient dose equivalent rate of ~ 330 nSv/h at the measurement point.

By observing the results of both Figures 3.23 and 3.24, admittedly, the radiation images resulting from the acquisition of 180 frames of 1 sec shutter time do not provide their precise actual shape (i.e. equiangular rectangles). A longer acquisition would plausibly have led to a more accurate reconstruction of such shapes. Nonetheless, the results present an amount of details more than sufficient for being correctly interpreted by a human eye.

By applying the radiation image compositing technique described in Section 3.3.5, the three γ -images resulting from such experiment have been stitched, resulting into a final coherent composite gamma image, which has been thus superimposed on its respective optical stitched image. See Figures 3.25 and 3.26.

The hotspot profile and superimposition resulting from the compositing of several decoded gamma images can be then compared with the hotspot profile resulting from a single measurement performed from a longer distance and shown in Fig. 3.23.

It can be seen that stitching radiation images can offer several advantages. In the first place, if a radioactive source exceeds the FOV of the gamma camera (e.g. long pipes in nuclear power plants), composed panorama γ -images allow the localization of the respective extended surfaces in only one image, preserving though their geometrical coherency.

Moreover, if the surface of a radioactive source needs to be radiologically characterized with accuracy or if its activity is considerably low, panorama gamma imaging allows the possibility of decreasing the distance between the gamma camera and such source, and still being able to localize it entirely within the same image, obtaining thus more detailed radiological information concerning its surface. Figure 3.26 is an example of such scenario, as with equal acquisition time

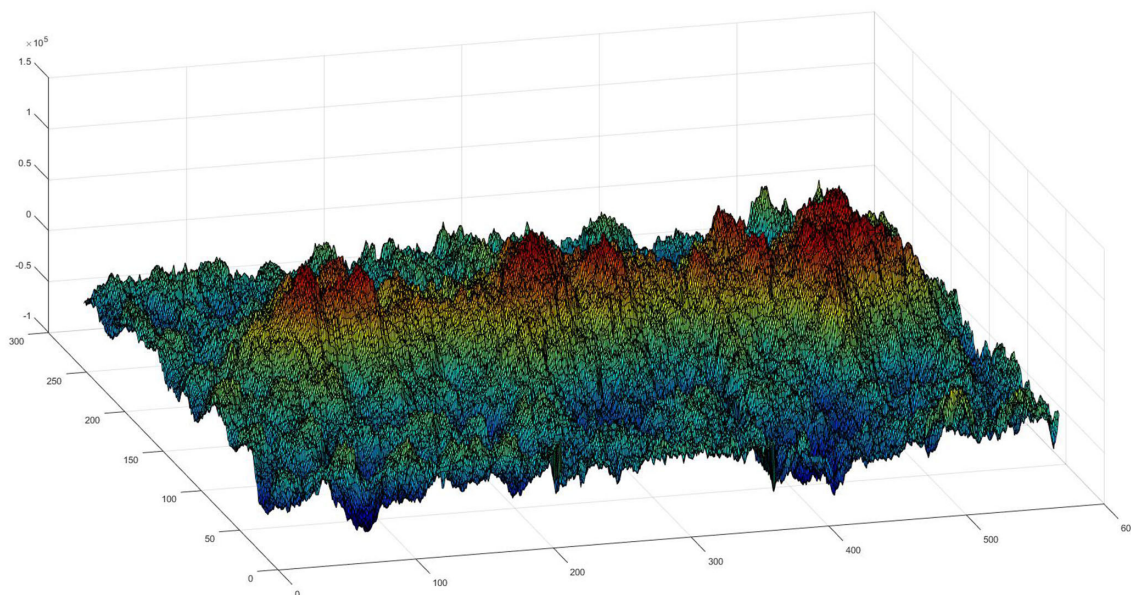


Fig. 3.25: Three-dimensional hotspot profile resulting from the radiation image stitching technique designed and implemented for the EduPIX. In this example, three radiation images resulting from three different measurements have been combined into a final coherent composite decoded γ -image.

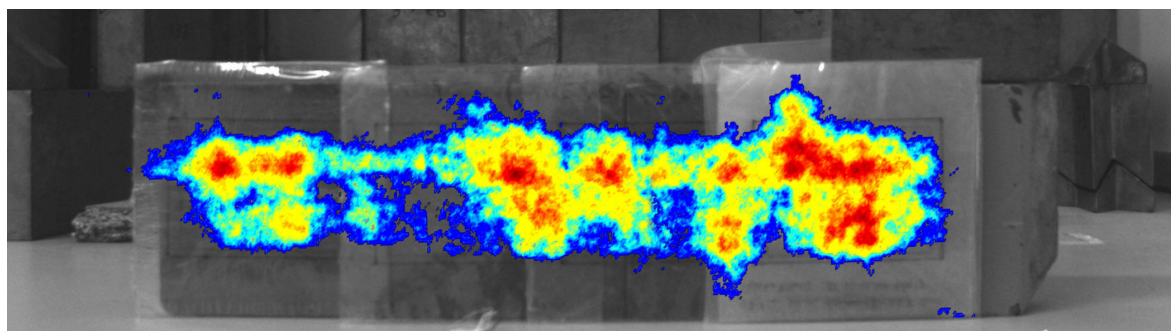


Fig. 3.26: A stitched gamma image resulting from three different measurements superimposed on the respective optical image.

the surface of a low-activity extended source is characterized with more accuracy from a shorter distance.

3.4.2 Panoramic images with planar and point sources

One of the advantages of panoramic gamma images is that they allow the radiological characterization of entire rooms within one single image, providing an amount of information that can help operators to remember the hotspot position also depending on their location within the interested area.

In order to test a scenario where multiple radioactive hotspots surround an operator, several sources were positioned in the laboratory of CEA Marcoule ("*Laboratoire simulation et techniques de démantèlement nucléaire*"). More specifically, the following sources have been placed at different random locations of the room (the decay scheme of each radionuclide can be found in Appendix C):

- ^{152}Eu with activity of 9.63 MBq, at 264 cm from the camera
- ^{133}Ba with activity of 9.92 MBq, at 182 cm from the camera
- ^{241}Am with activity of 0.15 MBq, at 120 cm from the camera
- ^{137}Cs with activity of 329 MBq, at 280 cm from the camera

For *each of the sources* above mentioned, 300 frames of 1 sec shutter time were acquired using the mask R7e4 in both mask and antimask measurements, for a total of 600 frames for each source.

In parallel, also the optical images have been captured, covering 360° of the horizontal FOV of the room and $\sim 66^\circ$ of its vertical FOV.

The result of such experiment is shown in Fig. 3.27.



Fig. 3.27: A panorama image with size 12574×2316 pixels, with an horizontal and vertical FOV respectively of 360° and 66° , resulting from the stitching of 80 optical images and the superimposition of 4 γ -images. For illustration purposes, the image is shown in black and white.

The visual details in the γ -images concerning each of the sources mentioned vary inevitably depending on their energy, activity, and their distance respect to the gamma camera. Nevertheless, the radiation images are correctly automatically reprojected and superimposed on the stitched final optical image without significant artifacts.

Inspired by the web application *Google Street View* [172], the EduPIX software and its graphical interface support also the creation of interactive virtual tours, allowing users to change panoramic scenes by simply clicking on a given position of the measurement result, pointed out by a landmark icon. Along with the possibility of creating panoramic images, such functionality potentially allows a quick navigation of entire nuclear power plants and facilities via a web-browser, and displaying the respective main radioactive hotspots at the same time.

3.4.3 Testing at the ATLAS detector

The EduPIX system was tested also at the LHC. In the context of a testing campaign of the EDUSAFE project, we had the unique opportunity to have access to the ATLAS facility and perform measurements in proximity to the ATLAS beam pipe. Fig. 3.28 shows on the right of the image the prototype with its motorized pan-tilt mounted on a tripod, in front of the ATLAS beam pipe.

The estimated dose at the camera location during the measurement varied between 3.5 and 4 $\mu\text{Sv/h}$, depending on the position and the orientation of the gamma camera. Due to the inevitable time constraints, the measurements performed concerned only the centres of the beam pipes, as the measurement statistics from other locations would have been too low. Nevertheless, the prototype was able to localize the position of the most significant surrounding radioactive hotspots. As a result, a panoramic gamma image was generated with a complete 360° horizontal FOV, shown in Figure 3.29.

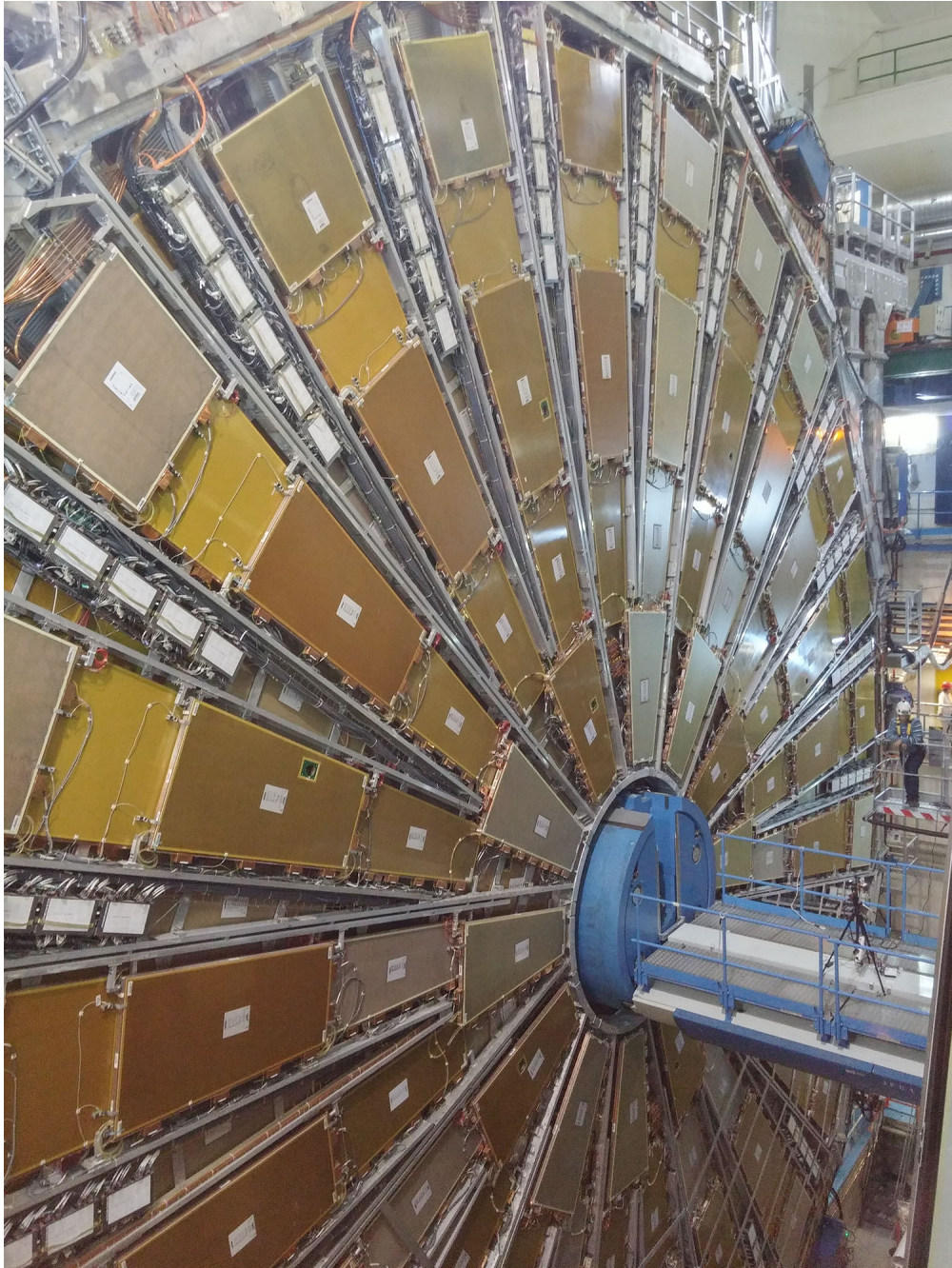


Fig. 3.28: Performing measurements with the prototype (on the right) at 2 meters from the ATLAS beam pipe. The estimated dose rate at the camera location ranged between 3.5 and 4 $\mu\text{Sv/h}$, depending on its position and orientation. The dose rate was measured with the CANBERRA instrument Colibri VLD (Very Low Dose).



Fig. 3.29: A panorama image with size 8494×1903 pixels, with an horizontal and vertical FOV respectively of 360° and 80° , resulting from the stitching of 120 optical images and the superimposition of 2 γ -images. For illustration purposes, the image is shown in black and white and two black stripes have been added, in order to obtain a $360^\circ \times 180^\circ$ format with a width/height ratio of $360/180 = 2$.

3.5 Conclusions

A panoramic gamma imaging prototype, the EduPIX, has been developed, as integral part of the personnel safety system used at the LHC, at CERN. Relying on the radiation imaging capabilities of the iPIX gamma camera, the prototype allows the localization of the main surrounding radioactive sources with a field of view of 360 degrees. As its use at the LHC is foreseen in environments that can be potentially highly radioactive, a procedure for autonomously obtaining panoramic images with both optical and radiation images has been proposed.

The method presented uses ORB, a feature detector and descriptor, and a probabilistic model to compute homographies for the overlapping captured optical images, and it applies, subsequently, the same homographies to their corresponding radiation images.

The results obtained with such method have shown its validity, reconstructing panorama γ -images representing sources that would potentially exceed the FOV of the camera if localized with only one measurement (e.g. long pipes in nuclear power plants), preserving though their geometrical coherency.

Moreover, the feasibility of autonomously analysing large rooms or facilities has been proved, displaying the respective result within one single image, thus providing an amount of information that can help operators to remember the hotspot position also depending on their location within the interested area.

Future perspectives include the validation of the proposed stitching algorithm by performing additional measurements involving large radioactive sources in real-life scenarios. Moreover, the implemented algorithm relies on the assumption that no occluding objects are present between the located sources and the instrument. As discussed, such limitation is due to the inherent low spacial resolution of the images obtained with the current version of the gamma camera. Improvements related to such aspect may lead in the future to the possibility of stitching images relying only on the visual features of the radiation images, such as corners or edges.

Furthermore, the current version of the algorithm makes only partial use of the Nvidia CUDA libraries [173]. The associated computational performances may be improved by relying more on the multiple cores of the graphics processing unit (GPU) of the computing board used and by further optimizing its pipeline [174].

Chapter 4

3-D localization of radioactive hotspots via portable gamma cameras

In Chapter 3, a method for the localization of the main surrounding radioactive hotspots with a field of view of 360 degrees has been proposed, allowing to overcome the limited FOV of the coded-aperture approach.

The present chapter focuses in the second and main motivation of the present study. That is, portable industrial gamma cameras for nuclear facilities provide only the two-dimensional (2-D) position concerning the radioactive emitting objects in the surrounding environment. For this reason, in the present chapter it is discussed the development of a portable γ -imaging system able to automatically retrieve the accurate 3-D position of the surrounding radioactive sources. The system is based on a stereo γ -camera combined and calibrated with a depth sensor and an optical camera.

Sections 4.1 and 4.2 establish the general context and provide the main aspects of the proof of concept developed for this study. Section 4.3 describes an experimental multi-modal calibration procedure and the calibration phantom designed and built for carrying it out. Section 4.4 analyses the obtained results regarding the accuracy of the parameters computed for each of the sensors involved, including those obtained for overlaying radiation information on optical images. The following part of the chapter is dedicated to the distance measurements estimated between the γ -camera and the located radioactive hotspots, discussing also the capability of the prototype to autonomously determine if an object is occluding the sought radioactive sources and generate 3-D point clouds integrating radiation information. Finally, Section 4.7 concludes this work and provides its main future perspectives.

4.1 General context

Three dimensional (3-D) machine vision has been subject of wide research in the last decades in many fields, such as computer vision, photogrammetry, and medical imaging. Such disciplines

are vast and many of their applications are deeply related, resulting in the design of methods that are inherently interdisciplinary. However, even the most advanced, recent, and complex of such methods typically involve the basic geometric primitives of the three-dimensional Euclidean space, linear algebra, and the fundamentals of *multi-view geometry*.

In general, the position of a point in the 3-D space is estimated from several views (projections) by identifying its position in each of the individual views available. When at least two points from two views are known to *correspond*, the respective rays intersect (ideally) at a unique three-dimensional point (see Fig. 4.1).

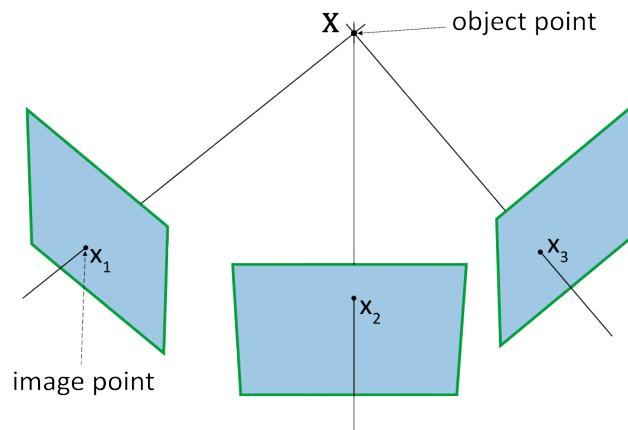


Fig. 4.1: A point \mathbf{X} in the 3-D space projected onto three views, resulting in three corresponding image points \mathbf{x}_1 , \mathbf{x}_2 , and \mathbf{x}_3 . In the ideal case, the respective rays intersect at \mathbf{X} .

The problem of determining the set of correspondences between two or more images is well-known in the literature, and when possible it can be simplified and reduced to one dimension, typically for computational efficiency.

An essential step for any imaging system able to generate two or more views is the calculation of the geometry of the cameras used, namely the geometrical properties of each single camera (i.e. *intrinsic parameters*), along with the rotation matrix \mathbf{R} and translation vector \mathbf{t} (i.e. *extrinsic parameters*), which describe the pose (position and orientation) of each camera in the world [175–177].

As explained in Chapter 3, image registration allows the alignment of two images of the same scene captured by a camera, leading to the possibility of stitching optical images with an overlapping region, and thus, in our context, applying the same transformations to the associated radiation images.

Similarly, the registration of two images is necessary also for the fusion of multimodal images. Fusion of different imaging methodologies such as X-ray computed tomography (CT), positron emission tomography (PET), and magnetic resonance imaging (MRI) has been subject of extensive study in the medical imaging literature [18, 21, 178], as the accurate overlay of the respective reconstructed images allows the combination of their clinical advantages. Nevertheless, as already explained in Chapter 3, little work has been done in the past concerning image registration in

the context of *portable* gamma cameras for nuclear facilities, and therefore also regarding the accurate fusion of multimodal images generated by such instruments, including the autonomous estimation of the distance of the surrounding radioactive sources respect to the camera.

In the present study, we employ calibration for establishing dense correspondences among images acquired and processed by different types of portable cameras. More specifically, we wish to accurately map the geometric information captured by two portable γ -cameras, an optical camera, and a *range-imaging* sensor¹.

Despite the heterogeneity of the types of instruments involved, the calibration technique here described is fully based on the properties of the perspective camera, applied therefore not only to the optical and depth sensors, as currently done in many computer vision applications, but also to γ -cameras based on the coded aperture technique.

Moreover, while most computer vision approaches for camera calibration are based on retrieving local correspondences from different images, one of the key-ideas is that we perform the calibration of each sensor independently by employing *the same world reference system*, and we then retrieve the relative poses of each couple of cameras from their pose in such world reference system. This approach is described more in detail in Section 4.3.3 and it has been experimentally validated, leading to satisfactory results, discussed in Section 4.4.

Two approaches are proposed to derive the 3-D position of surrounding radioactive sources and accurately fuse radiation images with both optical and depth information:

- The first approach consists in combining and accurately *calibrating* one of the γ -cameras with a range-imaging sensor. The depth camera integrated with the prototype is based on the structured-light technique (details concerning the specific device used are provided in Section 4.2.1). In general, a structured-light sensor is based on the projection of a light pattern on Lambertian surfaces² of the scene, by capturing points of the illuminated scene from one or more cameras (views). As the pattern is encoded, the correspondences between image points in the cameras can be computed, and the respective horizontal displacement is thus mapped into range by triangulation. The system resulting from the combination of a γ -camera and such device is thus able to retrieve the distance of radioactive hotspots by means of *pixel-wise mapping* between gamma and depth images.
- The second approach aims to automatically estimate the distance between the prototype and a radioactive source by calibrating both γ -cameras and then employing stereo disparity between the respective reconstructed images. Stereo disparity machine methods have been subject of a wide research from as early as in the seventies [180], inspiring many currently used range-imaging techniques, including, as mentioned, systems based on structured-light.

¹As defined in [179], a *range image* is a collection of distance measurements from a known reference coordinate system to surface points of one or more objects of interest. Such collection is typically represented by matrices, whose each cell represents in turn the distance to a given point in a scene. Such matrices are typically referred to as *depth maps* or *depth images*.

²A Lambertian surface provides uniform diffusion of the incident radiation such that its radiance is equal towards all directions from which it can be measured.

In order to evaluate the two proposed approaches, a proof of concept has been developed, resulting from the integration of all cameras above mentioned, and whose main aspects are provided in Section 4.2.

4.2 A portable proof of concept for 3-D gamma imaging

Similarly to the iPIX system and the EduPIX prototype, the proof of concept built for 3-D gamma imaging is also based on the combination of a 1 mm thick CdTe substrate bump-bonded to a Timepix chip and a tungsten coded aperture mask.

For reproducibility purposes, although connected to the same computing board used for the EduPIX (the ODROID-XU3), the device shares part of the same hardware of the iPIX γ -camera, including its optical sensor, the components used for shielding the areas behind the detector and its sides, and the relative position of the coded mask respect to the Timepix detector. Such parts have been assembled by the CANBERRA Loches site, resulting in the system shown in Figure 4.2.



Fig. 4.2: Part of the gamma imaging portable system used for retrieving the 3-D position of radioactive hotspots.

Such system has been then combined with the other components of the prototype, which are described below in the present section.

4.2.1 Combining a coded aperture gamma camera with a structured-light sensor

To retrieve the depth maps to be registered with the decoded gamma images, the Asus Xtion RGB-D camera has been chosen [181], due to its versatility and as a representative of the first generation of RGB-D sensors based on the Primesense structured-light technology [182].

In general, structured light systems simplify the correspondence problem through the emission of *unique* patterns by a given light projector. In the case of the ASUS Xtion, an infrared (IR) emitter and an IR depth sensor are used. The IR emitter projects infrared light beams, which are

reflected back by the surrounding surfaces and read by the depth sensor, associating each portion of the image with a specific pattern, which is typically referred to as *code word*. In other terms, the structured light patterns ease the computation of the correspondence between observed and projected pixels. Depth is then inferred for each corresponding pixel by means of a patented analysis algorithm [183]. Details concerning the procedure and the respective algorithm used by PrimeSense are not publicly available at the time of writing. However, based on their patents, it is plausible that such procedure is a combination of several techniques, including triangulation [184], depth from focus³ [185], and the analysis of the deformation of the pattern itself [186].

The accuracy error of the Asus Xtion increases quadratically with the distance of the surface to be measured, from a few millimetres (at 0.8 m distance) to about 4 cm at the maximum range of the sensor (4 m), which are comparable performances with those of the well-known Microsoft Kinect [181, 187]. Nonetheless, one of the reasons for which I chose the Asus Xtion is that, contrarily to the Microsoft Kinect, the former is powered exclusively via USB ports, without the need, therefore, of using an external AC adapter.

Figure 4.3 shows an example of an optical image coupled with the respective depth map acquired with the Asus Xtion, at the nuclear physics laboratory of the University of Caen Normandy.

For illustration purposes, the depth maps obtained with the ASUS Xtion are shown so that the shape of each object is perceived from *shading*, that is, where the pixel values of the shown depth images are proportional to the floating point values retrieved at the same coordinates from the depth maps⁴.



Fig. 4.3: Example of optical image coupled with the respective depth map.

Before being integrated with the prototype, the Asus Xtion has been disassembled from all unnecessary components, such as its plastic case and the microphone. Moreover, the electrical connections and some of the connectors have been strengthened with additional soldering, in order to increase the overall reliability of the system. The device has been then rigidly mounted on the γ -camera, so that even slight displacements between the position of all sensors could not occur. The resulting prototype is shown in Figure 4.4.

³The depth structure of a scene can be estimated by measuring the degree of blur for each Region of Interest (ROI) of the image under study.

⁴Each value in a given depth map can be interpreted, in general, as the product of the normal vector of the underlying surface at the measured point and the directional vector of a predefined light source.

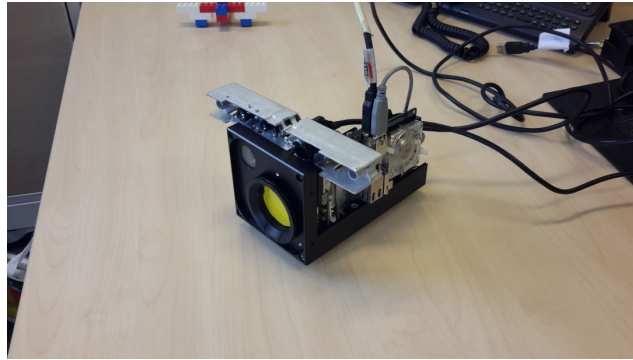


Fig. 4.4: First version of the acquisition prototype built and adopted for the experiments.

Optical image acquisition and distortion correction

To ensure the reproducibility of the proposed method concerning the registration between the visible and radiation images, the prototype uses the same optical camera of the iPIX γ -camera (the Imaging Source DFM 72BUC02-ML), which is based on a 1/2.5-inch Micron CMOS sensor and it captures images with size up to 2592×1944 pixels.

It is usually accepted that radial distortion is the most significant deformation introduced by the lens used. Loosely speaking, radial distortion causes in a given image straight lines to appear as circular arcs, invalidating one of the most important invariances preserved by the pinhole model, for which straight lines in the 3-D world correspond to straight lines in the image plane of the sensor. Several radial distortion models are available in the literature. For this experiment, in order to correct the systematically distorted image coordinates retrieved by the optical images, we used the algorithm for the estimation of a single lens distortion coefficient proposed in [188].

One may point out that also the optical camera of the Asus Xtion could have been adopted, since it is additionally already pre-calibrated with the depth sensor. Nevertheless, we used an independent optical camera to demonstrate the versatility of the calibration procedure described and proposed in Section 4.3, which can be thus carried out even with depth sensors that do not include pre-calibrated optical cameras.

4.2.2 A portable stereo gamma imager

The system above described has been assembled in order to assess the feasibility of the calibration between a γ -camera and a depth sensor, allowing the estimation of the distance of the surrounding radiation sources which are not occluded respect to the prototype. To estimate the distance of radioactive objects also in those situations in which an occluding object is present between them and the measurement instrument, a second gamma camera has been integrated with the system. For simplicity, we refer hereinafter to the first gamma camera as left γ -camera and to second one as right γ -camera.

Also the right γ -camera shares the same main components of the iPIX (that is, the same coded mask and detector, including the spacial relation of their respective positions). In fact, the

second gamma camera is an earlier version of the iPIX system, which was built and used during the first phases of its development, before being released as a product. Although not strictly necessary, such choice simplified both the overall assembling of the prototype and the experiments performed, facilitating both the execution of the calibration procedure and the implementation of the algorithms proposed in the remainder of this chapter. An alternative would have been the adoption of a detector with multiple chip tiles, such as, for example, the WidePIX detector [189], combining it with a customized coded mask with a pattern adapted to its wider sensitive area. At this stage of development, however, such solution has been considered unnecessary.

Moreover, the depth sensor has been repositioned, and the right γ -camera has been also rigidly and mechanically joined to the other components of the prototype. The resulting system, which is the final version of the proof of concept built for the present study, is shown in Figure 4.5.

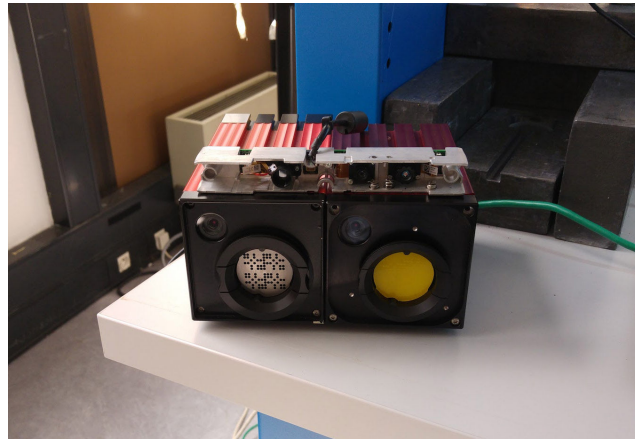


Fig. 4.5: The final version of the acquisition prototype built and adopted for the experiments, consisting of two gamma imaging systems with the respective optical cameras, and a depth sensor.

4.3 A versatile multi-modal camera calibration

To calibrate different types of portable measurement devices such as γ -cameras, depth sensors, and optical cameras, a multi-modal calibration procedure has been designed and carried out. Such procedure requires only one radioactive point source, which in our case was a ^{241}Am point source of ~ 360 MBq activity.

More specifically, the internal and external parameters of the two γ -cameras, the depth sensor, and the optical camera are individually computed, using an experimental phantom intentionally quick to build, simple, and inexpensive. This allows the registered data to be inherently matched and projected to a *common* 3-D reference system, assuming that the information acquired from each of the adopted cameras refers to the same physical objects.

4.3.1 Basic concepts

In Chapter 1, an informal description concerning the operating principle of pinhole gamma cameras has been provided. As the name suggests, from a geometrical perspective, such approach is based on the pinhole model and its geometry.

The prototype built for the calibration procedure proposed with this study is based instead on the coded aperture technique. Compared to pinhole gamma cameras, instruments based on the coded aperture imaging approach significantly improve the signal-to-noise ratio of the acquired images, proportionally to the sum of the open areas of all the pinholes constituting the coded mask used [46]. However, the coded aperture approach preserves many of the properties of the pinhole camera, like its high angular resolution and more in general its *projective geometry*. For this reason, the calibration technique here described is also based on the properties of the pinhole model and perspective projection, which are therefore applied not only to optical and depth sensors, as typically done in many computer vision applications, but also to portable gamma cameras based on the coded aperture technique.

To establish a common terminology and ease the understanding of the procedure below proposed for calibrating the gamma camera with other sensors, an introduction of the geometry of the pinhole model, the basic concepts of camera calibration, and the fundamentals of multi-view geometry are provided below.

The geometry of the pinhole camera

In the representation of the basic pinhole camera, we consider the *central projection* of points in the three-dimensional space onto a plane. More specifically, assuming that the centre of projection (or *camera centre*) is the origin of a given Euclidean coordinate system, a point in space with coordinates $\mathbf{X} = (X, Y, Z)^\top$ is mapped to the point \mathbf{x} on the image plane $Z = f$ (or focal plane).

Figure 4.6 illustrates the 3-D point \mathbf{X} joined by a line with the *centre of projection* \mathbf{C} , crossing the image plane.

By similar triangles, and by observing Figure 4.6, the point $\mathbf{X} = (X, Y, Z)^\top$ is mapped to the point $(fX/Z, fY/Z, f)^\top$ on the image plane. As the latter are image coordinates, we can ignore the last coordinate, and we have:

$$(X, Y, Z)^\top \mapsto (fX/Z, fY/Z)^\top, \quad (4.1)$$

which describes the *projection mapping* from the Euclidean 3-space \mathbb{R}^3 to the Euclidean 2-space \mathbb{R}^2 . This is usually referred to as the mapping from world to image coordinates.

The centre of projection is typically called the *camera centre*, whereas the line from the camera centre perpendicular to the image plane is called *principal axis* of the camera. The point where the principal axis crosses the image plane is called the *principal point*.

Using homogeneous coordinates (see Section 3.3.1), we thus have:

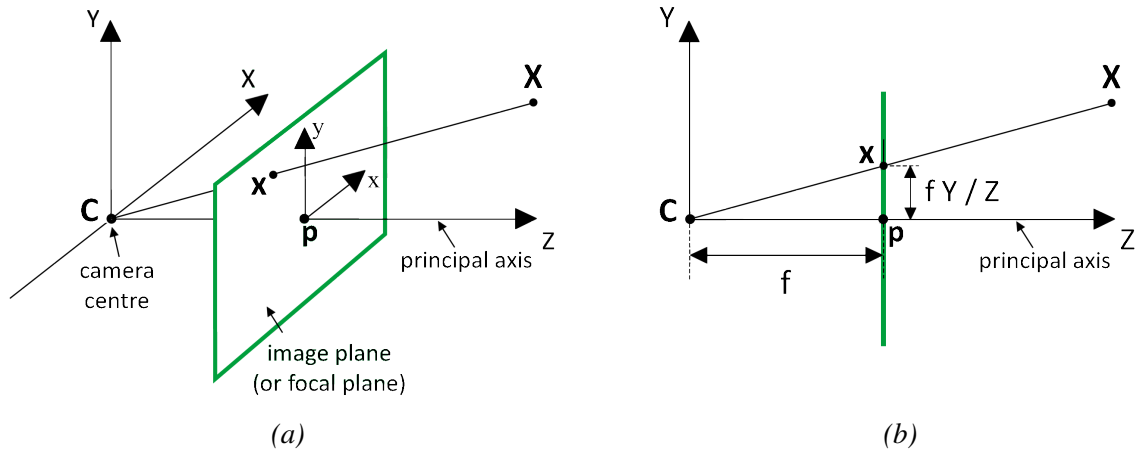


Fig. 4.6: A camera can be interpreted as a mapping between the 3-D world and a 2-D image. \mathbf{C} is the camera centre and \mathbf{p} is the principal point. The camera centre is placed in this case at the origin of the coordinate plane [146].

$$\begin{pmatrix} X \\ Y \\ Z \\ 1 \end{pmatrix} \mapsto \begin{pmatrix} fX \\ fY \\ Z \end{pmatrix}, \quad (4.2)$$

where the term on the right can be expressed as follows:

$$\begin{bmatrix} f & 0 & 0 \\ & f & 0 \\ & & 1 & 0 \end{bmatrix} \begin{pmatrix} X \\ Y \\ Z \\ 1 \end{pmatrix}. \quad (4.3)$$

As explained in [146], the matrix of Eq. 4.3 may be written as $\text{diag}(f, f, 1) [I | \mathbf{0}]$, where $\text{diag}(f, f, 1)$ is a diagonal matrix and $[I | \mathbf{0}]$ is a matrix divided up into a 3×3 identity matrix plus a column vector (here the zero vector).

We therefore refer to \mathbf{X} hereinafter as the *world point* represented by the homogeneous 4-vector $(X, Y, Z, 1)^\top$, whereas we refer to \mathbf{x} for denoting an *image point* as a homogeneous 3-vector. Finally, we refer to \mathbf{P} as the 3×4 homogeneous *camera projection matrix*. We can thus then rewrite Eq. 4.3 in a more compact way, as:

$$\mathbf{x} = \mathbf{P}\mathbf{X}, \quad (4.4)$$

which allows us to define the *camera matrix* \mathbf{P} for the pinhole model of central projection as

$$\mathbf{P} = \text{diag}(f, f, 1) [I | \mathbf{0}]. \quad (4.5)$$

In the expression of Eq. 4.1, we assumed that the origin of coordinates in the image plane is at the principal point. Nevertheless, as noted in [146], this might be not always the case. Therefore, more in general, we rewrite also Eq. 4.1 as a mapping

$$(X, Y, Z)^T \mapsto (fX/Z + p_x, fY/Z + p_y)^T, \quad (4.6)$$

where $(p_x, p_y)^T$ are the coordinates of the principal point. Similarly to how done above, we rewrite Eq. 4.6 in homogeneous coordinates, as

$$\begin{pmatrix} X \\ Y \\ Z \\ 1 \end{pmatrix} \mapsto \begin{pmatrix} fX + Zp_x \\ fY + Zp_y \\ Z \\ 1 \end{pmatrix} = \begin{bmatrix} f & p_x & 0 \\ f & p_y & 0 \\ 1 & 0 & 0 \end{bmatrix} \begin{pmatrix} X \\ Y \\ Z \\ 1 \end{pmatrix}. \quad (4.7)$$

If we now define

$$\mathbf{K} = \begin{bmatrix} f & p_x \\ f & p_y \\ 1 & 0 \end{bmatrix}, \quad (4.8)$$

then Eq. 4.7 can be written as

$$\mathbf{x} = \mathbf{K}[I \mid \mathbf{0}] \mathbf{X}_c. \quad (4.9)$$

The matrix \mathbf{K} of Eq. 4.9 is usually referred to with a number of terms, such as *camera calibration matrix*, *camera intrinsic matrix*, *internal camera parameters*, *internal parameters*, or simply *intrinsic parameters*, the terms are all synonymous. For the sake of simplicity, the matrix \mathbf{K} is hereinafter referred to only as *intrinsic parameters*, to highlight the fact that the parameters contained in such matrix are intrinsically related to the camera and the camera only.

Typically, the camera is assumed to be located at the origin of the Euclidean coordinate system with the principal axis of the camera point at the Z-axis. The 3-D point $(X, Y, Z, 1)^T$ is expressed in such coordinate system, which is usually referred to as *camera coordinate frame*. For this reason, we wrote the 3-D point as \mathbf{X}_c , where its subscript "c" is to emphasise that such point is expressed in the *camera coordinate frame*.

By contrast, 3-D points in space which are independent from the camera are expressed in terms of a different Euclidean coordinate frame, the *world coordinate frame*, as shown in Fig 4.7. The two coordinate frames are related via a rotation \mathbf{R} and a translation \mathbf{t} .

As explained in [146], if $\tilde{\mathbf{X}}$ is an inhomogeneous 3-vector representing a point in the world coordinate frame, and $\tilde{\mathbf{X}}_c$ represents the same point in the camera coordinate frame, then we have:

$$\tilde{\mathbf{X}}_c = \mathbf{R}(\tilde{\mathbf{X}} - \tilde{\mathbf{C}}), \quad (4.10)$$

where $\tilde{\mathbf{C}}$ represents the coordinates of the camera centre in the world coordinate frame, and \mathbf{R} is a 3×3 rotation matrix representing the *orientation* of the camera coordinate frame. Rewriting also Eq. 4.10 in homogeneous coordinates, we can compute the position of the point of interest \mathbf{X}_c in the camera coordinate frame as follows:

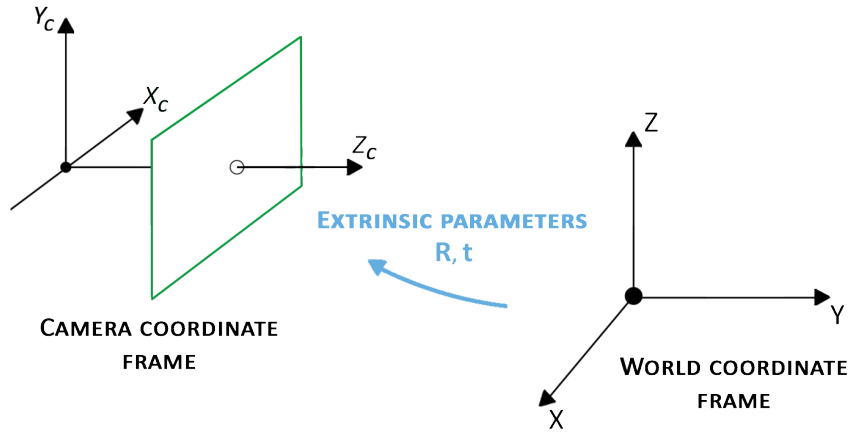


Fig. 4.7: The transformations world-to-camera coordinate frames.

$$\mathbf{x}_c = \begin{bmatrix} \mathbf{R} & -\mathbf{R}\tilde{\mathbf{C}} \\ 0 & 1 \end{bmatrix} \begin{pmatrix} X \\ Y \\ Z \\ 1 \end{pmatrix} = \begin{bmatrix} \mathbf{R} & -\mathbf{R}\tilde{\mathbf{C}} \\ 0 & 1 \end{bmatrix} \mathbf{X}. \quad (4.11)$$

Combining Eq. 4.11 and Eq. 4.9, we obtain:

$$\mathbf{x} = \mathbf{K}\mathbf{R}[I \mid -\tilde{\mathbf{C}}] \mathbf{X}, \quad (4.12)$$

where \mathbf{X} is now defined in a world coordinate frame, which is the general mapping of a pinhole camera. By observing Eq. 4.4, we can easily see that

$$\mathbf{P} = \mathbf{K}\mathbf{R}[I \mid -\tilde{\mathbf{C}}], \quad (4.13)$$

which has 9 degrees-of-freedom (DOF)⁵: 3 for \mathbf{K} (the elements f, p_x, p_y), 3 for \mathbf{R} , and 3 for $\tilde{\mathbf{C}}$.

The parameters of \mathbf{R} and $\tilde{\mathbf{C}}$ relate the orientation and position (pose) of the camera, respectively, and they are typically referred to as *external parameters*.

As suggested in [146], it is often convenient not to make the camera centre explicit, and instead to represent the world-to-camera transformation as $\tilde{\mathbf{X}}_c = \mathbf{R}\tilde{\mathbf{X}} + \mathbf{t}$. In this way, we can define the camera matrix simply as

$$\mathbf{P} = \mathbf{K}[\mathbf{R} \mid \mathbf{t}], \quad (4.14)$$

where $\mathbf{t} = -\mathbf{R}\tilde{\mathbf{C}}$, according to Eq. 4.13.

Epipolar geometry and the fundamental matrix

We described above the geometry of a single perspective camera, focusing on the projection of a 3-D scene onto the 2-D image plane of a given camera. However, many applications require

⁵In Mechanics, the "degrees of freedom" is the number of independent movements allowed for a rigid body.

the possibility of relating two perspective views. Such views may be either acquired sequentially from the same camera at different orientations/positions, as done for the panoramic procedure described in Chapter 3, or simultaneously, for example in a stereo rig.

Since each perspective view has an associated camera matrix, we have the camera matrix \mathbf{P} for the first view, the camera matrix \mathbf{P}' for the second one, and a 3-space point \mathbf{X} associated to both views, by the following respective relationships:

$$\mathbf{x} = \mathbf{P}\mathbf{X} \quad (4.15)$$

$$\mathbf{x}' = \mathbf{P}'\mathbf{X} \quad (4.16)$$

Image points \mathbf{x} and \mathbf{x}' *correspond* because they are the image of the *same* 3-space point \mathbf{X} .

Given an image point \mathbf{x} in the first view, we can constrain the position of the corresponding point \mathbf{x}' in the second view by using the *epipolar geometry*. A point \mathbf{x} in one view defines an *epipolar line* in the other view on which the corresponding point \mathbf{x}' lies (see Figures 4.8 and 4.9).

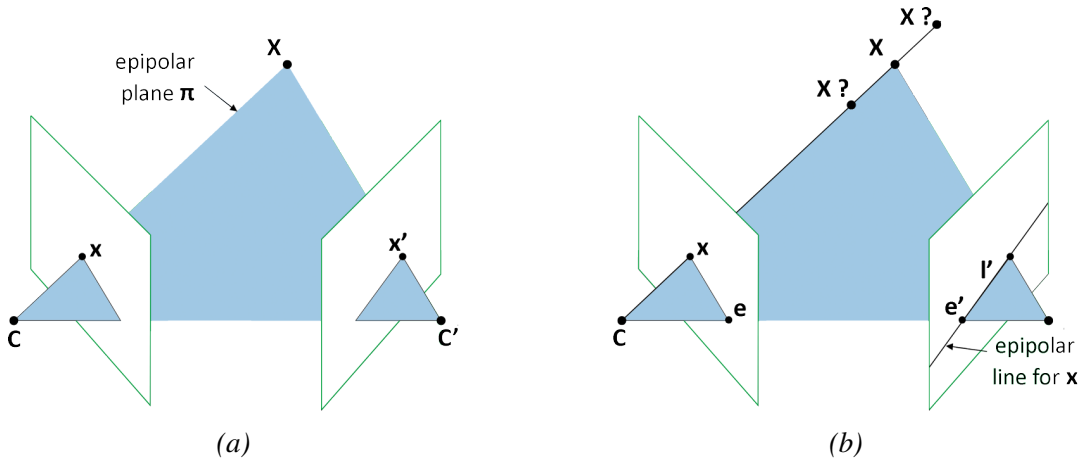


Fig. 4.8: (a) The two cameras are indicated by their centres \mathbf{C} and \mathbf{C}' and image planes. The camera centres, 3-space point \mathbf{X} , and its images \mathbf{x} and \mathbf{x}' lie in a common plane, π . (b) An image point \mathbf{x} back-projects to a ray in 3-space defined by the first camera centre, \mathbf{C} , and \mathbf{x} . This ray is imaged as a line \mathbf{l}' in the second view. The 3-space point \mathbf{X} which projects to \mathbf{x} must lie on this ray, so the image of \mathbf{X} in the second view must lie on \mathbf{l}' [146].

The epipolar line can be described as the projection in the second view (image) of the ray from the point \mathbf{x} through the camera centre \mathbf{C} of the first camera. In other terms, we have a mapping $\mathbf{x} \mapsto \mathbf{l}'$, which is the mapping from a point in the first view to its corresponding line in the other image. Such mapping is represented by the matrix \mathbf{F} , the *fundamental matrix*.

Given a set of point correspondences between two images, the fundamental matrix \mathbf{F} is defined by the equation:

$$\mathbf{x}'^T \mathbf{F} \mathbf{x} = 0 \quad (4.17)$$

for any pair of matching points $\mathbf{x} \leftrightarrow \mathbf{x}'$ in two images. Given the matches $\mathbf{x}_i \leftrightarrow \mathbf{x}'_i$, Eq. 4.17 is used to estimate the unknown matrix \mathbf{F} . If $\mathbf{x} = (x, y, 1)^T$ and $\mathbf{x}' = (x', y', 1)^T$, each point match leads

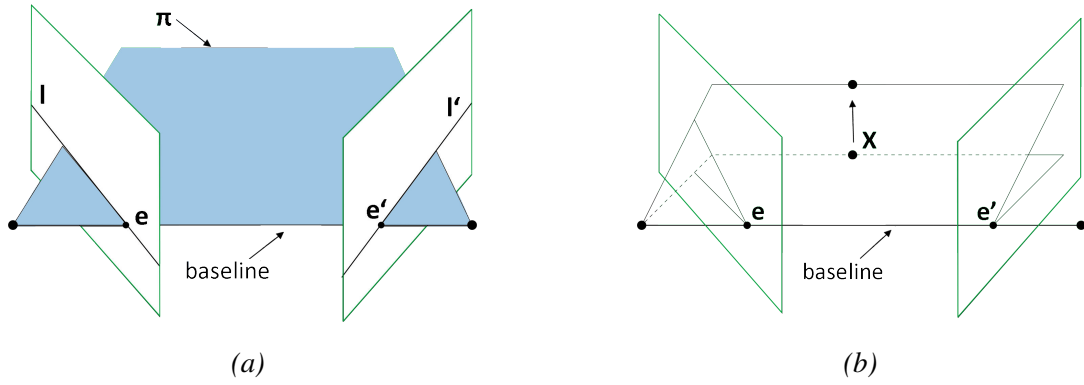


Fig. 4.9: (a) The camera baseline intersects each image plane at the epipoles \mathbf{e} and \mathbf{e}' . Any plane π containing the baseline is an epipolar plane, and intersects the image planes in corresponding epipolar lines \mathbf{l} and \mathbf{l}' . (b) As the position of the 3-D point \mathbf{X} varies, the epipolar planes rotate about the baseline. This family of planes is known as an epipolar pencil. All epipolar lines intersect at the epipole [146].

to one linear equation in the unknown entries of \mathbf{F} . The coefficients of this equation are easily written in terms of the known coordinates \mathbf{x} and \mathbf{x}' . That is, the equation corresponding to a pair of points $(x, y, 1)$ and $(x', y', 1)$ is:

$$x'xf_{11} + x'yf_{12} + x'f_{13} + y'xf_{21} + y'yf_{22} + y'f_{23} + xf_{31} + yf_{32} + f_{33} = 0. \quad (4.18)$$

Therefore, given n point matches, we obtain a set of linear equations of the form:

$$\mathbf{A}\mathbf{f} = \begin{bmatrix} x'_1x_1 & x'_1y_1 & x'_1 & y'_1x_1 & y'_1y_1 & y'_1 & x_1 & y_1 & 1 \\ \vdots & \vdots & \vdots & \vdots & \vdots & \vdots & \vdots & \vdots & \vdots \\ x'_nx_n & x'_ny_n & x'_n & y'_nx_n & y'_ny_n & y'_n & x_n & y_n & 1 \end{bmatrix} \mathbf{f} = \mathbf{0}, \quad (4.19)$$

which is a homogeneous set of equations. For a solution to exist, in theory matrix \mathbf{A} must have rank⁶ at most 8. Nevertheless, as explained in detail in [146], if the point coordinates are affected by noise, then the rank of \mathbf{A} may be equal to 9, since \mathbf{A} has 9 columns.

Consequently, the epipolar geometry depends only on the cameras and their baseline⁷. More specifically, it depends on their *relative pose* (relative position and orientation) and their intrinsic parameters, as defined above.

The detailed description of the geometric properties of the fundamental matrix go behind the scope of the present section. The interested reader regarding the most used methods for computing the fundamental matrix and the associated stability analysis is referred to [190, 146].

⁶The rank of a matrix is defined as (a) the maximum number of linearly independent column vectors in the matrix or (b) the maximum number of linearly independent row vectors in the matrix. Both definitions are equivalent.

⁷The baseline is the line joining the camera centres.

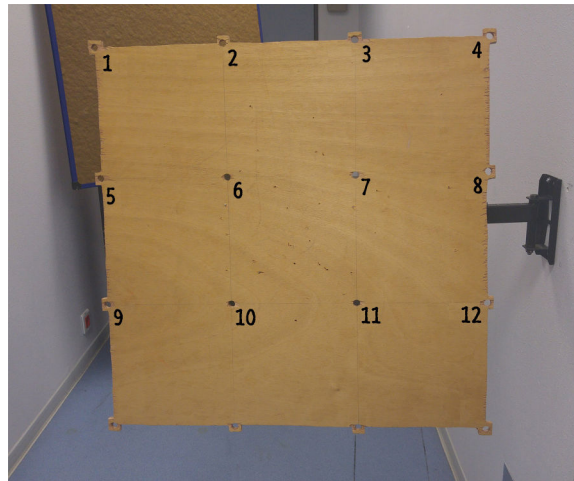


Fig. 4.10: Experimental phantom built and used for calibrating two γ -cameras, a depth sensor (the Asus Xtion), and an optical camera. Only the holes labelled with numbers were used in this study. The size of the board is $60 \times 60 \text{ cm}^2$, the holes have 10 mm diameter, and their respective axial separation (horizontal or vertical) is 200 mm.

4.3.2 Design of an experimental calibration phantom

The registration between the images generated by two γ -cameras, an optical, and a depth sensor requires a calibration phantom that facilitates the data acquisition performed with each sensor involved in the measurements.

Consequently, in order to accurately fix the above ^{241}Am point source, a board with 4×4 holes of 10 mm diameter has been built (see Figure 4.10).

The holes of the board can be interpreted as *calibration markers*, sometimes referred to also as *calibration points*, and due to their specific geometric configuration, we obtained a planar calibration pattern (*plane-based calibration* [191]), which was observed at different orientations from all cameras of the acquisition prototype system during the calibration procedure, as explained more formally in Section 4.3.3. The diameter of the holes was determined by the size of the radioactive point source support. The axial distance, both vertical and horizontal, between the centre of each hole is 200 mm.

As suggested in [192], calibration errors are often caused also by the inaccuracy regarding the coordinates of the markers constituting the pattern in the calibration target (in our case, the distances between the holes of the calibration phantom). For this reason, the distance between all holes was measured a second time with a Vernier caliper after the phantom had been built, in order to achieve sub-millimetre precision regarding their axial separation, and the calibration data were accordingly adjusted.

4.3.3 Multi-modal camera calibration

We refer to *multi-modal camera calibration* as the process of estimating:

- the intrinsic parameters \mathbf{K} of Eq. (4.8) for each camera \mathbf{C} (left γ -camera, right γ -camera, depth sensor, and optical camera), and
- the rigid transform mapping a pre-defined world reference system to each camera reference system, that is, \mathbf{R} and \mathbf{t} of Eq. (4.14).

Furthermore, in our case, we are not only interested in calibrating each sensor independently, but also in retrieving the relative pose between each couple of sensors, so that images acquired from different sensors can be mapped and overlaid for each possible pair of cameras involved.

The rigid transform of Eq. (4.14) has 6 degrees-of-freedom of movements (3 for the rotation and 3 for the translation), while the intrinsic parameters \mathbf{K} of Eq. (4.8) have only 4 degrees-of-freedom of movements. As explained in [177], a standard approach for the estimation of all the parameters above is to retrieve N correspondences $\{\mathbf{X}_j, \mathbf{x}_j\}$ (being $j = 1, \dots, N$), therefore retrieving some points \mathbf{X}_j in the world reference system and their respective projections \mathbf{x}_j on the images acquired by the cameras.

By solving Equations (4.9)-(4.14) for each correspondence, we obtain:

$$\mathbf{x}_j = \mathcal{P}(\mathbf{K}(\mathbf{R}\mathbf{X}_j + \mathbf{t})) \quad (4.20)$$

where \mathcal{P} is a mapping function from a 3-D point \mathbf{X} and a pixel \mathbf{x} on the image plane, and it gives a non-linear system of $2N$ equations for determining the 10 unknown parameters (6 external and 4 internal).

Although, in theory, correspondences for $N = 5$ points are sufficient for retrieving all the internal and external parameters of all sensors involved, we placed the ^{241}Am source over $N = 12$ different locations (the labelled holes of Fig. 4.10), in order to collect a larger number of correspondences. All the parameters were then estimated in a least-square fit, for a good resilience to measurement errors, solved with the Levenberg-Marquardt Algorithm [193].

As already mentioned, the proposed calibration method is deliberately based on *only one* radioactive point source, in order to significantly maximize its reproducibility. The calibration procedure considered a series of measurements with the prototype rigidly fixed, whereas the phantom was located at different positions/orientations, covering as much as possible the intersection of the FOVs of the sensors involved. That is, for each chosen position/orientation of the phantom, the ^{241}Am source was placed, *sequentially*, over the 12 chosen holes, and separate gamma images were captured with both left and right γ -cameras (only in mask mode), depth sensor, and optical camera.

While the acquisition of the depth and optical images is quite straightforward and almost instantaneous, the retrieval of the location of each radioactive hotspot on the phantom clearly depends on the characteristics of the adopted γ -camera(s). In order to obtain the positions of the ^{241}Am point source with respect to the image plane of the γ -cameras, we collected with both of them 30 frames of 1 sec shutter time, only in mask mode, for each calibration point (i.e. source position). Such collected data were more than sufficient in our case to accurately locate the

source since, as shown in Fig. 2.15, the response of the Timepix detector is highly sensitive to the predominant γ -ray (~ 59 keV) emitted by this radionuclide.

To provide a clear idea of the experimental setup adopted for performing the calibration, Fig. 4.11 shows how the prototype was placed in front of the phantom while performing all measurements.

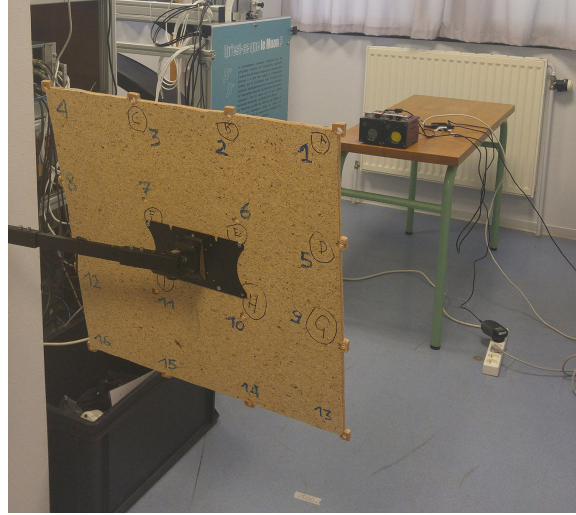


Fig. 4.11: Experimental setup for calibrating a stereo gamma camera, an optical camera, and a depth sensor, rigidly mounted and integrated within the prototype, which was fixed in front of the phantom designed and built for the experiment.

Once for a given position/orientation the 12th set of measurements was concluded, a cut-off threshold was applied to the 12 radiation images (the same threshold used for the measurements and results discussed in Chapter 2 was used) and then they were combined (i.e. summed) in one single image, obtaining thus a gamma image with 12 sources for both left and right γ -cameras.

Consequently, for each given position/orientation of the calibration phantom, four images were obtained (two gamma images, the depth map, and the optical image). We refer to such set of images as *calibration frameset* or simply *frameset*. Figure 4.12 shows an example of frameset with the four images obtained concerning the first chosen position/orientation of the phantom during the experiment.

At the end of the experiment, we obtained $M = 12$ different framesets. We could have used all 16 holes available on the phantom or obtained more calibration images, but we considered $N = 12$ and $M = 12$ to be overall a sufficient number of correspondences (in this specific case $N = M = 12$ is only a coincidence).

More formally, if N is the number of correspondences and M the number of framesets obtained, our calibration procedure is based on the following measurements:

$$\{\hat{S}_{L0}, \hat{S}_{R0}, D_0, V_0\}, \{\hat{S}_{L1}, \hat{S}_{R1}, D_1, V_1\}, \{\hat{S}_{Li}, \hat{S}_{Ri}, D_i, V_i\}, \{\hat{S}_{LM-1}, \hat{S}_{RM-1}, D_{M-1}, V_{M-1}\},$$

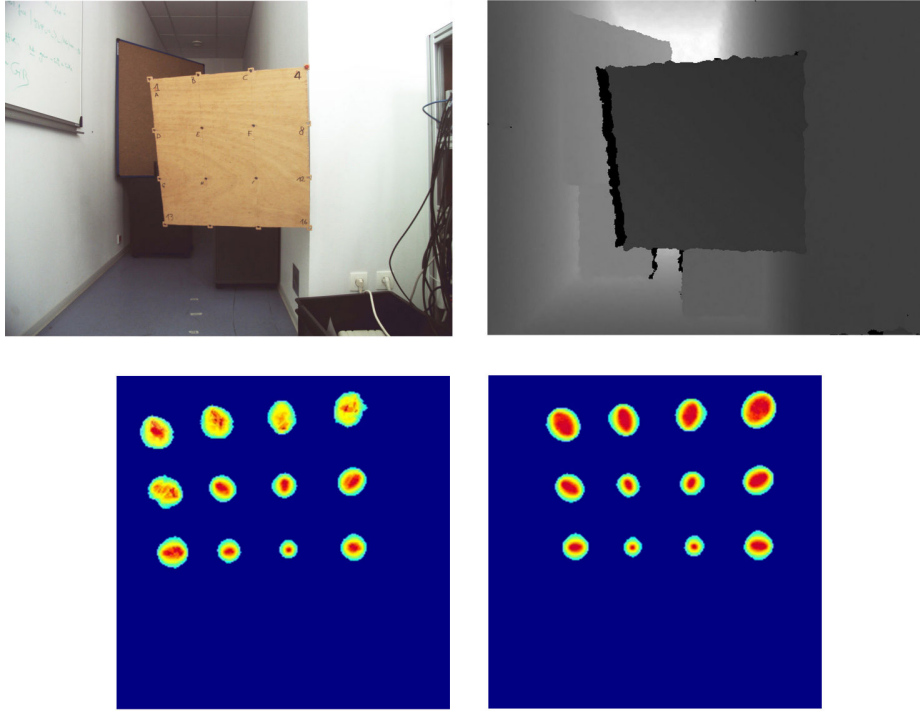


Fig. 4.12: Example of calibration frameset: optical image, depth map, and left and right γ -images, all captured with the experimental phantom rigidly fixed in the same position/orientation respect to the prototype. The proposed calibration procedure is deliberately based on only one radioactive point source, in order to significantly maximize its reproducibility.

where D stands for depth map, V stands for visible (optical) image, while \hat{S}_L and \hat{S}_R stand respectively for the reconstructed γ -images with the left and right gamma cameras (see Section 1.2.2), each containing the positions (image coordinates) of the N sources.

Every frameset needs to be acquired without moving the phantom with respect to the prototype. This ensures that the poses estimated for each camera for a given frameset will be relative to the same world reference system, which is defined as being built-in to the phantom.

Once the M framesets have been obtained, the pixels showing the 12 calibration points on the phantom are labelled on each image, in order to retrieve the needed 3-D/2-D correspondences. The (x,y) coordinates of the radioactive sources in the radiation images were computed using the OpenCV library [136], by retrieving the coordinates of the centroid of each source, whereas from the depth and optical images they were extracted and labelled manually, as this task requires a relatively little amount of time.

Afterwards, the algorithm derives the intrinsic and extrinsic parameters of the gamma, depth, and optical cameras, separately. During this phase, the pose of each camera with respect to the phantom reference system for each frameset (*absolute pose*) is also retrieved. Then, the position of each sensor with respect to the others is obtained by inverting and combining the poses computed during the previous step. For example, solving the relation between the absolute pose of the left γ -camera, $\{\mathbf{R}_{\gamma_L}^i, \mathbf{t}_{\gamma_L}^i\}$, respect to the absolute pose of the depth sensor, $\{\mathbf{R}_d^i, \mathbf{t}_d^i\}$, on the i -th frameset, we obtain:

$$\begin{aligned}\mathbf{R}_{d \rightarrow \gamma L}^i &= \mathbf{R}_{\gamma L}^i (\mathbf{R}_d^i)^\top \\ \mathbf{t}_{d \rightarrow \gamma L}^i &= -\mathbf{R}_{\gamma L}^i (\mathbf{R}_d^i)^\top \mathbf{t}_d^i + \mathbf{t}_{\gamma L}^i,\end{aligned}\tag{4.21}$$

where $(\cdot)^\top$ denotes the transpose operator.

For a more robust measurement, the final relative pose $\{\mathbf{R}_{\gamma L}, \mathbf{t}_{\gamma L}\}$ is accounted by averaging the relative pose estimates over all the M framesets. More concretely, all rotation matrices are first converted to the corresponding unit quaternion representation [194], and then the mean of all resulting quaternion rotations was obtained by using the method described in [195]. Such pose allows to project a 3-D point expressed in the depth camera reference system on the depth maps.

The same procedure is employed to retrieve all the other relative poses.

4.3.4 Summary of the experimental setup

The steps for carrying out the calibration procedure above described are summarized as follows. The prototype was fixed as rigidly as possible on a adequate support. Then, *for each frameset*, the following steps were followed:

1. *Positioning of the board*: the calibration phantom (Fig. 4.11) was positioned and oriented so that its holes (calibration markers) were visible in all FOVs of the four sensors (i.e. the intersection of the FOVs of all cameras involved).
2. *Data acquisition*:
 - (a) the optical image of the phantom was captured and stored,
 - (b) the depth map was computed,
 - (c) the ^{241}Am source was placed over the $N = 12$ holes of the phantom, and, for every hole, the gamma acquisition for both left and right γ -cameras was performed, performing thus $N = 12$ measurements (only in mask mode) for each γ -camera.
3. *Data analysis and processing*: the 2-D coordinates of the position of each hole/source were retrieved for:
 - (a) the optical image,
 - (b) the depth map, and
 - (c) the reconstructed gamma images representing the 12 positions of the ^{241}Am point source as located from by two γ -cameras (see Fig. 4.12).

During the experiment, we have captured $M = 12$ framesets following the above steps. Once all frames were acquired and processed, the algorithm had the correspondences needed to estimate all the intrinsic/extrinsic parameters of the γ -cameras and the other sensors.

4.4 Calibration results and multimodal image registration

The whole calibration procedure described in Sections 4.3.3 and 4.3.4 has been performed. The intrinsic and extrinsic parameters of the two γ -cameras, the depth sensor, and the optical camera were computed, along with the relative poses of each pair of sensors (i.e. the spatial relation between the cameras), which are retrieved by inverting and combining the obtained absolute poses.

In this section, a qualitative and quantitative evaluation of the calibration accuracy for each single calibrated camera are provided, along with the description of the methods for registering the different types of images using the camera matrices computed and the relative poses between each pair of sensors.

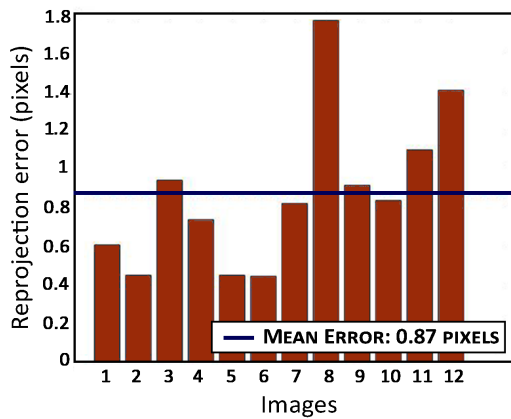
4.4.1 Evaluation of the reprojection error

Once the 3-D coordinates of all calibration points are determined, we began the evaluation of the parameters computed for all cameras involved in the multi-modal calibration by calculating the respective mean reprojection error. Such measure can be interpreted as the average deviation between each point in an image of a given camera and the corresponding world point reprojected on such image [146].

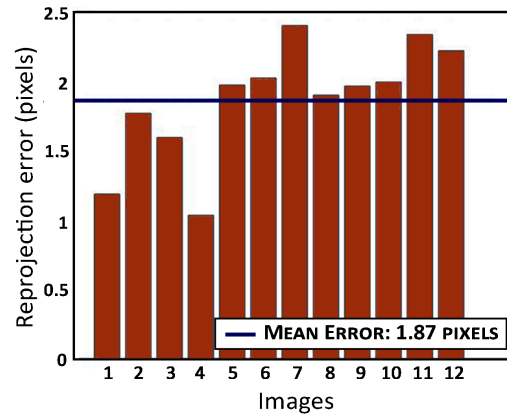
Experimental results showed that by collecting $M = 12$ calibration framesets, the mean reprojection error achieved with the calibration procedure proposed was below 1 pixel for all cameras involved, with the exception of the depth camera. The summary of the results of such analysis is shown in Fig. 4.13.

The left and right γ -cameras have been calibrated with a reprojection error of 0.73 and 0.81 pixel, respectively. The error concerning the depth sensor, however, is 1.87 pixels. This is probably due to a higher inaccuracy during the extraction from the depth maps of the coordinates of the holes situated in the central part of the phantom. By observing the phantom in any of the respective depth maps produced by the depth camera (for example the depth image of Fig. 4.12), it is possible to see that the central holes labelled with the numbers 6, 7, 10, and 11 are not visible (holes are labelled in Fig. 4.10), since the experimental phantom built is intentionally planar. For this reason, we shaped the phantom so that all the external holes situated on its sides would be detectable in each depth map, providing thus the possibility of retrieving the coordinates of such holes also in the depth image, and consequently the estimation of the position of the remaining holes.

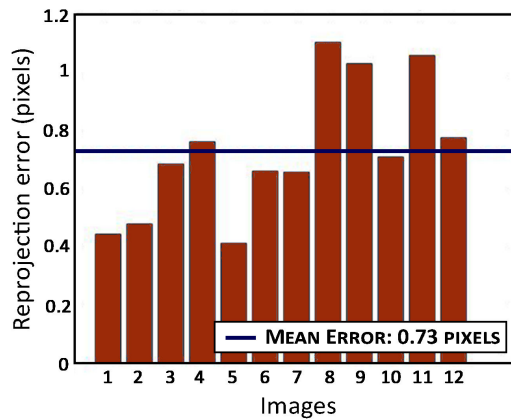
Despite such slight difference concerning the reprojection error of the depth camera, and considering the number of correspondences collected, we consider the overall error achieved for all cameras satisfactory. Moreover, although the mean reprojection error achieved for the γ -cameras is below one pixel, the spacial resolution typically provided by the radiation images reconstructed by portable gamma cameras did not require, admittedly, sub-pixel accuracy.



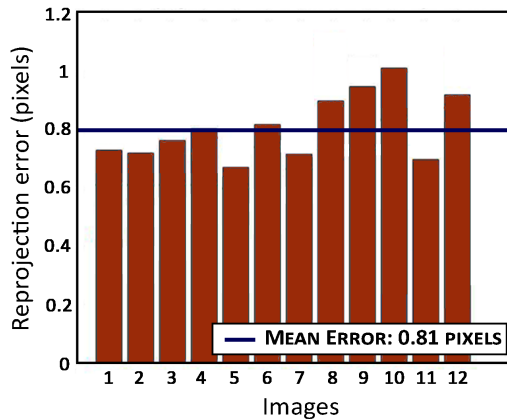
(a) Mean reprojection error for the parameters of the optical camera.



(b) Mean reprojection error for the parameters of the depth sensor.



(c) Mean reprojection error for the parameters of the left γ -camera.



(d) Mean reprojection error for the parameters of the right γ -camera.

Fig. 4.13: Mean reprojection error concerning all cameras involved in the multi-modal calibration. With the exception of the depth sensor, the mean reprojection error concerning all cameras was below 1 pixels.

4.4.2 Registration of optical and radiation images

When dealing with different types of cameras (or when moving the centre of the same camera), the image coincidence between the respective generated views is lost. The displacement that occurs between the views is called *parallax*. When superimposing onto an optical image a radiation image obtained by means of a coded mask, both problems are present: the cameras are intrinsically different, and their respective centres are inevitably located in distinct positions. For this reason, a parallax occurred also with the iPIX system during the superimposition phase, notably for radioactive sources with distances less than 5 metres from the camera. Methods for correcting such displacement are typically called *parallax error adjustment* or simply *parallax adjustment*.

When processing the radiation information acquired with the Timepix and the coded mask, it was needed to manually provide to the software of the γ -camera the source-to-detector distance, in metres. Such information was then used for adjusting the size of the γ -image and translate each respective pixel according to the distance provided. Such kinds of methods though present several problems. In the first place, the superimposition can be coherently performed only if the person using the γ -camera already knows which object is supposed to be radioactive. In some situations, such aspect might limit the benefit of using a portable γ -camera, as the position respect to the camera concerning the surrounding radioactive hotspots is not always known a priori. Another type of scenario that might occur is when more than one source is detected in the FOV of the gamma camera. If all sources are not located at the same distance respect to the detector, and if at least one of the sources is located at less than 5 metres from the camera, the information concerning only one hotspot can be correctly superimposed, while that of the other sources won't be correctly overlaid.

Using the intrinsic and extrinsic parameters obtained during the calibration procedure described in Section 4.3.3, it is possible to accurately map the gamma image points to world points, and then reproject the resulting 3-D points on the X-Y plane of the optical camera, significantly reducing the parallax occurring between the images.

In other terms, the decoded gamma image is superimposed onto the respective optical image using the intrinsic and extrinsic parameters obtained. We can evaluate the error occurred during such overlay phase by calculating the mean distance between the centre of a point source detected in the radiation image and the centre of the same source in the optical image (the latter is manually extracted). We refer to such evaluation method as *visual analysis*.

More specifically, we initially labelled and stored the coordinates of each pair of centres of the sources in the optical/gamma images (a total of 144 pairs were collected). Then, the mean value of the Euclidean distances between the (x,y) coordinates of all pairs was computed, providing a mean displacement error of 0.984 pixel, where the pairs of visible/radioactive coordinates were collected from images where the phantom was located at an average distance of less than 1 metre from the camera.

Figure 4.14 shows an example of result where all sources placed on the experimental phantom were autonomously and accurately superimposed on the optical image (the pixelated effect of



Fig. 4.14: Reconstructed gamma image, representing the position of 12 radioactive hotspots on the experimental phantom, automatically reprojected on the visible image using the intrinsic and extrinsic parameters retrieved by means of the proposed procedure of the optical and γ -cameras used.

the radiation sources is caused by the intrinsic difference of the sizes of the optical and radiation images).

4.5 Automatic retrieval of the distance of surrounding radioactive sources

In Section 4.4.2 the registration and procedure for mapping optical and radiation images have been discussed. Similarly to how done between the γ -cameras and the optical camera, also the depth maps can be remapped to both optical and gamma images, as the calibration data of each sensor were stored and the relative pose between each pair of cameras is also known.

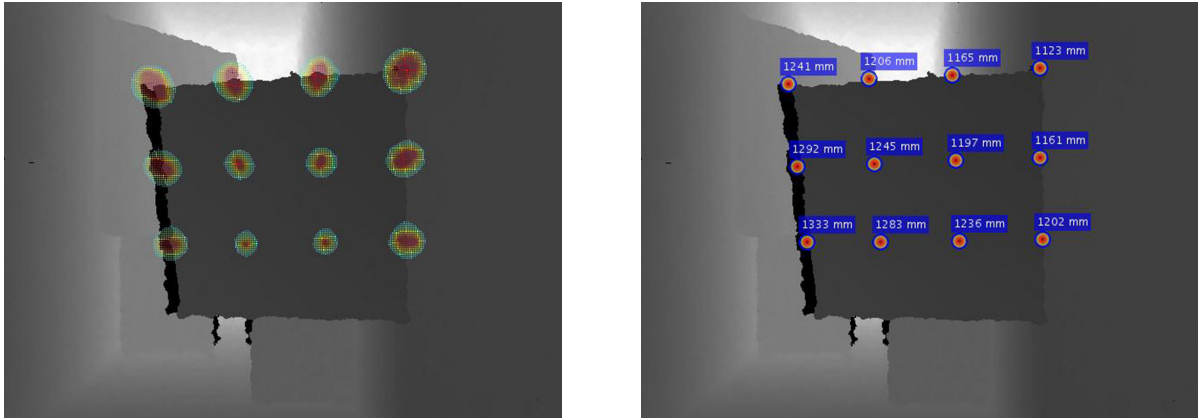
Consequently, by registering the radiation images with the depth maps computed by the depth camera, the distance of the radioactive sources under study can be automatically estimated. Such method is below discussed.

4.5.1 Depth maps and radiation images mapping

To test the validity of the intrinsic and extrinsic parameters computed concerning the depth camera, the image points representing radioactive hotspots in a radiation image can be reprojected on the respective depth map, and vice versa. The evaluation of the camera matrices has been carried out on both the collected data during the execution of the calibration, and, moreover, on additional independent test measurements performed with the calibrated prototype, after the calibration procedure had been completed.

Figure 4.15a shows a depth map superimposed by the radiation image already considered and shown in Fig. 4.14. On the other hand, the values retrieved from the depth map were also associated, in *mm*, to each pixel of interest of the γ -image. For example, in Fig. 4.15b, the distance

source-to-camera has been associated to the local maximum of each hotspot, which in this specific case represents the centre of each radioactive point source.



(a) Example of radiation image superimposed on the associated depth image by means of pixel-wise mapping.

(b) Source-to-detector distance automatically retrieved from the depth map for each centre of the located radioactive sources.

Fig. 4.15: Radiation image reprojected on the X-Y plane of the depth image using the camera matrices computed and the relative pose information between the depth and left γ -camera of the prototype.

As the calibration data can easily be stored and the spatial relation between all sensors is also known, the depth maps can be remapped to both optical and gamma images also for any measurements performed after the calibration procedure has been carried out.

Figure 4.16 shows one of the results concerning a measurement independent from those performed for the calibration, obtained by placing the ^{241}Am source in front of the acquisition prototype thus already calibrated.

Before acquiring the images with all four sensors (i.e. the two γ -cameras, the depth sensor, and the optical camera), the reference distance between the source and the prototype was measured using a laser meter (the Leica Disto D210). According to its specifications [196], the maximum error of this device is 0.1 mm/m for measurements up to 30 m and 0.15 mm/m beyond this distance. Between the centre of the left γ -cameras and the ^{241}Am point source, the laser meter measured a source-to-detector distance of 2016 mm.

Concerning such experiment, our prototype automatically estimated this distance to be 2014 mm, retrieving automatically the information from the depth map computed by the Asus Xtion. Thus, its associated error in this case was ~ 2 mm.

Figure 4.17 shows another result concerning a measurement where the prototype was tested with a ^{137}Cs point source of ~ 261 MBq activity, placed in front of the system. In this case, our prototype automatically estimated the source-to-detector distance to be 1855 mm, whereas, for the same distance, the Leica Disto D210 device measured 1858 mm. According to this experiment, the associated error was thus ~ 3 mm.

With both radioactive sources (^{241}Am and ^{137}Cs), the information concerning their localization was automatically reprojected and superimposed on the optical image with an error below one

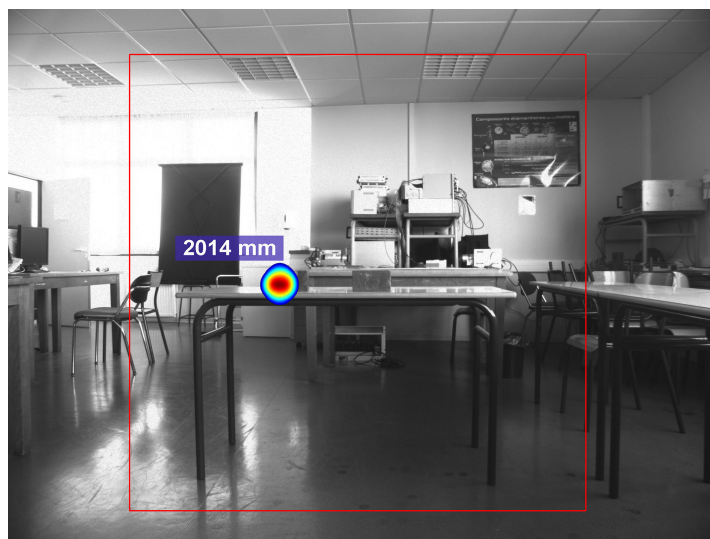


Fig. 4.16: Position and distance automatically retrieved by the prototype for an ^{241}Am point source of $\sim 360\text{ MBq}$ activity.

pixel. The accuracy of the registration seems thus not dependent on the energy of the emitted γ -rays.

4.5.2 Stereo gamma imaging

The results above described concerned the registration between the left γ -camera of the prototype and the Asus Xtion depth camera, allowing thus the estimation of the distance of the surrounding radiation sources that are not occluded respect to the cameras. Nevertheless, some scenarios may require the estimation of the distance of radioactive objects also when an occluding object is present between the radiation source and the instrument.

In general, image registration can be applied for extracting information regarding the distance of an object of interest using *triangulation*, retrieving thus the 3-D position of a given point (or set of points) from a stereo pair of registered images. Such problem consists typically of four main phases: selection of the set of points of interest in the first view, determination of the coordinates of the *corresponding* set of points in the second view, computation of the fundamental matrix F , and then estimation of the distance from one of the cameras to the object of interest via triangulation.

Among the steps mentioned, finding the stereo correspondences in a given pair of images is often one of the most challenging tasks. Such problem is significantly simplified when using *active* range sensing methods such as the coded structured-light technique (introduced in Section 4.1 and adopted for example also by the Asus Xtion camera), which is also based upon the triangulation principle, and where the correspondence problem is solved by using an artificial source of illumination. Nonetheless, when dealing with passive techniques, finding stereo correspondences by means of triangulation needs to be achieved by considering only the ambient illumination. In such contexts, *image rectification* methods [197, 198] are typically used for determining the



Fig. 4.17: Position and distance automatically retrieved by the prototype for a ^{137}Cs point source of ~ 261 MBq activity.

transformations needed for each image plane such that the epipolar lines in the original images map to *horizontally* aligned lines in the transformed images. A set of rectified images can be thought of as acquired by an ideally geometrically aligned stereo rig, obtained by rotating the cameras around the centre of their baseline. When the images are rectified, computing stereo correspondences is considerably simpler, as the search for the corresponding point in the second view is performed along the horizontal lines of the rectified images.

Whereas the triangulation approach is typically applied to cameras with lens systems, in our context we wish to estimate the distance of the surrounding radioactive sources by means of triangulation with two horizontally aligned coded aperture gamma cameras. We refer to such technique as *stereo gamma imaging*.

The centres of the calibrated gamma cameras have been accurately aligned, both horizontally and vertically, so that their image planes are coplanar. Therefore, in principle, the need of image rectification is greatly decreased. Another aspect to consider in stereo gamma imaging is that γ -rays do not suffer from the problem of partial occlusion, since situations where the radioactive source of interest is efficaciously shielded only respect to one gamma camera (while thus being detectable only from the second camera) are extremely rare, and they are therefore not taken in consideration by the method proposed. Consequently, in our case the search of stereo correspondences in two γ -images is substantially simplified.

During the procedure described in section 4.3.3, the coefficients of the internal parameters of both gamma cameras have been computed, along with the poses of each sensor with respect to each other. Therefore, it is possible to relate the image points of the two radiation images similarly to how we proceeded for the superimposition between optical and the gamma cameras, allowing the retrieval of the distance also concerning radioactive sources that may be occluded respect to

the camera. The displacement between the mapped coordinates of corresponding points in the two views of the γ -cameras (i.e. representing the same radioactive object) is called *disparity*.

A simplified illustration of the geometry of our stereo gamma camera prototype is provided in Fig. 4.18. The two γ -cameras have a baseline distance b . As mentioned, both detectors/coded masks are respectively coplanar. The same radioactive source S is reconstructed with both the left γ -camera and right γ -camera.

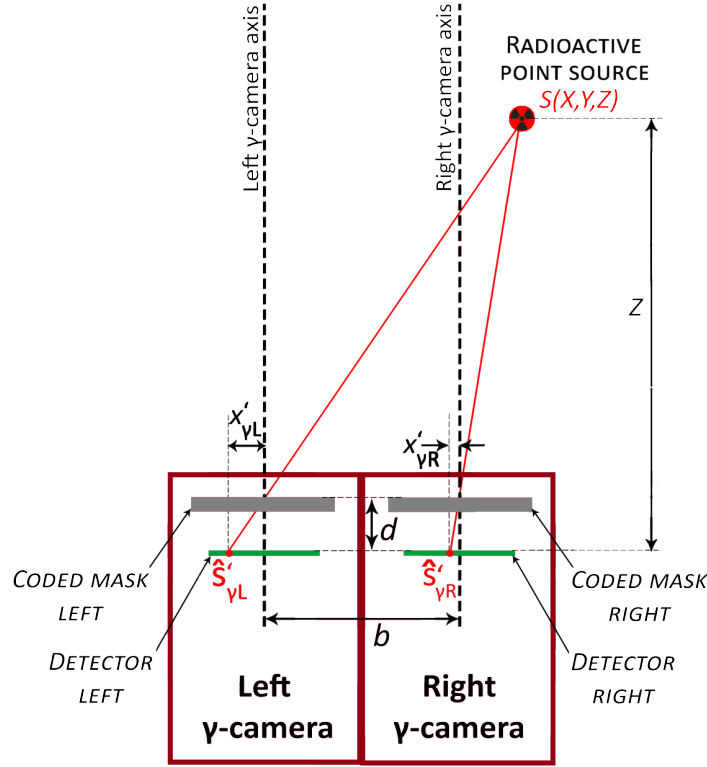


Fig. 4.18: Representation of a radioactive source reconstructed with two γ -cameras. The displacement between the positions of the two points ($\hat{S}_{\gamma L}$ and $\hat{S}_{\gamma R}$) is the disparity. The distance between the centres of the two detectors is the baseline, b . The shown components are not to scale and the reconstruction of the points $\hat{S}_{\gamma L}$ and $\hat{S}_{\gamma R}$ via the coded aperture technique is simplified for illustration purposes.

In Fig. 4.18, the radioactive source S is reconstructed in two different γ -images at the coordinates of $\hat{S}_{\gamma L}$ and $\hat{S}_{\gamma R}$ (see Eq. 1.6), respectively. The displacement of $\hat{S}_{\gamma L}$ and $\hat{S}_{\gamma R}$ is the disparity.

Since the distance d between the mask and the detector is known from the intrinsic parameters, and the baseline b is retrieved from the extrinsic parameters (i.e. the distance between the centres of the two cameras), we have:

$$\frac{X}{Z} = \frac{x'_{\gamma L}}{d} \quad (4.22)$$

and

$$\frac{X - b}{Z} = \frac{x'_{\gamma R}}{d}. \quad (4.23)$$

Combining Eq. 4.22 and Eq. 4.23, we obtain:

$$Z = \frac{b d}{x'_{\gamma L} - x'_{\gamma R}} \quad (4.24)$$

Therefore, we can retrieve the distance of radioactive sources by considering the disparities of the corresponding points retrieved from a pair of reconstructed γ -images.

Although the distance between the coded aperture and the detector can be retrieved from the intrinsic parameters, and the baseline b can be computed using the extrinsic parameters, such distances could be already known a priori or they could also be measured directly on the prototype in our case, for example with a Vernier caliper.

Moreover, if the image coordinates $\hat{S}_{\gamma L}$ and $\hat{S}_{\gamma R}$ satisfy $y'_{\gamma L} = y'_{\gamma R}$ and Z has been calculated, in such context we can retrieve the position of the 3-D point $\mathbf{S} = (X, Y, Z)^T$ by computing:

$$X = \frac{b x'_{\gamma L}}{x'_{\gamma L} - x'_{\gamma R}}, \quad (4.25)$$

and similarly

$$Y = \frac{b y'_{\gamma}}{x'_{\gamma L} - x'_{\gamma R}}, \quad (4.26)$$

with $y'_{\gamma} = y'_{\gamma L} = y'_{\gamma R}$.

Consequently, we can estimate the 3-D position of a radioactive source $\mathbf{S} = (X, Y, Z)^T$ by means of stereo gamma imaging using the formulas in Equations 4.24, 4.25, and 4.26.

Results of distance retrieval by means of stereo gamma imaging

In a pair of registered images, as explained above, the disparity is the displacement between two corresponding points. If such disparity is computed for each pixel of the images, the resulting matrix is called *disparity map*. In our case, however, we wish to estimate the distance of radioactive sources which typically cover only a portion of the FOV of the gamma camera, or even only a point if the localized source is a radioactive point source. For this reason, we estimate the distance of the surrounding sources by considering only the points of interest in the respective gamma images, which in the case of radioactive point sources correspond (ideally) to the maximum value occurring in the point spread function (PSF) resulting from the deconvolution of a measurement obtained with Eq. 1.6. Nevertheless, if some artifacts are present within the result of a measurement (for example caused by excessive background radiation or low statistics) or if the located radioactive source is not a point source, the coordinates of the image points representing the radiation source of interest might need to be manually chosen or extracted.

Concerning all experiments below discussed, all the reference distances were measured with the laser distance meter Leica Distro D210, *without* considering the space between the external side of the mask and the detector, which is 15.9 mm when using the R7e4 mask. All measurements

below described were performed with such mask. Therefore, for the sake of simplicity, we refer hereinafter to distance *source-to-camera* as the distance between the radiation source of interest and the coded mask of the gamma camera, rather than its detector. Consequently, the distance estimated by the stereo gamma camera is calculated using the formula of Eq. 4.24 and then adjusted accordingly (i.e. by simply subtracting 15.9 mm to each distance measurement).

We performed an initial experiment involving the ^{57}Co planar source with 429 kBq activity already used for some measurements discussed in Chapter 3 (Fig. 3.11). In order to test the stereo gamma imaging technique for small distances, the prototype was placed and oriented so that the centre of the source was at exactly 36 cm from the coded mask of the γ -camera, providing a dose rate at the measurement point of ~ 340 nSv/h. The resulting 3-D profile plots and radiation images for both gamma cameras are shown in Fig. 4.19. As explained above, the 3-D profile plot of the decoded matrix shows the registered counts associated to each Timepix pixel after the deconvolution process.

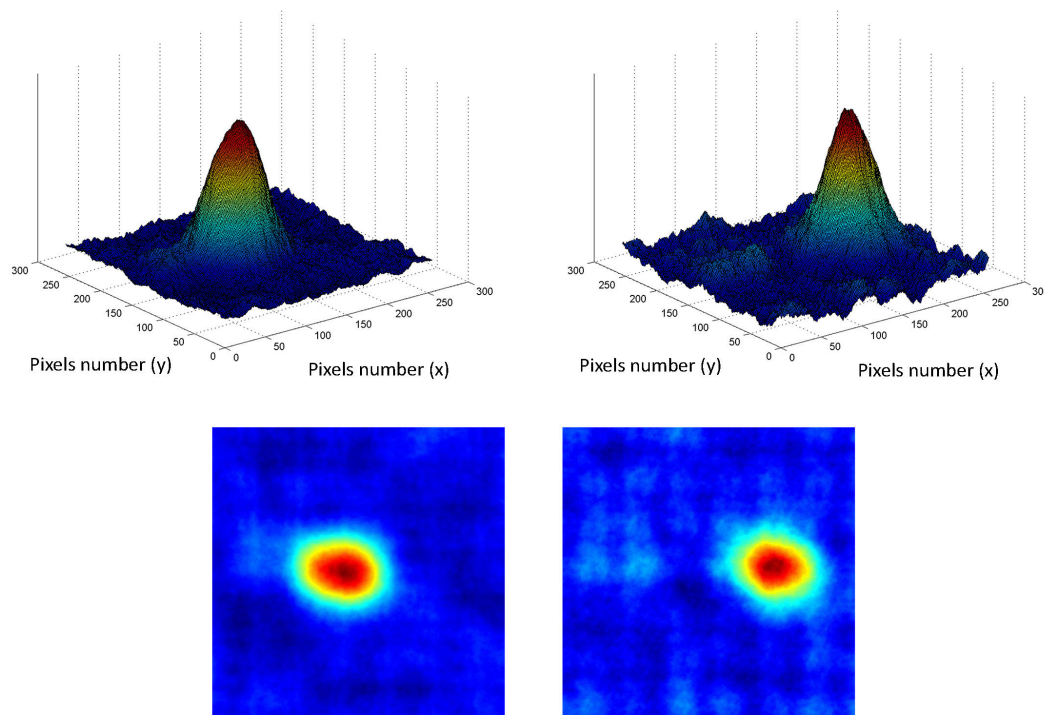


Fig. 4.19: Hotspot profiles and radiation images resulting from a measurement involving a planar ^{57}Co source with activity of 429 kBq, placed at 36 cm from the stereo gamma camera and providing an ambient dose equivalent rate of ~ 340 nSv/h at the measurement point.

To estimate the distance of such source, the disparity was calculated by considering the maximum value occurring in the point spread function in both left and right radiation images. The estimated distance by means of triangulation was 36.2 cm. Consequently, for this specific measurement, the error was 2 mm.

Several experiments have been then carried out with increased source-to-camera distances and considering different scenarios.

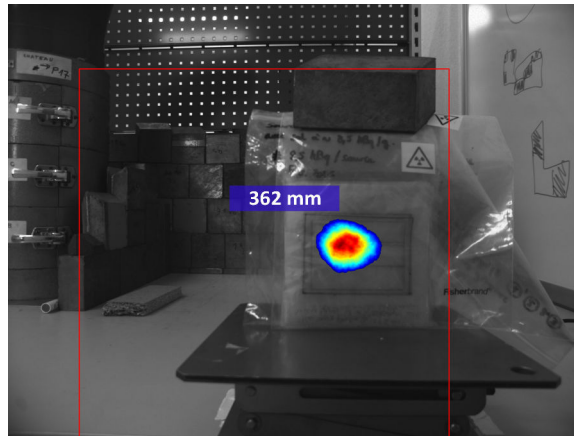


Fig. 4.20: Distance automatically retrieved for a planar ^{57}Co source with activity of 429 kBq and at 36 cm from the stereo gamma camera, providing an ambient dose equivalent rate of ~ 340 nSv/h at the measurement point. The reference distance according to the Leica Disto D210 was 36 cm. The error in this specific case was thus 2 mm.

For example, we performed a measurement with the same ^{241}Am point source of ~ 360 MBq used for the calibration (but in an independent setup) at a measured distance of 125 cm from the prototype, providing a dose rate of ~ 1 $\mu\text{Sv/h}$ at the measurement point.

The distance has been initially computed by retrieving the value from the registered depth image, similarly to how done in the experiments discussed in Section 4.5.1. In this case, the value automatically retrieved from the depth camera was 1245 mm, against a reference measured distance of 1250 mm. For the same experimental setup, the distance estimated by the stereo gamma camera was 1200.1 mm. Therefore, with the first method an error of 5 mm occurred, whereas it was of ~ 5 cm with the stereo gamma imaging method. The results of such experiments are summarized in Figures 4.21 and 4.22.

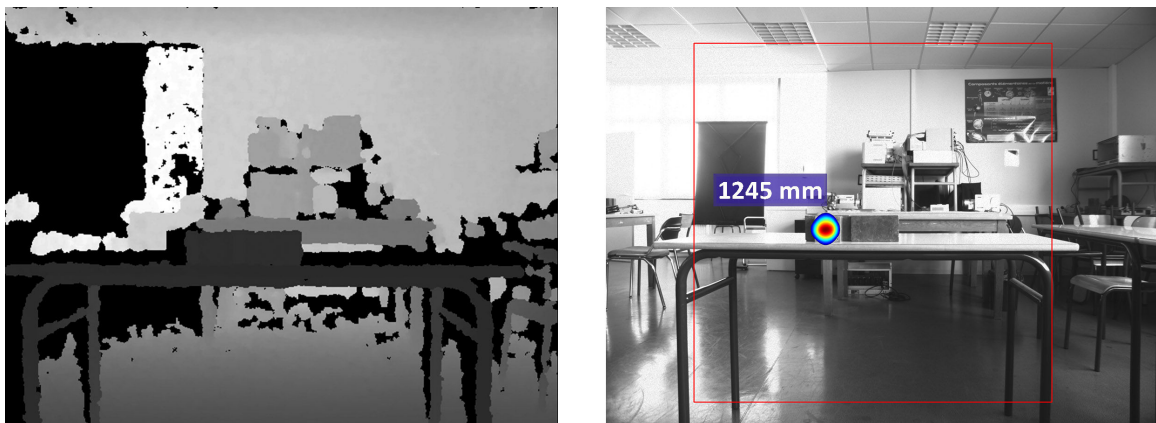


Fig. 4.21: Depth image (on the left) and radiation image superimposed on the respective optical image (on the right). For this measurement, 60 frames of 1 sec shutter time were collected with the left gamma camera, only in mask position. The ^{241}Am source of ~ 360 MBq was placed at 125 cm from the prototype. A value of 124.5 cm was automatically retrieved from the registered depth map. The error was thus 0.5 cm.

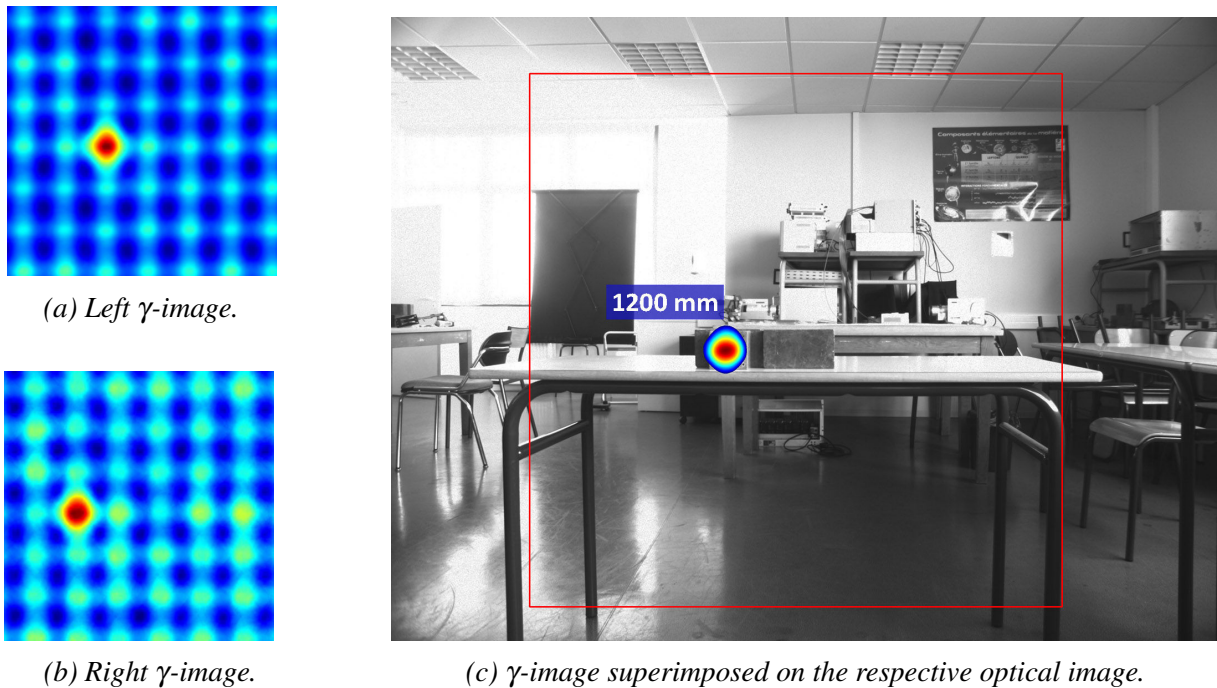


Fig. 4.22: Results concerning the position and the estimated distance of an ^{241}Am source of ~ 360 MBq, placed at 125 cm from the stereo gamma camera prototype. The left radiation image (a) is the result of 60 collected frames of 1 sec shutter time in mask mode, while for the right radiation image (b) 90 frames were collected with the same shutter time. A value of 120.01 cm was automatically retrieved by means of stereo gamma imaging. The error was therefore ~ 5 cm.

In order to evaluate the proposed stereo gamma imaging method and compare it with the values retrieved from the registered depth images, similar experiments have been performed by placing the ^{241}Am source at several measured distances, such as 250 cm, 300 cm, and 400 cm. A summary of the respective results is provided in Section 4.5.4, in Table 4.1. An example of such measurements is provided in Figures 4.23 and 4.24, where the ^{241}Am point source was placed at 300 cm from the prototype, and 120 frames of 1 sec shutter time were collected with both γ -cameras, only in mask position.

At three metres of distance between the instrument and the radioactive source, a distance of 292.7 cm was automatically retrieved by means of stereo gamma imaging, with an error of thus 7.3 cm. For the same experiment, the value retrieved from the registered depth image was 303.7 cm. Therefore, in this case the error was of 3.7 cm.

4.5.3 Integration of structured-light techniques and stereo gamma imaging for portable gamma cameras

As mentioned above, one of the main motivations behind the study and development of a stereo gamma imaging method concerns those situations where an object occludes the radioactive source respect to the gamma camera, in which case the depth image inevitably returns a misleading result,

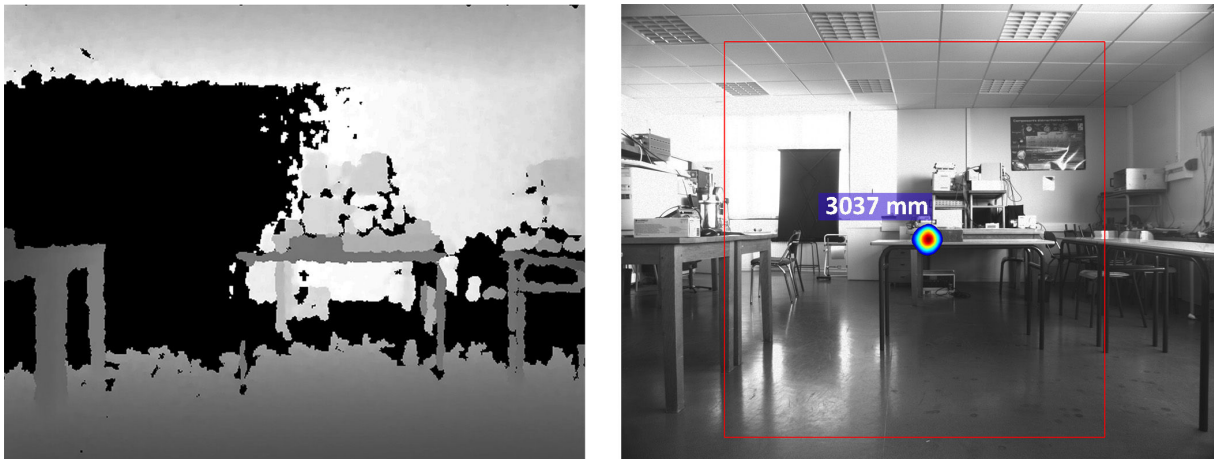


Fig. 4.23: Depth image (on the left) and radiation image superimposed on the respective optical image (on the right). For this measurement, 120 frames of 1 sec shutter time were collected, only in mask position. The ^{241}Am source of ~ 360 MBq was placed at 300 cm from the prototype. A value of 303.7 cm was automatically retrieved from the registered depth map. The error was therefore 3.7 cm.

even if it was accurately registered with the radiation image. For this reason, we have simulated such kind of scenario by placing the above ^{241}Am source in front of a wall and the prototype on the other side of the same wall, at a measured distance of 190 cm and with the two γ -cameras pointed towards the source (see Figures 4.25 and 4.26).

The decoded matrix resulting from the measurement collected with the right gamma camera clearly presents a number of artifacts in this specific case, for which no measurements were performed in antimask position with both γ -cameras. However, such artifacts do not prevent the possibility of unequivocally recognizing the source and retrieving therefore the coordinates of the respective centre.

In such scenario, the registered depth camera returned a value of 840 mm from the corresponding coordinates of the depth map, which was evidently referred to the distance of the wall respect to the camera. Conversely, by computing the position of the radioactive source via triangulation, the source-to-camera distance was estimated to be 186.4 cm, with an error of ~ 3.6 cm. Although such error is higher compared for example to that of the result shown in Fig. 4.20, this result clearly indicated that the radiation emitting surface was behind the wall.

In other terms, if the distance retrieved by the two methods considerably differs, it is possible to autonomously determine (and thus inform the operator) that the located radioactive source is occluded by the object(s) in front of the instrument and, moreover, the estimated actual distance of the source.

The threshold for automatically determining the presence of an occluding object is a function of the expected accuracy concerning the estimation of the distance by the stereo gamma camera, which in turn is a function of the source-to-camera distance. Such aspect is discussed in more detail in Section 4.5.4.

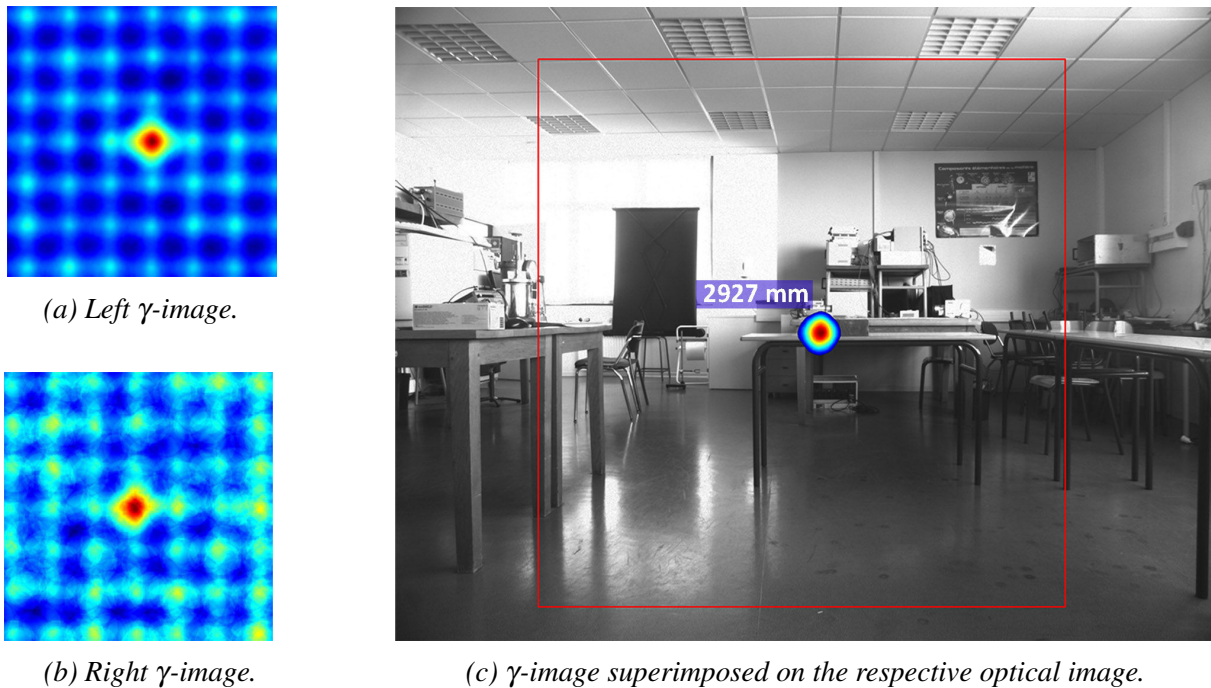


Fig. 4.24: Results concerning the position and distance of an ^{241}Am source of ~ 360 MBq, placed at a measured distance of 300 cm from the prototype. 120 frames of 1 sec shutter time were collected in mask mode with each γ -camera. A value of 292.7 cm was automatically retrieved by means of stereo gamma imaging, with an error of 7.3 cm.



Fig. 4.25: (a) An ^{241}Am source of ~ 360 MBq activity placed behind a wall while (b) the prototype is on the other side of the same wall, pointed at the source at a total measured distance of 190 cm, and providing an ambient dose equivalent rate of ~ 320 nSv/h at the measurement point.

Another experiment regarding occluded radiation sources was performed by placing a ^{137}Cs source of 329 MBq activity inside a barrel with diameter of 60 cm. The barrel was placed so that the centre of its horizontal axis was at 280 cm from the head of the prototype. The ^{137}Cs source was then carefully placed inside the barrel (at the centre of its horizontal axis).

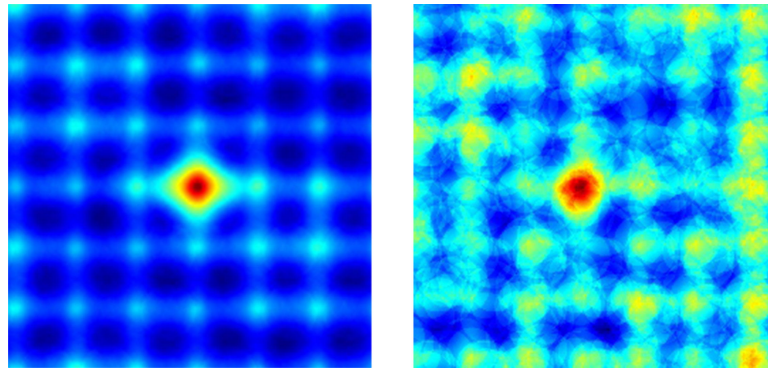


Fig. 4.26: Left and right radiation images generated by the stereo gamma camera. For this measurement, 180 frames of 1 sec shutter time were collected with each detector, only in mask position.

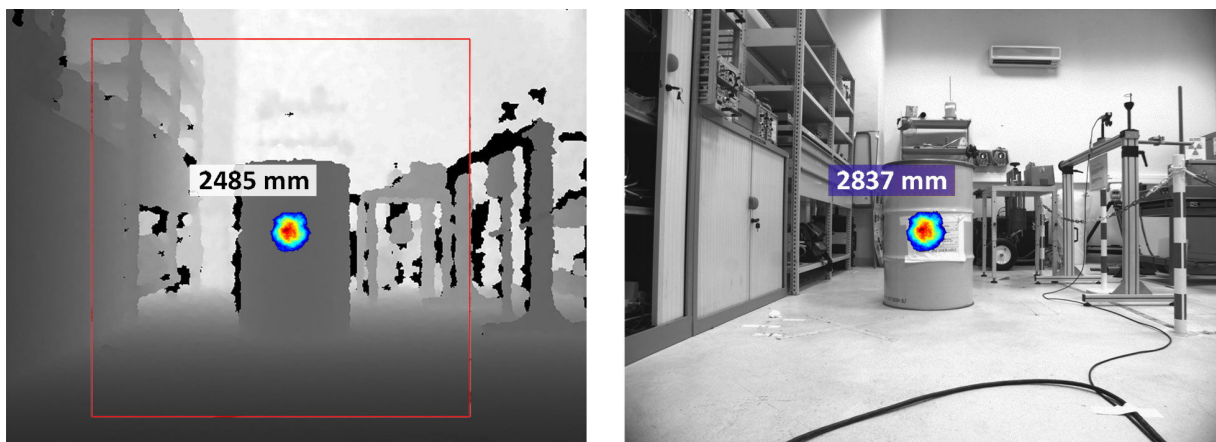


Fig. 4.27: A ^{137}Cs source of 329 MBq activity placed inside a barrel with diameter of 60 cm. The barrel was placed so that its horizontal centre was at 280 cm from the prototype. The source was then carefully placed at such distance inside the barrel. For this measurement, 300 frames of 1 sec shutter time were collected with both gamma cameras, in mask and antimask positions. In the left view, the distance retrieved from the depth map at the location of the centre of the located source is displayed. In the right view, the distance retrieved by means of stereo gamma imaging is displayed (Laboratoire simulation et techniques de démantèlement nucléaire, CEA Marcoule).

Similarly to the previously discussed experiment, where the radiation source was occluded by a wall, also in this case the distance could be not correctly estimated by the depth camera of the prototype. For scenarios of this kind, the proof of concept supports a view called *dual view* (Fig. 4.27), which is automatically shown depending on the threshold above mentioned and where the radiation image is displayed in two different views. In the first (left) view, the localized radiation source is accurately registered and superimposed on the associated depth image, and the distance retrieved from the depth map is displayed. In the second (right) view, the radiation image is registered and superimposed on the respective optical image, and in this case the distance is retrieved by means of stereo gamma imaging and displayed.

As shown in Fig. 4.27, the value retrieved from the depth map considerably differs from actual distance of the source, since the latter is located at the centre of the barrel. For this specific

experiment, a value of 283.7 cm was automatically retrieved by using the implemented stereo gamma imaging technique. The error was thus 3.7 cm.

4.5.4 Accuracy evaluation of the stereo gamma camera

In Sections 4.5.2 and 4.5.3, a series of experiments conducted with the proof of concept developed for this study has been discussed. The prototype has been placed at varied positions respect to a radiation source, and the distance between the camera has been evaluated accordingly.

In our context, the accuracy can be defined as the error between the real and estimated distances of the radioactive source with respect to the camera. We refer to such error as ΔZ . On the other hand, the geometric resolution depends on the calculation of the disparity, and it can be interpreted as the smallest distinguishable magnitude, in mm/pixel, at a given source-to-detector distance.

The theoretical error concerning the distance estimated with the proposed stereo gamma camera can be computed as follows.

$$\Delta Z = \frac{b d}{x'_{\gamma L} - x'_{\gamma R}} - \frac{b d}{(x'_{\gamma L} - x'_{\gamma R}) + \varepsilon_d} = \frac{Z^2 \varepsilon_d}{b d + Z \varepsilon_d}, \quad (4.27)$$

where:

- b is the distance between the centres of the two detectors/masks (baseline),
- d is the distance between the external side of the coded mask and the detector,
- $x'_{\gamma L} - x'_{\gamma R}$ is the disparity between the positions of the two corresponding points representing a radioactive source S and reconstructed, respectively, in the left and right radiation images (see Eq. 1.6), and
- ε_d is the error concerning the disparity computed from the two radiation images.

By observing the relation at the end of Eq. 4.27, it can be noticed that if b and d are constant and ε_d is such that $Z \varepsilon_d \ll b d$, the distance error grows quadratically with the source-to-detector distance:

$$\Delta Z \approx \frac{Z^2 \varepsilon_d}{b d}. \quad (4.28)$$

The error ε_d depends in turn on two important factors, that is, the resolution of the sensors used and the correspondence error (i.e. the accuracy of the estimation of the coordinates of the corresponding points). In our case, the point of interest (i.e. the radiation source whose distance we want to calculate) needs to be chosen depending on the context. In the easiest scenario, it could be the centre of a source, if the radiation emitting object is a radioactive point source. Otherwise, it could be a specific point within an extended radioactive source, such as a pipe or a barrel. The accuracy of the coordinates of the point of interest inherently depends on the quality of the

Table 4.1: Distances retrieved by means of the calibrated depth sensor and the stereo γ -camera proof of concept

Source	Activity	Reference Distance*	Distance depth map	Δ 1 st approach	Distance via stereo	Δ 2 nd approach	Occluded
^{57}Co	429 kBq	36 cm	-	-	36.2 cm	0.2 cm	No
		50 cm	-	-	52.5 cm	2.5 cm	No
^{241}Am	360 MBq	125 cm	124.5 cm	-0.5 cm	120.0 cm	-5 cm	No
		190 cm	84 cm	-106 cm	186.4 cm	-3.6 cm	Yes
		200 cm	204.6 cm	4.6 cm	184.7 cm	-15.3 cm	No
		207 cm	204.5 cm	-2.5 cm	198.1 cm	-8.9 cm	No
		230 cm	233.3 cm	3.3 cm	223.8 cm	-6.2 cm	No
^{137}Cs	329 MBq	280 cm	248.5 cm	31.5 cm	283.7 cm	3.7 cm	Yes
^{241}Am	360 MBq	300 cm	303.7 cm	3.7 cm	292.7 cm	-7.3 cm	No
		400 cm	381.6 cm	-18.4 cm	376.2 cm	-23.8 cm	No

*Measured by means of a laser meter (Leica Disto D210) and considering the thickness of the occluding objects, if any.

measurement itself, but also on the spatial (angular) resolution that can be achieved by the gamma camera. Concerning the latter, although competitive when compared to portable gamma cameras used for nuclear facilities, the current resolution of the Timepix sensor can be considered quite low in comparison to that of the (optical) cameras typically used for stereo vision applications.

To provide an overall idea of the accuracy achievable by the proof of concept developed and to compare the two approaches proposed, in Table 4.1 a summary of the measurements performed is provided.

A solution for decreasing the average error ΔZ in the case of the stereo gamma camera and improving its accuracy at longer distances is increasing the baseline, which in the case of the prototype is 92 mm. However, the drawback of a larger baseline is that the distance where the FOVs of the left and right γ -cameras begin to overlap also increases, extending therefore also the minimal distance that is possible to estimate with the stereo gamma camera. Such minimal distance is typically referred to as Z_{near} , and it is:

$$Z_{near} = \frac{2b}{\tan(\theta_{FOV})}. \quad (4.29)$$

Figure 4.28 plots the theoretical calculated disparity (in pixels) between corresponding points in two given radiation images as a function of the estimated distance values (in mm), assuming the pixel size of the Timepix sensor, which is 55 μm , the baseline b of the stereo camera prototype (92 mm), and a distance d between the coded mask and the detector of 15.9 mm.

It can be observed in the plot of Figure 4.28 that, in our context, the disparity rapidly decreases at only few pixels for distances greater than 4 or 5 metres. That is, at these ranges, an error of only 1 or 2 pixels in the calculation of the disparity leads to significant errors concerning the estimation of the source-to-detector distance. For this reason, the developed prototype may be

Fig. 4.28: Theoretical calculation of the disparity of two corresponding points in two given radiation images as a function of the distance values (in mm).

used for estimating ranges up to 4 or 5 metres in its current configuration. For larger distances, the accuracy can be improved by simply increasing the mask-detector distance d (obtaining, moreover, also a higher angular resolution) and/or the baseline b of the γ -cameras.

To provide a more specific and quantitative idea of the average error regarding the developed instrument, the theoretical error ΔZ has been computed as a function of several source-to-detector distances, up to 10 metres. Moreover, such relation has been calculated for different assumed baselines, as the distance between the centres of the two gamma cameras is the easiest modification that may be made in future versions of the device. The summary of the relation between the error ΔZ , the distance of the radioactive source, and the baseline of the prototype is shown in Fig. 4.29.

4.6 Volumetric representation of radioactive hotspots

As thoroughly explained in [199], given two sets of 3-D points in two different coordinate systems, and representing the geometric shape of the same object, *3-D shape registration* consists in estimating the optimal rotation and translation which align (i.e. register) the two sets minimizing their distances via a mean-square distance metric.

In general, to generate a complete 3-D model of an object (or scene) of interest, the following steps are necessary:

1. Data acquisition
2. Registration between the generated views
3. Integration (fusion) of views

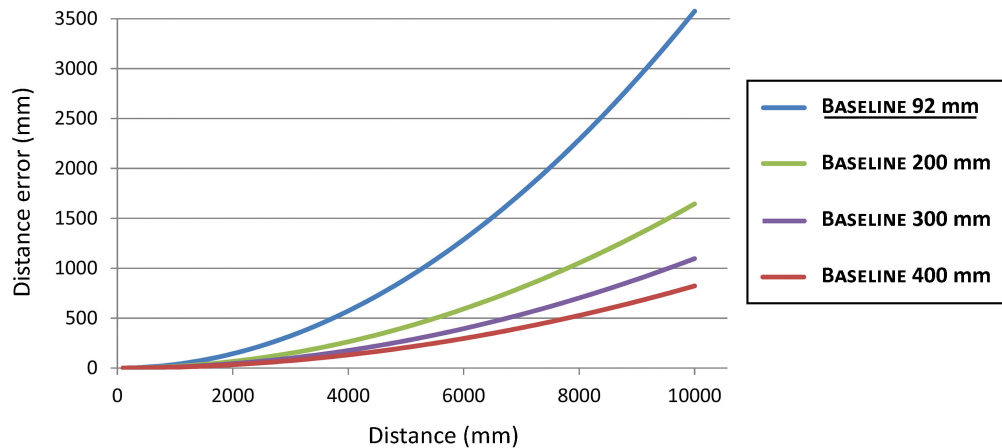


Fig. 4.29: Error ΔZ , in mm, as a function of the source-to-detector distance and the baseline of the stereo gamma camera (the baseline of the prototype built for this study is 92 mm).

4. Data representation and visualization

More specifically to our context, in Section 4.3.3 we projected the 3-D data points representing a radioactive object as sensed by all cameras of the prototype (i.e. optical, depth, and gamma cameras) into a common 3-D coordinate frame.

When superimposing a radiation image, for example onto the respective optical image, we reprojected such 3-D points into the optical camera coordinate frame, using the intrinsic and extrinsic parameters estimated by means of the algorithm described in Section 4.4.2.

However, to generate the 3-D shape of objects of interest, in this case we use the same 3-D data set obtained to create a multimodal *point cloud*⁸ representation of the radioactive surface under study. Therefore, the developed proof of concept allows the registration in the three-dimensional space of the radiation images with the multiple depth maps obtained with the *calibrated* Asus Xtion and optical camera of the prototype.

By employing the Robot Operating System (ROS) [200], a widely known open source framework for robot software development, and the libraries provided by PCL (Point Cloud Library) for point cloud processing [201, 202], the calibrated depth and optical cameras integrated within the prototype continuously track and store their 6 degrees-of-freedom pose respect to the scene, generating the respective coloured point cloud. Figure 4.30 shows an example acquired and reconstructed with the prototype in a laboratory of the CANBERRA site, in Montigny-le-Bretonneux.

In order to reconstruct the geometries of the surrounding scene and estimate the 6-DOF pose of the cameras, the implementation of the proof of concept is mainly based onto a descriptor for 3-D point cloud data called *Point Feature Histogram* (PFH) [201, 203]. Point Feature Histograms allow the registration of the views using a robust variant of the popular ICP (Iterative Closest Point) algorithm [199], and they are invariant to position, orientation, and point cloud density.

⁸A point cloud in a 3-D coordinates system can be defined as a collection of data points representing the shape of a given object.



Fig. 4.30: 3-D coloured point cloud representing a CANBERRA laboratory in Montigny-le-Bretonneux, acquired and processed with the prototype. In this example, no radiation sources were present.

The interested reader is referred to [204, 203, 201] for an exhaustive discussion of the theory and computation model of such descriptor.

4.6.1 Data acquisition for 3-D gamma point clouds

The 3-D model shown in Fig. 4.30 was acquired in less than one minute. Data captured by means of the RGB and depth cameras can be rapidly acquired from multiple perspectives, as both of these sensors are able to generate a number of frames per each second. More specifically, in the case of the optical sensor used for the prototype⁹, it is possible to acquire up to 6 frames per second (fps) of size 2592×1944 pixels, whereas the Asus Xtion camera allows the acquisition of up to 30 depth images of size 640×480 pixels.

On the other hand, as widely discussed in Chapter 2 and Chapter 3, a measurement involving a radiation source may require dozens of seconds or also several minutes, depending on the overall radiological conditions at the measurement point. Although such performances can be considered satisfactory in the context of gamma imaging, they inherently allow the acquisition of little geometrical information compared to the other cameras integrated within the prototype.

Moreover, in our case, we performed the measurements and obtained only two radiation images for each experiment, respectively from the left and right γ -cameras. This was intentional in the case of point sources. As originally defined by Euclid: “A *point* is that which has no parts, or which has no magnitude”. Therefore, in the context of 3-D shape registration and reconstruction, performing several measurements from different perspectives of a radioactive point source cannot provide, of course, useful information concerning its shape. However, as shown and discussed in Section 4.5.2, localising a radioactive point source from two different perspectives with the stereo

⁹As a reminder, the optical camera used for the prototype is the *The Imaging Source DFM 72BUC02-ML*, which is intentionally the same camera used with the iPIX system.

gamma camera provides, indeed, useful information concerning the *position* of the radioactive point source in the 3-D space. For this reason, the prototype considers both the approaches proposed in the previous sections for estimating the 3-D position of a radioactive source to be registered within each point cloud.

Three-dimensional data structure

The dense point cloud generated by the proof of concept is represented and stored via the *PLY polygon file format* [205], a format for storing graphical objects described as a collection of polygons. The PLY format has been chosen as it is widely supported by the Point Cloud Library, and it can be read by a number of *computer-aided design* (CAD) softwares, useful for both visualization and post processing purposes.

As summarised in [205], a typical PLY object definition is simply a list of (x, y, z) triples for vertices, and a list of faces described by indices. Therefore, a PLY file describes an object as a collection of vertices, faces, and other possible elements or properties, such as colour, texture coordinates, transparency, or range data confidence.

The structure of a typical PLY file is as follows:

```
Header
Vertex List
Face List
(lists of other elements)
```

The header consists of a description of the remainder of the file for each element type, including its name (e.g. "edge"), how many of such elements are in the object, and a list of the properties associated with the element. After the header, there is a list of elements for each element type, presented in the order described in the header.

The interested reader is referred to [205] for an exhaustive description of the PLY format and several examples of simple shapes, such as cubes or custom-defined elements.

4.6.2 Multimodal fusion with the 3-D position of radiation sources

To merge radiation information into the 3-D scene, the gamma images were acquired and registered with the respective depth and optical images at the end of the point cloud acquisition (i.e. at the last pose), using the calibration information obtained as described and shown in Sections 4.3.3 and 4.5, respectively.

The sparse distance information concerning the radioactive source can be either estimated from the disparity calculated from the left and right gamma images of the stereo gamma camera, or from the radiation image registered with the associated depth map. At the current state of development of the proof of concept, this choice is to be made manually by adjusting dedicated parameters in the implementation code.

The last viewpoints so obtained are then fused with the rest of the scene in a similar manner of the previous ones. The only difference is that the colour intensities associated to the pixels acquired via the optical camera are replaced by the colour intensities associated to the radiation image in the corresponding overlapping 3-D positions, where the resolution of the associated (x, y, z) triples is limited by the expected distance resolution of the gamma cameras, as shown in Section 4.5.4.

Such procedure results into a global radiation surface-based representation. Fig. 4.31 shows a *preliminary* result obtained and stored in PLY format, and rendered via the MeshLab software [206]. The results shown in this figure were derived from the same experimental setup described in Chapter 3 (Fig. 3.13).

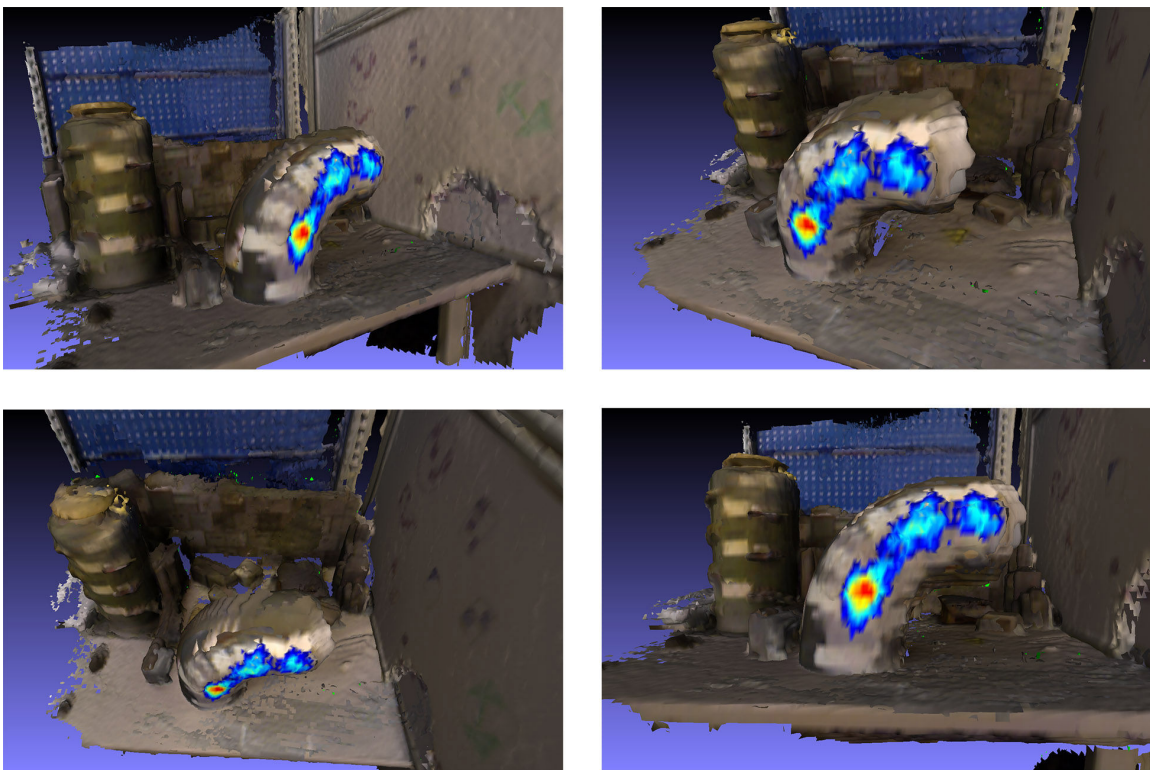


Fig. 4.31: Point cloud generated by the prototype and rendered via MeshLab, representing the results obtained with mask R7e4 and by placing several ^{57}Co sources adjacently, in order to simulate a pipeline elbow with 1716 kBq of total activity, at an average distance of 64 cm from the gamma camera. The associated ambient dose equivalent rate at the measurement point was ~ 280 nSv/h (experiment performed at the CEA LIST laboratory, at Saclay).

Although being preliminary results, we were able to obtain the 3-D shapes of all the objects in the scene of interest, along with the associated information regarding the radioactive hotspots surrounding the prototype. In the shown images, the MeshLab 3D mesh processing software was used. However, as PLY supports the ASCII encoding standard, each generated point cloud can be read and manipulated via a number of softwares or programming languages, including MATLAB or Python, allowing therefore the application of the post processing functionalities included within software or environment used.

For example, as shown in Fig. 4.32, it is possible to easily extract metric information concerning both the physical objects and the radioactive surfaces from the point clouds obtained.

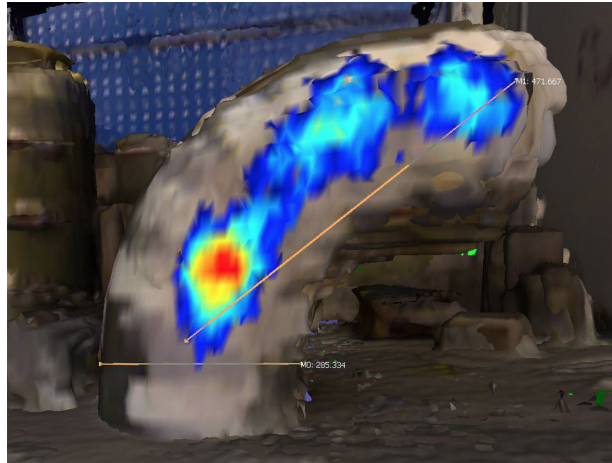


Fig. 4.32: Portion of the multimodal point cloud of the radioactive pipe as rendered by MeshLab. The little orange arrows and the respective quantities (expressed in mm) are displayed by MeshLab when extracting metric information from the scene under study.

In the case of the MeshLab software, this is achieved by simply activating the dedicated functionality from its GUI, and by clicking with a mouse twice in the two points to be measured (depending on the software used, such procedure may slightly change).

The 3-D models integrating radiological information can be useful also for those scenarios where sources are occluded by some object(s) respect to the gamma camera. An example of this kind has been shown in Section 4.5.3, in Fig. 4.27, where we placed a ^{137}Cs source of 329 MBq activity inside a barrel with diameter of 60 cm. With the same experimental setup, we also acquired the respective point cloud model. See Fig. 4.33.

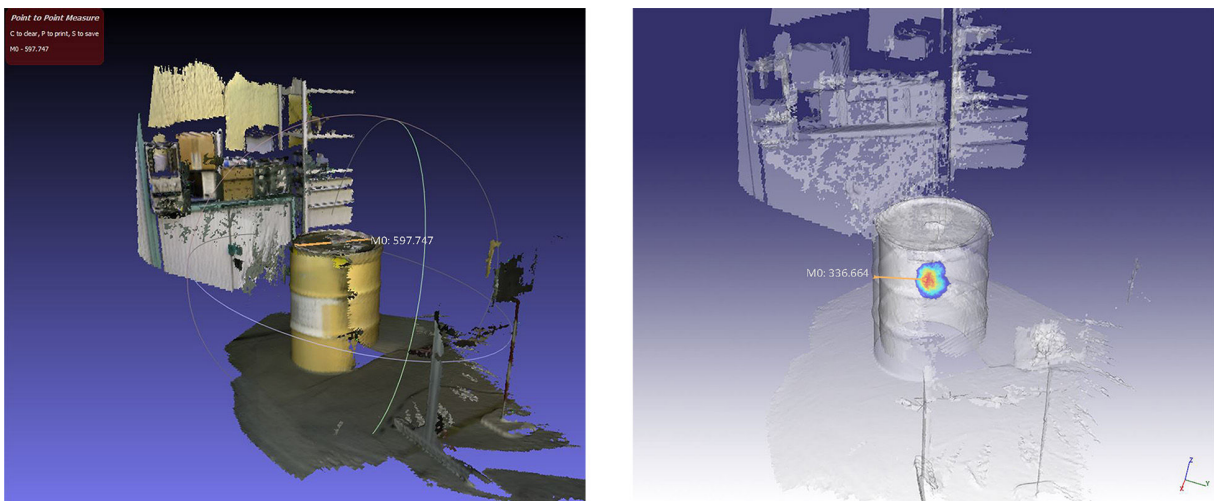


Fig. 4.33: Two point clouds generated by the prototype and rendered by MeshLab regarding a ^{137}Cs source of 329 MBq activity, placed inside a barrel with diameter of 60 cm. The experiment was conducted at the CEA Marcoule laboratory (Laboratoire simulation et techniques de démantèlement nucléaire).

As explained in Section 4.5.3, the barrel was placed so that its horizontal centre was at 280 cm from the prototype. The source was then carefully placed at such distance from the instrument, but inside the barrel. For this measurement, 300 frames of 1 sec shutter time were collected with both gamma cameras, in mask and antimask positions. In this example, on the left it is shown the model with the opacity of each element at 100%. On the right view, for illustration purposes, the same barrel is rendered by setting a transparency of 50% and without displaying the RGB information captured by the optical camera. The distance between the centre of the located source and the surface of the barrel is retrieved and displayed by simply clicking twice in the two points whose distance needs to be measured.

As these examples show, in the context of the development of a proof of concept, the Asus Xtion demonstrated a significant versatility when reconstructing the 3-D model of the surrounding environment, especially considering its low cost and high accessibility. However, depending on the light conditions and geometrical aspects of the scene to be reconstructed, multiple point clouds had to be acquired in some cases. For example, the point clouds shown in Fig. 4.33 are the result of three different models consecutively acquired, and then manually aligned by means of third parties software, such as MeshLab in our case.

Combined with the source-to-detector distance retrieved by the two approaches proposed with this study, the fusion of the 3-D position of the located radioactive sources with point clouds have several immediate applications. For example, the corresponding results can be used for providing further inputs regarding the analysis of the geometries of the environment and the respective radiological characterization, using Monte Carlo transport physics codes, such as MCNPX or FLUKA.

4.7 Conclusions

A portable γ -imaging platform has been developed, able to automatically compute the 3-D position of the radiation sources located within its field of view as well as their distance source-to-detector. The 3-D position of surrounding radiation emitting objects is estimated by means of two approaches: 1) an accurate registration between the depth maps computed by a calibrated depth camera and the radiation images obtained with a γ -camera, and 2) by using triangulation with the radiation images generated by a stereo γ -camera, allowing the estimation of the distance even for radioactive sources located behind an occluding object (e.g. a wall).

In order to calibrate all sensors involved, a multimodal calibration procedure has been designed and tested. Such procedure is flexible, as it uses an experimental phantom intentionally easy to build and inexpensive, allowing to perform all measurements using a single radioactive point source. Additionally, by carrying out such procedure, an optimal superimposition has been achieved, allowing the registration between optical images and the associated gamma images with sub-pixel accuracy.

Moreover, a preliminary technique for generating point clouds integrating the 3-D position of the located radioactive sources has been proposed. The corresponding results can be used for providing further inputs regarding the analysis of the geometries of the environment and the respective radiological characterization.

The obtained results validate the modeling of a deconvoluted signal acquired by means of a coded aperture γ -camera as an image captured by a pinhole perspective camera. This confirms that radiation signals and coded aperture γ -cameras can be treated as any other modality captured by pinhole-equivalent cameras such as the ones based on optical or depth sensors.

Future work includes calibrating the gamma camera with a type of depth sensor allowing longer range capabilities (e.g. Time-of-Flight [207]), and improving the accuracy and the resolution error of the stereo gamma camera by increasing either the distance mask-detector or the baseline of the two γ -cameras.

A perspective that can be also envisaged concerns the development of methods for integrating, directly, the 3-D radioactive point clouds generated by means of the proposed approaches with the geometries of Monte Carlo transport physics codes, such as MCNPX or FLUKA.

Furthermore, future perspectives also involve the accurate visualization of measured radiations with augmented reality technologies, such as head-mounted displays (HMD).

Chapter 5

General conclusions and perspectives

In this thesis a gamma camera capable of retrieving the 3-D position of the surrounding radioactive sources has been presented.

Current portable gamma imaging systems provide only the two-dimensional position regarding the located sources, whereas the methods proposed allow the estimation of the distance between the instrument and each hotspot, and, moreover, the localization in the 3-D space also when an occluding object is present between the radiation source and the gamma camera.

The first part of this work consisted in collaborating with the CANBERRA team to both the development of the software of the iPIX gamma camera and the experimental characterization of its performances. The main results of the latter have been partially documented in Chapter 2 and published in [10].

In view of the results obtained with ISO narrow X-ray beams at the Karlsruhe Institute of Technology (KIT) at varied acceleration voltages and currents, where I performed the measurements with colleagues of the iPIX CANBERRA team, we have observed that the Timepix shutter time is a critical parameter for an effective localization of radioactive hotspots. According to such results, the iPIX is able to autonomously select, among other parameters, the appropriate shutter time, in order to avoid signal distortions on the Timepix detector due to pulse pile-up and/or summation effects.

Results have shown that the iPIX camera has an angular resolution between 2.5° and 6.0° (depending on the coded mask used), and a significant high response sensitivity at low energies. For example, an ^{241}Am source providing an estimated dose rate of only 10 nSv/h at the measurement point was unambiguously located within 4 sec of data collection time. Similar tests have been also conducted with a ^{137}Cs and a ^{60}Co source (providing 100 nSv/h and 1 $\mu\text{Sv/h}$ dose rates at the measurement point, respectively); in both cases the sources were localised with less than 150 sec of data collection time.

The iPIX experimental characterization has demonstrated that the mask R7e8 can be applied at almost the whole energy range of interest (10 keV - 1.5 MeV), whereas the mask R13e2 is limited to low photon energies only (e.g. 59 keV γ -rays of ^{241}Am , whose detection usually indicates the

presence of plutonium in nuclear wastes). As an intermediate application, mask R7e4 is able to localise radioactive sources in the medium photon energy range of ^{137}Cs .

Finally, the iPIX dose rate response curve was analysed with several standard ^{137}Cs sources of different activities, showing a linear behaviour over a wide range covering nearly 8 decades (10^{-6} – 10^1 Sv/h).

The same detector hardware configuration and localisation capabilities of the CANBERRA iPIX system, documented in Chapter 2, have represented the starting point of the algorithms which I proposed in Chapter 3 and Chapter 4.

As a known disadvantage of the coded aperture imaging approach is its limited field of view, I developed the EduPIX prototype, a coded aperture gamma camera allowing the localisation of the main surrounding radioactive objects with a FOV of 360° . The EduPIX has been developed in the context of EDUSAFE, a Marie Skłodowska-Curie Actions project, coordinated by CERN, as integral part of the personnel safety system used at the Large Hadron Collider.

In Chapter 3 the main aspects of the EduPIX prototype are therefore described along with the associated stitching algorithm I proposed for generating panorama γ -images. Such method preserves the geometrical coherency also of those radiation emitting objects that, if localised within only one measurement, may exceed the FOV of the camera (e.g. long pipes in nuclear power plants). As its use at the LHC is foreseen in environments that can be potentially highly radioactive, the procedure for obtaining panoramic images has been completely automated with both optical and radiation images, using a motorized and programmable pan-tilt device for accurate positioning.

The implemented algorithm mainly uses ORB, a binary feature descriptor and detector, and a probabilistic model to compute homographies for the overlapping captured optical images, and it applies, subsequently, the same homographies to their corresponding radiation images.

To validate the method proposed, we simulated, in laboratory conditions, a scenario where multiple radioactive hotspots surround an operator. As a result, all radiation images were located with a FOV of 360 degrees without significant artifacts, and they were coherently superimposed on the stitched final optical image.

The EduPIX platform was also tested at the LHC, at CERN, in the context of an EDUSAFE testing campaign. We performed the measurements in front of the ATLAS beam pipe, localising the position of the most significant surrounding radioactive hotspots and generating, accordingly, a panoramic gamma image with a complete 360° horizontal FOV.

All results obtained with the EduPIX are displayed via a dedicated web application and user interface specifically developed for the prototype, allowing the rendering of panoramic images in spherical coordinates (θ, ϕ) and the creation of interactive virtual tours. More specifically, the final user can change scenes (i.e. spherical superimposed images) by simply clicking (or tapping, when using a touchscreen) on a given position of the obtained panorama images, which is pointed out by a landmark icon. By using any web-browser supporting HTML5, such functionality potentially allows the creation of virtual tours that can be used, for example, for quickly navigating

entire nuclear power plants and radiation facilities while displaying the main located radioactive hotspots.

The panoramic EduPIX gamma camera has been developed to overcome the limited FOV of the previous gamma cameras based on the coded aperture technique. However, also the EduPIX provides only directional information (2-D) concerning the located radiation sources, which is the main limitation that motivated the present study concerning current portable gamma cameras for industrial facilities. For this reason, the prototype evolved into a second portable γ -imaging system, able to automatically compute the 3-D location of the radiation sources located within its field of view as well as their distance source-to-detector.

The 3-D position and distance of the surrounding radiation emitting objects are estimated by means of two proposed approaches:

- An accurate registration between the depth maps computed by a calibrated depth camera and the radiation images obtained with a coded aperture γ -camera. The resulting system is thus able to retrieve the distance of radioactive hotspots via a *pixel-wise mapping* between gamma and depth images.
- By using triangulation with the radiation images generated by a stereo γ -camera, allowing the estimation of the distance even for radioactive sources located behind an occluding object (e.g. a wall).

The two techniques have been compared in terms of feasibility and accuracy. The corresponding results showed that while in a few cases the first approach yields more accurate results, the stereo gamma imaging method can be more flexible, due to the possibility of providing the distance of the located sources with acceptable accuracy also in case of occluding objects between the hotspot and the instrument. Moreover, by increasing the baseline of the stereo gamma camera, its maximum measurable range can be easily extended.

The integration of the two methods allows the prototype to also determine, autonomously, if an occluding object is present between the source and the instrument. More specifically, if the distance retrieved by the two approaches considerably differs, the algorithm determines if the located radioactive source is occluded by the object(s) in front of the gamma camera. The threshold for automatically determining such presence is a function of the expected accuracy of the distance estimated by the stereo gamma camera, which in turn, as shown in Chapter 4, is a function of the actual distance of the source. Such functionality can help identifying, for example, surrounding radioactive hotspots occluded by large objects during decommissioning or verification procedures of nuclear power plants to be dismantled.

The accurate registration between all depth maps and radiation images has been achieved by calibrating the cameras involved. For this purpose, a multimodal calibration procedure has been designed and tested. Such procedure is flexible, as it uses an experimental phantom intentionally easy to build and inexpensive, and it requires only a single radioactive point source, which in our case was a ^{241}Am point source of ~ 360 MBq activity.

Additionally, by carrying out such procedure, an optimal superimposition between optical and gamma images has been achieved, as the two types of images could be registered with sub-pixel accuracy.

Furthermore, a preliminary technique for generating point clouds integrating the 3-D position of the located radioactive sources has been proposed. The corresponding results can be used for providing further inputs regarding the analysis of the geometries of the environment and the respective radiological characterization.

From a more general point of view, the obtained results validate the modeling of a reconstructed signal acquired by means of a coded aperture γ -camera as an image captured by a pinhole camera. This confirms that radiation signals and coded aperture γ -cameras can be treated as any other modality captured by pinhole-equivalent imaging systems, such as the ones based on optical or depth sensors.

Future work includes calibrating the gamma camera with a type of depth sensor allowing longer range capabilities (e.g. Time-of-Flight), and improving the accuracy and the resolution error of the stereo gamma imaging system by using gamma cameras with higher spacial resolution, or, simply, by increasing either the distance mask-detector or the baseline of the two detectors used.

A perspective that can be also envisaged concerns the development of methods for integrating and registering the 3-D radioactive point clouds generated by the prototype with the geometries of Monte Carlo transport physics codes, such as MCNPX or FLUKA.

Finally, future work involves the accurate visualization of measured radiations with augmented reality technologies, such as head-mounted displays (HMD).

References

- [1] International Atomic Energy Agency. Radiological Characterization of Shut Down Nuclear Reactors for Decommissioning Purposes. Technical Report 389, IAEA, 1998.
- [2] T. Nonova, D. Stankov, A. Mladenov, and K. Krezhov. Radiological Characterization Activities During The Partial Dismantling Of The IRT–Sofia Research Reactor Facilities. *Romanian Journal of Physics*, 59(9-10):976–988, 2014.
- [3] B. Ahier. Strategic aspects of nuclear radiological emergency management. planning for effective decision making. consequence management and transition to recovery. *Nuclear Energy Agency News*, 28(1):15–17, 2010.
- [4] International Atomic Energy Agency. Combating Illicit Trafficking in Nuclear and other Radioactive Material. Technical Report 6, IAEA, 2007.
- [5] L. Lucas, L. Pibida, M. Unterweger, and L. Karam. Gamma-ray emitting test sources for portal monitors used for homeland security. *Radiation Protection Dosimetry*, 113(1):108–111, 2005.
- [6] C. Le Goaller, G. Thellier, O. Gal, F. Lainé, H. Carcreff, and G. Imbard. The development and improvement of the ALADIN gamma camera to localise gamma activity in nuclear installations. Technical Report SCAN-0002010, 1998.
- [7] O. Gal, C. Izac, F. Jean, F. Lainé, C. Lévêque, and A. Nguyen. CARTOGAM - a portable gamma camera for remote localisation of radioactive sources in nuclear facilities. *Nuclear Instruments and Methods in Physics Research Section A: Accelerators, Spectrometers, Detectors and Associated Equipment*, 460(1):138–145, 2001.
- [8] O. Gal, M. Gmar, O. P. Ivanov, F. Lainé, F. Lamadie, C. Le Goaller, C. Mahé, E. Manach, and V. E. Stepanov. Development of a portable gamma camera with coded aperture. *Nuclear Instruments and Methods in Physics Research Section A: Accelerators, Spectrometers, Detectors and Associated Equipment*, 563(1):233–237, 2006.
- [9] M. Gmar, M. Agelou, F. Carrel, and V. Schoepff. GAMPIX: A new generation of gamma camera. *Nuclear Instruments and Methods in Physics Research Section A: Accelerators, Spectrometers, Detectors and Associated Equipment*, 652:638–640, 2011.
- [10] K. Amgarou, V. Paradiso, A. Patoz, F. Bonnet, J. Handley, P. Couturier, F. Becker, and N. Mena. A comprehensive experimental characterization of the iPIX gamma imager. *Journal of Instrumentation*, 11(08):P08012, 2016.
- [11] H. Lemaire. *Développement d'une caméra gamma de troisième génération*. PhD thesis, University of Caen Normandy, 2015.
- [12] K. A. Hughes et al. Use of gamma ray imaging instrumentation in support of TRU waste characterization challenges. *Proceedings Waste Management*, 4, 2004.

- [13] S. Dubos, H. Lemaire, S. Schanne, O. Limousin, F. Carrel, V. Schoepff, and C. Blondel. ORIGAMIX, a CdTe-based spectro-imager development for nuclear applications. *Nuclear Instruments and Methods in Physics Research Section A: Accelerators, Spectrometers, Detectors and Associated Equipment*, 787:302–307, 2015.
- [14] M. Woodring, D. Souza, S. Tipnis, P. Waer, M. Squillante, G. Entine, and K. P. Ziock. Advanced radiation imaging of low-intensity gamma-ray sources. *Nuclear Instruments and Methods in Physics Research Section A: Accelerators, Spectrometers, Detectors and Associated Equipment*, 422(1):709–712, 1999.
- [15] D. Matsuura, K. Genba, Y. Kuroda, H. Ikebuchi, and T. Tomonaka. ASTROCAM 7000HS Radioactive Substance Visualization Camera. *Mitsubishi Heavy Industries Technical Review*, 51(1):68–75, 2014.
- [16] C. G. Wahl et al. The Polaris-H imaging spectrometer. *Nuclear Instruments and Methods in Physics Research Section A: Accelerators, Spectrometers, Detectors and Associated Equipment*, 784:377–381, 2015.
- [17] F. Maes, A. Collignon, D. Vandermeulen, G. Marchal, and P. Suetens. Multimodality image registration by maximization of mutual information. *IEEE Transactions on Medical Imaging*, 16(2):187–198, 1997.
- [18] J. B. Maintz and M. A. Viergever. A survey of medical image registration. *Medical image analysis*, 2(1):1–36, 1998.
- [19] D. Hill, P. G. Batchelor, M. Holden, and D. J. Hawkes. Medical image registration. *Physics in medicine and biology*, 46(3):R1, 2001.
- [20] J. Pluim, J. B. Maintz, and M. A. Viergever. Mutual-information-based registration of medical images: a survey. *IEEE Transactions on Medical Imaging*, 22(8):986–1004, 2003.
- [21] M. S. Judenhofer et al. Simultaneous PET-MRI: a new approach for functional and morphological imaging. *Nature medicine*, 14(4):459–465, 2008.
- [22] T. Wendler, J. Traub, S. I. Ziegler, and N. Navab. Navigated three dimensional beta probe for optimal cancer resection. *Medical Image Computing and Computer-Assisted Intervention—MICCAI 2006*, 9(Pt 1):561–569, 2006.
- [23] T. Wendler, A. Hartl, T. Lasser, J. Traub, F. Daghighian, S. I. Ziegler, and N. Navab. Towards intra-operative 3D nuclear imaging: reconstruction of 3D radioactive distributions using tracked gamma probes. *Medical Image Computing and Computer-Assisted Intervention—MICCAI 2007*, 10(Pt 2):909–917, 2007.
- [24] G. H. KleinJan, N. S. van den Berg, M. N. van Oosterom, T. Wendler, M. Miwa, A. Bex, K. Hendricksen, S. Horenblas, and F. W. van Leeuwen. Toward (Hybrid) Navigation of a Fluorescence Camera in an Open Surgery Setting. *Journal of Nuclear Medicine*, 57(10):1650–1653, 2016.
- [25] M. N. van Oosterom, M. A. Engelen, N. S. van den Berg, G. H. KleinJan, H. G. van der Poel, T. Wendler, C. J. van de Velde, N. Navab, and F. W. van Leeuwen. Navigation of a robot-integrated fluorescence laparoscope in preoperative SPECT/CT and intraoperative freehand SPECT imaging data: a phantom study. *Journal of Biomedical Optics*, 21(8):086008–086008, 2016.

- [26] Y.F. Du, Z. He, G. F. Knoll, D. K. Wehe, and W. Li. Evaluation of a Compton scattering camera using 3-D position sensitive CdZnTe detectors. *Nuclear Instruments and Methods in Physics Research Section A: Accelerators, Spectrometers, Detectors and Associated Equipment*, 457(1):203–211, 2001.
- [27] M. Frandes, B. Timar, and D. Lungeanu. Image Reconstruction Techniques for Compton Scattering Based imaging: An Overview. *Current Medical Imaging Reviews*, 12(2):95–105, 2016.
- [28] W. C. Röntgen. Ueber eine neue Art von Strahlen. II. *Sonderabdruck aus den Sitzungsberichten der Würzburger Physik.-medic. Gesellschaft*, 1896. DOI:<http://dx.doi.org/10.1007/978-3-662-13247-0>.
- [29] D. E. Copeland and E. W. Benjamin. Pinhole camera for gamma-ray sources. *Nucleonics (Ceased publication)*, 5(2):44–9, 1949.
- [30] H. O. Anger. Use of a Gamma-Ray Pinhole Camera for in vivo studies. *Nature*, 170(4318):200–201, 1952.
- [31] H. O. Anger. Scintillation camera. *Review of scientific instruments*, 29(1):27–33, 1958.
- [32] H. O. Anger. Scintillation camera with multichannel collimators. *Journal of Nuclear Medicine*, 5(7):515–531, 1964.
- [33] T. E. Peterson and L. R. Furenlid. SPECT detectors: the Anger Camera and beyond. *Physics in medicine and biology*, 56(17):R145, 2011.
- [34] J. L. Matteson et al. CdZnTe arrays for astrophysics applications. In *Hard X-Ray and Gamma-Ray Detector Physics, Optics, and Applications*, pages 160–175, 1997.
- [35] V. V. Nagarkar, J. S. Gordon, S. Vasile, P. Gothoskar, and F. Hopkins. High resolution X-ray sensor for non-destructive evaluation. *IEEE Transactions on Nuclear science*, 43(3):1559–1563, 1996.
- [36] E. Van and W. E. Carel. Inorganic scintillators in medical imaging. *Physics in medicine and biology*, 47(8):R85, 2002.
- [37] G. E. Smith. Nobel lecture: The invention and early history of the CCD. *Reviews of modern physics*, 82(3):2307, 2010.
- [38] The Nobel Foundation. The Nobel Prize in Physics 2009. http://www.nobelprize.org/nobel_prizes/physics/laureates/2009/. Accessed: 25 Jan 2017.
- [39] W. S. Boyle and G. E. Smith. Charge coupled semiconductor devices. *Bell Labs Technical Journal*, 49(4):587–593, 1970.
- [40] F. J. Beekman and G. A. de Vree. Photon-counting versus an integrating CCD-based gamma camera: important consequences for spatial resolution. *Physics in medicine and biology*, 50(12):N109, 2005.
- [41] C. Mahé. Practical Workshop on Characterization and Visualization Technologies in DD&R. In *International Decommissioning Network (IDN)*, Marcoule, France, 2011.
- [42] O. Gal, F. Jean, F. Lainé, and C. Lévêque. The CARTOGAM portable gamma imaging system. In *IEEE Nuclear Science Symposium*, pages 725–729, 1999.

- [43] H. H. Barrett and F. A. Horrigan. Fresnel zone plate imaging of gamma rays; theory. *Applied Optics*, 12(11):2686–2702, 1973.
- [44] O. P. Ivanov, A. N. Sudarkin, V. E. Stepanov, and L. I. Urutskoev. Portable X-ray and gamma-ray imager with coded mask: performance characteristics and methods of image reconstruction. *Nuclear Instruments and Methods in Physics Research Section A: Accelerators, Spectrometers, Detectors and Associated Equipment*, 422(1):729–734, 1999.
- [45] S. R. Gottesman and E. E. Fenimore. New family of binary arrays for coded aperture imaging. *Applied optics*, 28(20):4344–4352, 1989.
- [46] E. Caroli, J. B. Stephen, G. Di Cocco, L. Natalucci, and A. Spizzichino. Coded aperture imaging in X-and gamma-ray astronomy. *Space Science Reviews*, 45(3-4):349–403, 1987.
- [47] L. Mertz and N. O. Young. Fresnel transformations of images. *International Conference on Optical Instrument*, 128:44–49, 1996.
- [48] N. M. Ceglio, D. T. Attwood, and E. V. George. Zone-plate coded imaging of laser-produced plasmas. *Journal of Applied Physics*, 48(4):1566–1569, 1977.
- [49] R. H. Dicke. Scatter-Hole Cameras for X-Rays and Gamma Rays. *The Astrophysical Journal*, 153:L101, 1968.
- [50] J. G. Ables. Fourier Transform Photography: A new method for X-ray Astronomy. *Publications of the Astronomical Society of Australia*, 1(04):172–173, 1968.
- [51] G. Vedrenne and J. L. Atteia. *Gamma-Ray Bursts: The brightest explosions in the Universe*. Springer/Praxis Books, 2009.
- [52] E. E. Fenimore and T. M. Cannon. Coded aperture imaging with uniformly redundant arrays. *Applied optics*, 17:337–347, 1978.
- [53] A. Busboom, B. Elders, and H.D. Schotten. Uniformly redundant arrays. *Experimental Astronomy*, 8(2):97–123, 1998.
- [54] H. D. Lüke and A. Busboom. Mismatched filtering of periodic and odd-periodic binary arrays. *Applied optics*, 37(5):856–864, 1998.
- [55] G. K. Skinner. Imaging with coded-aperture masks. *Nuclear Instruments and Methods in Physics Research*, 221(1):33–40, 1984.
- [56] J. Gunson and B. Polychronopoulos. Optimum design of a coded mask X-ray telescope for rocket applications. *Monthly Notices of the Royal Astronomical Society*, 177(3):485–497, 1976.
- [57] M. H. Finger and T. A. Prince. Hexagonal uniformly redundant arrays for coded-aperture imaging. In *International Cosmic Ray Conference*, volume 3, 1985.
- [58] X. Llopart and M. Campbell. First test measurements of a 64k pixel readout chip working in single photon counting mode. *Nuclear Instruments and Methods in Physics Research Section A: Accelerators, Spectrometers, Detectors and Associated Equipment*, 509(1):157–163, 2003.
- [59] M. Chmeissani et al. First experimental tests with a CdTe photon counting pixel detector hybridized with a Medipix2 readout chip. *IEEE Transactions on Nuclear Science*, 51(5):2379–2385, 2004.

- [60] M. Gmar, O. Gal, C. Le Goaller, O. P. Ivanov, V. N. Potapov, V. E. Stepanov, F. Lainé, and F. Lamadie. Development of coded-aperture imaging with a compact gamma camera. *IEEE Transactions on Nuclear Science*, 51(4):1682–1687, 2004.
- [61] J. Braga et al. A new mask-antimask coded-aperture telescope for hard X-ray astronomy. *Experimental astronomy*, 2(2):101–113, 1991.
- [62] G. Aad et al. The ATLAS experiment at the CERN Large Hadron Collider. *Journal of Instrumentation*, 3(08):S08003, 2008.
- [63] X. Llopart et al. Timepix, a 65k programmable pixel readout chip for arrival time, energy and/or photon counting measurements. *Nuclear Instruments and Methods in Physics Research Section A: Accelerators, Spectrometers, Detectors and Associated Equipment*, 581:485–494, 2007.
- [64] T. Takahashi and S. Watanabe. Recent progress in CdTe and CdZnTe detectors. *IEEE Transactions on Nuclear Science*, 48(4):950–959, 2001.
- [65] K. Biswas and M. Du. What causes high resistivity in CdTe. *New Journal of Physics*, 14(6):063020, 2012.
- [66] R. H. Redus, J. A. Pantazis, T. J. Pantazis, A. C. Huber, and B. J. Cross. Characterization of CdTe detectors for quantitative X-ray spectroscopy. *IEEE Transactions on Nuclear Science*, 56(4):2524–2532, 2009.
- [67] R. Aamir, N. G. Anderson, A. Butler, P. Butler, S. P. Lansley, R. M. Doesburg, M. Walsh, and J. L. Mohr. Characterization of Si and CdTe sensor layers in Medipix assemblies using a microfocus X-ray source. In *2011 IEEE Nuclear Science Symposium and Medical Imaging Conference*, pages 4766–4769, 2011.
- [68] D. Turecek et al. Pixelman: a multi-platform data acquisition and processing software package for Medipix2, Timepix and Medipix3 detectors. *Journal of Instrumentation*, 6(01):C01046, 2011.
- [69] K. Akiba et al. The Timepix telescope for high performance particle tracking. *Nuclear Instruments and Methods in Physics Research Section A: Accelerators, Spectrometers, Detectors and Associated Equipment*, 723:47–54, 2013.
- [70] J. Jakubek et al. Spectrometric properties of Timepix pixel detector for X-ray color and phase sensitive radiography. In *IEEE Nuclear Science Symposium*, pages 2323–2326, 2007.
- [71] C. Teyssier et al. Performance of the Medipix and Timepix devices for the recognition of electron-gamma radiation fields. *Nuclear Instruments and Methods in Physics Research Section A: Accelerators, Spectrometers, Detectors and Associated Equipment*, 650(1):92–97, 2011.
- [72] International Organization for Standardization. *X and gamma reference radiation for calibrating dosimeters and dose-rate meters and for determining their response as a function of photon energy - Part 4: Calibration of area and personal dosimeters in low energy X reference radiation fields*. International Organization for Standardization, 2004.
- [73] International Commission on Radiological Protection. Conversion Coefficients for Use in Radiological Protection against External Radiation. *Annals of the ICRP (International Commission on Radiological Protection)*, 26(3-4), 1996.

- [74] K. Amgarou et al. Evaluation of the next generation gamma imager. In *Third International Conference on Advancements in Nuclear Instrumentation Measurement Methods and their Applications (ANIMMA)*, pages 1–6, 2013.
- [75] S. Myers. The LEP collider, from design to approval and commissioning. Technical Report CERN-91-08, CERN, 1991.
- [76] M. Benedikt, P. Collier, V. Mertens, J. Poole, and K. Schindl. LHC design report, Volume III, The LHC injector chain. Technical Report CERN-2004-003-V-3, CERN, 2004.
- [77] S. L. Glashow. Partial-symmetries of weak interactions. *Nuclear Physics*, 22(4):579–588, 1961.
- [78] S. Weinberg. A model of leptons. *Physical review letters*, 19(21):1264, 1967.
- [79] A. Salam and J. C. Ward. Electromagnetic and weak interactions. *Physics Letters*, 13(2):168–171, 1964.
- [80] G. Hooft and M. Veltman. Regularization and renormalization of gauge fields. *Nuclear Physics B*, 44(1):189–213, 1972.
- [81] The CDF Collaboration. Observation of top quark production in pp collisions with the collider detector at Fermilab. *Physical review letters*, 74(14):2626, 1995.
- [82] CDMS Collaboration. Dark matter search results using the silicon detectors of CDMS II. Technical Report arXiv:1304.4279, CDMS, 2013.
- [83] J. T. Seeman. The Stanford linear collider. *Annual Review of Nuclear and Particle Science*, 41(1):389–428, 1991.
- [84] W. Kozanecki. The PEP-II B-factory: Status and prospects. *Nuclear Instruments and Methods in Physics Research Section A: Accelerators, Spectrometers, Detectors and Associated Equipment*, 446(1):59–64, 2000.
- [85] T. Aaltonen et al. Combination of Tevatron searches for the standard model Higgs boson in the $W^+ W^-$ decay mode. *Physical review letters*, 104(6):061802, 2010.
- [86] H. Abramowicz and A. C. Caldwell. HERA collider physics. *Reviews of Modern Physics*, 71(5):1275, 1999.
- [87] S. Kurokawa and E. Kikutani. Overview of the KEKB accelerators. *Nuclear Instruments and Methods in Physics Research Section A: Accelerators, Spectrometers, Detectors and Associated Equipment*, 499(1):1–7, 2003.
- [88] LHC Study Group and European Organization for Nuclear Research. *Design study of the Large Hadron Collider (LHC): a multiparticle collider in the LEP tunnel*. Number 3. 1991.
- [89] The CMS Collaboration. The CMS experiment at the CERN LHC. *Journal of Instrumentation*, 3(08):S08004, 2008.
- [90] A. Alves Jr. et al. The LHCb detector at the LHC. *Journal of Instrumentation*, 3(08):S08005, 2008.
- [91] G. Anelli et al. The TOTEM experiment at the CERN Large Hadron Collider. *Journal of Instrumentation*, 3(08):S08007, 2008.

- [92] K. Aamodt et al. The ALICE experiment at the CERN LHC. *Journal of Instrumentation*, 3(08):S08002, 2008.
- [93] L. Evans and P. Bryant. LHC machine. *Journal of Instrumentation*, 3(08):S08001, 2008.
- [94] L. Evans. *The Large Hadron Collider: a marvel of technology*. EPFL Press, 2009.
- [95] W. Armstrong et al. ATLAS: technical proposal for a general-purpose pp experiment at the Large Hadron Collider at CERN. Technical report, CERN, 1994.
- [96] The ATLAS Collaboration. ATLAS detector and physics performance technical design report. Technical Report ATLAS-TDR-14, CERN, 1999.
- [97] G. Aad et al. Observation of a new particle in the search for the Standard Model Higgs boson with the ATLAS detector at the LHC. *Physics Letters B*, 716(1):1–29, 2012.
- [98] I. Dawson. Radiation background simulation and verification at the LHC: Examples from the ATLAS experiment and its upgrades. Technical Report ATL-COM-INDET-2012-108, CERN, 2012.
- [99] J. Pinfold. Lucid, the Luminosity Monitor for ATLAS - A status report. In *Astroparticle, Particle and Space Physics, Detectors and Medical Physics Applications*, pages 364–370, 2008.
- [100] S. Baranov, M. Bosman, I. Dawson, V. Hedberg, A. Nisati, and M. Shupe. Estimation of radiation background, impact on detectors, activation and shielding optimization in ATLAS. Technical Report ATL-GEN-2005-001, CERN, 2005.
- [101] M. Capeans, T. Flick, R. Vuillermet, G. Darbo, H. Pernegger, K. Einsweiler, M. Garcia-Sciveres, M. Elsing, O. Rohne, and C. Gemme. ATLAS insertable B-layer technical design report. Technical Report CERN-LHCC-2010-013. ATLAS-TDR-19, CERN, 2010.
- [102] ATLAS Collaboration. ATLAS Insertable B-Layer Technical Design Report Addendum. Technical Report ATLAS-TDR-019-ADD-1, CERN, 2012.
- [103] Council Directive. Council Directive 96/29/Euratom of 13 may 1996 laying down basic safety standards for the protection of the health of workers and the general public against the dangers arising from ionizing radiation. *Official Journal of the European Union*, 39(L159):1–114, 1996.
- [104] International Commission on Radiological Protection. 1990 recommendations of the international commission on radiological protection. *Annals of the ICRP (International Commission on Radiological Protection)*, 21(1-3), 1991.
- [105] Protection contre le rayonnement ionisants, no 1420. *Journal Officiel de la Republique Francaise*.
- [106] Recueil des dispositions législatives et réglementaires concernant la protection de la population et des travailleurs contre les dangers des rayonnements ionisants. *Journal Officiel de la Republique Francaise*.
- [107] Décret no. 2002-460 du 4 avril 2002 - relatif à la protection generale des personnes contre les dangers des rayonnement ionisants. *Journal Officiel de la Republique Francaise*.
- [108] Décret no. 2003-296 du 31 mars 2003 - relatif à la protection generale des personnes contre les dangers des rayonnement ionisants. *Journal Officiel de la Republique Francaise*.

- [109] Le Département fédéral de l'intérieur Confederation suisse. Ordonnance sur l'utilisation des sources radioactives non-scellées du 21 novembre 1997. *RO 1997 2923*.
- [110] International Atomic Energy Agency. Radioprotection, CERN Safety Codes. Technical Report F Rev., CERN, 2006.
- [111] O. Brüning, P. Collier, P. Lebrun, S. Myers, R. Ostojic, J. Poole, and P. Proudlock. LHC design report (Volume II, The LHC infrastructure and general services). Technical Report CERN-2004-003-V-2, CERN, 2004.
- [112] D. Warner et al. CERN heavy-ion facility design report. Technical Report CERN-93-01, CERN, 1993.
- [113] E. Kugler et al. The new CERN-ISOLDE on-line mass-separator facility at the PS-Booster. *Nuclear Instruments and Methods in Physics Research Section B: Beam Interactions with Materials and Atoms*, 70(1-4):41–49, 1992.
- [114] M. Chanel. LEIR: the low energy ion ring at CERN. *Nuclear Instruments and Methods in Physics Research Section A: Accelerators, Spectrometers, Detectors and Associated Equipment*, 532(1):137–143, 2004.
- [115] K. Schindl. The injector chain for the LHC. Technical Report CERN-PS-99-018-DI, CERN, 1999.
- [116] O. Beltramello, H. J. Burckhart, S. Franz, M. Jaekel, M. Jeckel, S. Lüders, G. Morpurgo, F. dos Santos Pedrosa, K. Pommès, and H. Sandaker. The detector safety system of the ATLAS experiment. *Journal of Instrumentation*, 4(09):P09012, 2009.
- [117] A. B. Poy et al. The detector control system of the ATLAS experiment. *Journal of Instrumentation*, 3(05):P05006, 2008.
- [118] CERN. CSAM (CERN Safety Alarm Monitoring). <https://espace.cern.ch/CSAM>. Accessed: 2 Jan 2017.
- [119] S. Lüders, R. B. Flockhart, G. Morpurgo, and S. M. Schmeling. The CERN Detector Safety System for the LHC experiments. In *9th International Conference on Accelerator and Large Experimental Physics Control Systems*, pages 13–17, 2003.
- [120] A. J. Millington. *The Large Hadron Collider: The Greatest Adventure in Town and Ten Reasons Why it Matters, as Illustrated by the ATLAS Experiment*. World Scientific, 2016.
- [121] CERN. CERN Bulletin Issue No. 07-08/2016 - Monday 15 february 2016 - EDUSAFE, Augmented Reality for improved safety. <https://cds.cern.ch/journal/CERNBulletin/2016/07/News%20Articles/2130668>. Accessed: 2 Jan 2017.
- [122] CERN. EDUSAFE, Education in advanced VR/AR safety systems for maintenance in extreme environments. <http://edusafe.web.cern.ch/edusafe>. Accessed: 2 Jan 2017.
- [123] H. Marcus and H. Hermann. Heterogeneity by the Numbers: A Study of the ODROID XU+E big.LITTLE Platform. In *6th Workshop on Power-Aware Computing and Systems (HotPower 14)*, 2014.
- [124] V. Kraus, M. Holik, J. Jakubek, M. Kroupa, P. Soukup, and Z. Vykydal. FITPix—fast interface for Timepix pixel detectors. *Journal of Instrumentation*, 6(01):C01079, 2011.

- [125] International Telecommunication Union Recommendations (ITU-R). *BT.601-7: Studio encoding parameters of digital television for standard 4:3 and wide screen 16:9 aspect ratios*. ITU-R, 2011.
- [126] R. Ferzli and L. J. Karam. A No-Reference Objective Image Sharpness Metric Based on the Notion of Just Noticeable Blur (JNB). *IEEE Transactions on Image Processing*, 18(4):717–728, 2009.
- [127] R. Ferzli and L. J. Karam. No-reference objective wavelet based noise immune image sharpness metric. In *12th IEEE International Conference on Image Processing (ICIP)*, volume 1, pages I–405–8, 2005.
- [128] I. Sobel and G. Feldman. A 3x3 Isotropic Gradient Operator for Image Processing. Never published but presented at a talk at the Stanford Artificial Project, 1968.
- [129] J. Prewitt. Object enhancement and extraction. *Picture processing and Psychopictorics*, 10(1):15–19, 1970.
- [130] J. Canny. A computational approach to edge detection. *IEEE Transactions on Pattern Analysis and Machine Intelligence*, (6):679–698, 1986.
- [131] G. T. Shrivakshan and C. Chandrasekar. A comparison of various edge detection techniques used in image processing. *International Journal of Computer Science Issues*, 9(5):272–276, 2012.
- [132] C. Liu, W. T. Freeman, R. Szeliski, and S. B. Kang. Noise estimation from a single image. In *IEEE Computer Society Conference on Computer Vision and Pattern Recognition*, pages 901–908, 2006.
- [133] Future Technology Devices International Ltd. D2XX drivers for FTDI devices. <http://www.ftdichip.com/Drivers/D2XX.htm>, 2016. Accessed: 2 Jan 2017.
- [134] T. Bray. The Javascript object notation (JSON) data interchange format. [http://https://tools.ietf.org/html/rfc7159.html](http://tools.ietf.org/html/rfc7159.html), 2014–. Accessed: 6 March 2017.
- [135] E. Jones, T. Oliphant, and P. Peterson. SciPy: Open source scientific tools for Python. <http://www.scipy.org>, 2001–. Accessed: 6 March 2017.
- [136] G. Bradski and A. Kaehler. *Learning OpenCV: Computer vision with the OpenCV library*. O’Reilly Media, Inc., 2008.
- [137] B. Lawson and R. Sharp. *Introducing HTML5*. New Riders, 2011.
- [138] T. Porter and T. Duff. Compositing digital images. In *ACM Siggraph Computer Graphics*, volume 18, pages 253–259, 1984.
- [139] B. A. Smith et al. The Jupiter system through the eyes of Voyager 1. *Science*, 204(4396):951–972, 1979.
- [140] B. A. Smith et al. A new look at the Saturn system: The Voyager 2 images. *Science*, 215(4532):504–537, 1982.
- [141] M. Brown and D. G. Lowe. Automatic Panoramic Image Stitching using Invariant Features. *International Journal of Computer Vision*, 74(1):59–73, 2007.
- [142] D. G. Lowe. Distinctive image features from scale-invariant keypoints. *International journal of computer vision*, 60(2):91–110, 2004.

- [143] E. Rublee, V. Rabaud, K. Konolige, and G. Bradski. ORB: An efficient alternative to SIFT or SURF. In *IEEE International Conference on Computer Vision (ICCV)*, pages 2564–2571, 2011.
- [144] M. Calonder, V. Lepetit, C. Strecha, and P. Fua. Brief: Binary robust independent elementary features. In *European Conference on Computer Vision*, pages 778–792, 2010.
- [145] E. Rosten and T. Drummond. Machine learning for high-speed corner detection. In *European Conference on Computer Vision*, pages 430–443, 2006.
- [146] R. Hartley and A. Zisserman. *Multiple view geometry in computer vision*. Cambridge University Press, 2003.
- [147] J. Gallier. *Basics of Projective Geometry*. Springer, 2011.
- [148] B. D. Lucas and T. Kanade. An Iterative Image Registration Technique with an Application to Stereo vision. In *Proceedings of the 7th International Joint Conference on Artificial Intelligence*, pages 674–679, 1981.
- [149] I. E. Richardson. *H. 264 and MPEG-4 video compression: video coding for next-generation multimedia*. John Wiley & Sons, 2004.
- [150] B. Zitova and J. Flusser. Image registration methods: a survey. *Image and Vision Computing*, 21(11):977–1000, 2003.
- [151] K. Mikolajczyk and C. Schmid. A performance evaluation of local descriptors. *IEEE Transactions on Pattern Analysis and Machine Intelligence*, 27(10):1615–1630, 2005.
- [152] L. G. Brown. A Survey of Image Registration Techniques. *ACM Computing Surveys*, 24(4):325–376, 1992.
- [153] D. R. Peddle, P. M. Teillet, and M. A. Wulder. *Radiometric image processing*. Springer, 2003.
- [154] D. L. Milgram. Computer methods for creating photomosaics. *IEEE Transactions on Computers*, 24(11):1113–1119, 1975.
- [155] D. L. Milgram. Adaptive techniques for photomosaicking. *IEEE Transactions on Computers*, 100(11):1175–1180, 1977.
- [156] P. Soille. Morphological image compositing. *IEEE Transactions on Pattern Analysis and Machine Intelligence*, 28(5):673–683, 2006.
- [157] M. Everingham, L. Van Gool, C. Williams, J. Winn, and A. Zisserman. The pascal visual object classes (voc) challenge. *International Journal of Computer Vision*, 88(2):303–338, 2010.
- [158] H. Samet. *The Design and Analysis of Spatial Data Structures*. Addison-Wesley, 1990.
- [159] P. N. Yianilos. Data structures and algorithms for nearest neighbor search in general metric spaces. In *Proceedings of the fourth annual ACM-SIAM symposium on Discrete algorithms*, pages 311–21, 1993.
- [160] J. S. Beis and D. G. Lowe. Shape indexing using approximate nearest-neighbour search in high-dimensional spaces. In *IEEE Computer Society Conference on Computer Vision and Pattern Recognition (CVPR)*, pages 1000–1006, 1997.

- [161] M. A. Fischler and R. C. Bolles. Random sample consensus: a paradigm for model fitting with applications to image analysis and automated cartography. *Communications of the ACM*, 24(6):381–395, 1981.
- [162] P. J. Huber et al. Robust estimation of a location parameter. *The Annals of Mathematical Statistics*, 35(1):73–101, 1964.
- [163] P. J. Rousseeuw. Least median of squares regression. *Journal of the American statistical association*, 79(388):871–880, 1984.
- [164] P. Torr and A. Zisserman. MLESAC: A new robust estimator with application to estimating image geometry. *Computer Vision and Image Understanding*, 78(1):138–156, 2000.
- [165] P. Torr and C. Davidson. Impsac: Synthesis of importance sampling and random sample consensus. *IEEE Transactions on Pattern Analysis and Machine Intelligence*, 25(3):354–364, 2003.
- [166] M. Brown and D. G. Lowe. Recognising panoramas. In *Proceedings of the Ninth IEEE International Conference on Computer Vision (ICCV)*, page 1218, 2003.
- [167] P. Burt and E. Adelson. The Laplacian pyramid as a compact image code. *IEEE Transactions on communications*, 31(4):532–540, 1983.
- [168] R. Szeliski. Image mosaicing for tele-reality applications. In *Proceedings of the Second IEEE Workshop on Applications of Computer Vision*, pages 44–53, 1994.
- [169] S. E. Chen. Quicktime VR: An image-based approach to virtual environment navigation. In *Proceedings of the 22nd annual conference on Computer graphics and interactive techniques*, pages 29–38, 1995.
- [170] R. Szeliski and H. Shum. Creating full view panoramic image mosaics and environment maps. In *Proceedings of the 24th annual conference on Computer graphics and interactive techniques*, pages 251–258, 1997.
- [171] N. Greene. Environment mapping and other applications of world projections. *IEEE Computer Graphics and Applications*, 6(11):21–29, 1986.
- [172] D. Anguelov, C. Dulong, D. Filip, C. Frueh, S. Lafon, R. Lyon, A. Ogale, L. Vincent, and J. Weaver. Google Street View: Capturing the world at street level. *Computer*, 43(6):32–38, 2010.
- [173] M. Harris. Many-core GPU computing with NVIDIA CUDA. In *Proceedings of the 22nd annual International Conference on Supercomputing (ICS)*, pages 1–1, 2008.
- [174] M. Adam, C. Jung, S. Roth, and G. Brunnert. Real-time Stereo-Image Stitching using GPU-based Belief Propagation. In *Vision, Modeling, and Visualization Workshop, 2009*, pages 215–224, 2009.
- [175] R. Tsai. A versatile camera calibration technique for high-accuracy 3D machine vision metrology using off-the-shelf TV cameras and lenses. *IEEE Transactions on Robotics and Automation*, 3:323–344, 1987.
- [176] R. Tsai and R. K. Lenz. A new technique for fully autonomous and efficient 3D robotics hand/eye calibration. *IEEE Transactions on Robotics and Automation*, 5(3):345–358, 1989.
- [177] Z. Zhang. A flexible new technique for camera calibration. *IEEE Transactions on Pattern Analysis and Machine Intelligence*, 22(11):1330–1334, 2000.

- [178] A. A. Goshtasby. *2-D and 3-D image registration: for medical, remote sensing, and industrial applications*. John Wiley & Sons, 2005.
- [179] P. J. Besl. Active, optical range imaging sensors. *Machine vision and applications*, 1(2):127–152, 1988.
- [180] D. Marr and T. Poggio. *Cooperative computation of stereo disparity*. Springer, 1976.
- [181] H. Gonzalez-Jorge, B. Riveiro, E. Vazquez-Fernandez, J. Martínez-Sánchez, and P. Arias. Metrological evaluation of Microsoft Kinect and Asus Xtion sensors. *Measurement*, 46(6):1800–1806, 2013.
- [182] B. Freedman, A. Shpunt, M. Machline, and Y. Arieli. Depth mapping using projected patterns, April 3 2012. US Patent 8,150,142.
- [183] B. Freedman, A. Shpunt, M. Machline, and Y. Arieli. Depth mapping using projected patterns, 2010. US Patent 12/522,171.
- [184] A. Shpunt, G. Medioni, D. Cohen, E. Sali, and R. Deitch. Depth mapping based on pattern matching and stereoscopic information, Feb 2011. US Patent App. 12/844,864.
- [185] B. Freedman, A. Shpunt, and Y. Arieli. Depth mapping using optical elements having non-uniform focal characteristics, July 23 2013. US Patent 8,494,252.
- [186] J. Garcia and Z. Zalevsky. Range mapping using speckle decorrelation, 2008. US Patent 7,433,024.
- [187] K. Khoshelham and E. O. Elberink. Accuracy and resolution of Kinect depth data for indoor mapping applications. *Sensors*, 12(2):1437–1454, 2012.
- [188] A. W. Fitzgibbon. Simultaneous linear estimation of multiple view geometry and lens distortion. In *Proceedings of the IEEE Conference on Computer Vision and Pattern Recognition*, volume 1, pages I–I, 2001.
- [189] ADVACAM s.r.o. WidePIX Large Area Camera. [http://http://www.advacam.com/en/products/widepix1x5](http://www.advacam.com/en/products/widepix1x5), 2016. Accessed: 5 Jan 2017.
- [190] Q. Luong and O. D. Faugeras. The fundamental matrix: Theory, algorithms, and stability analysis. *International Journal of Computer Vision*, 17(1):43–75, 1996.
- [191] P. F. Sturm and S. J. Maybank. On plane-based camera calibration: A general algorithm, singularities, applications. In *IEEE Computer Society Conference on Computer Vision and Pattern Recognition*, volume 1, pages 432–437, 1999.
- [192] J. Lavest, M. Viala, and M. Dhome. Do we really need an accurate calibration pattern to achieve a reliable camera calibration? In *European Conference on Computer Vision*, pages 158–174, 1998.
- [193] J. J. Moré. *The Levenberg-Marquardt algorithm: implementation and theory*. Springer, 1978.
- [194] D. M. Shuster. A survey of attitude representations. *Navigation*, 8(9):439–517, 1993.
- [195] F. L. Markley, Y. Cheng, J. L. Crassidis, and Y. Oshman. Averaging quaternions. *Journal of Guidance, Control, and Dynamics*, 30(4):1193–1197, 2007.

- [196] Leica Camera AG. Leica DISTO D210 manual. http://survey.crkennedy.com.au/sites/default/files/downloads/Leica%20DISTO%20D210%20MAN%20788217_en.pdf, 2016. Accessed: 22 Jan 2017.
- [197] A. Fusiello, E. Trucco, and A. Verri. A compact algorithm for rectification of stereo pairs. *Machine Vision and Applications*, 12(1):16–22, 2000.
- [198] C. Loop and Z. Zhang. Computing rectifying homographies for stereo vision. In *IEEE Computer Society Conference on Computer Vision and Pattern Recognition*, volume 1, pages 125–131, 1999.
- [199] P. J. Besl and N. D. McKay. Method for registration of 3-D shapes. In *Robotics-DL tentative*, pages 586–606, 1992.
- [200] M. Quigley, K. Conley, B. Gerkey, J. Faust, T. Foote, J. Leibs, R. Wheeler, and A. Y. Ng. ROS: an open-source Robot Operating System. In *ICRA workshop on open source software*, volume 3, page 5, 2009.
- [201] R. B. Rusu, G. Bradski, R. Thibaux, and J. Hsu. Fast 3D recognition and pose using the viewpoint feature histogram. In *IEEE/RSJ International Conference on Intelligent Robots and Systems (IROS)*, pages 2155–2162, 2010.
- [202] R. B. Rusu and S. Cousins. 3D is here: Point cloud library (PCL). In *IEEE International Conference on Robotics and Automation (ICRA)*, pages 1–4, 2011.
- [203] R. B. Rusu, N. Blodow, and M. Beetz. Fast point feature histograms (FPFH) for 3D registration. In *IEEE International Conference on Robotics and Automation (ICRA)*, pages 3212–3217, 2009.
- [204] R. B. Rusu, Z. C. Marton, N. Blodow, M. Dolha, and M. Beetz. Towards 3D point cloud based object maps for household environments. *Robotics and Autonomous Systems*, 56(11):927–941, 2008.
- [205] P. Bourke. Ply-polygon file format. <http://http://paulbourke.net/dataformats/ply>, 2009. Accessed: 17 Jan 2017.
- [206] P. Cignoni, M. Callieri, M. Corsini, M. Dellepiane, F. Ganovelli, and G. Ranzuglia. MeshLab: an open-source mesh processing tool. In *Eurographics Italian Chapter Conference*, pages 129–136, 2008.
- [207] A. Kolb, E. Barth, R. Koch, and R. Larsen. Time-of-flight cameras in computer graphics. In *Computer Graphics Forum*, pages 141–159, 2010.
- [208] International Commission on Radiological Protection. Recommendations of the international commission on radiological protection. *Annals of the ICRP (International Commission on Radiological Protection)*, 37(2-4), 2007.
- [209] International Commission on Radiation Units and Measurements. Quantities and units in Radiation Protection dosimetry. Technical Report 51, ICRU, 1993.
- [210] International Commission on Radiological Protection. ICRP statement on tissue reactions and early and late effects of radiation in normal tissues and organs – Threshold doses for tissue reactions in a Radiation Protection context. *Annals of the ICRP (International Commission on Radiological Protection)*, 41(1/2), 2012.

Appendix A

Radiation protection basics

Radiation protection essentially aims at controlling exposure to ionizing radiation¹ for preventing acute damage and limiting the risk of long-term effects in humans to acceptable levels. For this purpose, the International Commission on Radiation Protection (ICRP) has defined, in its Publication 60 [104], a radiation protection system, which still prevails today, allowing evaluation of the extent of exposure to ionizing radiation from intakes of radionuclides as well as from both whole and partial body external irradiation. This fully contemplates the following three objectives:

- The characterization of the radiation fields and their interactions with matter from physical and measurable quantities; the so-called **primary quantities**.
- The definition of **limiting quantities** that play a central role for estimating the stochastic health risk due to long-term radiation exposures at low doses, and from which legal limits to the public and occupational radiation exposures can be created.
- The establishment of a series of **operational quantities**, to be used in practical controls of external radiation fields, as limiting quantities are not directly measurable.

The ICRP publication 103 [208] lastly replaced and updated some recommendations as well as several radiation and tissue weighting factors.

Primary quantities

The three primary quantities most widely used in radiation protection are: **fluence**, **kerma** and **absorbed dose**. All of them are scalar physical quantities that characterize the radiation field and their interaction with matter.

¹Ionizing radiation refers to both charged-particles (e.g., electrons or protons) and neutral particles (e.g., photons or neutrons) that can produce ionization in a medium. This ionization in the case of neutral particles is an indirect process since they first produce charged-particles, which in turn transfer energy to the surrounding atoms.

Fluence

Fluence, Φ , is defined by the number of particles dN traversing an (imaginary) sphere, divided by the cross-sectional area dS of this latter. That is:

$$\Phi = \frac{dN}{dS}. \quad (\text{A.1})$$

Its SI unit is cm^{-2} and when divided by the exposure time, it is known as *fluence rate* or $\dot{\Phi}$ with the general unit of $\text{cm}^{-2} \text{s}^{-1}$.

As illustrated in Fig. A.1, the definition of such imaginary sphere allows that the corresponding cross-sectional area perpendicular to the direction of each incoming particle is accounted for so. Therefore, fluence does not depend on the direction distribution of the incoming particles.

It is also very common in dosimetric calculations to express fluence in terms of the lengths of the particle trajectories:

$$\Phi = \frac{\sum dl}{dV}, \quad (\text{A.2})$$

where $\sum dl$ is the sum of all the lengths of particle trajectories in the volume dV of the considered sphere.

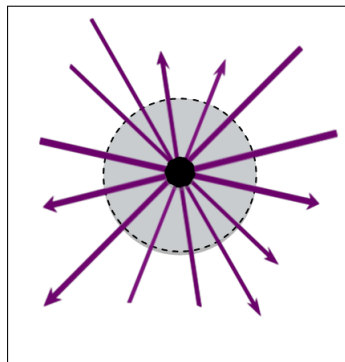


Fig. A.1: Illustration of the particle fluence definition.

Kerma

Kerma², \mathbf{K} , is the sum of the initial kinetic energies per unit mass of the charged particles that are released by indirectly ionizing or uncharged radiation, such as photons and neutrons, in a sample of matter. The SI unit of kerma is one joule per kilogram (J kg^{-1}) and its special name is Gray (Gy). When divided by the exposure time it is known as *kerma rate* or $\dot{\mathbf{K}}$ with the most common unit of mGy/h.

²Kerma is an acronym for "*Kinetic Energy Released per unit Mass*". The final "a" being added principally to avoid confusion with the German word "*kern*", which means nucleus.

Absorbed dose

The absorbed dose or simply "*dose*", D , is the *mean* energy imparted by ionizing radiation to matter per unit mass of this latter. Similarly to kerma, its SI unit is the Gray (Gy) and when divided by the exposure time it is known as *dose rate* or \dot{D} with the most common unit of mGy/h.

The definition of absorbed dose has the scientific rigor required for a basic physical quantity as it implicitly takes into account the different radiation interactions with matter inside and outside the specified volume. It does not, however, consider the atomic structure of matter and the stochastic nature of the radiation interactions at a microscopic level.

Comparison between kerma and absorbed dose

Kerma depends only on the local interactions of the incident uncharged radiation whereas the absorbed dose also considers all the secondary charged particles, originally released in the surrounding medium, that are able to reach the considered volume depositing energy in it. In general, when the kinetic energy transferred by an uncharged particle takes at a certain point, its subsequent imparting of energy to matter, which gives rise to the absorbed dose, is spread over distances determined by the ranges of the induced secondary charged particles.

The global difference between these two quantities is emphasized in Fig. A.2. According to this figure, under an idealized case in which there is no effect, such as attenuation, influencing the incident uncharged radiation, kerma will remain independent of the depth within matter whereas the absorbed dose will start from zero at the entrance surface until reaching its maximum close to kerma. Beyond this build-up region, a charged-particle equilibrium³ is maintained for deeper layers.

Nevertheless, if attenuation of the incident uncharged radiation is not ignored, kerma will normally start from a highest value at the entrance surface and will exponentially decrease with depth. In turn, the absorbed dose will firstly rise from zero at the entrance surface until reaching a transient equilibrium and will then decrease along with kerma.

Limiting quantities

The major drawback of the primary quantities is their inadequacy to estimate the ionizing radiation risk due to induced stochastic health effects. This risk depends both on the type of organ or tissue and on the different types of ionizing radiation. For that reason, additional quantities have been defined to take into account variations in the biological effectiveness of each ionizing radiation as well as the different sensitivities of human organs and tissues to the same amount of absorbed dose.

³That is, for any charged-particle leaving the considered space there a new one entering it.

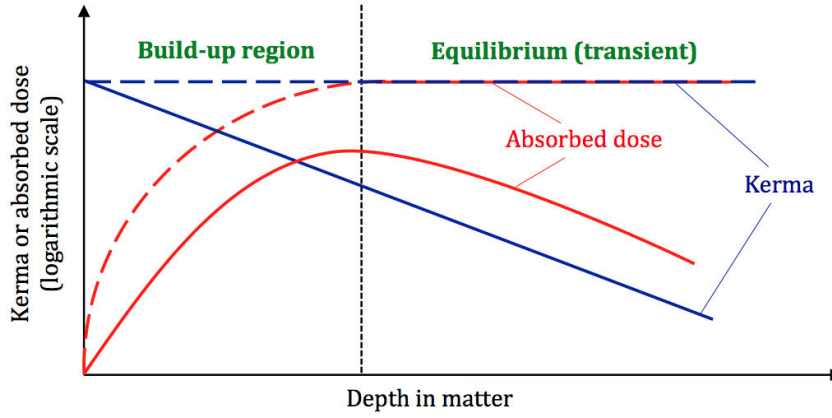


Fig. A.2: Absorbed dose and kerma as function of the depth within matter with (dashed lines) and without (solid lines) attenuation for an incident uncharged radiation.

Equivalent dose

The equivalent dose in a human organ or tissue, H_T , is a radiation-weighted dose quantity which takes into account the type of ionizing radiation as follows:

$$H_T = \sum_R w_R \mathbf{D}_{T,R}, \quad (\text{A.3})$$

where $\mathbf{D}_{T,R}$ is the absorbed dose in the human organ or tissue T by the ionizing radiation R and w_R is the radiation weighting factor. The sum is performed over all types of radiations involved. The SI unit of the equivalent dose is J kg^{-1} and has the special name of Sievert (Sv). When divided by the exposure time, it is known as *equivalent dose rate* or \dot{H}_T with the most common unit of mSv/h.

The Sievert unit is also used for the effective dose as well as for operational dose quantities (see the following sections) although the meaning of each one of them is not the same. Therefore, care must be taken to ensure that the dosimetric quantity being used is clearly stated.

The values of w_R were defined largely on the basis of the relative biological effectiveness (RBE) of the different types of ionizing radiation. They are specified in terms of type and, in the case of neutrons, in terms of energy of radiation either incident on the human body or emitted by radionuclides residing in the body, see Table A.1.

$$w_R = \begin{cases} 2.5 + 18.2 \exp\left(-\frac{\ln^2(E_n)}{6}\right), & E_n < 1 \text{ MeV} \\ 5.0 + 17.0 \exp\left(-\frac{\ln^2(2E_n)}{6}\right), & 1 \text{ MeV} \leq E_n \leq 50 \text{ MeV} \\ 2.5 + 3.25 \exp\left(-\frac{\ln^2(0.04E_n)}{6}\right), & E_n > 50 \text{ MeV} \end{cases} \quad (\text{A.4})$$

Table A.1: Radiation weighting factors. Source: [208].

Radiation Type	w_R
Photons	1
Electrons	1
Muons	1
Protons	2
Charges pions	2
Alpha particles	20
Fission fragments	20
Heavy ions	20
Neutrons	see Eq. (A.4)

Effective dose

The notion of effective dose, \mathbf{E} , was defined to take into account that the probability of biological effects depends on both the type of ionizing radiation and the irradiated human organ or tissue. It can be calculated as the tissue-weighted sum of the equivalent doses over all organs and tissues of the human body considered to be sensitive to the induction of cancer and/or genetic mutations:

$$\mathbf{E} = \sum_T w_T H_T = \sum_T w_T \sum_R w_R \mathbf{D}_{T,R} \quad (\text{A.5})$$

where w_T is the weighting factor for the considered tissue T (with $\sum_T w_T = 1$).

As stated above, the SI unit of the effective dose is the Sievert (Sv) and when divided by the exposure time it is known as the *effective dose rate* or $\dot{\mathbf{E}}$ with the most common unit of mSv/h. The recommended w_T values for different organs and tissues are given in Table A.2. They are based on the last epidemiological data for cancer induction.

Table A.2: Recommended tissue weighting factors. Source: [208].

Tissue	w_T	$\sum_T w_T$
Bone-marrow (red), colon, lung, stomach	0.12	0.72
Breast, gonads, remainder tissues ⁴	0.08	0.08
Bladder, oesophagus, liver, thyroid	0.04	0.16
Bone surface, brain, salivary glands, skin	0.01	0.04
	Total	1

Operational quantities

Neither the effective dose, E , nor the equivalent dose, H_T , are quantities that can be measured in a straight forward manner. For this reason, they cannot be used directly in the case of external radiation monitoring. This circumstance has forced the development of operational quantities to be used in both environmental and individual monitoring of external radiation fields allowing, in principle, a conservative estimate of the above limiting quantities under nearly all irradiation conditions.

Up to three operational dose quantities, which are measurable and traceable to metrology standards, are required for each specified task in radiological protection to surrogate E and H_T (see Table A.3). These include area monitoring for controlling the radiation in workplaces, and personal dosimetry for the control and diminution of individual exposures. While measurements with an area monitor are preferably performed free in air, personal dosimeters are worn on the body. As a consequence, in a given situation, the radiation field 'seen' by an area monitor free in air differs from that 'seen' by a personal dosimeter worn on the body where the radiation field may be influenced by the backscatter and absorption of radiation in the body itself.

Using the scheme of Table A.3, it is not necessary to use the former terms '*strongly penetrating ionizing radiation*' and '*weakly penetrating ionizing radiation*' in specifying the range of application of these operational quantities. The International Commission on Radiation Units and Measurements (ICRU) in its Report 51 [209] stated that $H^*(10)$ and $H_p(10)$ are designed for monitoring strongly penetrating ionizing radiation (e.g., photons above 12 keV and neutrons) whereas $H'(0.07, \Omega)$ and $H_p(0.07)$ are applied for monitoring low-penetrating ionizing radiation (e.g., beta particles). Furthermore, $H_p(0.07)$ is also used for monitoring the skin dose from all ionizing radiation. For the special case of controlling the dose to the eye lens, $H'(3, \Omega)$ and $H_p(3)$ are strongly recommended. In fact, the ICRP publication 118 revised downwards the occupational exposure limits associated to this organ because of the recent epidemiological studies that showed a higher incidence of cataracts than expected at low doses (< 0.5 Gy) [210].

The definitions of three operational quantities are given below.

Ambient dose equivalent

The ambient dose equivalent, $H^*(10)$, is the absorbed dose that would be, by the corresponding expanded⁵ and aligned⁶ field, at a depth of 10 mm on the radius of the ICRU sphere (see Fig. A.3) of 30 cm diameter, 1 g cm⁻³ mass density and made of a tissue equivalent material⁷, located at the point of interest and oriented opposite to the direction of such aligned field. With this definition,

⁴Such as adrenals, extra-thoracic region, gallbladder, heart, kidneys, lymphatic nodes, muscle, tongue, mucosa, pancreas, prostate, small intestine, spleen, thymus, and uterus/cervix.

⁵A hypothetical radiation field in which the spectral and the angular fluence have the same value in all points of a sufficiently large volume to ensure a homogeneous exposition.

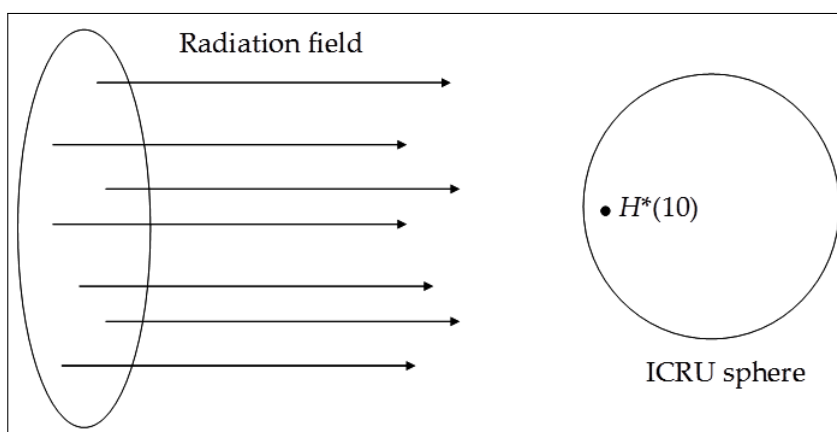
⁶A hypothetical radiation field in which the fluence is unidirectional.

⁷Chemical composition: 76.2% oxygen + 11.1% carbon + 10.1% hydrogen + 2.6% nitrogen.

Table A.3: Radiation protection operational quantities.

Task	Operational quantities	
	Area monitoring	Individual monitoring
	Ambient dose equivalent	Personal dose equivalent
Control of effective dose	$H^*(10)$	$H_p(10)$
	Directional dose equivalent	Personal dose equivalent
Control of equivalent dose to skin	$H'(0.07, \Omega)$	$H_p(0.07)$
Control of equivalent dose to eye lens	$H'(3, \Omega)$	$H_p(3)$

$H^*(10)$ should hypothetically estimate the effective dose \mathbf{E} regardless of the irradiation geometry. When divided by the exposure time, it is known as *ambient dose equivalent rate* or $\dot{H}^*(10)$.

Fig. A.3: Concept of ambient dose equivalent $H^*(10)$.

Directional dose equivalent

The directional dose equivalent, $H'(d, \Omega)$, at a given point in a radiation field, is the dose equivalent that would be produced by the corresponding expanded field in the ICRU sphere at a depth d , on a radius in a specified direction Ω (see Fig. A.4). When divided by the exposure time, it is known as *directional dose equivalent rate* or $\dot{H}'(d, \Omega)$.

For low-penetrating radiation the recommended depth is 0.07 mm and the directional dose equivalent must be $H'(0.07, \Omega)$.

Personal dose equivalent

The personal dose equivalent, $H_p(d)$, is the dose equivalent in ICRU tissue at a depth d in a human body below the position where an individual dosimeter is worn. When divided by the exposure time, it is known as *personal dose equivalent rate* or $\dot{H}_p(d)$.

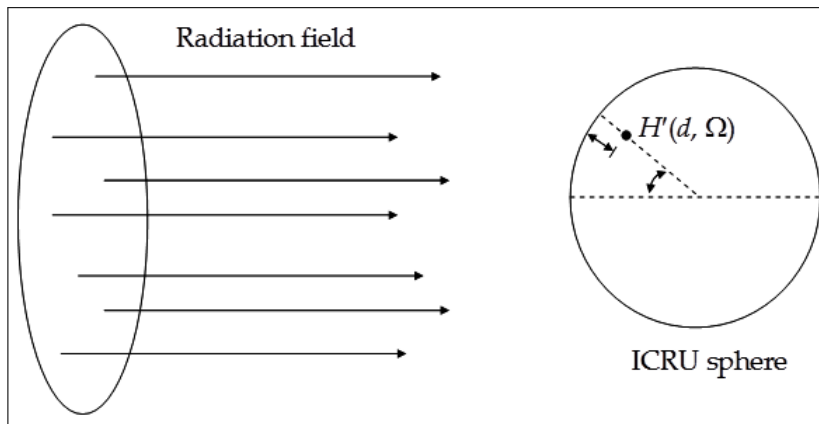


Fig. A.4: Concept of the directional dose equivalent, $H'(d, \Omega)$.

For the assessment of effective dose a depth $d = 10$ mm is recommended, whereas the recommended depth for assessing equivalent dose to the skin is $d = 0.07$ mm. As stated above, it has been proposed that a depth $d = 3$ mm would be more appropriate to control the equivalent dose to the eye lens.

Calibration procedures

Calibration of area monitor in terms of $H^*(10)$ and $H'(d, \Omega)$ is performed free in air by determining the appropriate primary quantity (i.e., air kerma for photons, fluence for neutrons and absorbed dose for electrons)⁸ and applying the corresponding energy-dependent conversion coefficients given in [104].

On the opposite, as illustrated in Fig. A.5, calibration of $H_p(d)$ needs the use of an appropriate personal dosimeter mounted on a slab phantom representing parts of human bodies. For this purpose, the following three phantoms are frequently proposed (see Fig. A.6):

- A PMMA cube filled with water to simulate the human torso with external dimensions of $30 \text{ cm} \times 30 \text{ cm} \times 15 \text{ cm}$. All of its walls are 10 mm thick except the front one that must not exceed 2.5 mm thick.
- A PMMA circular cylinder, of 73 mm diameter and 300 mm length, filled with water to simulate a lower human arm or leg. Its lateral wall must be 2.5 mm thick while the corresponding bottom and cover plates are 10 mm thick each.
- A PMMA rod of 19 mm diameter and 300 mm length to simulate a human finger.

Conversion coefficients relating between the primary (air kerma in the case of photons) and operational quantities must be calculated assuming vacuum outside of the ICRU sphere and the above ISO phantoms.

⁸This is only true in Radiation Protection; however, for medical therapeutic applications, absorbed dose (to water) is also used for photons and air kerma for neutrons in order to well calibrate the quality properties of the planned irradiation beams.

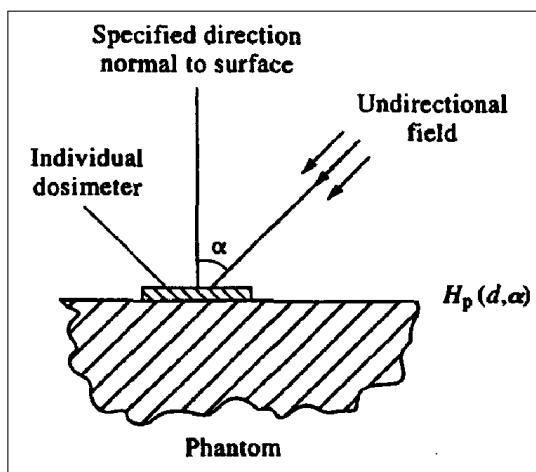


Fig. A.5: Calibration of the personal dose equivalent, $H_p(d)$.



Fig. A.6: ISO phantoms representing parts of human bodies (torso, arm, and finger).

Appendix B

KIT measurement results

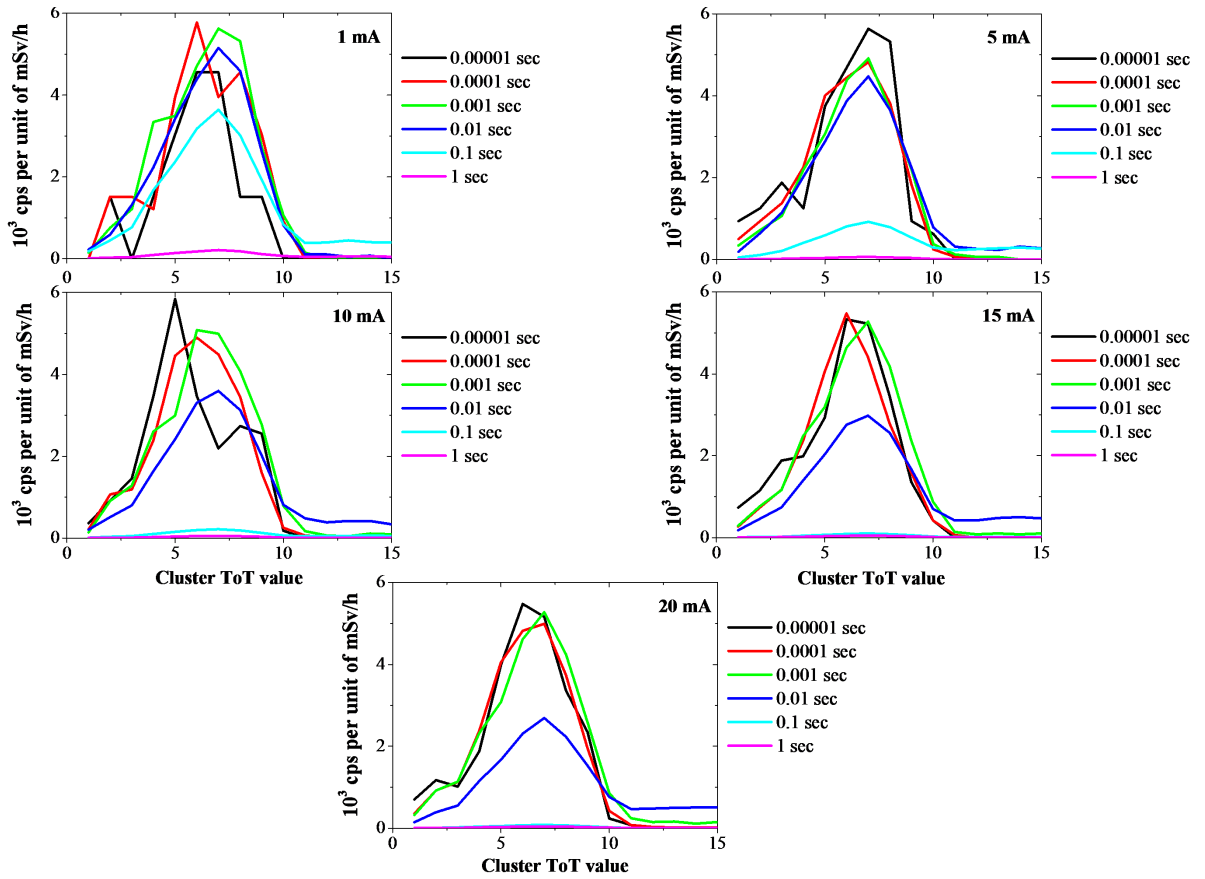


Fig. B.1: Cluster ToT distributions measured with the mask R7e8 under different shutter-times for the N-15 ($E_{mean} = 13.3$ keV) X-ray narrow beams of varied currents. Owing to the photoelectric process there is a single full-energy peak.

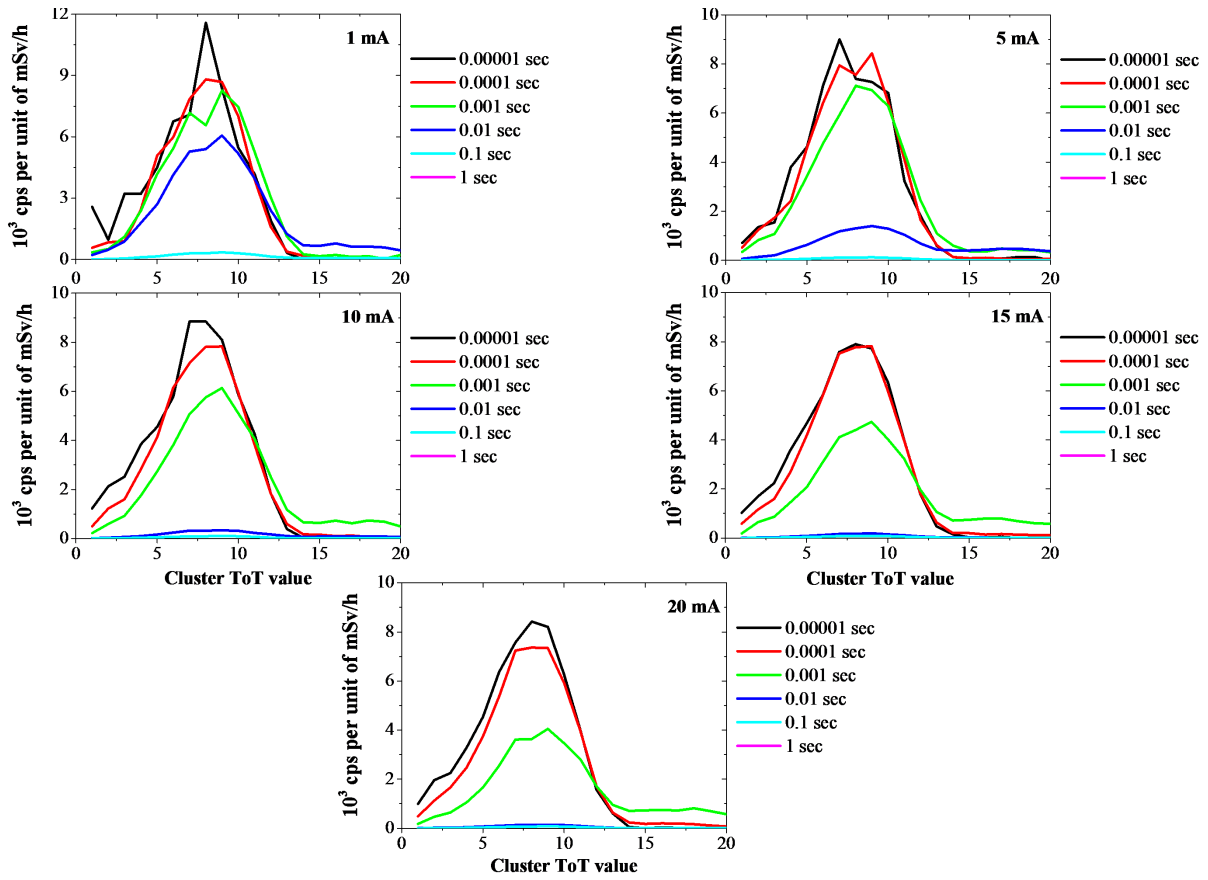


Fig. B.2: Cluster ToT distributions measured with the mask R7e8 under different shutter-times for the N-20 ($E_{mean} = 16.9$ keV) X-ray narrow beams of varied currents. Owing to the photoelectric process there is a single full-energy peak.

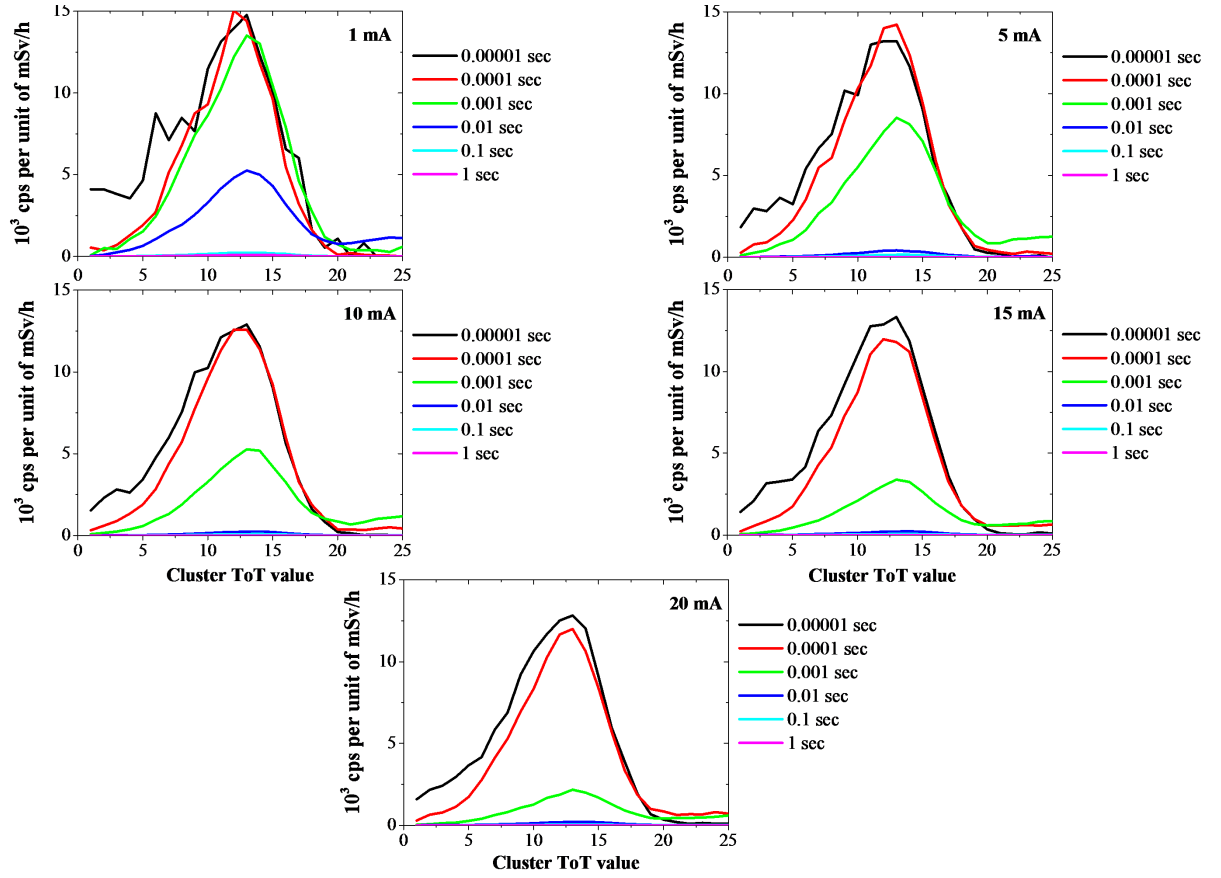


Fig. B.3: Cluster ToT distributions measured with the mask R7e8 under different shutter-times for the N-30 ($E_{mean} = 24.6$ keV) X-ray narrow beams of varied currents. Owing to the photoelectric process there is a single full-energy peak.

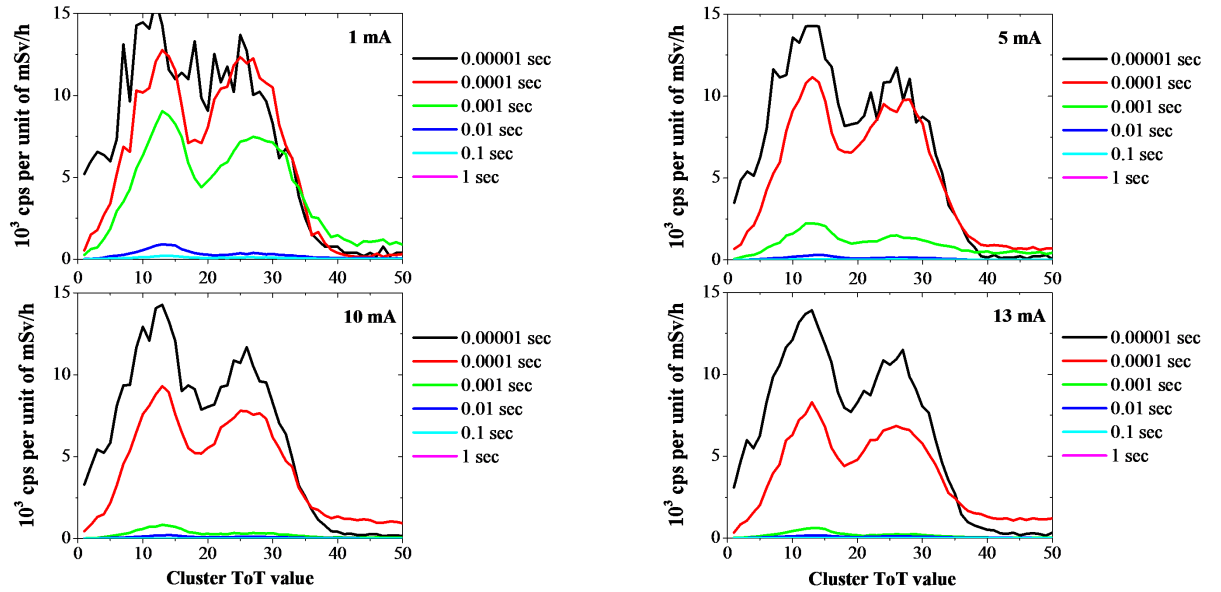


Fig. B.4: Cluster ToT distributions measured with the mask R7e8 under different shutter-times for the N-60 ($E_{mean} = 47.6$ keV) X-ray narrow beams of varied currents. Besides the full-energy peak, an additional one appears on the left at around 13 ToT (i.e. $1.4 \mu\text{s}$).

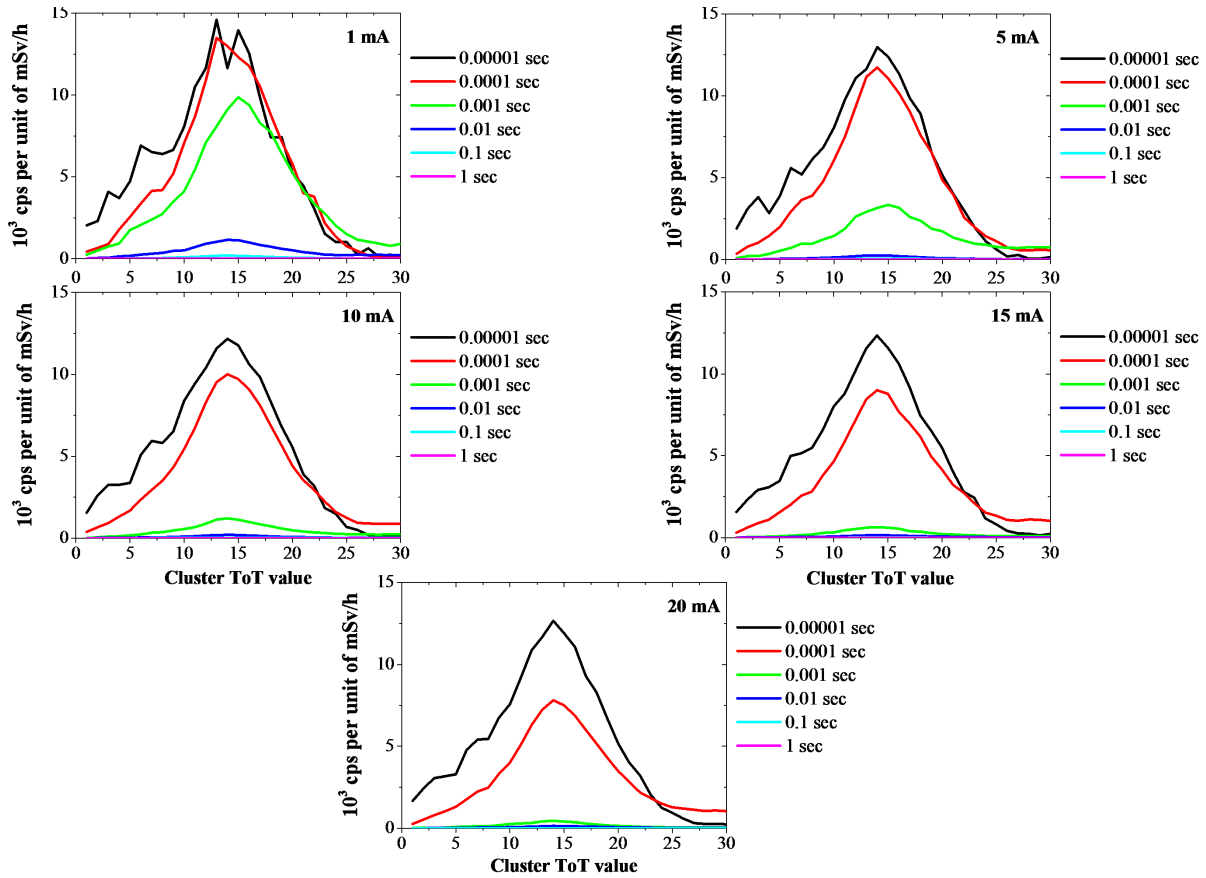


Fig. B.5: Cluster ToT distributions measured with the mask R7e8 under different shutter-times for the N-40 ($E_{\text{mean}} = 33.0$ keV) X-ray narrow beams of varied currents. Owing to the photoelectric process there is a single full-energy peak.

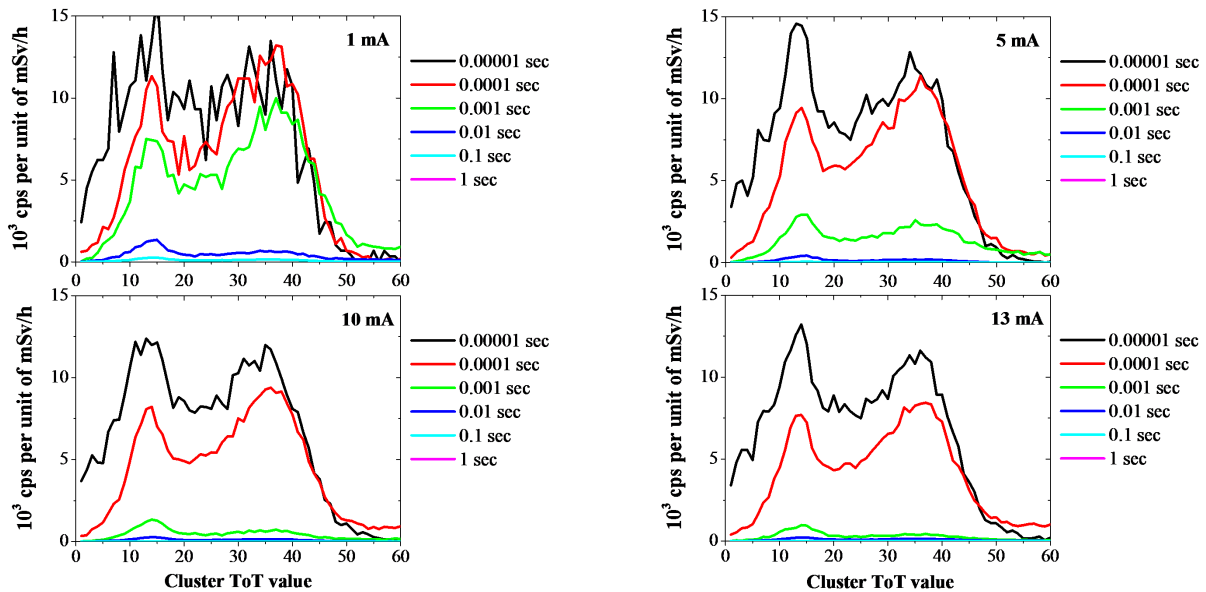


Fig. B.6: Cluster ToT distributions measured with the mask R7e8 under different shutter-times for the N-80 ($E_{\text{mean}} = 65.3$ keV) X-ray narrow beams of varied currents. Unlike the full-energy peak, the additional one does not move to the right with increasing the incident photon energy.

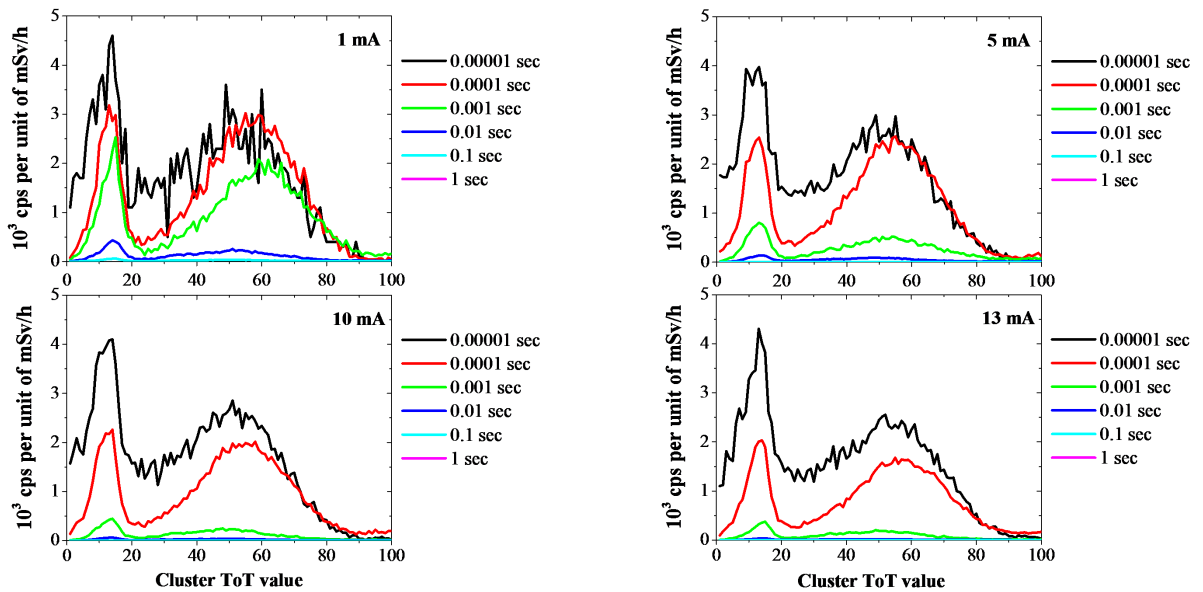


Fig. B.7: Cluster ToT distributions measured with the mask R7e8 under different shutter-times for the N-150 ($E_{\text{mean}} = 118.4$ keV) X-ray narrow beams of varied currents. Unlike the full-energy peak, the additional one does not move to the right with increasing the incident photon energy.

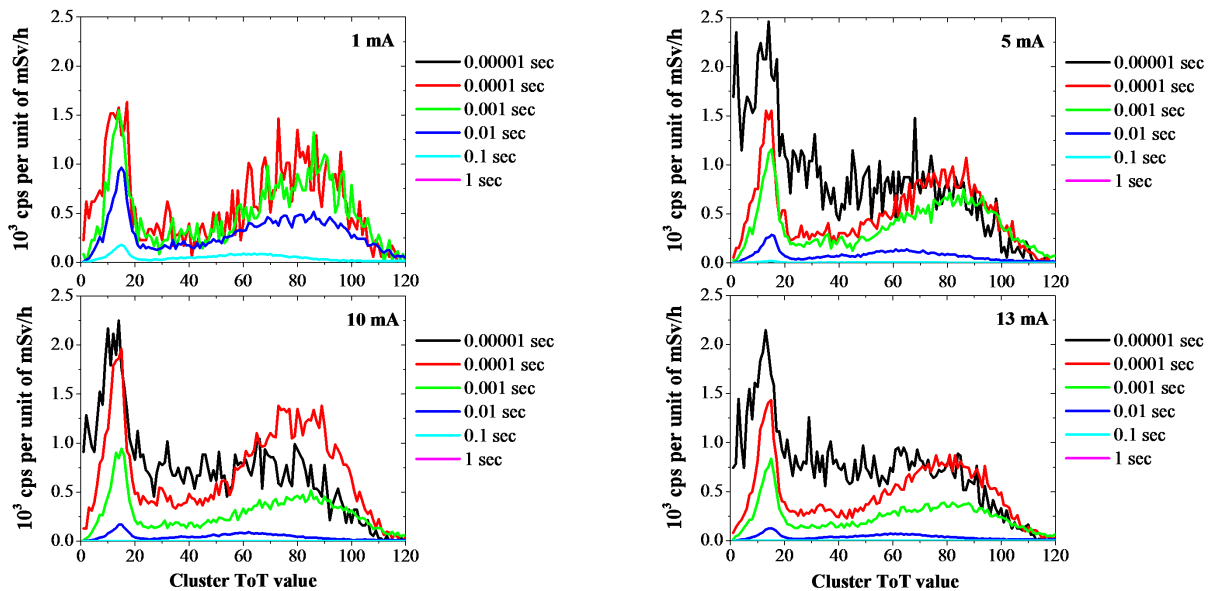


Fig. B.8: Cluster ToT distributions measured with the mask R7e8 under different shutter-times for the N-200 ($E_{\text{mean}} = 154.5$ keV) X-ray narrow beams of varied currents. Data obtained with a 10^{-5} sec shutter-time and at low (1 mA) beam input current were statistically insignificant and are not reproduced here. Unlike the full-energy peak, the additional one does not move to the right with increasing the incident photon energy.

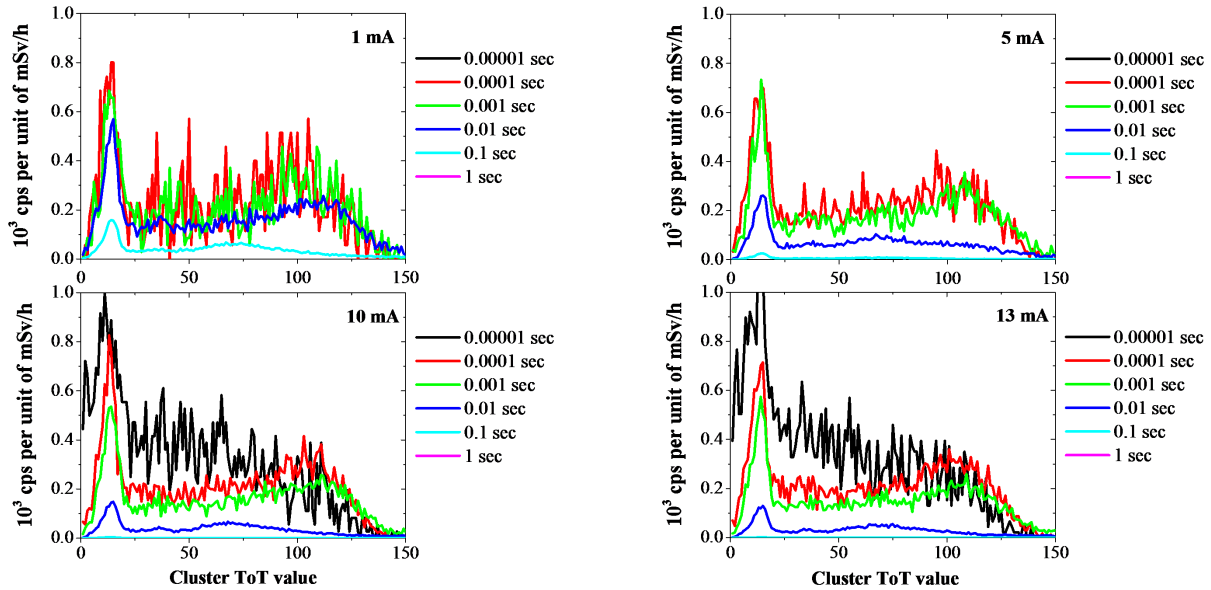


Fig. B.9: Cluster ToT distributions measured with the mask R7e8 under different shutter-times for the N-250 ($E_{\text{mean}} = 207.3$ keV) X-ray narrow beams of varied currents. Data obtained with a 10^{-5} sec shutter-time and at low (1 mA) beam input current were statistically insignificant and are not reproduced here. The measurement files for 10^{-5} sec shutter-time and 5 mA beam input current were corrupted. The full-energy peak is no longer visible whereas the additional one is still appearing.

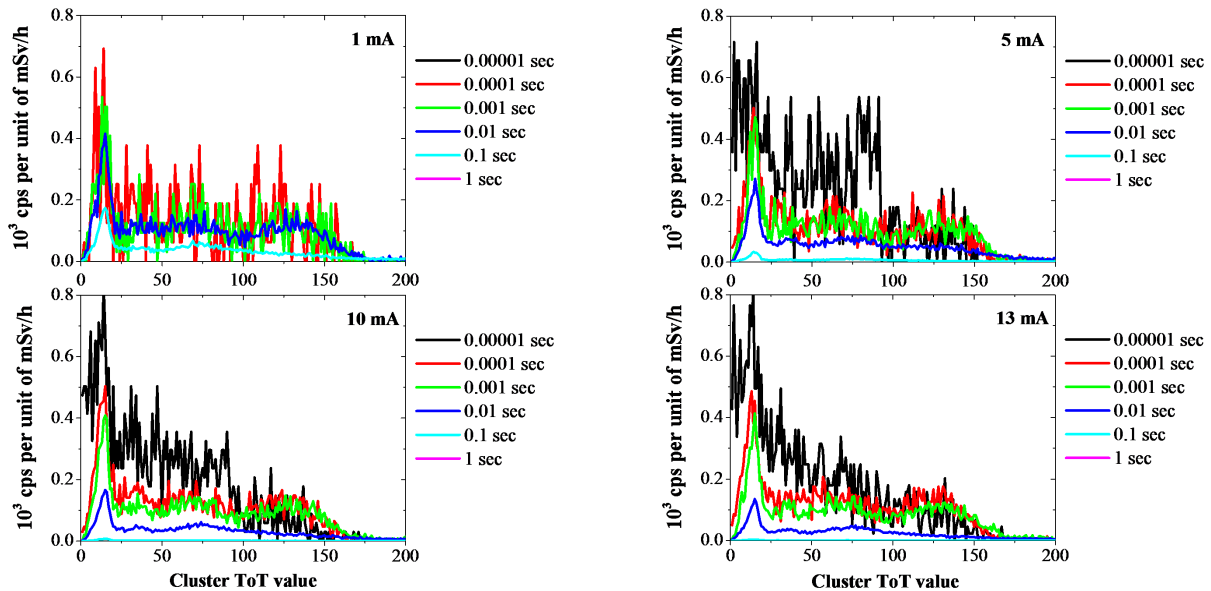


Fig. B.10: Cluster ToT distributions measured with the mask R7e8 under different shutter-times for the N-300 ($E_{\text{mean}} = 247.5$ keV) X-ray narrow beams of varied currents. Data obtained with a 10^{-5} sec shutter-time and at low (1 mA) beam input current were statistically insignificant and are not reproduced here. The full-energy peak is no longer visible whereas the additional one is still appearing.

Table B.1: ISO X-ray narrow beams (15-60 kV) together with the measured ambient dose equivalent rates at varied input currents (details are provided in the text).

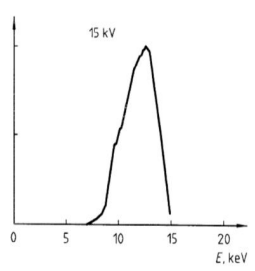
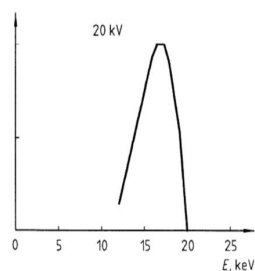
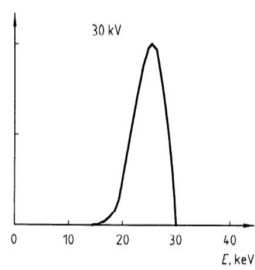
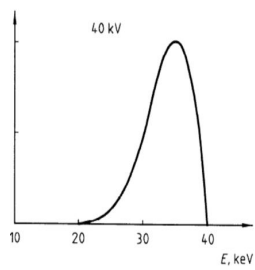
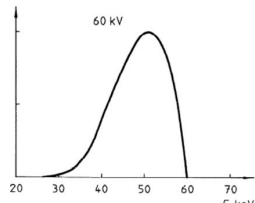
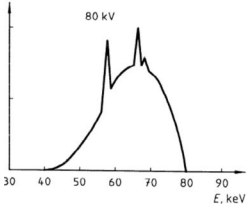
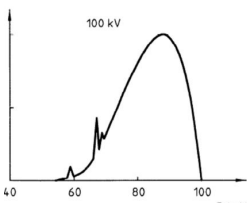
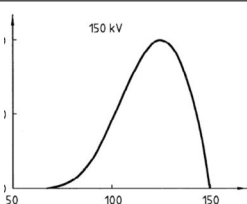
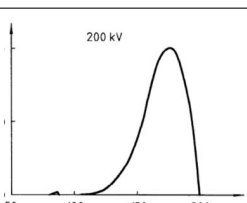
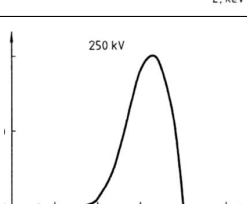
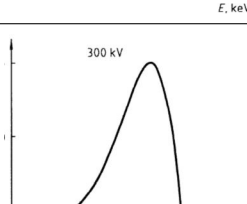
ISO reference	Distance	Beam Inputs		Mean Energy	$\dot{H}^*(10)$ (mSv/h)	Energy Spectrum
		Voltage	Current			
N-15	200 cm	15 kV	1 mA	13.3 keV	0.34 ± 0.02	
			5 mA		1.64 ± 0.08	
			10 mA		3.27 ± 0.16	
			15 mA		4.91 ± 0.25	
			20 mA		6.56 ± 0.33	
N-20	200 cm	20 kV	1 mA	16.9 keV	1.58 ± 0.08	
			5 mA		7.89 ± 0.39	
			10 mA		15.72 ± 0.79	
			15 mA		23.6 ± 1.2	
			20 mA		31.5 ± 1.6	
N-30	200 cm	30 kV	1 mA	24.6 keV	1.83 ± 0.09	
			5 mA		9.23 ± 0.46	
			10 mA		18.44 ± 0.92	
			15 mA		27.5 ± 1.4	
			20 mA		36.8 ± 1.8	
N-40	200 cm	40 kV	1 mA	33.0 keV	3.91 ± 0.19	
			5 mA		19.51 ± 0.98	
			10 mA		38.5 ± 1.9	
			15 mA		57.3 ± 2.9	
			20 mA		76.2 ± 3.8	
N-60	200 cm	60 kV	1 mA	47.6 keV	2.59 ± 0.13	
			5 mA		13.15 ± 0.66	
			10 mA		26.5 ± 1.3	
			13 mA		34.5 ± 1.7	

Table B.2: ISO X-ray narrow beams (80-300 kV) together with the measured ambient dose equivalent rates at varied input currents (details are provided in the text).

ISO reference	Distance	Beam Inputs		Mean Energy	$\dot{H}^*(10)$ (mSv/h)	Energy Spectrum
		Voltage	Current			
N-80	200 cm	80 kV	1 mA	65.3 keV	1.45 ± 0.07	
			5 mA		7.47 ± 0.37	
			10 mA		14.93 ± 0.75	
			13 mA		19.42 ± 0.97	
N-100	200 cm	100 kV	1 mA	83.8 keV	0.57 ± 0.03	
			5 mA		2.91 ± 0.16	
			10 mA		5.83 ± 0.29	
			13 mA		8.03 ± 0.40	
N-150	200 cm	150 kV	1 mA	118.4 keV	5.00 ± 0.25	
			5 mA		25.4 ± 1.3	
			10 mA		50.6 ± 2.5	
			13 mA		67.7 ± 3.4	
N-200	200 cm	200 kV	1 mA	164.5 keV	1.78 ± 0.09	
			5 mA		9.14 ± 0.46	
			10 mA		18.68 ± 0.93	
			13 mA		24.2 ± 1.2	
N-250	200 cm	250 kV	1 mA	207.3 keV	1.75 ± 0.09	
			5 mA		9.00 ± 0.46	
			10 mA		18.02 ± 0.93	
			13 mA		22.8 ± 1.2	
N-300	200 cm	300 kV	1 mA	247.5 keV	1.59 ± 0.08	
			5 mA		8.37 ± 0.42	
			10 mA		16.87 ± 0.84	
			13 mA		22.2 ± 1.1	

Appendix C

Summary of the laboratory radioactive sources used

Summary of the decays schemes of each radionuclide used

- ^{241}Am , with half-life of 432.6 years, decays 100% by alpha transition to ^{237}Np . Most of the decay (84.6%) populate the excited level of ^{237}Np with energy of 59.54 keV. It thus predominantly radiates through its daughter the 59.54 keV γ -ray with an emission intensity¹ of 35.92%.
- ^{57}Co , with half-life of 271.8 days, disintegrates by 100% electron capture to the excited levels of 706.42 keV (0.18%), and 136.47 keV (99.82%) in ^{57}Fe . It thus predominantly radiates through its daughter The following two γ -rays of interest: 122.06065 keV (85.51%) and 136.47356 keV (10.71%).
- ^{137}Cs , with half-life of 30.05 years, disintegrates by beta minus emission to the ground state of ^{137}Ba (5.7%) and via the 661 keV isometric level of ^{137}Ba (94.4%) which has a half-life of 2.55 min. It thus predominantly radiates through its daughter the 661.657 keV γ -ray with an emission intensity of 84.99% as well as the following three X-rays: 31.8174 keV (1.95%), 32.1939 keV (3.59%) and 36.4457 keV (1.055%).
- ^{60}Co , with half-life of 5.2711 years, mainly disintegrates by beta minus emission to two excited levels (1173.228 keV and 1332.492 keV) of ^{60}Ni . It thus predominantly radiates through its daughter the 1173.228 keV and 1332.492 keV γ -rays with an emission intensity of 99.85% and 99.9826%, respectively.

¹The emission intensity is by definition the number of emitted particles accompanying each disintegration of the radioactive nucleus.

- ^{152}Eu , with half-life of 13.522 years, disintegrates 72.1% by electron-capture and about 0.027% by emission of positrons to ^{152}Sm and by beta minus emission (27.9%) to ^{152}Gd . It thus radiates through its daughter up to eighteen X- and γ -rays of interest with energies ranging from 39.5229 keV to 1408.03 keV.
- ^{133}Ba , with half-life of 10.539 years, disintegrates by electron-capture mainly to two ^{133}Cs excited levels of 437 keV (85.4%) and of 383 keV (14.5%) with three very minor branches to the 160 keV, 81 keV excited levels and the ground state. It thus predominantly radiates through its daughter up to eleven X- and γ -rays of interest with energies ranging from 30.6254 keV to 383.8485 keV.

The reader is referred to <http://www.nucleide.org/Laraweb/> for more information about the decay schemes of the above radionuclides.

Table C.1: Sources of the irradiators made available by the CANBERRA Loches site (Chapter 2).

Radionuclide	Nominal activity	Reference date
^{137}Cs	3 GBq - 30 TBq	01/11/2011
^{241}Am	1.85 GBq	14/04/2014
^{137}Cs	300 MBq	26/06/2013
^{60}Co	70 MBq	18/11/2011
^{241}Am	414 kBq	06/07/2011
^{137}Cs	401 kBq	16/06/2011
^{60}Co	372 kBq	16/06/2011

X-ray beams

All the KIT X-ray beams, along with their theoretical energy distributions, are listed in Appendix B, in Tables B.1 and B.2.

Table C.2: Low-activity planar sources fabricated and made available by the "Laboratoire de Métrologie de l'Activité Laboratoire National Henri Becquerel" (LNHB). Département Métrologie, Instrumentation et Information, CEA Saclay.

Number of units	Radionuclide	Surface activity* (kBq/cm ²)	Nominal activity	Reference date
3	⁵⁷ Co	3.65	429 kBq	30/04/2016
3	⁵⁷ Co	7.37	143 kBq	30/04/2016
3	²⁴¹ Am	3.65	144 kBq	13/01/2015

*To verify the fabrication procedure, a low activity ⁵⁷Co solution (about 13 kBq/g) was used to prepare the sources and assess their homogeneity using an auto-radiographer (10 min exposure time). The standard deviation obtained was 13% for 10 mm² and 9% for 40 mm², respectively.

Table C.3: Radioactive sources made available by the University of Caen Normandy.

Radionuclide	Nominal activity	Reference date
²⁴¹ Am	370 MBq	11/07/2000
¹³⁷ Cs	370 MBq	17/05/2001

Table C.4: Radioactive sources made available by the "Laboratoire simulation et techniques de démantèlement nucléaire", CEA Marcoule.

Radionuclide	Current activity
²⁴¹ Am	150 kBq
¹³⁷ Cs	329 MBq
¹⁵² Eu	9.63 MBq
¹³³ Ba	9.92 MBq

List of tables

2.1	Low-activity point sources used for sensitivity measurements.	28
2.2	Minimum localization time (considering data collection only).	32
2.3	Comparison between CARTOGAM and iPIX in terms of minimum localization time (considering data collection only).	32
2.4	Determination of the iPIX angular resolution.	38
3.1	Annual limits for personal effective doses as laid down in European legislations.	48
3.2	Dose limits in any consecutive 12-month period at CERN during maintenance and emergency activities.	49
3.3	Low-activity planar sources used at CEA-LIST Saclay.	58
4.1	Distances retrieved by means of the calibrated depth sensor and the stereo γ -camera proof of concept	123
A.1	Radiation weighting factors. Source: [208].	155
A.2	Recommended tissue weighting factors. Source: [208].	155
A.3	Radiation protection operational quantities.	157
B.1	ISO X-ray narrow beams (15-60 kV) together with the measured ambient dose equivalent rates at varied input currents (details are provided in the text).	167
B.2	ISO X-ray narrow beams (80-300 kV) together with the measured ambient dose equivalent rates at varied input currents (details are provided in the text).	168
C.1	Sources of the irradiators made available by the CANBERRA Loches site (Chapter 2).	170
C.2	Low-activity planar sources fabricated and made available by the "Laboratoire de Métrologie de l'Activité Laboratoire National Henri Becquerel" (LNHB). Département Métrologie, Instrumentation et Information, CEA Saclay.	171
C.3	Radioactive sources made available by the University of Caen Normandy.	171
C.4	Radioactive sources made available by the "Laboratoire simulation et techniques de démantèlement nucléaire", CEA Marcoule.	171

List of figures

1.1	Illustration of the scintillation camera proposed by Anger in [31].	4
1.2	Main pinhole gamma cameras developed by CEA and CANBERRA.	5
1.3	Diagram of the detector of the CARTOGAM gamma imaging system [7].	6
1.4	Illustration of the principle of the coded aperture technique. In this example, incoming photons emitted from a radioactive source hit a coded mask, casting a shadow of part of its pattern onto a position-sensitive detector.	7
1.5	(a) A Fresnel Zone Plate (FZP) pattern with three opaque rings and (b) its auto-correlation function [46].	7
1.6	HURA masks designed and built (in tungsten) for the ALADIN and CARTOGAM gamma cameras [8].	8
1.7	The Medipix2 chip.	9
1.8	The GAMPIX gamma camera developed by CEA LIST [9].	10
2.1	The iPIX gamma camera (left) and a cross-sectional view (right), not to scale, showing its main components and relevant dimensions. The camera has three coded masks (see Section 2.3), which are labelled by different colours to facilitate their identification during measurements.	13
2.2	Comparison between MPX and ToT modes of the Timepix chip.	15
2.3	ToT value vs. full deposited gamma energy for single-pixel clusters.	16
2.4	Illustration of the charge sharing effect (left) and the application of the cluster reconstruction method (right).	17
2.5	Summation of succeeding pulses due to excessive shutter time.	18
2.6	Illustration of the pulse pile-up effect.	18
2.7	Pattern designs for the iPIX coded aperture masks.	19
2.8	(a) Drawing of the KIT X-ray irradiation facility with a reference ionization chamber located at the measurement point, and (b) preparing the respective measurements with the iPIX γ -camera.	20
2.9	CANBERRA "big" ^{137}Cs irradiator.	21
2.10	Other CANBERRA irradiation equipment.	21

2.11 Cluster ToT distributions measured with the mask R7e8 under different shutter times for the N-100 ($E_{\text{mean}} = 83.8$ keV) X-ray narrow beams of varied currents. When the shutter time is correctly chosen (i.e. 10^{-4} sec), the associated count rates per unit of mSv/h do not change when only the X-ray beam current is varied. Data obtained with a 10^{-5} sec shutter time and at low (1 mA) beam input current were statistically insignificant, and are not reproduced here. Unlike the full-energy peak, the additional one does not move to the right with increasing the incident photon energy.	23
2.12 ToT-photon energy calibration curve for the iPIX gamma camera.	24
2.13 Measured ^{137}Cs spectrum with iPIX.	25
2.14 Dose response curves for the ^{137}Cs radioactive source measured directly with iPIX using the mask R7e4. A similar behavior was also observed with the mask R7e8.	26
2.15 Dose calibration factor of the iPIX as a function of the incident photon energy. . .	27
2.16 Cluster size distributions measured with the mask R7e8 for X-ray narrow beams. . .	27
2.17 Cluster size distributions measured with the mask R7e8 for ^{137}Cs and ^{60}Co	28
2.18 Measurement results of the iPIX obtained in automatic mode with a 412 kBq ^{241}Am point source located at a distance of 48 cm with varied background radiation. With the exception of the mask R13e2, all measurements were performed both in mask and antimask positions. The location of the considered radioactive sources are indicated by white arrows. At very close source-to-detector distances (i.e. less than 50 cm), slight mismatches occurred when superimposing the radiation image onto the respective optical image.	29
2.19 Measurement results of iPIX obtained in automatic mode with a 368 kBq ^{137}Cs point source located at a distance of 64.5 cm with varied background radiation. All measurements were performed both in mask and antimask positions. The location of the considered radioactive sources are indicated by white arrows.	30
2.20 Measurement results of iPIX obtained in automatic mode with a 226 kBq ^{60}Co point source located at a distance of 22.3 cm with varied background radiation. All measurements were performed both in mask and antimask positions. The location of the considered radioactive sources are indicated by white arrows. . . .	31
2.21 Results obtained with the 1.85 GBq ^{241}Am source located at a distance of 330 cm from the iPIX with natural background radiation condition ($0.1 - 0.2$ $\mu\text{Sv/h}$). The shutter time was set by the iPIX to 1 sec, and 200 frames were collected in mask and antimask positions (100 + 100) for the measurements performed with masks R7e8 and R7e4, whereas 200 frames only in mask position were collected with the R13e2 mask. The cut-off threshold applied for the superimposition of the radiation image onto the optical image is 70% for all measurements.	33

- 2.22 Results obtained with the 1.85 GBq ^{241}Am source located at a distance of 330 cm from the iPIX with an enhanced background dose rate of 310 $\mu\text{Sv/h}$ generated by the ^{137}Cs source of the CANBERRA small irradiator. The shutter time was set by the iPIX to 1 sec, and 200 frames were collected in mask and antimask positions (100 + 100) for the measurements performed with masks R7e8 and R7e4, whereas 200 frames only in mask position were collected with the R13e2 mask. The cut-off threshold applied for the superimposition of the radiation image onto the optical image is 70% for all measurements. 34
- 2.23 Results obtained with the 1.85 GBq ^{241}Am source located at a distance of 330 cm from the iPIX with an enhanced background dose rate of 215 $\mu\text{Sv/h}$ generated by the ^{60}Co source of the CANBERRA small irradiator. The shutter time was set by the iPIX to 1 sec, and 200 frames were collected in mask and antimask positions (100 + 100) for the measurements performed with masks R7e8 and R7e4, whereas 200 frames only in mask position were collected with the R13e2 mask. The cut-off threshold applied for the superimposition of the radiation image onto the optical image is 70% for all measurements. 34
- 2.24 Normalized count rates observed for the masks R7e4 and R7e8 at varied pan or tilt rotation angles obtained with the ^{137}Cs source. 35
- 2.25 Mask self-collimation effect. 35
- 2.26 iPIX results at varied pan angles. 36
- 2.27 Illustration of the mirroring effect at the limit of the iPIX field of view. Radiation of the two peripheral sources (radiation direction indicated with red and blue arrows) project identical portions of the mask pattern onto the detector surface. 36
- 2.28 Vertical and horizontal axial profile of the hotspot peak. 37
- 2.29 Measurement results of three identical ^{241}Am sources with mask R7e4 at different separation angles. 38
- 2.30 Measurement results of three identical ^{241}Am sources with mask R7e8 at different separation angles. 39
- 3.1 Diagram of the CERN accelerator complex. Protons are initially accelerated through a series of particle accelerators to increasingly higher energies (at time of writing, up to 13 TeV). Afterwards, such accelerated particles enter in two separate beam pipes and travel in opposite directions though the main LHC ring with circumference of 27 km, colliding in four particle detectors: ATLAS, CMS, ALICE, and LHCb. Image: CERN. 43
- 3.2 CERN Control Centre during the first high-energy collisions in the LHC on 30 March 2010. Image: CERN. 43
- 3.3 Cut-away view of the ATLAS detector. The dimensions of the detector are 25 m in height and 44 m in length. The overall weight of the detector is approximately 7000 tonnes [62]. Image: CERN. 44

3.4	Short access scenario. One half of the inner region of the ATLAS experiment during standard access. The dose rates in the two access areas are also shown. The calculation was performed for one year of running at $10^{34} \text{ cm}^{-2}\text{s}^{-1}$ luminosity and five days of cooling off [100].	46
3.5	Long access scenario. The central part of the ATLAS experiment during Inner Detector access. The dose rates in the two access areas are also shown. The calculation was performed for one year of running at $10^{34} \text{ cm}^{-2}\text{s}^{-1}$ luminosity and five days of cooling off [100].	46
3.6	The battery-powered EduPIX γ -camera prototype developed for EDUSAFE.	52
3.7	The EduPIX prototype (left) and the motorized pan-tilt unit adopted for remotely changing its position and orientation (right).	53
3.8	Representation of a rectangular (planar) source S of width w and length l . The detector is at distance D from the center of plane S	57
3.9	Planar ^{57}Co source of size $7 \text{ cm} \times 5.5 \text{ cm}$ with activity of 429 kBq at 50 cm from the gamma camera, providing an ambient dose equivalent rate of $\sim 340 \text{ nSv/h}$ at the measurement point.	58
3.10	3-D hotspot profile resulting from a measurement of a planar ^{57}Co source with activity of 429 kBq at 50 cm from the gamma camera, providing an ambient dose equivalent rate of $\sim 340 \text{ nSv/h}$ at the measurement point.	59
3.11	Measurement results obtained with a 429 kBq planar source located at a distance of 50 cm	59
3.12	Combination of planar ^{57}Co sources by placing them all adjacently respect to each other in order to simulate a pipeline elbow with 1716 kBq of total activity, at an average distance of 64 cm from the gamma camera. The three ^{57}Co sources with stronger activity (429 kBq) were placed on the left respect to the FOV of the γ -camera, whereas the ^{57}Co sources with activity of 143 kBq were stitched to the pipe so that they would be visualized in the center area of the FOV of the gamma camera prototype. The associated ambient dose equivalent rate at the measurement point was $\sim 280 \text{ nSv/h}$	60
3.13	Results obtained with mask R7e4 and by placing several ^{57}Co sources adjacently to simulate a pipeline elbow with 1716 kBq of total activity, at an average distance of 64 cm from the gamma camera. Several cut-off thresholds were applied during the superimposition phase for comparison purposes.	61
3.14	Results obtained with mask R7e4 and by placing several ^{57}Co sources adjacently in order to simulate a pipeline elbow.	62

- 3.15 Hotspot profile and superimposition results of a measurement performed involving two different radionuclides. Two ^{57}Co sources with activity of 143 kBq (total 286 kBq) were overlapped and placed on the right respect to the image plane of the gamma camera prototype, while two ^{241}Am sources with activity of 144 kBq (total 288 kBq) were overlapped and placed on its left. 63
- 3.16 Main functionalities of the EduPIX system provided by its graphical user interface. In this example, the buttons "clear γ -acquisition" and "superimpose γ -image" are greyed out as they are available only when an acquisition is in progress. 65
- 3.17 A general outline of the main steps of image stitching. Given a sequence of images, the geometric transformations between consecutive pairs of images are computed during the image registration phase. Once the images have been registered, they are reprojected according to the transformations found in the previous step, resulting in one single, wider image. Finally, the image compositing phase consists in compensating and mitigating the remaining colour discontinuities occurring in the overlapping regions, in order to create an image without any evident artifacts detectable by a human being. 67
- 3.18 Illustration of the two automated main acquisition phases with the EduPIX prototype of the optical images to be stitched. During the first phase of the acquisition, the images are acquired vertically (a). Once the horizontal 360° FOV has been entirely covered, each image previously vertically stitched is then horizontally stitched with the remaining ones. 67
- 3.19 After a set of distinctive keypoints are found, they are matched and interpreted as local descriptors, in order to establish the correspondence between the features detected in the first image and those detected in the reference image. 70
- 3.20 A panorama image with size 7234×1681 pixels captured and generated by the EduPIX prototype, using one single optical camera and a motorized pan-tilt unit, and resulting from the stitching of 80 optical images. The implemented algorithm allows the prototype to autonomously capture high-quality pictures, find and match consistent sets of invariant features, correctly register the images, and compose them together. Clearly, no radiation sources were present in this example. The images that have been stitched together were thus not superimposed by any radiation map in this example. 74
- 3.21 Combination of six planar ^{57}Co sources with 1716 kBq of total activity. 78
- 3.22 Hotspot profile resulting from the combination of six planar ^{57}Co sources with 1716 kBq of total activity, at an average distance of 52 cm from the gamma camera, providing an ambient dose equivalent rate of ~ 330 nSv/h at the measurement point. As the sources had equal activity, it is possible to notice a loss in counts while approaching the limits of the FOV (see Section 2.4.7 for more details concerning the off-axis response of the gamma camera). 79

- 3.23 Radiation image superimposed on the respective optical image resulting from the combination of six planar ^{57}Co sources with 1716 kBq of total activity, at an average distance of 52 cm from the gamma camera, providing an ambient dose equivalent rate of ~ 330 nSv/h at the measurement point. 79
- 3.24 The results of the superimposition of three different measurements performed with the gamma camera prototype, placed at three different pan angles (-30° , 0° , and 30°) from a combination of six planar ^{57}Co sources with 1716 kBq of total activity. The average distance between the sources and the gamma camera was 16 cm, providing an ambient dose equivalent rate of ~ 330 nSv/h at the measurement point. 80
- 3.25 Three-dimensional hotspot profile resulting from the radiation image stitching technique designed and implemented for the EduPIX. In this example, three radiation images resulting from three different measurements have been combined into a final coherent composite decoded γ -image. 81
- 3.26 A stitched gamma image resulting from three different measurements superimposed on the respective optical image. 81
- 3.27 A panorama image with size 12574×2316 pixels, with an horizontal and vertical FOV respectively of 360° and 66° , resulting from the stitching of 80 optical images and the superimposition of 4 γ -images. For illustration purposes, the image is shown in black and white. 83
- 3.28 Performing measurements with the prototype (on the right) at 2 meters from the ATLAS beam pipe. The estimated dose rate at the camera location ranged between 3.5 and 4 $\mu\text{Sv/h}$, depending on its position and orientation. The dose rate was measured with the CANBERRA instrument Colibri VLD (Very Low Dose). . . . 85
- 3.29 A panorama image with size 8494×1903 pixels, with an horizontal and vertical FOV respectively of 360° and 80° , resulting from the stitching of 120 optical images and the superimposition of 2 γ -images. For illustration purposes, the image is shown in black and white and two black stripes have been added, in order to obtain a $360^\circ \times 180^\circ$ format with a width/height ratio of $360/180 = 2$. . . 86
- 4.1 A point \mathbf{X} in the 3-D space projected onto three views, resulting in three corresponding image points \mathbf{x}_1 , \mathbf{x}_2 , and \mathbf{x}_3 . In the ideal case, the respective rays intersect at \mathbf{X} 90
- 4.2 Part of the gamma imaging portable system used for retrieving the 3-D position of radioactive hotspots. 92
- 4.3 Example of optical image coupled with the respective depth map. 93
- 4.4 First version of the acquisition prototype built and adopted for the experiments. . 94
- 4.5 The final version of the acquisition prototype built and adopted for the experiments, consisting of two gamma imaging systems with the respective optical cameras, and a depth sensor. 95

- 4.6 A camera can be interpreted as a mapping between the 3-D world and a 2-D image. \mathbf{C} is the camera centre and \mathbf{p} is the principal point. The camera centre is placed in this case at the origin of the coordinate plane [146]. 97
- 4.7 The transformations world-to-camera coordinate frames. 99
- 4.8 (a) The two cameras are indicated by their centres \mathbf{C} and \mathbf{C}' and image planes. The camera centres, 3-space point \mathbf{X} , and its images \mathbf{x} and \mathbf{x}' lie in a common plane, π . (b) An image point \mathbf{x} back-projects to a ray in 3-space defined by the first camera centre, \mathbf{C} , and \mathbf{x} . This ray is imaged as a line \mathbf{l}' in the second view. The 3-space point \mathbf{X} which projects to \mathbf{x} must lie on this ray, so the image of \mathbf{X} in the second view must lie on \mathbf{l}' [146]. 100
- 4.9 (a) The camera baseline intersects each image plane at the epipoles \mathbf{e} and \mathbf{e}' . Any plane π containing the baseline is an epipolar plane, and intersects the image planes in corresponding epipolar lines \mathbf{l} and \mathbf{l}' . (b) As the position of the 3-D point \mathbf{X} varies, the epipolar planes rotate about the baseline. This family of planes is known as an epipolar pencil. All epipolar lines intersect at the epipole [146]. . . . 101
- 4.10 Experimental phantom built and used for calibrating two γ -cameras, a depth sensor (the Asus Xtion), and an optical camera. Only the holes labelled with numbers were used in this study. The size of the board is $60 \times 60 \text{ cm}^2$, the holes have 10 mm diameter, and their respective axial separation (horizontal or vertical) is 200 mm. 102
- 4.11 Experimental setup for calibrating a stereo gamma camera, an optical camera, and a depth sensor, rigidly mounted and integrated within the prototype, which was fixed in front of the phantom designed and built for the experiment. 104
- 4.12 Example of calibration frameset: optical image, depth map, and left and right γ -images, all captured with the experimental phantom rigidly fixed in the same position/orientation respect to the prototype. The proposed calibration procedure is deliberately based on only one radioactive point source, in order to significantly maximize its reproducibility. 105
- 4.13 Mean reprojection error concerning all cameras involved in the multi-modal calibration. With the exception of the depth sensor, the mean reprojection error concerning all cameras was below 1 pixels. 108
- 4.14 Reconstructed gamma image, representing the position of 12 radioactive hotspots on the experimental phantom, automatically reprojected on the visible image using the intrinsic and extrinsic parameters retrieved by means of the proposed procedure of the optical and γ -cameras used. 110
- 4.15 Radiation image reprojected on the X-Y plane of the depth image using the camera matrices computed and the relative pose information between the depth and left γ -camera of the prototype. 111

- 4.16 Position and distance *automatically* retrieved by the prototype for an ^{241}Am point source of ~ 360 MBq activity. 112
- 4.17 Position and distance *automatically* retrieved by the prototype for a ^{137}Cs point source of ~ 261 MBq activity. 113
- 4.18 Representation of a radioactive source reconstructed with two γ -cameras. The displacement between the positions of the two points ($\hat{S}_{\gamma L}$ and $\hat{S}_{\gamma R}$) is the disparity. The distance between the centres of the two detectors is the baseline, b . The shown components are not to scale and the reconstruction of the points $\hat{S}_{\gamma L}$ and $\hat{S}_{\gamma R}$ via the coded aperture technique is simplified for illustration purposes. 114
- 4.19 Hotspot profiles and radiation images resulting from a measurement involving a planar ^{57}Co source with activity of 429 kBq, placed at 36 cm from the stereo gamma camera and providing an ambient dose equivalent rate of ~ 340 nSv/h at the measurement point. 116
- 4.20 Distance automatically retrieved for a planar ^{57}Co source with activity of 429 kBq and at 36 cm from the stereo gamma camera, providing an ambient dose equivalent rate of ~ 340 nSv/h at the measurement point. The reference distance according to the Leica Disto D210 was 36 cm. The error in this specific case was thus 2 mm. 117
- 4.21 Depth image (on the left) and radiation image superimposed on the respective optical image (on the right). For this measurement, 60 frames of 1 sec shutter time were collected with the left gamma camera, only in mask position. The ^{241}Am source of ~ 360 MBq was placed at 125 cm from the prototype. A value of 124.5 cm was automatically retrieved from the registered depth map. The error was thus 0.5 cm. 117
- 4.22 Results concerning the position and the estimated distance of an ^{241}Am source of ~ 360 MBq, placed at 125 cm from the stereo gamma camera prototype. The left radiation image (a) is the result of 60 collected frames of 1 sec shutter time in mask mode, while for the right radiation image (b) 90 frames were collected with the same shutter time. A value of 120.01 cm was automatically retrieved by means of stereo gamma imaging. The error was therefore ~ 5 cm. 118
- 4.23 Depth image (on the left) and radiation image superimposed on the respective optical image (on the right). For this measurement, 120 frames of 1 sec shutter time were collected, only in mask position. The ^{241}Am source of ~ 360 MBq was placed at 300 cm from the prototype. A value of 303.7 cm was automatically retrieved from the registered depth map. The error was therefore 3.7 cm. 119
- 4.24 Results concerning the position and distance of an ^{241}Am source of ~ 360 MBq, placed at a measured distance of 300 cm from the prototype. 120 frames of 1 sec shutter time were collected in mask mode with each γ -camera. A value of 292.7 cm was automatically retrieved by means of stereo gamma imaging, with an error of 7.3 cm. 120

- 4.25 (a) An ^{241}Am source of ~ 360 MBq activity placed behind a wall while (b) the prototype is on the other side of the same wall, pointed at the source at a total measured distance of 190 cm, and providing an ambient dose equivalent rate of ~ 320 nSv/h at the measurement point. 120
- 4.26 Left and right radiation images generated by the stereo gamma camera. For this measurement, 180 frames of 1 sec shutter time were collected with each detector, only in mask position. 121
- 4.27 A ^{137}Cs source of 329 MBq activity placed inside a barrel with diameter of 60 cm. The barrel was placed so that its horizontal centre was at 280 cm from the prototype. The source was then carefully placed at such distance inside the barrel. For this measurement, 300 frames of 1 sec shutter time were collected with both gamma cameras, in mask and antimask positions. In the left view, the distance retrieved from the depth map at the location of the centre of the located source is displayed. In the right view, the distance retrieved by means of stereo gamma imaging is displayed (Laboratoire simulation et techniques de démantèlement nucléaire, CEA Marcoule). 121
- 4.28 Theoretical calculation of the disparity of two corresponding points in two given radiation images as a function of the distance values (in mm). 124
- 4.29 Error ΔZ , in mm, as a function of the source-to-detector distance and the baseline of the stereo gamma camera (the baseline of the prototype built for this study is 92 mm). 125
- 4.30 3-D coloured point cloud representing a CANBERRA laboratory in Montigny-le-Bretonneux, acquired and processed with the prototype. In this example, no radiation sources were present. 126
- 4.31 Point cloud generated by the prototype and rendered via MeshLab, representing the results obtained with mask R7e4 and by placing several ^{57}Co sources adjacently, in order to simulate a pipeline elbow with 1716 kBq of total activity, at an average distance of 64 cm from the gamma camera. The associated ambient dose equivalent rate at the measurement point was ~ 280 nSv/h (experiment performed at the CEA LIST laboratory, at Saclay). 128
- 4.32 Portion of the multimodal point cloud of the radioactive pipe as rendered by MeshLab. The little orange arrows and the respective quantities (expressed in mm) are displayed by MeshLab when extracting metric information from the scene under study. 129
- 4.33 Two point clouds generated by the prototype and rendered by MeshLab regarding a ^{137}Cs source of 329 MBq activity, placed inside a barrel with diameter of 60 cm. The experiment was conducted at the CEA Marcoule laboratory (Laboratoire simulation et techniques de démantèlement nucléaire). 129
- A.1 Illustration of the particle fluence definition. 152

A.2	Absorbed dose and kerma as function of the depth within matter with (dashed lines) and without (solid lines) attenuation for an incident uncharged radiation.	154
A.3	Concept of ambient dose equivalent $H^*(10)$	157
A.4	Concept of the directional dose equivalent, $H'(d, \Omega)$	158
A.5	Calibration of the personal dose equivalent, $H_p(d)$	159
A.6	ISO phantoms representing parts of human bodies (torso, arm, and finger).	159
B.1	Cluster ToT distributions measured with the mask R7e8 under different shutter-times for the N-15 ($E_{\text{mean}} = 13.3$ keV) X-ray narrow beams of varied currents. Owing to the photoelectric process there is a single full-energy peak.	161
B.2	Cluster ToT distributions measured with the mask R7e8 under different shutter-times for the N-20 ($E_{\text{mean}} = 16.9$ keV) X-ray narrow beams of varied currents. Owing to the photoelectric process there is a single full-energy peak.	162
B.3	Cluster ToT distributions measured with the mask R7e8 under different shutter-times for the N-30 ($E_{\text{mean}} = 24.6$ keV) X-ray narrow beams of varied currents. Owing to the photoelectric process there is a single full-energy peak.	163
B.4	Cluster ToT distributions measured with the mask R7e8 under different shutter-times for the N-60 ($E_{\text{mean}} = 47.6$ keV) X-ray narrow beams of varied currents. Besides the full-energy peak, an additional one appears on the left at around 13 ToT (i.e. $1.4 \mu\text{s}$).	163
B.5	Cluster ToT distributions measured with the mask R7e8 under different shutter-times for the N-40 ($E_{\text{mean}} = 33.0$ keV) X-ray narrow beams of varied currents. Owing to the photoelectric process there is a single full-energy peak.	164
B.6	Cluster ToT distributions measured with the mask R7e8 under different shutter-times for the N-80 ($E_{\text{mean}} = 65.3$ keV) X-ray narrow beams of varied currents. Unlike the full-energy peak, the additional one does not move to the right with increasing the incident photon energy.	164
B.7	Cluster ToT distributions measured with the mask R7e8 under different shutter-times for the N-150 ($E_{\text{mean}} = 118.4$ keV) X-ray narrow beams of varied currents. Unlike the full-energy peak, the additional one does not move to the right with increasing the incident photon energy.	165
B.8	Cluster ToT distributions measured with the mask R7e8 under different shutter-times for the N-200 ($E_{\text{mean}} = 154.5$ keV) X-ray narrow beams of varied currents. Data obtained with a 10^{-5} sec shutter-time and at low (1 mA) beam input current were statistically insignificant and are not reproduced here. Unlike the full-energy peak, the additional one does not move to the right with increasing the incident photon energy.	165

- B.9 Cluster ToT distributions measured with the mask R7e8 under different shutter-times for the N-250 ($E_{\text{mean}} = 207.3$ keV) X-ray narrow beams of varied currents. Data obtained with a 10^{-5} sec shutter-time and at low (1 mA) beam input current were statistically insignificant and are not reproduced here. The measurement files for 10^{-5} sec shutter-time and 5 mA beam input current were corrupted. The full-energy peak is no longer visible whereas the additional one is still appearing. 166
- B.10 Cluster ToT distributions measured with the mask R7e8 under different shutter-times for the N-300 ($E_{\text{mean}} = 247.5$ keV) X-ray narrow beams of varied currents. Data obtained with a 10^{-5} sec shutter-time and at low (1 mA) beam input current were statistically insignificant and are not reproduced here. The full-energy peak is no longer visible whereas the additional one is still appearing. 166